

# **Combustion Modification by Non-Thermal Plasma**

## **Dissertation**

zur Erlangung des akademischen Grades

**Doktoringenieur  
(Dr.-Ing.)**

von M. Sc. Ali BOURIG

geb. am 18. April 1982 in Iknioune (Marokko)

genehmigt durch die  
Fakultät für Verfahrens- und Systemtechnik der  
Otto-von-Guericke-Universität Magdeburg.

Promotionskommission:

Prof. Christophe Laux (Vorsitz)

Prof. Dominique Thévenin (Gutachter)

Prof. Jean-Pierre Martin (Gutachter)

Prof. Uwe Riedel (Gutachter)

eingereicht am: 6. April 2009

Promotionskolloquium am: 16. Juli 2009





**UNIVERSITÉ D'ORLÉANS**  
**OTTO-VON-GUERICKE-UNIVERSITÄT MAGDEBURG**  
**Institut de Combustion Aérodynamique Réactivité & Environnement (ICARE)**  
**CNRS, Orléans, France**  
**Lehrstuhl für Strömungsmechanik und Strömungstechnik (LSS)**  
**Magdeburg, Germany**

A Thesis submitted to the Faculties  
of  
Verfahrens und Systemtechnik (Magdeburg) and Science and Technology (Orléans)  
by

**Ali BOURIG**

For the degree of Doctor-Engineer

Defence: **16 July 2009**

Discipline / Speciality: Energy and Process

**COMBUSTION MODIFICATION BY  
NON-THERMAL PLASMA**

**THESIS directed by :**

[M. Jean-Pierre MARTIN]  
[M. Dominique THEVENIN]

[Research director, ICARE, CNRS]  
[Professor, LSS, Otto von Guericke University, Magdeburg]

**EXAMINATORS :**

[M. Christophe LAUX]  
[M. Uwe RIEDEL]

[Professor, EM2C, Ecole Centrale Paris]  
[Professor, Stuttgart University]

**JURY :**

[M. Christophe LAUX]  
[M. Jean-Pierre MARTIN]  
[M. Dominique THEVENIN]  
[M. Uwe RIEDEL]

[Professor, EM2C, Ecole Centrale Paris] Jury president  
[Research director, ICARE, CNRS]  
[Professor, Otto von Guericke University, Magdeburg]  
[Professor, Stuttgart University]

This work was carried out at the Otto-von-Guericke University, Faculty of Process and Systems Engineering, and at ICARE from the Centre National de la Recherche Scientifique (CNRS) with support of the Region Centre and Land Sachsen-Anhalt and of the European Union, under INTAS project n°: 03-51-4736.

Ali Bourig.  
The University of Orléans, the University of Magdeburg, 2009  
Supervisors : Jean-Pierre Martin and Dominique Thévenin

# Acknowledgments

A thesis is seldom the work of a single person in isolation, particularly in a European context; it is the result of a research activity involving a bunch of people. I am pleased now to acknowledge those who have, in various ways, contributed.

First of all, I express my sincere thanks to my supervising professors, Dominique Thévenin and Jean-Pierre Martin, for their guidance and support and for permitting me to perform this work in their laboratories. This work is the result of their constant inspiration and positive encouragements, for giving me the opportunity to develop this experience abroad and challenging me every day to make me a better scientist. I want to thank the ICARE institute and the Lehrstuhl für Strömungsmechanik and Strömungstechnik for giving me permission to begin this thesis in the first instance.

I wish to express my profound gratitude to my co-advisers, Viviana Lago and Katharina Zähringer, for their support, patience and guidance all along my thesis. The freedom of work and the constant encouragements they gave me while I began plasma physics and optical diagnostics studies were really important.

I take the opportunity to thank once again Katja and Dominique. They put a roof over my head when I arrived in Magdeburg and I felt at home ever since.

Although doing a Ph D is somehow a lonely process you need many people to collaborate with, whose skills allow the project to mature. I wish to thank our project partners from Heat and Mass Transfer Institute in Minsk: Prof. Academician Sergey Zhdanok, Fiodar Pliavaka, Sergey Gorbатов, and Sergey Shushkov. I am also grateful to my friend Kiryl Pliavaka, Ph.D student and INTAS young fellow scientist. I would like to express my sincere gratitude to all of them, for continuing support and collaboration, as well as for their help particularly in setting up and operating the pulsed power supply!

Thanks to the people of the CIAM, Moscow in name of Pr. Starik, people of the MSU in name of Pr. Shatalov, people of IFPHT, Kiev in name of Dr. Naumov and Dr. Zizak from the CNR, Milano. I am also grateful to Dr. Motoshi Goto from the National Institute for Fusion Science in Japan for sending me the collisional Radiative numerical code for Helium and Pr. Andrew Orr-Erring from Bristol University for providing me the PGOPHER<sup>®</sup> code.

Furthermore, I would like to thank the members of my reading committee, Pr. Christophe Laux and Pr. Uwe Riedel for taking the time to assess my manuscript. Your advices for some final corrections are greatly appreciated.

At last but not least, I wish to thank those who funded this work: The Region Centre (France) and the Sachsen-Anhalt Land (Germany). This research is also supported by a grant from the French-German University. Also, the present work is linked to the European INTAS project titled “Kinetics and Mechanism of Ignition/Combustion Initiated by Electronically Excited Singlet Oxygen” (INTAS Ref. No: 03-51-4736). This program is an international association for promotion of co-operation with scientists from the new independent states of the former Soviet Union.

I also wish to thank the many people who helped me and the time spent and discussions from science to philosophy. Thanks to the technical persons from Orleans and Magdeburg for their constant help and collaboration. Thanks to Emerson, Rachid, Alper, Gabor, Tobias, Andreas, Thomas, Raman, Santosh, Mohammed and Hemdan for their exceptional friendship. My best regards are sent to my Hiwis :”the 3 Martins” for their investment in my experimental Ph.D work.

Finally, the 5<sup>th</sup> of January 2008 was an important date of my life; I thank Jean-Pierre, Marie-France, Viviana and Philippe for their presence for my wedding.

So this is the time for a last and personal word. During those 3 years in Orléans and Magdeburg I shared a lot of nice moments with a lot of people. Throughout these years I have met a lot of people outside and inside the work sphere that contributed to make this adventure possible and enjoyable. Finally, the purpose of this page is to say thank you to all of you!

*This dissertation is dedicated to my wife for her help and encouragement, and to my father, mother, brothers and sisters for their encouragement and extensive support.*

*“La recherche scientifique est un sport individuel que l'on est obligé de pratiquer en équipe”.*

***Roger Rimet***

# Preface

## Before this study

The actual collaboration was initiated more than 15 years ago during the first exchanges, in the framework of international conferences, between Dr. Jean-Pierre Martin and Prof. Academician Serguei Zhdanok. It was indeed shaped during stay of Serguei Zhdanok in 1993 in the team of Jean Pierre Martin, on a SPI CNRS red position.

Several stays of young researchers strengthened the collaboration between 1993 and 1995 (P. Porshnev and L. Porshneva performed several stays of 3 months, on subventions of the SPI and DRI of the CNRS). They intensified as part of two INTAS projects, among which one was still active for my Ph.D project.

Combustion efficiency plays a critical role in energy production and environmental pollution. The development of any efficient combustion methodology demands detailed experimental studies, relevant theoretical modelling and numerical simulations in order to achieve a comprehensive understanding of the underlying fundamentals of the combustion process. Several research groups work on the effect of an electric field on the flame behaviour. The main ideas are the possibility to apply electric fields for stabilization of the flames, reducing soot formation, increasing flame velocity, extending flammability limits or increasing flame luminosity.

The goal of the present Ph.D study is to look for alternative approaches capable to improve the efficiency of combustion. A novel idea to reach this goal includes the use of excited oxygen molecules, which can either be in vibrationally and/or in electronically excited states.

A numerical and an experimental study of combustion with excited species have been carried out with non-equilibrium physical-chemical kinetics in gases and plasma during two INTAS projects 00-55-6556 and 03-51-4736 « Kinetics and Mechanism of Ignition/combustion initiated by Electronically Excited Singlet Oxygen » by joint efforts of researchers from France, Germany, Italy, Belarus, Russia and Ukraine. INTAS projects were organised as an international co-operation and were managed by a consortium of research teams including 7 laboratories :

- ICARE institute (Dr. J-P. Martin, CNRS, Orleans) ;
- Heat and Mass Transfer Institute (Prof. S. Zhdanok, HMTI, Minsk, Belarus) ;
- Institute of Fundamental Problems for High Technology (Dr. V. Naumov, IFHPT, Kiev, Ukraine) ;
- MSU-Moscow State University (Dr. O.P. Shatalov, Moscow, Russia) ;
- Central Institute of Aviation Motors (CIAM) (Prof. A.M. Starik, CIAM, Moscow) ;
- Milano-CNR (Dr. Zizak) ;
- Heidelberg University (Prof. J. Wolfrum and J. Warnatz).

## Presentation of the partners

The present Ph.D project, supported by region Centre and Sachsen-Anhalt is constituted of four steps (two experimental parts and two numerical parts) carried out respectively in Orléans and in Magdeburg and co-supervised by the German and French partners. The work plan is divided in two parts ; first 18 months took place at ICARE and the last 18 working months took place within the laboratory partner in Magdeburg.

## Objectives and contents of the Ph.D project

Increasing the efficiency of combustion processes is one of the greatest challenges for the future due to the limited fossil fuel resources and their environmental impact. In this context, plasma assisted combustion processes are of great importance for future technical developments. Among different existing technologies, a significant attention is given to possible combustion intensification by plasma. Activation of either combustible or oxidizer leading to production of active molecules,

atoms and radicals can be realized by electrical discharges, laser radiation, UV radiation, chemiluminescence reactions and so on... One of the most effective and energy favourable methods of excitation of vibrational and electronic states of atoms and molecules is electron impact with gas in a volume electrical discharge. Through excitation of internal degrees of freedom of molecules, that leads to a modification of electron configuration, the reactivity of molecules changes. Electronic excitation can also influence the course of a chemical reaction by increasing the energy content of the system or by affecting access to different potential energy surfaces by changing spin, orbital symmetry, or spin-orbit level.

The project is devoted to research in the field of combustion assisted by nonthermal plasma. Work objectives consist on the development of a method of plasma assisted combustion for higher fuel burning efficiency based on acceleration of chain reactions by excitation of internal degrees of freedom of oxygen molecules. The scientific idea consists in the realization of the most effective and energy favourable method of excitation of O<sub>2</sub> molecules in their two first electronic states: O<sub>2</sub>(a<sup>1</sup>Δ<sub>g</sub>) and O<sub>2</sub>(b<sup>1</sup>Σ<sub>g</sub><sup>+</sup>), also called singlet oxygen. This can open new and potentially important possibilities in combustion technologies since it will provide high efficiency in terms of promotion of combustion and low pollutants emission.

The project is divided into four parts :

1- First of all, a state of the art concerning nonthermal plasma, electronically excited oxygen generation and plasma assisted combustion is undergone.

2- After that, the method to produce excited oxygen species is chosen and necessary plasma facilities were designed and built.

In a first step, production of excited oxygen is performed via an electric discharge technique. Objectives of this first study concern the feasibility to excite oxygen in its singlet electronics states O<sub>2</sub>(a<sup>1</sup>Δ<sub>g</sub>) and O<sub>2</sub>(b<sup>1</sup>Σ<sub>g</sub><sup>+</sup>) and excited atomic oxygen. The second step was a study of the effects of systematic changes in operating parameters with the objective of maximizing the excited oxygen species yield.

3- Finally, development of hybrid burners and methods of supplying excited oxygen are presented. This comprises the steps of exciting an oxygen gas mixture in a plasma discharge zone thereby forming an excited oxygen discharge flux, and transferring it into a flame reaction zone disposed next to the plasma discharge zone. Several experimental burners working at atmospheric and reduced pressure and integrating discharge reactors are developed. The analysis of effects of singlet oxygen excitation on basic characteristics of combustion with development and optimization of combined plasma-burners are undergone. Also, the role of the excited species (molecules, atoms and radicals) in the intensification of combustion is investigated.

4- In parallel, modelling of the energy distribution in the discharge is presented for pure and diluted oxygen gas mixtures. The numerical modelling of the combustion processes in the presence of electronically excited oxygen molecules is carried out. It is relevant to stress that works related to reactions of electronically excited oxygen are still limited and its influence on basic characteristics of combustion, such as ignition thresholds, ignition delay and burning velocity, even in H<sub>2</sub>/O<sub>2</sub> mixtures is has still not been studied properly.

## Summaries

**Ali BOURIG**

### **MODIFICATION DE LA COMBUSTION EN PRESENCE D'ESPÈCES EXCITÉES**

Aujourd'hui, il semble que la méthode la plus prometteuse pour intensifier la combustion repose sur l'excitation hors-équilibre du mélange gazeux, qui permet ainsi de modifier la cinétique chimique. Pour obtenir une excitation efficace des degrés de liberté électronique et vibrationnel des molécules, l'utilisation d'une alimentation pulsée associée à une énergie des électrons adéquate est proposée. Ce travail de thèse porte sur l'application de générateur d'impulsion électrique haute fréquence capable de délivrer des pulses de 20 kilovolts pendant 20 nanosecondes ayant des temps de montée de l'ordre de 5 nanosecondes en combustion. Cette étude s'articule autour de deux grands axes de recherche. Le premier est la génération, à pression atmosphérique et à pression réduite, d'espèces excitées (oxygène électroniquement excité  $O_2(a^1\Delta_g)$ ,  $O_2(b^1\Sigma_g^+)$  et oxygène atomique excité) ainsi que leur caractérisation par spectroscopie d'émission. Le second axe de recherche concerne leur utilisation pour l'intensification de la combustion. La première partie expérimentale s'est focalisée sur la génération d'oxygène électroniquement excité par plasma décharge à barrière diélectrique et décharge croisée dans des mélanges  $O_2/He$  et  $O_2/Ar$ . La décharge croisée est une cellule à barrière diélectrique pulsée qui est croisée avec une composante continue (DC). Dans ce cas, l'étape d'ionisation est réalisée par la DBD pulsée alors que la composante continue supporte le courant électrique entre chaque pulse. Le gaz produit par cette installation est étudié de manière exhaustive par spectroscopie d'émission. Ce travail, indispensable pour caractériser l'installation et obtenir les conditions initiales nécessaires pour les calculs de flamme, repose sur différents spectromètres et caméras. La première des applications potentielles dans le domaine de la combustion concerne l'intensification de la combustion par activation de l'oxygène. La conception de prototypes de brûleurs hybrides, intégrant un réacteur plasma nous a permis de valider cette technique d'intensification de la combustion et de la comparer à une flamme classique sans plasma.

Enfin, la modélisation des paramètres fondamentaux d'une flamme de prémélange et de diffusion est entreprise par le logiciel CHEMKIN. L'effet promoteur de l'oxygène excité sur une flamme d'hydrogène a pu être modélisé.

### **COMBUSTION MODIFICATION USING EXCITED SPECIES**

Nowadays it seems that the most promising method for accelerating combustion is the non-equilibrium excitation of the gas mixture components, which allows one to affect the chemical reaction kinetics. To enable more efficient excitation of the electronic and vibrational degrees of freedom, one should use short-duration (nanosecond) pulses with a high reduced electric field.

The present work focuses on the application of high frequency high voltage pulse discharges capable of delivering an electric pulse of 20 kV during 20 ns with controlled voltage rise time of 5 ns and at a frequency up to 25 kHz in combustion. This study articulates around two major research axis; that of the generation of excited species and particularly the feasibility to produce excited oxygen species in its singlet electronic states  $O_2(a^1\Delta_g)$  and  $O_2(b^1\Sigma_g^+)$  by a non-thermal electric discharge, at reduced pressure until atmospheric pressure and its characterization by emission spectroscopy. The second research axis concerns their use for the intensification of combustion. The experimental part of the study concerns investigation of singlet oxygen production in the application of a dielectric barrier discharge in  $O_2/He$  and  $O_2/Ar$  binary mixtures. The second discharge is a special crossed discharge plasma-chemical reactor that has been developed. This crossed discharge consists of a hybrid discharge in which short high voltage pulses produce ionization while a comparatively low electric field supports the electric current between ionizing pulses. The gas produced by this installation is intensively studied by emission spectroscopy. This work, indispensable to characterize the installation and to obtain initial conditions necessary for flame calculations, relies on different spectrometers and intensified camera. The first potential in the combustion field is to significantly improve combustion efficiency and reduce pollutant emissions using oxidizer "activation". Conception and development of

hybrid plasma burner prototypes, integrating crossed discharge plasma reactor allows us to validate this application by comparing with a classical flame without plasma activation. Finally, modelling of premixed flame fundamental parameters is undergone with CHEMKIN software. The promoting effect of excited oxygen on hydrogen flame has been characterized.

## **VERRINGERUNG DER ABGASEMISSIONEN AUS DER VERBRENNUNG DURCH DIE VERWENDUNG VON ANGEREGTEN RADIKALEN**

Heutzutage scheint es, daß die vielversprechendste Methode Verbrennung zu intensivieren, auf der Nichtgleichgewicht-Anregung des Gasmisches beruht, die erlaubt die chemische Reaktionskinetik zu beeinflussen. Um effiziente Anregung der elektronischen und vibrationellen Freiheitsgrade der Moleküle zu erreichen, sollten kurze (Nanosekunden-) Pulse mit einem stark reduzierten elektrischen Feld verwendet werden.

Die vorliegende Arbeit konzentriert sich auf die Anwendung von hochfrequenten Hochspannungspulsentladungen, die elektrische Pulse von 20 kV während 20 ns mit einer kontrollierten Spannungsanstieg-Flanke von 5 ns und einer Frequenz von bis zu 25 Kilohertz liefern. Diese Studie konzentriert sich um zwei Hauptforschungsachsen: die der Generation des angeregten Sauerstoffs,  $O_2(a^1\Delta_g)$  und  $O_2(b^1\Sigma_g^+)$ , mittels elektrischer Nichtthermalentladung, von reduziertem Druck bis zu atmosphärischem Druck und seine Charakterisierung durch Emissionsspektroskopie. Die zweite Forschungsachse betrifft die Verwendung von  $O_2^*$  für die Erhöhung der Verbrennungseffizienz. Der erste Teil der Studie betrifft die Untersuchung der angeregten-Sauerstoff Produktion durch eine dielektrische Barriere-Entladung in  $O_2/He$  und  $O_2/Ar$  Mischungen. Diese wird gekreuzt mit einer kontinuierlichen Gleichspannungs-Entladung. Diese Kreuz-Entladung besteht also aus einer hybriden Entladung, in der kurze Hochspannungspulse Ionisation erzeugen, während ein verhältnismäßig niedriges elektrisches Feld den elektrischen Strom zwischen dem Ionisieren von Pulsen unterstützt. Der erzeugte angeregte Sauerstoff wird ausführlich untersucht und somit Anfangsbedingungen für Berechnungen und die nachfolgende Verwendung in einem Brenner gewonnen. Dadurch soll die Verbrennungs-Leistungsfähigkeit bedeutend verbessert und die Schadstoff-Emissionen reduziert werden. Die Entwicklung von Prototypen des hybriden Plasmabrenners, die die Kreuz-Entladung beinhalten, erlaubten, diese Verbrennungsintensivierung nachzuweisen und mit einer klassischen Flamme ohne Plasmaaktivierung zu vergleichen.

Schließlich, wird die Beschreibung, einer Vormischflamme anhand von Modellen, durch die Software CHEMKIN unternommen. Sehr Die Verstärkende Wirkung des angeregten Sauerstoff auf eine Wasserstoffflamme konnte dabei gezeigt werden.



**Institut de Combustion Aérothermique Réactivité et  
Environnement (ICARE), 1C Avenue de la recherche  
scientifique, Orléans, France.**

**Lehrstuhl Strömungsmechanik & Strömungstechnik (LSS)  
Otto-von-Guericke Universität  
Universitätsplatz 2, D-39106 Magdeburg, Germany.**



**SACHSEN-ANHALT**

## Summary

Since primitive man mastered fire, which is considered to have taken place far back into the prehistoric period, the techniques for producing fire have been actively improved. Although the majority of substances is completely burned during the course of combustion and is converted to stable oxides, some of the substances are incompletely burned and yield various types of products, e.g., carbon monoxide, nitrogen oxides, aldehydes, and soot particles are exhausted. These substances are deleterious to the global environment and human health. Particularly dioxins, also known as environmental hormones act as endocrine disturbing chemicals.

All the countries of the world are required to take immediately measures against such pollution. In light of the present situation set forth, the object of the present project is to provide a combustion method, by which efficiency of combustion is increased with reduction of generation of harmful substances.

In 1992, at the Rio Earth summit, United Nations convention on climatic changes, today ratified by 186 countries, acknowledged the existence of the climatic change of human origin and imposed the primate of responsibility on industrial countries to fight against this pollution. Later, the Kyoto protocol concluded in December 1997 illustrated the necessity to fight against anthropique origin and reinforced pressure.

Requirements of the users and concerns of public health drive to an ineluctable hardening of acceptable norms for pollutant emissions of combustion systems (internal combustion engines, gas turbines, domestic boilers, industrial ovens...). Actually used methods, based on better operating conditions in the combustion chamber or on a subsequent catalytic depollution are efficient but cannot resolve this problem themselves because the limits of these techniques are reached. Among alternatives, the use of excited species in the combustion process to change the operation regime and reduce the direct emissions, or in post treatment stage to degrade pollutants, constitutes a research axis still not much explored. In view of this situation, the object of this project is to offer a method of combustion, by which the combustion efficiency would be increased and by limiting the pollutant emissions.

Oxygen which is contained in air and contributes to ordinary combustion has a multi-electron system in a stable ground state. The ground state of an oxygen molecule has a spin quantum number of one and hence corresponds to a multiplet state of spin degeneracy equal to three (hereinafter referred to as "triplet oxygen"). Oxygen molecules in a singlet state, i.e., an excited state, (hereinafter referred to as "singlet oxygen") are highly reactive and have a relatively short chemical lifetime.

In a case where triplet oxygen is converted to singlet oxygen, various reactions by singlet oxygen considerably differ from those by triplet oxygen, and hence products resulting from oxidation of a substance by singlet oxygen also considerably differ from products resulting from oxidation of a substance by triplet oxygen.

Accordingly, to solve the foregoing problem, the present project provides a method of converting a portion of the triplet oxygen molecules involved in combustion into singlet oxygen molecules. Among different possible techniques, electrical discharges are employed for exciting triplet oxygen to singlet oxygen. Singlet oxygen  $O_2(a^1\Delta_g)$  and  $O_2(b^1\Sigma_g^+)$  have an energy level of 22.5 kcal/mol and 36.5 kcal/mol higher than that of triplet oxygen in the ground state, respectively. Thus, when a substance to be burned is in the presence of highly reactive singlet oxygen, one can expect that the substance can be burned more efficiently at temperatures lower than that required for burning it in the presence of triplet oxygen.

The institute ICARE has already shown the possibility to improve the ignition of a combustion system and to reduce the production of soot particles by electronic excitation of oxygen. This study will concern, in a complementary way, numerical modelling and experimental studies of influence of electronic and vibrational excitation of oxygen on the enhancement of combustion and on the reduction of the pollutant emissions. This study articulates around two main research axes which are the generation of excited species by electrical discharge and its application in combustion.

The first potential applications in the field of combustion concerns the ignition of a combustible mixture and allowed different research teams to validate this technology of ignition and to compare it with a classical spark ignition. The second application concerns the stabilization by a discharge of a

lifted turbulent flame. This technique allows, for a given height of stabilization, to increase the gas flow speed by about 80 %. The electrical power injected into discharges corresponds to 1/1000<sup>th</sup> of the flame energy. As part of this study, the application of pulsed discharges, of high voltage, high frequency, with dielectric barriers and crossed discharges (i.e. pulsed discharge coupled with DC discharge), in a gaseous mixture containing oxygen, allows to generate some electronically excited molecular oxygen. The addition of gas diluent, helium, allows increasing the discharge efficiency.

Utilization of singlet oxygen for combustion reactions, e.g. burners, requires generation of a significant amount of singlet oxygen in a short period of time and a continuous supply of singlet oxygen to the combustion chamber. Utilization of electrical discharge is suitable for producing singlet oxygen from triplet oxygen, to be used for combustion reaction. In the present research project, singlet oxygen is produced by non-self sustained discharge by feeding, e.g., a triplet-oxygen-containing gas, into a discharge reactor together with a rare gas (helium, argon), and by application of an electric field of frequency on the order of tens of kilo-Hertz. As is experimentally demonstrated, singlet oxygen can be sustained in an excited state for some centimetres out of the discharge reactor at reduced pressure. As a result, sufficient time can be ensured to transport the singlet oxygen to the combustion zone, so as to contribute to combustion reaction.

The first experimental part was focused on the generation of excited oxygen by dielectric barrier discharge plasma with:

- The installation of the generator of excited oxygen within pressure range of  $7 \cdot 10^{-2}$  - 1 atmosphere. Bibliographic study confirmed that the quantity of excited oxygen by barrier discharge increased when the pressure in the generator decreases. It was thus decided to build a combustion test bench that can work at reduced pressure.
- Gas produced by this installation is then exhaustively studied by spectroscopy. This work, necessary to characterize the installation and to acquire initial conditions for modelling, rests on different available spectrometers.
- Protection of the environment from strong electromagnetic interferences generated by high voltage pulse generator and discharge load. It was therefore necessary to realize a Faraday cage and a mass plan of high quality.
- Afterwards, we focus on the development of discharge cells and on emission spectra analysis in view to produce, to identify electronically excited oxygen emission and to determine plasma rotational temperature. In cooperation with the researchers from Minsk and Kiev, we could accomplish the first detection of excited oxygen in a crossed discharge produced at atmospheric pressure. Up to now, this production had been done at reduced pressure.
- On the other hand, modelling of plasma showed that molecular oxygen, in order to be efficiently excited by electronic impact, requires an optimal electron energy. Therefore we have developed crossed discharge reactors. The crossed discharge reactor is a hybrid discharge in which on one hand high voltage short impulsions allow to ionize gas and on the other hand, a weak electrical field, created by a DC voltage supports the discharge between two pulses. The sustainer electrical field can be controlled independently and adjusted near optimum for oxygen excitation in its two electronically singlet states.

For experiments, a high frequency high-voltage pulsed power supply, capable of generation of electric pulses with peak amplitude up to 25 kV, pulse duration of ~10-20 ns, and repetition rate up to 25 kHz was applied, and an original flowing discharge cell was designed and optimized. The final crossed discharge set-up combined two high-voltage discharges in one chamber: a high frequency pulse dielectric barrier (DBD) discharge and a direct current (DC) discharge, which work in a pair. The DB consisted of two parallel electrode plates, made of stainless steel or copper, coated by ceramics. The DC had two opposite stainless steel electrodes, with shaped surfaces. The flow channel in the discharge cell had a rectangular section. Such avalanche controlled mode allowed to adjust the  $E/n$  close to the optimum for e-impact excitation of  $O_2^*$ .

The study of the electronically excited state  $O_2(b^1\Sigma_g^+)$  in a non-self sustained crossed discharge at relatively low pressure (100-300 Torr) allows detecting noticeable quantities of  $O_2(b^1\Sigma_g^+)$ . The discharge and post-discharge characterization by analysing the effects of pressure, DC sustainer voltage,  $O_2$  concentration as well as admixture of small quantities of NO on excited oxygen species evolution have been realized, allowing us to optimise the experimental conditions to maximize excited oxygen yield and to evidence production of excited oxygen species still up to 1 cm outside of the

CDR. The temperature, is a critical point for interpretation of the results. The temperature determination shows that the flow temperature rise in the discharge is rather modest, in the order of 10 to 60 K without NO, while 120 K is found with NO admixture in the O<sub>2</sub>/He gas mixture. Therefore, in the presence of NO, careful experiments should be done to distinguish the chemical and the heating effects of the discharge.

Applications of excited oxygen species in plasma-assisted combustion experiments concern the second experimental part. The study of a flat nonpremixed flame in counterflow configuration and a partially premixed flame generated in specially developed hybrid burners that integrate a crossed discharge plasma reactor is done. The study of the flame structure in presence or not of plasma is performed by emission spectroscopy and by imaging study by intensified CCD camera.

Using spectroscopy, it has been demonstrated that radical species concentrations increase noticeably when starting the CDR. Plasma activation leads to an increase of CH\* by 22%, of C<sub>2</sub>\* by 5% to 10%, of OH\* by 3%.

Nevertheless, a major problem appeared with this configuration: we have been unable to measure any excited oxygen in the flame region. Indeed, due to the counterflow configuration and under atmospheric conditions, the production of excited oxygen is reduced, and the deexcitation is very fast. Conditions are not optimal, leading to very low O<sub>2</sub>(b<sup>1</sup>Σ<sub>g</sub><sup>+</sup>) concentration. We suggest, in a second step, suitable modifications associated with a new burner adapted for optimal excited oxygen production and flame/excited oxygen interaction.

In this latest case, the combustion enhancement is evidenced and is increased when one is situated in the optimal conditions for excited oxygen production. For example, operating at higher flowrate, the penetration of excited species into the flame zone increases, thus increasing the observed flame intensification. The results evidence an average overproduction of OH\* (+37%), C<sub>2</sub>\* (+19%) and CH\* (+12%).

To conclude, electronically excited O<sub>2</sub>\* appears to be a very efficient way to promote methane combustion.

Finally, modelling of premixed flame fundamental parameters is undergone with CHEMKIN® software. The promoting effect of excited oxygen on hydrogen flame has been characterized. This work reports numerical results obtained for a premixed and a counterflow diffusion mode of combustion in a subsonic H<sub>2</sub>-O<sub>2</sub> mixture in the presence of excited oxygen molecules. The analysis showed that even a small number of O<sub>2</sub>\* molecules (5%) in the H<sub>2</sub>-O<sub>2</sub> mixture allows one to noticeably reduce the ignition delay time and to ignite the mixture at a lower temperature. The results obtained confirm qualitatively the observed intensification of combustion of a methane-oxygen mixture by means of excitation of O<sub>2</sub> molecules by electrical discharge.

## Résumé

Depuis que l'Homme à appris à maîtriser le feu, les techniques ont été activement améliorées. Pendant la combustion, certaines substances ne sont pas complètement brûlées et génèrent des sous-produits de différents types, tels le monoxyde de carbone, les oxydes d'azotes, les aldéhydes et les particules de suies. Ces substances sont nocives pour l'environnement et la santé humaine. Particulièrement, les dioxines, aussi connues comme des hormones environnementales, agissent comme des substances endocrines. Tous les pays du monde sont contraints de prendre des mesures immédiates contre cette pollution. En 1992, au Sommet de la Terre à Rio, la Convention-Cadre des Nations Unies sur les changements climatiques, aujourd'hui ratifiée par 186 pays, a reconnu l'existence du changement climatique d'origine humaine et imposé aux pays industrialisés le primat de la responsabilité pour lutter contre ce phénomène. Devant l'ampleur du problème et la nécessité exprimée de lutter contre l'origine anthropique, le protocole de Kyoto, conclu en décembre 1997 a renforcé la contrainte.

Ainsi, les exigences des utilisateurs et les préoccupations de santé publique conduisent à un durcissement inéluctable des normes tolérables pour les émissions polluantes des systèmes de combustion (moteurs automobiles, turbines à gaz, chaudières domestiques, fours industriels...). Les méthodes utilisées à ce jour, basées sur un meilleur réglage du point de fonctionnement dans la chambre de combustion ou sur une dépollution catalytique ultérieure sont efficaces mais ne peuvent résoudre à elles seules ce problème car les limites de ces procédés sont atteintes. Parmi les alternatives, l'utilisation d'espèces excitées au cours du processus de combustion pour changer le régime de fonctionnement et réduire les émissions directes, ou en phase de post-traitement pour dégrader et rendre inoffensives les espèces polluantes, constitue une piste encore peu explorée. En vue de cette situation, l'objet de ce projet est de proposer une méthode de combustion, par laquelle l'efficacité de combustion serait augmentée en limitant la production des émissions polluantes.

La molécule d'oxygène ( $O_2$ ) possède dans son état fondamental stable un système multi-électrons. Son nombre quantique de spin est égal à un et par conséquent correspond à un état de multiplicité égale à trois. Les deux premiers états électroniquement excités de cette molécule d'oxygène, aussi appelés oxygène singulet, possèdent une multiplicité de un. Ce sont des molécules hautement réactives qui possèdent une durée de vie relativement faible. L'oxygène singulet  $O_2(a^1\Delta_g)$  et  $O_2(b^1\Sigma_g^+)$  se situent à un niveau énergétique de 22.5 kcal/mol et 36.5 kcal/mol au dessus de l'état triplet fondamental, respectivement.

La combustion utilise traditionnellement l'oxygène dans son état fondamental comme oxydant. Une nouvelle conception consiste à rendre la combustion plus efficace en utilisant de l'oxygène excité soit vibrationnellement soit électroniquement.

Dans le cas où l'oxygène triplet est converti en oxygène singulet, les différentes réactions mettant en jeu l'oxygène singulet diffèrent considérablement de celles avec l'oxygène triplet, et par conséquent les produits de réactions de l'oxydation d'une substance par l'une ou l'autre des espèces sont aussi différents. Aussi, le combustible mis en jeu peut être brûlé de manière plus efficace et à des températures inférieures à celles nécessaires en présence d'oxygène fondamental. Ainsi, ce travail propose une méthode pour convertir une part de l'oxygène triplet impliqué en combustion en oxygène singulet et permet donc d'envisager la combustion d'une substance en présence d'oxygène singulet. Parmi différentes techniques envisageables, les décharges électriques sont utilisées. Le but fondamental de ce projet de thèse est de développer une approche nouvelle de la physico-chimie de la combustion en associant la physique des plasmas et la chimie de la combustion. Cette combustion activée ouvre des possibilités importantes sur l'efficacité de la combustion associée à une réduction des émissions polluantes.

L'institut ICARE a déjà démontré la possibilité d'améliorer l'allumage d'un système en combustion et de réduire la production de suies en provoquant l'excitation électronique de l'oxygène. L'étude portera, de manière complémentaire, sur la modélisation numérique et sur des études expérimentales de l'influence de l'excitation vibrationnelle et électronique de l'oxygène sur l'intensification de la combustion et sur la réduction des émissions polluantes. Cette étude s'articule autour de deux grands axes de recherche qui sont la génération d'espèces excitées par décharge électrique et la combustion. La première des applications potentielles dans le domaine de la

combustion concerne l'allumage d'un mélange combustible et a permis à différentes équipes de valider cette technique d'allumage et de la comparer à un allumage classique par étincelle. La seconde application concerne la stabilisation de flamme liftée turbulente en sortie d'injecteur, par un plan de décharge. Ce procédé permet, pour une hauteur de stabilisation donnée, d'augmenter la vitesse débitante de près de 80%. L'énergie électrique injectée dans les décharges streamer correspond à 1/1000ème de l'énergie de la flamme. Dans le cadre de cette étude, l'application de décharges pulsées, haute tension, haute fréquence, en configuration plan-plan à barrière diélectrique et croisée (décharge pulsée couplée à une composante continue), dans un mélange gazeux contenant l'oxygène, permet de générer de l'oxygène moléculaire et atomique électroniquement excité. L'ajout d'un gaz tampon, l'hélium, permet d'accroître l'efficacité de la décharge.

L'utilisation d'oxygène excité en combustion (par exemple dans les brûleurs) exige la production d'une quantité significative de cette molécule pendant une courte période et d'en fournir de manière continue à la chambre de combustion. L'utilisation de décharges électriques pulsées est adéquate. Nous avons alors expérimentalement prouvé que la durée de vie de l'oxygène dans son état singulet permet de l'extraire sur un centimètre en dehors de la zone de décharge et ce à pression réduite. Cette distance permet de garantir l'approvisionnement de l'oxygène excité à un foyer, pour ainsi contribuer à la combustion.

La première partie expérimentale s'est focalisée sur la génération d'oxygène excité par plasma décharge à barrière diélectrique avec:

- La mise en place du générateur d'oxygène excité à pression comprise entre  $7 \cdot 10^{-2}$  et 1 atmosphère. L'étude bibliographique a confirmé que la quantité d'oxygène excité par la décharge barrière augmente lorsque la pression dans le générateur est inférieure à la pression atmosphérique. Il a donc été décidé de prévoir un banc de combustion pouvant fonctionner à pression réduite.

- Le gaz produit par cette installation est ensuite étudié de manière exhaustive par spectroscopie d'émission. Ce travail, indispensable pour caractériser l'installation et obtenir les conditions initiales nécessaires pour les calculs, repose sur différents spectromètres disponibles au laboratoire (UV, visible).

- Protection de l'environnement contre les perturbations électromagnétiques générées par l'alimentation haute tension pulsée : suite aux premières expériences, nous avons détecté de fortes interférences électromagnétiques entre la cellule à décharge et l'environnement, il a donc fallu réaliser une cage de faraday et une mise à la terre de grande qualité.

- Nous nous sommes alors focalisé sur le développement de cellules à décharge et sur l'analyse spectrale des émissions du plasma en vue de détecter l'oxygène excité électroniquement et de déterminer la température de rotation du plasma. Nous avons, en coopération avec les chercheurs de Minsk et de Kiev, pu réaliser la première détection de l'oxygène excité dans une décharge produite à la pression atmosphérique. Jusque là, cette obtention avait été réalisée à pression réduite.

- D'autre part, la modélisation du plasma a montré que pour que l'oxygène moléculaire soit efficacement excité par impact électronique, il faut que l'énergie des électrons soit optimale. Pour cela, nous avons, dans un second temps développé une nouvelle cellule à décharge croisée. La cellule à décharge croisée est une décharge hybride au sein de laquelle d'une part de courtes impulsions haute tension permettent d'ioniser le gaz et d'autre part, un faible champ électrique, créé par une alimentation continue maintient la décharge entre deux pulses. Le champ électrique dit de maintien peut être contrôlé indépendamment et être ajusté près de l'optimum pour l'excitation de l'oxygène en ses deux états électroniquement excités.

Pour la partie expérimentale, un générateur d'impulsions électriques haute fréquence (jusqu'à 25 kHz), délivrant les pulses haute tension (jusqu'à 25kV), de courte durée (~10-20 ns) et avec des fronts de montées courts (~5 ns) est utilisé. Par ailleurs, une cellule à décharge croisée est développée et optimisée. La cellule à décharge finale combine deux décharges haute tension dans une seule enceinte : une décharge haute fréquence à barrières diélectriques (DBD) et une décharge à courant continu (DC), qui travaillent en paire. La DBD est constituée de deux électrodes plates en inox ou en cuivre, positionnées en parallèle et recouvertes d'un matériau diélectrique. La décharge DC est composée de deux électrodes en inox, positionnées en parallèle et ayant une forme spécifique. La cellule complète forme ainsi une section rectangulaire (paires d'électrodes parallèle deux à deux). La spécificité de cette décharge croisée, aussi appelé « mode d'avalanche électronique contrôlé » ou « décharge non entretenue » permet un ajustement précis de la valeur du champ électrique réduit ( $E/n$ )

correspondant à une énergie des électrons optimale pour la production d'oxygène électroniquement excité par impact électronique.

L'étude de la production d'oxygène électroniquement excité  $O_2(b^1\Sigma_g^+)$  par décharge croisée non entretenue à basse pression (100-300 Torr) a permis de détecter une quantité significative de  $O_2(b^1\Sigma_g^+)$ . Une étude paramétrique a permis de caractériser la décharge (dans le volume) et de la post-décharge (en sortie de cellule). L'effet de la pression, de la tension continue ( $U_{DC}$ ), de la concentration d'oxygène dans le mélange gazeux ainsi que l'addition d'une petite quantité de NO a permis d'identifier les conditions expérimentales optimales pour la production de  $O_2(b^1\Sigma_g^+)$ . Par ailleurs, l'analyse par spectroscopie d'émission de la post-décharge a mis en évidence la production d'oxygène excité et le maintien de sa présence 1 cm au-delà de la cellule à décharge.

De plus, la température, étant un point essentiel pour l'interprétation des résultats, est déterminée. Dans les conditions optimales de production d'oxygène excité, une élévation de 10 à 60 K sans la présence de NO et de 120 K en présence de NO est déterminée, respectivement. Ainsi, pour les expériences de combustion assistée par plasma, un plan d'expérience a permis de mettre en évidence un effet chimique et non thermique.

La seconde partie expérimentale concerne l'étude d'une flamme plate non prémélangée à contre-courant et une flamme partiellement prémélangée sur des brûleurs hybrides que nous avons conçus et développés et qui intègrent un réacteur plasma. L'étude du front de flamme en présence ou non de la décharge se fait par spectroscopie d'émission et par caméra intensifiée.

La spectroscopie d'émission est utilisée pour démontrer que la concentration des radicaux augmente de manière significative lorsque la décharge croisée est activée. Cette activation par plasma met en évidence une augmentation de 22% pour  $CH^*$ , de 5% pour  $C_2^*$  et de 3% pour  $OH^*$ .

Cependant, un frein majeur apparaît avec cette configuration : nous n'avons pas été en mesure de détecter d'oxygène excité dans la région de la flamme. En effet, la configuration à contre-courant ainsi que les conditions de pression (pression atmosphérique), font que la production d'oxygène excité est drastiquement réduite, et la désactivation est rapide. Les conditions ne sont donc pas optimales, et mènent à une concentration très faible de  $O_2(b^1\Sigma_g^+)$ .

Nous avons suggéré, dans un second temps, des modifications et le développement d'un nouveau brûleur plus adapté à une production optimale d'oxygène excité et permettant une interaction de ce dernier avec la zone de flamme. Dans ce cas, l'intensification de la combustion a pu être mise en évidence et une corrélation forte entre les conditions expérimentales optimales de production de  $O_2(b^1\Sigma_g^+)$  et l'effet sur la flamme est présenté. Par exemple, en augmentant les débits, la pénétration des espèces excitées dans la zone de réaction de la flamme est augmentée, et par conséquent l'effet promoteur observé sur la flamme est intensifié. Les résultats expérimentaux montrent une surproduction moyenne de 37% pour  $OH^*$ , 19% pour  $C_2^*$  et 12% pour  $CH^*$ . Ces résultats ont permis de conclure sur le fait que l'utilisation de l'oxygène électroniquement excité est un moyen efficace d'intensification de la combustion du méthane.

Finalement, la modélisation des paramètres fondamentaux d'une flamme de prémélange est entreprise par le logiciel CHEMKIN<sup>®</sup>. L'effet promoteur de l'oxygène excité sur la flamme d'hydrogène a pu être modélisé. Le chapitre III présente les résultats obtenus pour une flamme subsonique  $H_2-O_2$  de prémélange et de diffusion à contre-courant en présence d'oxygène excité (oxygène excité produit expérimentalement par décharge croisée à pression atmosphérique et pression réduite). Les calculs montrent qu'en présence d'une petite quantité d'oxygène excité (jusqu'à 5%) dans les gaz frais, les délais d'auto-inflammation sont réduits et le mélange peut être allumé à une température plus basse. Les résultats numériques confirment qualitativement les observations expérimentales d'intensification de la combustion (extension de la flamme et augmentation des radicaux).

# Zusammenfassung

Seitdem der Mensch das Feuer beherrscht, was auf die prähistorische Periode zurückgeht, ist die Technik, Feuer zu machen, aktiv verbessert worden. Obwohl die Mehrzahl von Materialien im Verlauf des Verbrennungsvorgangs völlig verbrannt und zu stabilen Oxyden umgewandelt wird, werden einige der Substanzen unvollständig verbrannt und ergeben verschiedene Typen von Produkten, z.B. Kohlenstoff-Monoxyd, Stickstoff-Oxyd, Aldehyde und Ruß-Partikel. Diese Substanzen sind der globalen Umwelt und menschlichen Gesundheit schädlich. Alle Länder der Welt sind aufgefordert Maßnahmen gegen solche Verschmutzungen zu ergreifen. Im Licht dieser gegenwärtigen Situation ist der Gegenstand des vorliegenden Projektes, eine Verbrennungs-Methode zur Verfügung zu stellen, durch die die Effizienz vergrößert, und/oder die Produktion von schädlichen Substanzen vermindert wird.

1992, wurde in Rio das Abkommen der Vereinten Nationen über die Klimaänderungen erzielt, das heute von 186 Ländern bestätigt, die Existenz der Klimaänderung, und deren menschlichen Ursprung anerkennt und den industrialisierten Ländern das Primat der Verantwortung zugeschrieben hat um gegen dieses Phänomen zu kämpfen.

Die Ansprüche der Verbraucher und die durch Emissionen hervorgerufenen gesundheitlichen Beeinträchtigungen führen weiterhin zu einer Verschärfung der tolerierbaren Normen für Verbrennungssysteme (Automotoren, Gasturbinen, Haushaltsheizkessel, industrielle Kessel...). Die heutzutage angewandten Methoden, basierend auf einer besseren Regelung des Betriebspunktes im Kessel oder auf einer nachfolgenden katalytischen Reinigung, sind effizient, stoßen aber immer mehr an ihre Grenzen. Unter den Alternativen ist die Verwendung von angeregten Spezies während der Verbrennung, um das Betriebsverhalten zu ändern und die direkten Emissionen zu mindern oder in einer zweiten Stufe, um Schmutzstoffe zu zersetzen und unschädlich zu machen, noch sehr wenig untersucht.

Die Verbrennung benutzt als Oxidationsmittel Sauerstoff normalerweise in seinem elektronischen Grund-Zustand. Eine neue Konzeption besteht darin, eine wirksamere Verbrennung durch angeregten Sauerstoff (vibrationnell oder elektronisch) zu erreichen. Das Grundziel dieses Projektes besteht darin, ein neues Verständnis der Physico-Chemie dieser Verbrennung zu entwickeln, das die Physik der Plasmen und die Chemie der Verbrennung vereint. Diese "aktivierte" Verbrennung eröffnet wichtige Möglichkeiten die Wirksamkeit der Verbrennung zu erhöhen und eine Verringerung der umweltverschmutzenden Emissionen zu erreichen.

Am Institut ICARE wurde die Möglichkeit bewiesen, das Zünden eines Systems zu verbessern und die Produktion des Rußes zu reduzieren, indem die elektronische Anregung des Sauerstoffs verwendet wurde. Diese Studie ergänzt nun das vorhandene Wissen um die numerische Beschreibung anhand von Modellen und die experimentelle Studie des Einflusses der vibrationnellen Anregung des Sauerstoffs auf die Intensivierung der Verbrennung und auf die Verringerung der umweltverschmutzenden Emissionen.

Diese Studie ist um zwei Forschungsachsen gegliedert, die die Generation von elektrisch angeregten Spezies und die Verbrennung sind. Die Erste der potenziellen Anwendungen auf dem Gebiet der Verbrennung betrifft das Zünden einer brennbaren Mischung. Verschiedenen Gruppen validierten diese Technik des Zündens und verglichen sie mit dem klassischen Zünden durch Funken. Die zweite Anwendung betrifft die Stabilisierung einer abgehobenen Flamme am Ausgang einer Einspritzdüse, durch eine Entladungsebene. Diese Methode ermöglicht es, für eine gegebene Stabilisierungshöhe, die Austrittsgeschwindigkeit um nahezu 80 % zu erhöhen. Die in die Entladung injizierte Elektroenergie entspricht 1/1000 der Energie der Flamme. Im Rahmen dieser Studie ermöglicht die Anwendung der gepulsten Entladung, in einer Mischung Helium - Sauerstoff, elektronisch angeregten atomaren und molekularen und Sauerstoff zu erzeugen. Der Zusatz des Gases Helium ermöglicht, die Wirksamkeit der Entladung zu steigern.

Der erste experimentelle Teil dieser Arbeit ist auf die Erzeugung von durch Plasma angeregtem Sauerstoff ausgerichtet:

- Die Bereitstellung des Sauerstoff-Generators, zwischen  $7 \cdot 10^{-2}$  bis 1 Atmosphäre. Die bibliografische Studie hatte bestätigt, dass die Menge des durch die Barriere-Entladung erzeugten angeregten

Sauerstoffs zunimmt, wenn der Druck im Generator unter dem Luftdruck liegt; es wurde daher beschlossen, einen Verbrennungsversuch vorzusehen, der bei reduziertem Druck funktionieren kann.

- Das durch diese Einrichtung hergestellte Gas wurde dann ausführlich mittels Emissions-Spektroskopie untersucht. Diese Arbeit, die unerlässlich ist, um die Installation zu charakterisieren und die notwendigen Anfangsbedingungen für die Berechnungen zu erhalten, wurde auf verschiedenen verfügbaren Spektrometern bei ICARE durchgeführt.

- In Kooperation mit den Forschern aus Minsk und Kiew, konnte der erste angeregte Sauerstoff in einer Entladung bei Luftdruck nachgewiesen werden. Bis dahin war er nur bei reduziertem Druck erhalten worden.

- Andererseits hat die Beschreibung anhand von Modellen des Plasmas gezeigt, dass molekularer Sauerstoff, damit er durch die elektrische Wechselwirkung wirksam angeregt wird, mit optimaler Energie der Elektronen angeregt werden muß. Dafür haben wir, in einem zweiten Schritt, eine neue Zelle mit einer Kreuzentladung entwickelt. Diese Kreuzentladung ist eine hybride Entladung, innerhalb derer kurze Hochspannungsimpulse es einerseits ermöglichen, das Gas zu ionisieren und andererseits, ein schwaches elektrisches Feld, das durch eine kontinuierliche Stromversorgung geschaffen wird, und die Entladung zwischen zwei Pulsen aufrechterhält. Dieses zweite elektrische Feld kann unabhängig kontrolliert werden und an das Optimum für die Anregung des Sauerstoffs in seinen zwei elektronisch angeregten Zuständen angepasst werden.

Für die Experimente wurde ein Hochfrequenz-Pulsgenerator verwendet, der elektrische Pulse mit Spannungen bis zu 25 kV, Pulsdauern von ~10-20 ns, Anstiegsflanken von 5 ns und Wiederholungsraten bis zu 25 kHz erzeugt. Damit wird eine Kreuzentladungszelle entwickelt und optimiert. Diese verbindet zwei Hochspannungsentladungen in einem Raum: eine hochfrequente dielektrische Barriereentladung (DBD) und eine kontinuierliche (DC) Entladung. Die DBD besteht aus zwei flachen Elektroden aus Edelstahl oder Kupfer, die parallel angebracht sind und mit dielektrischem Material bedeckt sind. Die DC-Entladung besteht aus zwei Edelstahlelektroden mit spezieller Form und parallel angeordnet. Die komplette Entladungszelle besitzt somit eine rechteckige Form mit den jeweils zwei parallelen Elektrodenpaaren an den Seiten. Die Besonderheit dieser Kreuzentladung, ist die präzise Einstellmöglichkeit des reduzierten elektrischen Felds  $E/n$  für eine optimale Produktion des angeregten Sauerstoffs.

Die Untersuchung der Produktion von elektronisch angeregtem Sauerstoff  $O_2(b^1\Sigma_g^+)$  mittels einer Kreuzentladung im Vakuum (100-300 Torr) hat es erlaubt signifikante Mengen von  $O_2(b^1\Sigma_g^+)$  zu erzeugen. Mittels einer Parameterstudie wurde die Entladungs- und Postentladungszone (am Ausgang der Entladungszelle) untersucht. Der Einfluß des Drucks, der Gleichspannung, der  $O_2$ -Konzentration sowie der Zumischung von kleinen Mengen NO auf die Produktion von angeregtem Sauerstoff wurde bestimmt und die optimalen experimentellen Bedingungen aufgezeigt. Mittels Emissionsspektroskopie konnte angeregter Sauerstoff noch ca. 1cm ausserhalb der Entladungszelle nachgewiesen werden.

Zusätzlich wurde die Temperatur, die einen wesentlichen Punkt bei der Interpretation der Endergebnisse darstellt, bestimmt. Bei den optimalsten Bedingungen zur Produktion von angeregtem Sauerstoff liegt die Temperaturerhöhung des Plasmas bei 60°C ohne Zusatz von NO und bei 120°C mit NO. Somit konnte der chemische und nicht thermische Einfluß des Plasmas auf die Verbrennung nachgewiesen werden.

Der zweite experimentelle Teil betrifft die Untersuchung einer flachen Gegenstromflamme und einer partiell vorgemischten Flamme. Diese hybriden Brenner beinhalten den Plasmareaktor. Die Untersuchung der Flammenfront in Anwesenheit oder nicht der Entladung wird mittels Emissionsspektroskopie und intensivierter Kamera durchgeführt.

Emissionsspektroskopie wird dabei verwendet, um den Anstieg der Radikalproduktion bei eingeschalteter Kreuzentladung nachzuweisen. Diese Aktivierung durch das Plasma führt zu einer Zunahme von CH um 22 %, von  $C_2$  um 5-10 % und von OH um 3 %.

Dennoch ergab sich ein Hauptproblem dieser Gegenstrom-Konfiguration: innerhalb der Flamme konnte kein angeregter Sauerstoff mehr nachgewiesen werden. Tatsächlich lag dies hauptsächlich an den atmosphärischen Bedingungen und der hohen Sauerstoffkonzentration, die bei dieser Konfiguration durch die Entladung geführt werden muß, was zu einem schnellen Quenching des angeregten Sauerstoffs führte. Die Bedingungen sind also nicht optimal und bedingen eine zu niedrige  $O_2(b^1\Sigma_g^+)$  Konzentration.

In einem zweiten Schritt, wird deshalb ein anderer Brenner vorgeschlagen, der besser auf die optimale Produktion von angeregtem Sauerstoff ausgerichtet ist, damit dieser mit der Flammenfront reagieren kann.

In diesem Fall kann eine Intensivierung der Verbrennung nachgewiesen werden, die sehr von den optimalen Bedingungen für die Sauerstoffproduktion abhängt. So wird zum Beispiel durch Erhöhung der Volumenströme eine bessere Durchdringung der Reaktionszone mit den angeregten Molekülen erreicht. Die Ergebnisse zeigen Erhöhung der Produktion von OH\* um 37%, von C<sub>2</sub>\* um 19% und von CH\* um 12%. Diese Ergebnisse zeigen somit die Effizienz von angeregtem Sauerstoff bei der Intensivierung von Verbrennungsvorgängen.

Schließlich, wird die Beschreibung, einer Vormischflamme anhand von Modellen, durch die Software CHEMKIN unternommen. Die verstärkende Wirkung des angeregten Sauerstoff auf eine Wasserstoffflamme konnte dabei gezeigt werden. Die Ergebnisse für eine H<sub>2</sub>-O<sub>2</sub> Vormischflamme und eine Gegenstromdiffusionsflamme in Gegenwart von angeregtem Sauerstoff werden in Kapitel III vorgestellt. Die Berechnungen zeigen, daß sogar eine geringe Menge O<sub>2</sub>\* (<5%) in der H<sub>2</sub>-O<sub>2</sub> Mischung erlaubt, die Zünd-Verzögerungszeit merklich zu reduzieren und die Mischung bei einer niedrigeren Temperatur zu entzünden. Die erhaltenen Ergebnisse bestätigen qualitativ die beobachtete Verbrennungsintensivierung einer Methan-Sauerstoff-Mischung mittels der Anregung von O<sub>2</sub> Molekülen durch die elektrische Entladung.

**Keywords** : nonequilibrium plasma, pulsed dielectric barrier discharge, combined crossed discharge, electronically excited oxygen species, singlet oxygen, O<sub>2</sub>(a<sup>1</sup>Δ<sub>g</sub>), O<sub>2</sub>(b<sup>1</sup>Σ<sub>g</sub><sup>+</sup>), plasma assisted combustion, combustion efficiency, pollutant emissions.

**Mots clés** : Plasma hors équilibre, décharge pulsée à barrières diélectriques, décharge croisée, oxygène électroniquement excité, oxygène singulet, O<sub>2</sub>(a<sup>1</sup>Δ<sub>g</sub>), O<sub>2</sub>(b<sup>1</sup>Σ<sub>g</sub><sup>+</sup>), combustion assistée par plasma, efficacité de la combustion, émissions polluantes.

**Schlüsselwörter** : Nichtgleichgewichts-Plasma, pulsierte dielektrische Barriere-Entladung, Kreuz-Entladung, elektronisch angeregter Sauerstoff, Singlet-Sauerstoff, O<sub>2</sub>(a<sup>1</sup>Δ<sub>g</sub>), O<sub>2</sub>(b<sup>1</sup>Σ<sub>g</sub><sup>+</sup>), Plasma unterstützte Verbrennung, Verbrennungs-Intensität, Schadstoff-Emissionen.

# Contents

<b>ACKNOWLEDGMENTS .....</b>	<b>4</b>
<b>PREFACE.....</b>	<b>7</b>
BEFORE THIS STUDY .....	7
PRESENTATION OF THE PARTNERS .....	7
OBJECTIVES AND CONTENTS OF THE PH.D PROJECT .....	7
<b>SUMMARIES.....</b>	<b>9</b>
<b>NOMENCLATURE.....</b>	<b>24</b>
<b>CHAPTER I : STATE OF THE ART.....</b>	<b>25</b>
<b>I.1. PLASMAS .....</b>	<b>26</b>
I.1.1. DEFINITION .....	26
I.1.2. EXAMPLES .....	26
I.1.3. COMPLETE THERMODYNAMICAL EQUILIBRIUM.....	26
I.1.4. THERMODYNAMICAL NONEQUILIBRIUM WITHIN A GAS.....	27
I.1.4.1. Definition.....	27
I.1.4.2. Nonequilibrium plasmas .....	27
<b>I.2. ELECTRIC DISCHARGE .....</b>	<b>28</b>
I.2.1. INTRODUCTION .....	28
I.2.2. DIELECTRIC BARRIER DISCHARGE.....	29
I.2.3. ATMOSPHERIC PRESSURE GLOW DISCHARGE.....	30
I.2.4. PULSED NANOSECOND DISCHARGE .....	30
I.2.4.1. Presentation .....	30
I.2.4.2. Nanopulsed discharge development : Fast Ionisation Wave.....	31
<b>I.3. ELECTRONICALLY EXCITED OXYGEN.....</b>	<b>31</b>
I.3.1. EXCITED OXYGEN IN NATURE .....	31
I.3.2. METHODS OF GENERATION OF EXCITED OXYGEN .....	32
I.3.2.1. Optical/laser production of singlet oxygen .....	32
I.3.2.2. Chemical generation .....	33
I.3.2.3. Electrical discharge plasma generation.....	33
I.3.3. LITERATURE RESULTS ON PRODUCTION OF EXCITED MOLECULAR OXYGEN .....	34
I.3.3.1. Crossed discharge reactor and reduced electric field.....	34
I.3.3.2. Experimental generation of $O_2(b^1\Sigma_g^+)$ and $O_2(a^1\Delta_g)$ .....	34
I.3.4. UTILISATION OF SINGLET OXYGEN.....	38
I.3.4.1. Oxygen-iodine laser applications.....	38
I.3.4.2. Cancer treatment application.....	38
I.3.4.3. Combustion applications.....	38
<b>I.4. IGNITION AND COMBUSTION PROMOTION BY THE ACTION OF A DISCHARGE .....</b>	<b>39</b>
I.4.1. CONTEXT .....	39
I.4.2. FLAME STABILIZATION .....	39
I.4.2.1. Pilot flame stabilization .....	39
I.4.2.2. Electric field stabilization .....	40
I.4.2.3. Nonequilibrium plasma stabilization .....	40
I.4.2.4. Arc-type plasma stabilization.....	40
I.4.3. COMBUSTION PROCESS AND EXCITED OXYGEN SPECIES .....	41
I.4.4. PLASMA ASSISTED IGNITION .....	42
I.4.4.1. ( $H_2/air$ ), ( $CH_4/air$ ) and ( $C_3H_8/air$ ) systems .....	42
I.4.4.2. ( $C_nH_{2n+2}/air$ ) systems ( $n>3$ ) .....	43
<b>I.5. CONCLUSION.....</b>	<b>44</b>

<b>CHAPTER II : IDENTIFICATION OF SPECIES AND TEMPERATURE MEASUREMENT BY EMISSION SPECTROSCOPY .....</b>	<b>45</b>
<b>II.1. INTRODUCTION.....</b>	<b>45</b>
<b>II.2. SPECTROSCOPIC DESCRIPTION OF OXYGEN MOLECULE.....</b>	<b>46</b>
II.2.1. O <sub>2</sub> POTENTIAL ENERGY CURVES.....	46
II.2.1.1. Presentation.....	46
II.2.1.2. Electronic configuration.....	47
II.2.2. BRANCHES AND SPECTRA.....	49
II.2.2.1. Structure.....	49
II.2.2.2. Cooperative emission bands.....	50
II.2.3. SELECTION RULES.....	52
II.2.3.1. Introduction.....	52
II.2.3.2. O <sub>2</sub> $b^1\Sigma_g^+ \rightarrow X^3\Sigma_g^-$ transition.....	52
II.2.3.3. O <sub>2</sub> $a^1\Delta_g \rightarrow X^3\Sigma_g^-$ transition.....	54
<b>II.3. STRUCTURE AND SIMULATION OF EXCITED O<sub>2</sub> EMISSION BANDS .....</b>	<b>55</b>
II.3.1. PRESENTATION.....	55
II.3.2. ROTATIONAL STRUCTURE.....	55
II.3.2.1. Energy of a molecule.....	55
II.3.2.2. Vibration mode.....	56
II.3.2.3. Rotation mode.....	56
II.3.2.4. Rovibronic structure.....	57
II.3.2.5. Fine structure of quantum states: rotational terms.....	57
II.3.3. O <sub>2</sub> ( $A^1\Delta_g$ ) (0,0) AND O <sub>2</sub> ( $B^1\Sigma_g^+$ ) (0,0) EMISSION SPECTRA SIMULATION.....	59
II.3.3.1. O <sub>2</sub> ( $b^1\Sigma_g^+$ , $v=0$ ) $\rightarrow$ O <sub>2</sub> ( $X^3\Sigma_g^-$ ) and O <sub>2</sub> ( $a^1\Delta_g$ , $v=0$ ) $\rightarrow$ O <sub>2</sub> ( $X^3\Sigma_g^-$ ) lines.....	59
II.3.3.2. Emission spectra simulation.....	61
II.3.3.3. Validation with other simulation codes.....	64
II.3.3.4. Rotational temperature effect on O <sub>2</sub> : $b^1\Sigma_g^+ \rightarrow X^3\Sigma_g^-$ (0,0) spectra.....	64
II.3.4. TEMPERATURE MEASUREMENTS.....	66
<b>II.4. SPECIES IDENTIFICATION.....</b>	<b>67</b>
II.4.1. SINGLET OXYGEN DETECTION TECHNIQUES.....	67
II.4.2. SPONTANEOUS EMISSION SPECTROSCOPY.....	69
II.4.2.1. Low resolution spectrometer.....	70
II.4.2.2. Medium resolution spectrometer.....	70
II.4.2.3. High resolution spectrometer.....	71
II.4.2.4. Wavelength calibration.....	71
II.4.2.5. Optics.....	72
II.4.3. DIRECT VISUALIZATION BY ICCD CAMERA.....	72
II.4.4. LASER INDUCED FLUORESCENCE.....	73
<b>II.5. CONCLUSIONS .....</b>	<b>74</b>
<b>CHAPTER III : MODELLING WORK.....</b>	<b>75</b>
<b>III.1. PLASMA MODELLING: ELECTRON ENERGY DISTRIBUTION FUNCTION.....</b>	<b>75</b>
III.1.1. INTRODUCTION.....	75
III.1.2. BOLTZMANN EQUATION RESOLUTION IN THE CASE OF A DISCHARGE.....	76
III.1.3. SIMULATIONS.....	76
III.1.3.1. Cross sections.....	76
III.1.3.2. Energy electron distribution function.....	76
III.1.3.3. Energy loss fractions for different processes including electronically excited oxygen.....	78
III.1.3.5. Interpretation of dilution effects on discharge.....	84
III.1.4. CONCLUSIONS ON EXCITATION.....	87
<b>III.2. MODELLING OF PLASMA-ASSISTED COMBUSTION .....</b>	<b>88</b>
III.2.1. INTRODUCTION.....	88
III.2.2. NUMERICAL MODELLING.....	88
III.2.3. FLAME PROPERTIES WITHOUT EXCITED SPECIES.....	89

III.2.3.1. Laminar flame speed.....	89
III.2.3.2. Influence of dilution.....	90
III.2.3.3. Auto-ignition delays.....	91
III.2.4. FLAME PROPERTIES WITH EXCITED OXYGEN SPECIES .....	92
III.2.4.1. Influence of $O_2^*$ on ignition delay.....	92
III.2.4.2. Influence of $O_2^*$ on laminar flame speed.....	93
III.2.4.3. Influence of $O_2^*$ on laminar premixed flame structure.....	93
III.2.4.4. Influence of $O_2^*$ on laminar premixed flame structure at other equivalence ratios.....	96
III.2.4.5. Influence of a high percentage of $O_2^*$ on laminar premixed flame.....	99
III.2.4.6. Influence of $O_2^*$ on laminar non-premixed counterflow flame structure.....	99
III.2.5. CONCLUSIONS ON PLASMA-ASSISTED COMBUSTION MODELLING .....	103
III.2.6. FURTHER REMARKS.....	103
<b>CHAPTER IV : EXPERIMENTAL GENERATION OF ELECTRONICALLY EXCITED OXYGEN SPECIES.....</b>	<b>105</b>
<b>IV.1. PULSE DIELECTRIC BARRIER DISCHARGE (DBD) PLASMA FACILITY.....</b>	<b>105</b>
IV.1.1. INTRODUCTION AND CHARACTERISTICS.....	105
IV.1.2. AC AGAINST PULSE POWER SUPPLY .....	106
IV.1.3. EXPERIMENTAL SET-UP FOR THE PULSED DIELECTRIC BARRIER DISCHARGE .....	106
IV.1.4. CHARACTERIZATION OF THE DIELECTRIC BARRIER DISCHARGE .....	109
IV.1.4.1. Electrical characteristics.....	109
IV.1.4.2. Optical emission spectroscopy.....	110
<b>IV.2. CROSSED DISCHARGE REACTOR (CDR).....</b>	<b>111</b>
IV.2.1. NON SELF SUSTAINED DISCHARGE .....	111
IV.2.2. CHARACTERIZATION OF CROSSED DISCHARGE REACTORS.....	112
IV.2.2.1. Introduction .....	112
IV.2.2.2. Motivation.....	112
IV.2.2.3. Experimental set-up for combined discharge reactor.....	112
IV.2.2.4. First crossed discharge reactors.....	114
IV.2.3. FINALLY RETAINED CDR.....	114
IV.2.3.1. Characterization of the discharge.....	115
IV.2.3.2. Electronically excited oxygen species production in He/ $O_2$ binary mixture.....	118
IV.2.3.3. $O_2(b^1\Sigma_g^+)$ generation in helium versus argon diluents.....	122
IV.2.3.4. Electronically excited oxygen production in He/ $O_2$ /NO ternary mixture.....	124
IV.2.3.5. Conclusions on oxygen excitation.....	126
IV.2.3.6. Temperature measurements .....	127
IV.2.4. PRESENCE OF EXCITED OXYGEN IN THE POST-DISCHARGE ZONE .....	131
IV.2.4.1. Introduction .....	131
IV.2.4.2. Spontaneous emission of $O_2(b^1\Sigma_g^+)$ and OI (777 nm).....	131
<b>IV.3. CONCLUSIONS.....</b>	<b>137</b>
<b>CHAPTER V : HYBRID BURNER DEVELOPMENT FOR COMBUSTION INTENSIFICATION.....</b>	<b>139</b>
<b>V.1. ATMOSPHERIC PRESSURE COUNTER-FLOW DIFFUSION FLAME.....</b>	<b>139</b>
V.1.1. GENERAL DESCRIPTION OF THE COUNTER-FLOW CONFIGURATION .....	139
V.1.2. HYBRID BURNER CONFIGURATION.....	141
V.1.3. PLASMA EFFECTS ON FLAME EMISSION SPECTROSCOPY.....	143
V.1.4. CONCLUSIONS ON COUNTERFLOW CONFIGURATION .....	145
<b>V.2. LOW PRESSURE CO-FLOW HYBRID BURNER FOR PARTIALLY PREMIXED COMBUSTION.....</b>	<b>146</b>
V.2.1. INTRODUCTION.....	146
V.2.2. HYBRID LOW-PRESSURE PARTIALLY PREMIXED PLASMA-BURNER.....	147
V.2.3. PLASMA WITHOUT FLAME .....	152
V.2.3.1. Direct images .....	152
V.2.3.2. Generation of excited oxygen species .....	153
V.2.4. PLASMA-ASSISTED COMBUSTION.....	154
V.2.4.1. Experimental flow conditions and measurement procedure .....	154
V.2.4.2. Direct flame visualization .....	156

<i>V.2.4.3. Spontaneous emission of flame front markers</i> .....	157
<i>V.2.4.4. Parameter study: influence of time, injection speed and DC sustainer voltage</i> .....	159
<i>V.2.4.5. Quantitative analysis of flame extension</i> .....	162
<i>V.2.4.6. Discussion and synthesis</i> .....	164
<b>V.3. CONCLUSIONS</b> .....	<b>165</b>
<b>CHAPTER VI : CONCLUSIONS AND PERSPECTIVES</b> .....	<b>167</b>
<b>REFERENCES</b> .....	<b>171</b>
<b>APPENDICES</b> .....	<b>183</b>
APPENDIX 1. HÜND VECTORIAL COUPLING .....	183
APPENDIX 2. COMPARISONS BETWEEN HITRAN, PGOPHER AND OUR SIMULATION PROGRAM .....	186
APPENDIX 3. EMISSION LINE IDENTIFICATION .....	188
APPENDIX 4. OXYGEN PLASMA KINETIC SCHEME.....	189
APPENDIX 5. REACTION SCHEME FOR HYDROGEN OXIDATION INVOLVING ELECTRONICALLY-EXCITED OXYGEN MOLECULES.....	190
APPENDIX 6. PULSE POWER SUPPLY PARAMETERS .....	195
APPENDIX 7. SPONTANEOUS EMISSION OF CH*, O*, C <sub>2</sub> * AND OH* .....	201
<b>CURRICULUM VITAE</b> .....	<b>206</b>
<b>OWN SCIENTIFIC PRODUCTION</b> .....	<b>208</b>

# Nomenclature

$c$	Light speed.....	[m.s <sup>-1</sup> ]
$E$	Energy.....	[J]
$\vec{E}$	Electric field.....	[V.m <sup>-1</sup> ]
$E/n$	Reduced electric field.....	[V.cm <sup>2</sup> ]
$f$	Frequency.....	[Hz]
$I$	Current.....	[A]
$\vec{M}$	Magnetic field.....	Tesla
$n$	Gas number density.....	[m <sup>-3</sup> ]
$n_e$	Electron density.....	[m <sup>-3</sup> ]
$p$	Pressure.....	[Pa]
$T_e$	Electron temperature.....	[K]
$T_{gas}$	Gas temperature.....	[K]
$T_r$	Rotational temperature.....	[K]
$T_v$	Vibrational temperature.....	[K]
$U_{DC}$	DC sustainer voltage.....	[V]
$V$	Discharge volume.....	[m <sup>3</sup> ]
$W$	Total deposited power in the discharge.....	[J]
$\rho$	Gas density.....	[kg.m <sup>-3</sup> ]
$\tau_i$	Ignition delay.....	[s]
$\nu$	Wavenumber.....	[cm <sup>-1</sup> ]
$\lambda$	Wavelength.....	[nm]

## Abbreviations

AC	Alternative current	ICOS	Integrated Cavity Output Spectroscopy
APDG	Atmospheric pressure glow discharge	INSB	Indium antimonide detector
CARS	Coherent anti-stokes Raman spectroscopy	O*=O( <sup>1</sup> D)	Singlet D atomic oxygen
CCD	Charge coupled device	OH*=OH( <sup>2</sup> Σ <sup>+</sup> )	Excited hydroxyl radical
CD	Discharge cell	O <sub>2</sub> *	Excited oxygen (O <sub>2</sub> (a <sup>1</sup> Δ <sub>g</sub> ) or O <sub>2</sub> (b <sup>1</sup> Σ <sub>g</sub> <sup>+</sup> ))
CDR	Crossed discharge reactor	ST	Shock-tube
COIL	Chemical oxygen iodine laser	FIW	Fast ionization wave
CRDS	Cavity ring down spectroscopy	ICLS	Intercavity laser Spectroscopy
DBD	Dielectric barrier discharge	LIF	Laser Induced fluorescence
DC	Direct current	NIR	Near-infrared
DDT	Deflagration detonation transition	OES	Optical emission spectroscopy
DOIL	Discharge oxygen iodine laser	OMA	Optical Multichannel
EEDF	Electron energy distribution function	PDE	Pulsed detonation engine
EPR	Electron paramagnetic resonance	PM	Photomultiplier
FWHM	Full-width at half-maximum	PS	Power supply
HVPPS	High voltage pulse power supply	$\nu$	Vibration quantum number
HVDCPS	High voltage direct current power supply	V <sub>OCl</sub>	Incident shock wave speed
HVPG	High voltage pulsed generator	V <sub>OCR</sub>	Reflected shock wave speed
ICCD	Intensified charge coupled device	VUV	Visible ultraviolet

# Chapter I : State of the art

## Abstract

---

All varieties of plasma-chemical systems are traditionally divided into two major categories: thermal and non-thermal ones. Thermal plasma (usually arcs) is associated with Joule heating, thermal ionization and enables to deliver high power (up to over 50 Megawatts) at high operating pressures. However, low excitation selectivity, very high gas temperature and electrode problems result in limited energy efficiency and applicability of thermal plasma sources. Non-thermal plasma (low pressure glow, radio frequency and microwave discharges) offers better selectivity and energy efficiency of plasma chemical reactions; it is able to operate efficiently at low temperatures. The basic feature of these various technologies is that they produce plasma in which the majority of the electrical energy primarily goes into the production of energetic electrons instead of heating the entire gas stream. These energetic electrons produce excited species, free radicals and ions as well as additional electrons through electron-impact ionization of background gas molecules. These excited species, in turn, can be used for many applications.

On another hand, combustion efficiency plays a critical role in energy production and environmental pollution. A challenging research axis concerns the use of plasmas to promote combustion. In this domain, several research prospects are carried out using electric arcs, lasers, and nonequilibrium plasmas. Nowadays, it seems that the most promising method for accelerating combustion is the non-equilibrium excitation of the gas mixture components, which allows one to affect the chemical reaction kinetics. Also, to enable more efficient excitation of the electronic and vibrational degrees of freedom, one should use short-duration (nanosecond) pulses [1].

Conventional combustion is based on fuel combustion in air where normal oxygen is the oxidative component. A novel idea of doing more efficient combustion is to use excited oxygen produced by nonthermal plasma, which can be in vibrational and/or in electronically excited states. This idea has been chosen in this study to promote combustion. It consists in exciting a part of molecular oxygen prior to the reaction with fuel. The interest of such species is their long radiative lifetime and high chemical reactivity.

The present study focuses on non thermal plasma discharge, production of excited oxygen molecules  $O_2(a^1\Delta_g)$  and  $O_2(b^1\Sigma_g^+)$  and finally, plasma assisted combustion technologies are presented.

---

# I.1. Plasmas

## I.1.1. Definition

Historically, the term "plasma" was used in physics for the first time by the American physicist Irving Langmuir in 1928 in analogy with the blood plasma, which the phenomenon looked like visually. A definition of plasma would be a 'soup' of electrons, positive and negative ions, neutrals and clusters. Plasma is also named 'fourth state of the matter' (together with solid, liquid and gas states). Another definition of a plasma is a gas (or a solid) which is subjected to sufficient energy to excite and dissociate the electrons from their atoms.

In the beginning, plasma indicated an overall neutral gas, entirely ionized. Then, one extended the definition to partially ionized plasmas, in which the proportions of charged particles are sufficient so that their behaviour differs from a neutral gas.

Plasma, ionized medium, is characterized by the densities of neutral species  $n$ , ions  $n_i$  and electrons  $n_e$ . In the case of reactive plasmas, energy is initially transferred to the electrons (which are the most mobile charged species) which then excite the background gas species. One distinguishes the elastic collisions which do not change internal energy or potential energy of neutral species but communicate a weak increase in their kinetic energy. For a sufficiently high electronic energy, the collisions will be inelastic with quantified change of the internal energy of the atom or molecule to produce the first excited states [2].

## I.1.2. Examples

Plasmas are extremely widespread in the universe since they constitute more than 99% of the known matter. On the other hand in our close environment, they pass almost unperceived since their conditions of appearance are very far from the conditions necessary to the needs for the terrestrial life. Thus, one distinguishes natural plasmas (stars, gas nebulas, pulsar; the aurora borealis, the lightning, solar wind and the ionosphere) and industrial plasma (discharges, lamps, screens, plasma torch, production of X-ray; propulsion plasma; nuclear fusion, plasmas treatment for deposition...). Among industrial plasmas, strong is to note many other applications which are still in an experimental state or of prototypes such as improvement of combustion, waste processing, radar, etc. In the classification of plasmas, each kind is characterized by particular physico-chemical properties.

## I.1.3. Complete thermodynamical equilibrium

Plasma contained inside an enclosure, thermally insulated and opaque to the radiation is in complete thermodynamic balance when the macroscopic parameters do not vary as long as the external conditions remain unchanged [3]. Under these conditions, all the particles which make the plasma, including the photons are in balance between them and with the enclosure walls, at a single temperature  $T$ .

The principal laws of statistical thermodynamics governing this balance are those of Planck, Maxwell, Boltzmann and Saha. The Boltzmann distribution law makes it possible to describe the equilibrium distribution in systems without interactions. Let us consider a system in equilibrium made up of a number  $N$  of molecules and total energy  $E$ . Even in equilibrium, there is a ceaseless redistribution of energy, due to the collisions between molecules; but not only between molecules but also between the various types of movements of the molecule (translation, vibration, rotation). However, each molecular state (same electronic level, but in another vibrational state for example), of energy  $\varepsilon_i$ , has a constant population  $n_i$  satisfying :

$$N = \sum_i n_i \text{ and } E = \sum_i n_i \cdot \varepsilon_i \quad (\text{Eq.I.1})$$

A distribution law gives the distribution of the  $n_i$  molecules on level  $i$ . This is the generalized Boltzmann distribution law :

$$\frac{n_i}{N} = \frac{g_i \cdot e^{-\beta \epsilon_i}}{\sum_j g_j \cdot e^{-\beta \epsilon_j}} \quad (\text{Eq.I.2})$$

$n_i$  is the number of molecule in a state  $i$ ,  $N$  is the total number of molecules and  $\beta = \frac{1}{kT}$  ;  $k$  is the Boltzmann constant and  $g_i$  is the degree of degeneration (i.e. statistical weight) of level  $i$ .

The Boltzmann distribution for the population  $n_i$  of the  $i^{\text{th}}$  energy level in relation to the population  $N_0$  of the fundamental state energy level (of energy  $E_0$ ) can be written as :

$$\frac{n_i}{N_0} = \frac{g_i}{g_0} \exp[-(E_i - E_0)/kT] \quad (\text{Eq.I.3})$$

In the case of a system in equilibrium, the temperatures of the various degrees of freedom (translational, rotational, vibrational, and electronic) are equal. The Maxwellian and Boltzmannian distributions determine the temperature of the considered system.

On the other hand, in the case of a nonequilibrium system, this single temperature does not exist. If in the various subsystems, the distribution speeds or energies can be approximated by the Maxwell or Boltzmann distribution functions, then these functions determine the temperatures associated with the various degrees of freedom quoted previously.

## I.1.4. Thermodynamical nonequilibrium within a gas

### I.1.4.1. Definition

A non-equilibrium thermodynamic situation may be reached at the time of an abrupt change of the macroscopic conditions (volume, pressure, temperature) of a gas considered as ionized. Examples of driving processes to reach a nonequilibrium thermodynamic system can be a sudden gas compression; a sudden gas relaxation; the application of a heating or a cooling process or the application of an external force to the gas (i.e. electric or magnetic field). For example, a shock will correspond to the increase in the translational energy of the heavy species [3].

In the case of external electric field application, the injected electric energy is initially transferred to the electrons which are then accelerated and carry out collisions with the particles of the medium. Excited, ionized species, radicals and photons are created, which interact in turn, between them and with the medium.

The main processes of energy exchange by collision are presented by Da Silva [4]. These energy exchanges are defined as follows: T-T; R-T; V-T; E-T; E-R; E-V; V-R and V-V. Where T stands for: Translation, V: Vibration, E: free Electron and R: Rotation. For example, the writing V-V means the energy exchange between two levels of vibration. Lastly, two other processes of energy exchange by collision relate to dissociation in thermal nonequilibrium for molecules vibrationally excited, process named V-D; and the dissociation by electronic impact, named E-D. These processes of energy exchanges do not have all the same efficiency.

As long as energy is not completely redistributed on all the modes of energy of the gas, one remains in a thermodynamic situation of non-equilibrium. Nevertheless, certain partial balances can be reached during the transition towards a thermodynamic equilibrium.

### I.1.4.2. Nonequilibrium plasmas

Electrons roughly have a mass 2000 times lower than ions, they have less inertia and are more reactive. It is thus easier to give energy to electrons than to heavier species. Mechanisms implied in

the processes of thermal plasma are characterized by the heating of the total gas volume. At equilibrium, one considers that the rotational temperature of the molecules  $T_{rot}$  is in balance with the temperature of translation of gas  $T_g$ . One can then differentiate plasmas in which only the electrons acquired enough energy to carry out reactions (essentially chemical reactions): the “cold” plasmas, from “hot” plasmas where ions are also energetic enough to influence the plasma behaviour. These denominations come owing to the fact that in the case of “cold” plasmas, the temperature (energy) of the electrons is much higher than that of ions  $T_i \ll T_e$ . The ions are regarded as "cold", non reactive species. In a nonequilibrium plasma, the average energy of the electrons varies typically between 1 and 10 eV, whereas the neutral and ionic species are "cold" at average energy of 0.025 eV.

The properties of nonthermal plasmas are of importance for industrial applications. Several applications require a near ambient temperature  $T_g$ . In addition, the principal function of a discharge is to produce active species in a gas, which implies that the electronic temperature  $T_e$  must be higher than the gas temperature.

The gas temperature can be controlled by different methods in their technical realization [5]: by limiting the time of transit of the gas in the zone of discharge, by cooling due to heat diffusion (material used in the discharge cell) or by using the mode of nanosecond pulsed discharge. In this study, we are going to pay attention to the latter case.

Detailed principles and fundamentals of low temperature plasmas can be found in [6, 7].

## I.2. Electric discharge

### I.2.1. Introduction

Recently, low temperature, high pressure plasmas have received a lot of attention because of their attractive features such as the reduced need of vacuum system and their ability to achieve gas phase chemistry without the need of elevated temperatures. Amongst the widely used devices to generate atmospheric pressure cold plasmas are “barrier” discharges and particularly “dielectric barrier discharges” (DBDs).

The article of Fridman et al. [8] is directed primarily towards the four most used and important varieties of nonthermal discharges: the corona discharge, the dielectric barrier discharge, the “gliding” arc discharge and the spark discharge. The basic characteristic of these various technologies is that they produce plasmas in which the majority of the electric power is initially used to produce energetic electrons, instead of increasing the temperature of the gas volume, thereby producing excited species and ions by electronic impact of the initial gas molecules as well as other electrons.

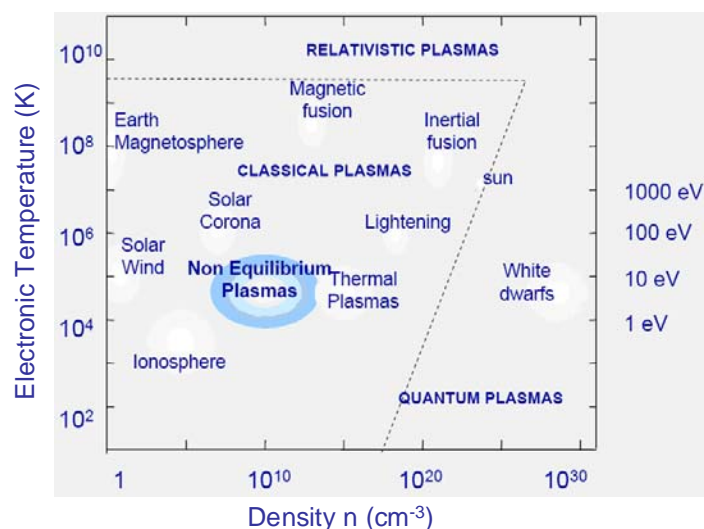


Fig.I.1. Density-temperature diagram (source: J.-P. Boeuf, LAPLACE, CNRS, Toulouse).

Figure I.1 allows observing that non equilibrium plasmas are characterized by weak electron and ion densities, in comparison to neutral molecules density. They are further characterized by a low ionization degree in contrast with thermal plasmas. It is worth noting that in such conditions, electron-neutral and ion-neutral collisions play an important role (excitation, ionization, dissociation).

To apply a plasma in a given field, it is necessary to understand which type of plasma is necessary (from the point of view of the discharge physics), which processes take place, which types of particles will be produced and what can be said about the efficiency of their production. In this report we will try to answer these questions for two non-equilibrium discharges: Dielectric barrier discharge (DBD) and combined DBD and DC discharge.

## I.2.2. Dielectric Barrier Discharge

The dielectric barrier discharge (DBD) configuration was first reported in 1857 by Siemens for the purpose of "ozonizing" air [9]. Up to date, the process of ozone production by DBD has been studied in detail and has been widely applied in industry [10, 11]. They are stable high pressure gas discharges capable of producing large densities of radical atomic and molecular species. Such non-thermal discharges are suitable for a wide range of applications, e.g. surface treatment (plastic foils, textiles, metals...), pollution control, sterilisation, UV and VUV light sources for pumping of laser, AC plasma display and others.

This discharge is a solution to avoid the formation of electric arc, which is always accompanied by a local overheating, generation of disturbance and of local shock waves. The principle is to use a dielectric barrier that covers at least one electrode in the discharge gap. The dielectric solid, is equivalent to a capacity and its charge limits the applied gas voltage and avoids the transition to an arc. In the majority of cases, DBDs are not uniform and consist of several micro-discharges distributed in the discharge gap [12].

As a rule, this discharge is generated in either a plane-to-plane or a coaxial geometry. The gap between electrodes is not larger than a few millimetres. An alternating voltage (hundreds of Hz to many kHz) is applied to the electrodes. When the applied voltage exceeds the breakdown value, electron avalanches occur, resulting in a "forest" of microstreamers forming conductive channels between the plates. Charge build-up on the dielectric during the current pulse reduces the net voltage across the gap. Eventually, the electric field in the plasma is unable to sustain the microstreamer, and the plasma at that location is extinguished. The area density of the randomly distributed microstreamers is sufficiently large that on the average, the entire gas is processed.

Typical characteristics of a micro-discharge are represented in Table.I.1 :

Lifetime	$(1-20) \cdot 10^{-9}$ s	Filament radius	$(50-100) \cdot 10^{-6}$ m
Intensity peak	0.1 A	Current density	$(0.1-1) \cdot 10^4$ kA $\cdot$ m <sup>-2</sup>
Electron density	$10^{20}-10^{21}$ m <sup>-3</sup>	Electronic energy	1-10 eV
Total transported charge	$(0.1-1) \cdot 10^{-9}$ C	Reduced electric field	1-2 Td
Total dissipated energy	$5 \cdot 10^{-6}$ J	Gas temperature	~320 K
Temperature increase	5 K		

Table I.1. Typical parameters of a micro-discharge [8].

The charge accumulation on the surface of the dielectric barrier decreases the electric field. This results in a termination of the current in a few nanoseconds after the discharge breakdown. The short lifetime of the microdischarges leads to a very weak increase of temperature and the plasma remains highly non-thermal. The gas temperature within the microdischarge depends on the total energy deposited, in the manner of energy dissipation and on the change of enthalpy due to chemical reactions [13].

### **I.2.3. Atmospheric pressure glow discharge**

The DBD are divided into two discharge modes: a homogeneous filament mode (FDBD) and a mode known as "glow" (GDBD) [4, 8]. Atmospheric pressure glow discharge (APGD) is a general name for discharges supporting nonequilibrium plasma at atmospheric pressure [14, 15].

At atmospheric pressure, there are three types of dielectric barrier discharges resulting from three different mechanisms :

- the glow DBD which results from the Townsend breakdown phenomenon ;
- the filamentary mode due to the streamer breakdown ;
- the homogeneous discharge formed by the covering of the streamer.

Several papers [16-21] reported experiments on atmospheric pressure glow discharge (APGD) in plane-to-plane electrodes geometry, which is more typical for dielectric barrier discharges. In the case of the filament mode, the discharge consists of a great number of "discharge filaments", which have nanosecond durations and which are distributed in a random way on the dielectric surface.

It is worth noting that the possible transitions between the previously described various modes are described by authors [22], which defined the mechanisms controlling the transition from filamentary to glow discharge at atmospheric pressure.

Finally, many industrial applications use the filament mode. However, for a homogeneous surface treatment or a thin layer deposit, the glow discharge mode has obvious advantages compared to the filament mode.

The glow discharge is characterized by diffuse and homogeneous plasma and by the presence of discharge "channels", which entirely cover the electrode surface [22]. The current intensity is periodic and its amplitude is approximately 30 times superior to that of a filament mode. Strong is to note that only the mechanism of Townsend breakdown (due to the secondary emission of the cathode induced by the bombardment of ions and metastables) can produce a glow discharge.

Another important characteristic of the glow discharge is underlined in the article of Gouda and Massines [22]. There is existence of reverse current peak when the polarity of the applied voltage changes. Indeed, at the time of polarity inversion, the dielectric solid polarity, in contact with gas, changes. The reversed field accelerates electrons, inducing a strong variation of the current which appears by this peak of reverse current. APGD makes it possible to arrange the homogeneous barrier discharge without phenomenon of streamer or other phenomena relating to the arcs. Different frequencies are necessary to excite the discharge. It can be a pulsed mode, a DC discharge and an AC current, RF discharges and  $\mu$ -wave discharges with associated frequencies of  $f=100$  kHz,  $100$  kHz $<f<100$  MHz and  $f>100$ MHz, respectively.

Closely related to dielectric barrier discharges, the dielectric surface discharges (DSD) are generated by surfaces of the dielectrics. The DSD decreases mainly the breakdown voltage of such systems. Two surface discharge modes are distinguished qualitatively according to the amplitude of the applied voltage: the complete mode or surface sliding arc and the incomplete mode or surface sliding corona. They are not extensively described here.

### **I.2.4. Pulsed nanosecond discharge**

#### **I.2.4.1. Presentation**

A pulsed uniform nanosecond gas discharge was first observed more than 100 years ago in 1893 by Thomson [23]. There exist two kinds of discharges when a high voltage short duration pulse is applied to a gas at atmospheric pressure and ambient temperature. Such a discharge is either a nonequilibrium streamer discharge for short pulse duration (tens of ns) or an equilibrium pulsed arc for longer pulses (hundreds of ns).

Initiation of the discharge with an abrupt slope of voltage (about  $1$  kV $\cdot$  ns $^{-1}$ ) at moderate gas densities is of great interest. Modern high voltage generators characterized by pulse amplitudes of tens and hundreds of kilovolts, voltage rise time in ns, pulse duration of tens of ns and repetitive frequency up to tens of kHz make it possible to create a spatially uniform discharge [1].

This kind of discharge will be used within our study. The reason is that these discharge parameters are particularly important for the problem of combustion/ignition of combustible mixtures. Moreover, the discharge can be produced within a large gas volume.

## I.2.4.2. Nanopulsed discharge development : Fast Ionisation Wave

The fast ionization wave (FIW) is a mode of discharge induced by a significant overvoltage of one electrode. The wave front moves with approximately  $10^7$ - $10^8$  m/s from one electrode (in overvoltage) to the other. The advantageous characteristics of the FIW are a good reproducibility of the phenomena as well as space homogeneity on a large gaseous volume. Also, using pulses, we are in presence of short times of the studied gas excitation [5, 24-26] and of high values of the electric field ( $E/n \sim 1000$  Td in the front of the FIW). The action of the FIW on gas generates various processes: excitation by electronic impact (gas internal degrees of freedom), dissociation and gas ionization characterized by the various forms of energy according to the reduced electric field  $E/n$  [27] :

- for weak ( $E/n$ )  $\sim 10^{-17}$ - $10^{-16}$  V/cm<sup>2</sup>, the majority of energy is transferred in molecules vibrational degree of freedom and is partly converted into rotation ;
- for values of ( $E/n$ ) of about  $10^{-15}$  V/cm<sup>2</sup>, we are in the presence of electronic excitation ;
- finally, for ( $E/n$ )  $\sim 4 \cdot 10^{-15}$  V/cm<sup>2</sup>, gas ionization by electronic impact becomes effective.

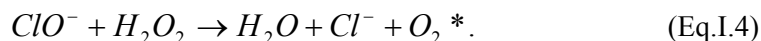
It is highlighted in the article [25] that nanopulsed discharges develop quasi-spherically and uniformly in space, starting from the high voltage electrode, with a propagation velocity of  $\sim 10^7$  m/s and in the pressure range of 13-133 Pa. The propagation velocity of the discharge is determined experimentally by Starikovskaia et al. [28] via the signals of capacitive gauges. In this case, the propagation velocity is  $10^8$  m/s. Anikin et al. [29] announce the typical values of the propagation velocity of a FIW as being  $2 \cdot 10^7$  to  $3 \cdot 10^7$  m/s. In the study of Bozhenkov et al. [24], the propagation velocity of the FIW is  $5 \cdot 10^7$  to  $9 \cdot 10^7$  m/s.

In study [25], Starikovskaia et al. consider two types of nanopulsed discharges of comparable nature: at relative low pressure ( $1$ - $1.33 \cdot 10^4$  Pa) and when the pulse voltage amplitude rises (at a rate of  $\sim 1$  kV/ns), the discharge develops in the form of a fast ionization wave (FIW). When the pressure increases, the discharge loses its spatial uniformity and thin channels (streamers) are propagated along the discharge space. The experiments are carried out with following gases: N<sub>2</sub>, O<sub>2</sub>, H<sub>2</sub>, CO and CH<sub>4</sub> and their mixtures, in a pressure range varying from 13 to  $4 \cdot 10^3$  Pa. The employed high voltage pulse generator characteristics, similar to the ones used in the present study, are presented in appendix 6. Rigorously speaking, the streamer and the FIW are caused by the same elementary processes. Their propagation is due to ionization by electronic impact in the discharge front.

## I.3. Electronically excited oxygen

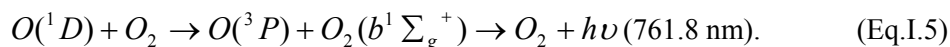
### I.3.1. Excited oxygen in nature

Oxygen is important not only as the “normal” diatomic molecule O<sub>2</sub>, as an atom in compounds and its involvement in chemical reactions, but also in its excited molecular states, singlet delta oxygen,  $a^1\Delta_g$ , and singlet sigma oxygen,  $b^1\Sigma_g^+$ . Singlet oxygen has been known since 1924. In 1979, Michael Kasha relates the accidental way in which singlet oxygen was re-discovered in 1960 by means of the reaction :



Singlet oxygen is quite reactive and is responsible for oxidative damage in a number of systems, including biological ones [30]. Moreover, excited states and other active species of oxygen are important to the world's carbon cycle because they contribute to the degradation of organic substances. Furthermore, species such as singlet oxygen ( $a^1\Delta_g$  and  $b^1\Sigma_g^+$ ), excited hydroxyl radical (OH\*), superoxide (O<sub>2</sub><sup>-</sup>), and alkyl peroxy radicals (ROO\*) are among the most important species in the aquatic environment. They are formed primarily by the action of sunlight on surface waters and are responsible for the indirect photochemical degradation of a wide variety of organic species [30].

Electron collisions with oxygen molecules are an important energy loss mechanism in the earth's ionosphere [31] and in the plasmas produced by electron beams. Additionally,  $O_2(b^1\Sigma_g^+)$  excited state is of considerable importance in atmospheric processes. In the thermosphere (begins at 90-100 km), it is a strong radiation source by this main reaction :



Lastly, the  $a^1\Delta_g$  state of  $O_2$  is of great interest as reagent of possible importance in atmospheric chemistry [32]. In the earth's upper atmosphere  $O_2(a^1\Delta_g)$  is produced primarily from the photolysis of ozone, and its concentration reaches a maximum of about  $4.10^{10}\text{cm}^{-3}$  at 50 km during the day time [33]. Atmospheric airglow has been measured from the ground, aircraft, balloons, and rockets and using a high-resolution spectrometer on a telescope. The  $1.27 \mu\text{m}$  emission from  $O_2(^1\Delta_g)$  and the 762 nm emission of  $O_2(b^1\Sigma_g^+)$  are major components in airglow. These species can be formed by direct absorption of UV radiation, e.g. :



and by photodissociation of ozone :



where  $O^*$  is an excited oxygen atom.

Recombination of oxygen atoms is another mechanism :



where  $M$  is a third body collision partner. The complete analysis of airglow spectra is very complicated and many other reactions are taken into account.

## I.3.2. Methods of generation of excited oxygen

Singlet oxygen can be generated using diverse methods, including thermal means, optical/laser energy, electrical/electromagnetic excitation, or a combination of these approaches. Singlet oxygen may also be generated through reactions of a chemical fuel additive or a laser-excited chemical additive [34, 35].

### I.3.2.1. Optical/laser production of singlet oxygen

The most common means of singlet oxygen generation is photosensitization<sup>1</sup> or, more precisely, energy transfer to  $O_2^*$  from an excited state of a sensitizer, which is formed by the absorption of light in a specific wavelength region. Singlet oxygen photosensitization is highly favoured in nature. This is due to the very special electronic configuration of molecular  $O_2$ . Therefore, energy transfer quenching of both excited singlet and triplet states is spin allowed, in contrast to many competing deactivation processes. Moreover, the excitation energies of both  $O_2(b^1\Sigma_g^+)$  and  $O_2(a^1\Delta_g)$  are lower than the energy state of many organic triplets, and in most cases, the energy difference is small enough to make the process fast enough to make it irreversible. Finally, the very small size of the  $O_2$  molecule allows for particularly rapid diffusion in many media, hardly any intermolecular process is able to compete with oxygen reaction. Hence, any excited state that is sufficiently long-lived to allow for intermolecular interactions is likely to react with  $O_2$ .

Singlet oxygen photosensitization is observed in any chemical system where light is absorbed in the presence of molecular oxygen. In many cases, energy transfer results in the formation of both  $O_2(a^1\Delta_g)$  and  $O_2(b^1\Sigma_g^+)$ . However, the spin-allowed  $b^1\Sigma_g^+ \rightarrow a^1\Delta_g$  deactivation occurs with extremely high rate constants in the condensed phase, and with unit efficiency in any medium; thus all  $O_2(b^1\Sigma_g^+)$  will be finally recovered as  $O_2(a^1\Delta_g)$ .

---

<sup>1</sup> Photosensitization is a process of transferring the energy of absorbed light. After absorption, the energy is transferred to the considered reactants. The sensitizer in chemoluminescence is a chemical compound, capable of light emission after it has received energy from a molecule, which became excited previously in the chemical reaction.

$O_2(a^1\Delta_g)$  can also be produced in photo-dissociation of ozone by UV-radiation at  $\lambda=253.7$  nm ( $O_3$  photolysis).

Another approach consists on laser-induced excitation of electronic states of oxygen molecule. A gaseous mixture containing oxygen is exposed to a laser pulse with a duration  $\tau_p$  and wavelength that is in resonance with the wavelength of the  $X^3\Sigma_g^- \rightarrow b^1\Sigma_g^+$  and  $X^3\Sigma_g^- \rightarrow a^1\Delta_g$  transitions. These electronic excitation wavelengths can be generated by Nd:YAG and dye laser [36].

### I.3.2.2. Chemical generation

Exothermic chemical reactions may generate singlet oxygen as a product. These reactions are often chemiluminescent owing to radiative decay of the  $O_2^*$ .

Singlet oxygen can be generated by reaction of  $Cl_2$  in a basic  $H_2O_2$  solution. Then, exothermic chemical reactions may generate singlet oxygen as a product, illustrated by the following well established hypochlorite-peroxide reaction :

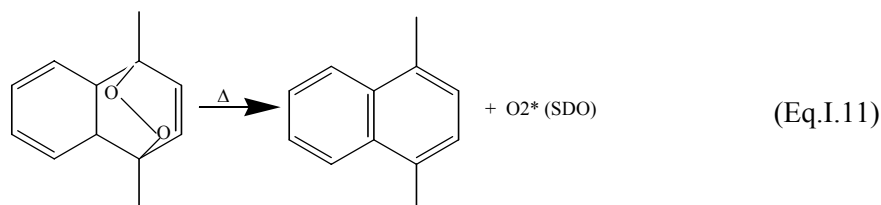


Moreover, a purely chemical and very effective way of generation of  $O_2^*$  exploits the following reaction (in liquid phase) :



This reaction takes place in a thin near-surface liquid layer, and yields close to unity can be obtained (because production of  $O$ ,  $O_3$  and other excited species, possible quenchers, are not encountered in the purely chemical system).

Furthermore, energy-rich compounds that generate  $O_2(a^1\Delta_g)$  by thermal decomposition include phosphate ozonides :  $(RO)_3PO_3 \rightarrow (RO)_3PO + O_2(a^1\Delta_g)$  and endoperoxides such as 9,10-diphenylanthracene peroxide (DAP) :



### I.3.2.3. Electrical discharge plasma generation

An alternative procedure for singlet oxygen production is its generation in an electrical discharge [37, 38]. First observation of singlet oxygen produced by an electrical discharge was made by Foner and Hudson [39] in a very long, typically 1 m, U-shaped discharge tube with hollow electrodes, operating at a pressure of several kPa in an AC glow regime.

Furthermore, electrical generation has been mainly used for laser gain application. In this case, production of excited oxygen is completed by direct electron impact on the ground state oxygen molecules or by deactivation of higher excited states. Moreover, singlet oxygen can be generated in plasmas produced by electron beams or by DC glow discharge.

In our experimental work, singlet oxygen is generated in a non-selfsustained crossed discharge. The discharge consists of high-voltage, short pulse duration, high repetition rate pulsed discharge, which produces ionization in the flow, and a low-voltage DC discharge which sustains current in a decaying plasma between the pulses. The sustainer voltage can be independently varied to maximize the energy input into electron impact excitation of singlet delta oxygen.

Also, electrodeless discharge, where the gas is excited by an external source of radiowaves or microwaves established in gaseous oxygen, allows generating singlet oxygen as well as other species including oxygen atoms and ozone.

## I.3.3. Literature results on production of excited molecular oxygen

### I.3.3.1. Crossed discharge reactor and reduced electric field

According to numerical simulations of Napartovich et al. [40], for  $O_2(a^1\Delta_g)$  and  $O_2(b^1\Sigma_g^+)$ , because of the non-optimized electric field in a plasma, a self-sustained electric discharge in pure oxygen has no chance of achieving a high ( $\geq 15\%$ ) yield. Recent investigations on electric discharge production of  $O_2(a^1\Delta_g)$  consisted on engineering the reduced electric field  $(E/n)^2$  nearer to the optimum value for  $O_2(a^1\Delta_g)$  production. In pure oxygen, a value around  $10^{-16} \text{ V cm}^2$  ( $=10 \text{ Td}$ ) is given by several authors. A very important remark is that in such conditions, only the non self-sustained discharges can exist. The reduced electric field is too weak for a self-sustained discharge mode.

It was in 1980's when Dr A. Hill developed a new method for the generation of singlet delta oxygen molecules using a so-called controlled avalanche process (CAP) [40]. This method consists in a hybrid discharge in which short high voltage pulses produce ionization while a comparatively low electric field supports the electric current between ionizing pulses. The supporting field at the phase of the plasma decay is close to the optimum for excitation of the singlet oxygen. These values of  $E/n$  are considerably lower than in the case of self-sustained electric discharges (DC, RF, or  $\mu$ -wave) :  $(E/n) \sim (1-10) \cdot 10^{-16} \text{ V cm}^2$  [41]. For example, Ionin et al. [34] used a pulsed electron beam sustained discharge facility to study a non self-sustained discharge in oxygen gas mixtures. Moreover, Verdeyen et al. [42] used a similar idea to that of Hill. A larger part of the energy deposited in the plasma is supplied by an inductive RF discharge with comparatively low electric field strength. Ionization is produced by an AC high voltage applied independently to the plasma volume. It is important that the energy deposited in the short pulses composes only several percent of total energy input. A yield of 15% of  $O_2(a^1\Delta_g)$  was achieved by Napartovich et al. [40]. For the plasma with an external source of ionization (electron beam [34], additional ionizing pulses [40]), the value of  $E/n$  can be controlled independently of electric current, allowing optimum conditions for production of singlet oxygen in the plasma discharge.

The paper of Hicks et al. [41] presents the experimental generation of singlet oxygen at high pressure (up to 380 Torr), by a non self-sustained crossed discharge supplied with a mixture ( $O_2/He$ ) for discharge oxygen iodine laser (DOIL) application. The discharge consists of a high voltage pulsed discharge and a low voltage continuous discharge. The continuous discharge component maintains the pulsed discharge between two pulses and is characterized by a value of the reduced electric field ranging between  $0.3 \cdot 10^{-16}$  and  $0.65 \cdot 10^{-16} \text{ V cm}^2$ .

This same approach will be used within our study to generate singlet oxygen at atmospheric and reduced pressure and for combustion applications.

### I.3.3.2. Experimental generation of $O_2(b^1\Sigma_g^+)$ and $O_2(a^1\Delta_g)$

#### I.3.3.2.1. Reduced electric field effect

Experimental research on the dependence of the production of  $O_2(a^1\Delta_g)$  according to the  $E/n$  parameter was carried out by Vasiljeva et al. [43]. For the mixture  $Ar:O_2 = 99:1$  and for fixed deposited energy  $w$ , there exists an optimal value of  $E/n$  such as the  $O_2(a^1\Delta_g)$  pumping is maximal.

The experimental results show that the optimal value of  $E/n$  corresponds to the most optimal electronic temperature, which is only very slightly higher than the energy of the excited electronic level of  $O_2(a^1\Delta_g)$  :  $T_e \sim 1-1.2 \text{ eV}$ .

Moreover, Ionin et al. [34] show also the dependence of the specific energy deposited to excite  $O_2$  in its first singlet state with the reduced electric field and show that this specific energy increases with the increase in the  $E/n$  ratio. For the mixture  $O_2/Ar$  (1:1), the maximum of energy used to form  $O_2(a^1\Delta_g)$  is 56% with  $E/n=0.69 \cdot 10^{-16} \text{ V cm}^2$ . According to the results of this study, while increasing

---

<sup>2</sup> Reduced electric field is the ratio of the electric field above the number density expressed in  $\text{V cm}^2$ . It can also be expressed in Townsend units where 1 Townsend =  $10^{-21} \text{ V m}^2$ .

( $E/n$ ), the part of energy deposited which is used for  $O_2$  dissociation increases quickly, and in parallel, that intended for the excitation of singlet oxygen decreases.

Furthermore, Napartovich et al. [40] calculated via a positive column DC discharge model, an optimal value of  $E/n \sim 10^{-16} \text{ V} \cdot \text{cm}^2$  at a pressure of 10 Torr and for pure  $O_2$ . This same value is predicted by the GlobalKin<sup>®</sup> model used in the study of Stafford and Kushner [44] for a discharge in pure  $O_2$  and at  $P=3$  Torr. It is observed that this optimal value of  $E/n$  (for which the  $O_2(a^1\Delta_g)$  excitation is maximum) decreases progressively with the increase in percentage of diluent:  $E/n=0.3 \cdot 10^{-16} \text{ V} \cdot \text{cm}^2$  for the mixture (99%He/1% $O_2$ ). When the percentage of helium increases in the mixture, the specific energy intended for the excitation of  $O_2(a^1\Delta_g)$  decreases. That is explained by the fact that with the addition of He, the rate of excitation of  $O_2(a^1\Delta_g)$  by direct electronic impact decreases.

Besides, the electron energy balance as a function of the reduced electric field strength is simulated by Napartovich et al. [40]. Fig.I.2 shows the obtained results :

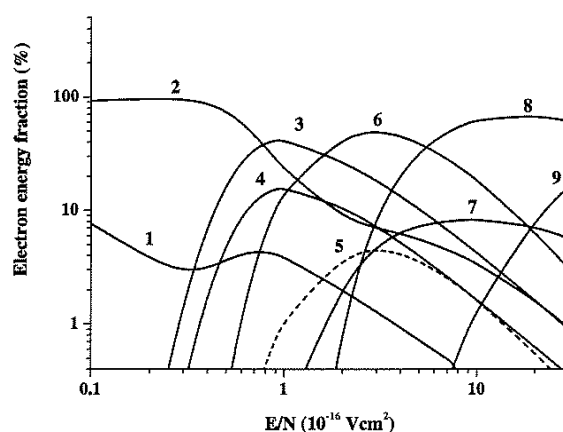


Fig.I.2. Electron energy fractions spent for different processes for pure  $O_2$  at  $P=10$  Torr : 1, elastic losses and rotational excitation; 2, vibration; 3,  $a^1\Delta_g$ ; 4,  $b^1\Sigma_g^+$ ; 5, attachment; 6, effective electronic level  $O_2^*$  with threshold 4.5eV; 7, dissociation into atoms  $O(^3P)$ ; 8, dissociation into  $O(^3P)$  and  $O(^1D)$  atoms; 9, ionisation [40].

We can see from this simulation that the energy fraction spent in the direct excitation of  $O_2(a^1\Delta_g)$  is quite high, approaching a maximum of 43% at  $E/n=0.87 \cdot 10^{-16} \text{ V} \cdot \text{cm}^2$ . For  $O_2(b^1\Sigma_g^+)$ , the maximum of 17% is approached at  $E/n=0.8 \cdot 10^{-16} \text{ V} \cdot \text{cm}^2$ . Therefore, it is expected that the presence of  $O_2(a^1\Delta_g)$  in the gas will have a significant influence on the electron energy distribution function and energy balance. This issue will be discussed later in section III.1.

### I.3.3.2.2. Deposited energy and pressure effects

A numerical modelling of Stafford and Kushner [44] showing the evolution of the singlet oxygen yield according to the specific energy deposited, shows that singlet oxygen yield increases linearly with the specific energy deposited in  $O_2$  until reaching a saturation at 5-8 eV/molecule, and then decreases when the dissociation of  $O_2$  starts to dominate the kinetics. It is worth noting that when the maximum yield is reached for singlet oxygen, we have dissociated 50% of  $O_2$ , and that more than 90% of dissociation is reached when the specific energy deposited is 20 eV/molecule. At 30 eV, the quasi totality of oxygen is dissociated, and an additional increase in specific energy deposited is used for again exciting and ionizing the atomic species O.

Let us recall that the excitation energy of  $O_2(a^1\Delta_g)$  is of 0.98 eV, and we introduce 5 to 8 eV/molecule. Thus, as more energy is deposited in the oxygen molecules, dissociation increases, which reduces the number of molecules available that can be excited.

Moreover, it is observed that when energy increases, the  $O_2(a^1\Delta_g)$  and  $O(^3P)$  densities increase and reach a maximum, and this maximum is reached more quickly when the pressure increases. In other words, "optimal" energy decreases with the increase in pressure [45].

Other studies show that this quenching of singlet oxygen is conditioned by the strong values of atomic oxygen density, whose production in a discharge is stimulated by high values of  $E/n$  and

energy deposited [43]. Moreover, Ionin et al. [34] determine a specific energy deposited for  $O_2(a^1\Delta_g)$  maximum excitation at  $P=30$  Torr and for  $E/n=1.5 \cdot 10^{-16} \text{ V} \cdot \text{cm}^2$  ( $\leftrightarrow E/p=4 \text{ kV/cm/atm}$ ).

Another study, that of Rakhimova et al. [46] worked on the effect of energy deposition in J/mol on  $O_2(a^1\Delta_g)$  yield. It was necessary to be located under the optimum energy conditions applied to the  $O_2$ /diluent mixture, corresponding to values of  $E/n$  close to 10 Td. Finally, McCluskey [30], after initial investigations of singlet delta oxygen, incorrectly concluded that more singlet oxygen delta should be produced at higher pressure. Even for its high radiative lifetime and its low rate of collisional quenching, singlet oxygen yield should be decreased when one works at high pressure. The study of Gray and Ogryzlo [47] works with pressure of 10 Torr, permitting to produce and detect a higher concentration of  $O_2(a^1\Delta_g)$ .

Research on the kinetic processes of the production and destruction of singlet oxygen reveals that the rate of  $O_2(a^1\Delta_g)$  and  $O_2(b^1\Sigma_g^+)$  deactivation increases with the increase in the pressure [41, 43]. Therefore, except in the low pressure cases ( $P \ll 1 \text{ atm}$ ), it is believed that electronic excitation of molecules does not play a great role in combustion chemistry. It is then difficult to imagine how it is possible to produce such excited species in a large amount at high pressures ( $P \geq 1 \text{ atm}$ ).

### I.3.3.2.3. Dilution effects by helium or argon

In a general way, one can expect that the fraction of electron energy intended for the direct excitation of singlet oxygen decreases when a diluent, atomic or molecular additives are added to the gas. However, the importance of diluent addition in order to have a weak collisional quenching by resonant energy transfer of the diluent with singlet oxygen has to be highlighted. Moreover, the replacement of pure oxygen by oxygen/diluent gas mixtures makes it significantly possible to increase the energy deposited per  $O_2$  molecule and to more easily reach the level of excitation necessary for singlet oxygen [40, 43]. We will see in our experimental work that in the case of argon dilution, it is possible that  $O_2(b^1\Sigma_g^+)$  is quickly relaxed by resonant energy transfer quenching or by collisions with the argon atoms.

Furthermore, Martin et al. [32] studied the quenching of electronically excited  $O_2(b^1\Sigma_g^+)$  by fundamental  $O_2$  and  $N_2$ . They succeeded in producing small quantities of  $O_2(b^1\Sigma_g^+, v=0)$  by direct excitation of molecular oxygen gas mixture. Thus, the quenching rate of  $O_2(b^1\Sigma_g^+)$  by  $O_2$  is measured by decrease of the fluorescence signal,  $k=(4.0 \pm 0.4) \cdot 10^{-17} \text{ cm}^3/\text{molecule}\cdot\text{s}$ . Moreover, the rate of quenching by  $N_2$  is obtained:  $k_{N_2}=(2.2 \pm 0.1) \cdot 10^{-15} \text{ cm}^3/\text{molecule}\cdot\text{s}$ . The authors underlined the sensitivity of the quenching of  $O_2(b^1\Sigma_g^+)$  in the presence of impurities, for example, due to discharge cell degasification.

In addition, Napartovich et al. [40] conclude, starting from numerical simulations, that the use of  $O_2/Ar$  mixtures is more advantageous than  $O_2/He$ , because of an increase in the discharge effectiveness and of a reduction in the gas temperature for the same energy deposited in  $O_2(a^1\Delta_g)$ . Also, the dependency of  $O_2(a^1\Delta_g)$  yield according to the  $O_2$  percentage in  $O_2/Ar$  and  $O_2/He$  mixtures is experimentally studied by Vasiljeva et al. [43]. The deposited energy and the reduced electric field is taken constant and close to optimal  $E/n$ . The authors observe that this ratio increases when the percentage of  $O_2$  in the mixture decreases. Moreover, for the same percentage of  $O_2$ , this ratio is higher for the mixtures with argon than those with helium. This observation is directly in contradiction with the observations of Hicks et al. [48]. Indeed, the latter study suggests that  $O_2(b^1\Sigma_g^+)$  and  $O_2(a^1\Delta_g)$  states are more quickly relaxed by energy resonant transfer quenching by collisions with the argon atoms than with helium ones. The authors of the study [43], who observe the opposite, explain that by energy losses of the electrons in elastic collisions, which are more important in  $O_2/He$  mixtures. Thus, mixtures diluted in argon with small quantities of  $O_2$  would be optimal to produce a relatively high singlet oxygen rate.

Finally, Ionin et al. [34] use mixtures of  $O_2$  diluted in argon in a non self-sustained discharge by electron beam. The authors observed that when increasing the percentage of argon in the mixture (at a fixed pressure of 30 Torr), the specific input energy increases. This energy increases also while increasing the  $E/p$  ratio.

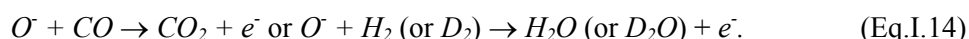
To conclude, contradictions exist on the benefit effects of diluents for singlet oxygen generation. Therefore, within the present study, we will both use theoretical and experimental approaches to check these points.

#### I.3.3.2.4. Effect of additives

Logically, additives would induce an additional quenching of singlet oxygen and consequently a reduction in its yield.

The authors of [43] modelled the production rate of  $O_2(a^1\Delta_g)$  by a pulsed discharge in a  $O_2/Ar$  gas mixture and in the presence of small quantities of  $H_2$  or  $CO$ . The authors show that a non self-sustained discharge in a mixture containing small  $O_2$  quantity diluted in an inert gas was strongly stratified and not uniform. One of the means of suppression of these instabilities resides in the addition of active molecular compounds, which will accelerate the detachment of the negative ions electrons but also make it possible to increase considerably the energy deposited in the plasma.

Water is a known vibrational deactivator of oxygen. Findlay [49] adds a quantity of steam to molecular oxygen excited by discharge at an oxygen pressure of 2 Torr. The results show that the intensity of the 762 nm emission band is drastically reduced. Furthermore, by adding small amounts of  $CO$  or  $H_2$  (~5%) to  $O_2/Ar$  mixtures, discharge oscillations disappeared, and he obtained a monotonically rising function of the electron drift velocity with  $E/n$ . Moreover, these additives result in a considerable enhancement of the specific energy input. The major reaction that occurs is with  $O^{\cdot}$ .



This results in the enhancement of the concentration of free electrons, the discharge current and the specific input energy.

Moreover, when maintaining a non-self-sustained discharge in gas mixtures with molecular additives  $CO$ ,  $H_2$  or  $D_2$ , the efficiency of  $O_2(a^1\Delta_g)$  can be as high as 40%. An increase of the specific energy input up to 1.5 eV per molecular component explains that. Carroll et al. [50] produced  $O_2(a^1\Delta_g)$  by an RF electric discharge at low pressure (5-15 Torr). The discharge production of  $O_2(a^1\Delta_g)$  was enhanced by the addition of a small proportion of  $NO$  to lower the average ionization threshold and thereby also lower the sustaining value of  $E/n$  of the gas mixture. Indeed,  $NO$  has a lower ionization threshold than  $O_2$  and  $He$ , thus the addition of  $NO$  enhances the production of electrons, which increases the conductivity of the plasma, which reduces the electric field needed to sustain the plasma and, consequently, the key parameter  $E/n$  is reduced.

It is also reported that small quantities of  $NO_2$  could be employed to scavenge excess  $O$  atoms via the reaction  $O+NO_2 \rightarrow NO+O_2$  (responsible for a part of  $O_2(a^1\Delta_g)$  and  $I(^2P_{1/2})$  quenching) and then enhancing  $O_2(a^1\Delta_g)$  production. Indeed, the study of Rawlins et al. [38] used additional reagents,  $NO$  and  $NO_2$ .

The transposability of this last approach will be experimentally tested in the present work in order to increase the production of singlet oxygen in combined discharge reactor.

#### I.3.3.2.5. Temperature effect

The oxygen emission band intensities at 634 nm, 480 nm and 380 nm are determined in [47]. The effect of the temperature on the interactions between the various molecules is studied. For that purpose, a temperature range of 77 K to 300 K is considered. At constant pressure, when the temperature is reduced to  $T=130$  K,  $O_2(X^3\Sigma_g^-)$  and  $O_2(a^1\Delta_g)$  concentrations increase. Indeed, the variation of the concentration according to the temperature follows the perfect gas law. Hence, below 130 K, the authors observe a fall in the concentration in  $O_2(a^1\Delta_g)$ , mainly due to wall deactivation.

For  $O_2(b^1\Sigma_g^+)$  species, its concentration increased faster with the temperature decrease than that of  $O_2(a^1\Delta_g)$ . This can be explained by the fact that  $O_2(b^1\Sigma_g^+)$  diffusion to the walls is weaker at low temperature than for  $O_2(a^1\Delta_g)$ .

Finally, Vasiljeva et al. [43] underline that the deactivation rate of singlet oxygen increases with the increase of the gas temperature.

Thanks to these points, we got some insights on how to produce electronically excited oxygen species and how to optimize it. Our final goal is to use these reactive species for combustion applications.

### I.3.4. Utilisation of singlet oxygen

#### I.3.4.1. Oxygen-iodine laser applications

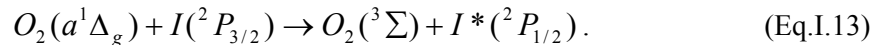
Excited oxygen states are potentially important sources of stored energy; especially,  $O_2(a^1\Delta_g)$  and  $O_2(b^1\Sigma_g^+)$  can efficiently transfer energy to iodine atoms. This process has received huge attention for oxygen-iodine laser application [34, 38, 41, 43, 45, 48, 51-53]. The idea of producing  $O_2(a^1\Delta_g)$  in a gas discharge to excite iodine lasers was formulated for the first time by Fournier and Bonnet in 1980. Great success has been obtained in the research and development of a chemical oxygen-iodine laser (COIL) where singlet delta oxygen is generated by chemical reactions; and of a discharge oxygen iodine laser (DOIL) where it is generated by an electrical discharge. However, applications of COILs are limited [34, 44].

The generation of singlet oxygen in an electrical discharge DOIL has been known since the 1950s [34] but with negative results. Its recent development attracted considerable attention [34, 37, 38, 40, 43, 45, 48, 50, 54-56], especially after measuring positive gain in a supersonic laser cavity and the successful laser power generation.

In both cases, the excitation of the singlet delta oxygen is transferred to iodine molecules which are then the active lasing medium [43, 48, 57, 58], emitting photons when changing its electronic state :



The electronic transition of the iodine atom emits light at 1315 nm. Atomic iodine in the excited state  $I^*(^2P_{1/2})$  is produced by near-resonant energy transfer between the singlet delta oxygen  $O_2(a^1\Delta_g)$  molecule and the iodine atom ground state  $I(^2P_{3/2})$  [59] :



#### I.3.4.2. Cancer treatment application

The utilization of singlet oxygen in cancer cell destruction also exists. Photodynamic therapy is a combined light-plus-drug treatment for malignant tumors and particularly for the treatment of obstructing cancer of the esophagus and early stage cancer of the bronchus. Singlet oxygen initiates peroxidation reactions and direct cancer cell killing may be involved as well.

The following part will present literature results on plasma assisted combustion technologies.

#### I.3.4.3. Combustion applications

Singlet oxygen has also been used for combustion applications. They enhance the performance of internal combustion engines, diesel engines in particular [60]. This control takes place just prior to, and in the initial stages of fuel injection and so, the mixing of singlet oxygen with fuel can be done either prior to, or during combustion.

In addition, a novel approach to control combustion processes by laser-induced excitation of oxygen molecules is presented in [36]. Singlet oxygen molecules are supposed to enhance the chain reactions in gaseous combustible mixtures. This application will be developed in section I.4.3.

Further effects of excited oxygen on combustion are detailed in the following section.

## **I.4. Ignition and combustion promotion by the action of a discharge**

### **I.4.1. Context**

In response to modern challenges in combustion applications, various approaches have been proposed to enhance the ignition and combustion in hydrogen–oxygen and hydrocarbon–oxygen mixtures by the means of electrical discharges.

In the present section, the studies related to the effects of plasma on :

- flame stabilisation ;
- flame intensification ;
- and flame ignition are presented.

There exist two principal types of application of a discharge in combustion: the first consists in igniting the mixture surface with low flowrates and constant burning velocities (e.g. by heating); the second consists in the treatment of the mixture by the discharge. The possibility of the "non thermal" initiation of chemical reactions by a pulsed discharge constitutes a vast research field. The interest to intensify combustion in gas phase systems by the use of gas discharges is to create combustion chambers, where this takes place at very high speeds. This research axis has experienced an upsurge during the last few years [1, 61]. Several approaches exist :

- heating of a mixture by a plasma torch or arc [62, 63] ;
- generation of appreciable amounts of chemically active atoms and radicals due to electron impact dissociation of reactants [28, 64] ;
- and excitation of molecules to vibrational and electronic states by a specially arranged electrical discharge [65-67].

Nonequilibrium modes are analyzed in the literature as the most promising in increasing combustion efficiency and reducing pollutant emissions, and with energy input negligible in comparison with the burner's chemical power.

Finally, various numerical approaches have been proposed to describe the ignition and combustion in presence of different types of plasma. The fact that the excited atoms and molecules react much faster than the non-excited ones and may markedly decrease the ignition temperature, reduce the induction time and increase the efficiency of combustion will be discussed in chapter III.

### **I.4.2. Flame stabilization**

#### **I.4.2.1. Pilot flame stabilization**

Reducing NO<sub>x</sub> emissions from combustion chambers is a major challenge. One approach has been to operate at lean mixtures in order to reduce flame temperature, which in turn, reduces the production of NO<sub>x</sub>. However, lean burning can lead to serious combustion instabilities, which can result in flame extinction [68]. Various stabilization methods have been implemented for both diffusion and premixed flames. These include pilot flames, recirculation flow via bluff bodies, swirl, electric fields, and plasmas.

The first technique concerns the use of a rich pilot flame to reattach the combustion process. To attach a hydrocarbon flame to a burner lip, Han and Mungal [69], Muñoz and Mungal [70] and Carter et al. [71] used a hydrogen pilot flame in a coflow jet diffusion flame. Moreover, Prakash et al. [72] increased premixed flame stability by controlling the flow rate split between a bypass line and the main fuel line. Tachibana et al. [73] investigated the effect of secondary fuel injection location on premixed combustion instability. Typical examples of bluff body and swirl stabilization can be found in [74], [75], and [76]. However, these methods have an intrinsic limit in that the main energy transfer occurs predominantly in the form of thermal energy, which implies that a portion of energy is lost. Moreover, this technique significantly increases the level of NO<sub>x</sub> generated. Electric field stabilization is then an interesting alternative [77].

### **I.4.2.2. Electric field stabilization**

Flame stability can be obtained by controlling flow convection in the flame reaction zone with electric fields. The stabilization effect is caused by an “ionic wind” between the applied electric field and the “chemiionized” species in the flame reaction zone. In particular, Calcote et al. [78, 79] observed flame deflection and blowout limit extension of a Bunsen burner exposed to a DC electric field. The blowout limit of a premixed methane/air flame is then increased by a factor 4. More marginal in comparison to studies with DC fields, investigations of blowout limit and burning velocity under alternating current (AC) were also reported in [80-83].

Work regarding the interaction between flames and plasma discharges can be found for example in [84-86]. Within these papers, plasma jets are used to increase flame speed and expand the flammability limit of premixed flames.

Finally, an alternative possibility is the use of an electric discharge (in the form of an arc or a HF spark [87]) to reattach a flame and to keep the NO<sub>x</sub> levels acceptable.

### **I.4.2.3. Nonequilibrium plasma stabilization**

Recent activity to investigate novel flame stabilization approaches has included the use of nonequilibrium discharges for combustion enhancement (extended flammability limits and reduced ignition delay times), such as dielectric barrier discharges (DBDs) and nanosecond pulsed discharges for premixed flames [88-100]. In this case, the typical added energy is 0.1 to 1% compared to that of typical hydrogen pilot flames. Corresponding studies on the stability of diffusion flames are relatively rare. Kim et al. [101] found that a coflow lifted methane jet flame is stable under application of a nanosecond pulsed discharge in coflow velocities of up to 20 times the laminar flame speed. They determine the optimal discharge placement in a methane jet in cross flow [77].

Furthermore, the use of pulsed and continuous plasma jets, for the ignition of a lean mixture and the stabilization of the flame in a supersonic flow is promising. An example of application is the flame stabilization in a gas turbine under conditions which tend to extinguish the flame. Another application relates to the diesel engines ignition in extreme cold climate: a small plasma jet is used. In the study of Warris and Weinberg [102], pulsed and continuous plasma jets are used to stabilize fast (5-30 m/s) lean propane/air mixture flames. The results clearly show a large extension of flame stabilization and hold on in the presence of plasma jets. Moreover, the mixture ignition and the flame hold on occur at values well below the lower flammability limits.

Plasma-assisted combustion and stabilization of a turbulent premixed flame using nanosecond repetitively pulsed discharges is studied in [103] and [104], respectively. A related study of Galley et al. [90] concerns the extension of the flammability of a lean mixture. Moreover, pulsed nanosecond plasma has been shown to stabilize lean premixed atmospheric pressure propane-air flames [90]. A nanosecond repetitively pulsed plasma generator capable of delivering an electric pulse of 10 kV during 10 ns at a frequency of up to 30 kHz is used to stabilize and improve the efficiency of a 25 kW lean premixed propane/air flame at atmospheric pressure. The plasma significantly extends the region of flame stability, in a much wider range of fuel equivalence ratios and flow rates. This example demonstrates the possibility of increasing the combustion efficiency with the addition of a 75 W discharge (0.3%). Also, the spontaneous emission of OH and CH radicals increases by at least 40% in the presence of the discharge.

### **I.4.2.4. Arc-type plasma stabilization**

Other research activities study flame sustain by an arc type electric discharge to stabilize the combustion. For example, arc-type plasma stabilization of supersonic H<sub>2</sub>/O<sub>2</sub> combustion mixtures is used within the framework of scramjet combustors.

In the same goal, but with a different electric discharge, Choi et al. [87] studied the stabilization of lean propane/air premixed flames. Low power arcs and high frequency sparks are used. Low power arcs significantly lowered the lean limits of flammability. The results showed that the lean

flammability limit decreases from equivalence ratios of 0.62 to 0.55 at a flow rate of 330 cm<sup>3</sup>/s. Similar effects are observed with a spark discharge. In this study, the minimum equivalence ratio drops from 0.58 to 0.43 (~25% decrease) at a flow rate of 240 cm<sup>3</sup>/s. Finally, it is worth noting that similar reductions in the lean limit of combustion are observed at higher flow rates.

It has to be kept in mind that the plasma generates its own NO<sub>x</sub>. The decrease in equivalence ratio, permitted by the presence of the discharge, can be compensated by the own plasma NO<sub>x</sub> production [87]. However, in larger burners, this balance should be in favour of NO<sub>x</sub> reduction.

### I.4.3. Combustion process and excited oxygen species

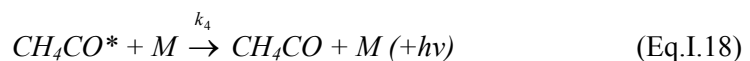
Electronically excited species and ions produced in a discharge may also influence the process of combustion. In high voltage nanopulsed discharges oxygen and nitrogen ions can be present. In general, their concentrations should be relatively low because Coulomb forces are long-range, and recombination of positive ions and electrons are very fast. However, ions can be exploited locally to promote combustion and anchor a flame.

Furthermore, under the conditions of discharge in a gas mixture, there is the possibility to generate active species by the dissociation of O<sub>2</sub> by electronic impact, and also reduce the energy threshold of chemical reactions, for example, involving the singlet state of O<sub>2</sub>. At present, relatively little is known about the possible effects of electronically excited species on combustion kinetics. However, if present in critical concentrations, they may reduce ignition delay time, because typical recombination / relaxation energies tend to be very high (of order 10 eV against 1 eV for recombination of radicals). The possibility of combustion improvement either through the excitation of an oxidizer [105] or the fuel molecules [106] is a growing and promising research topic. The potentiality of the control of combustion processes by using electronically excited oxygen molecules has been studied by Smirnov et al. [107]. The experiments presented in [107] demonstrate that the excitation of O<sub>2</sub> molecules to the singlet electronic state at low pressure  $P = 10\text{--}20$  Torr makes it possible to significantly reduce the induction zone length in a premixed subsonic H<sub>2</sub>-O<sub>2</sub> low pressure flow and confirm the conclusion of the theoretical studies of Starik et al. [66, 67]. The excitation of O<sub>2</sub> molecules to the states  $a^1\Delta_g$  and  $b^1\Sigma_g^+$  by a laser, significantly decreases the induction period and ignition temperature, by up to 300 K [105]. The present study relies on the excitation of O<sub>2</sub> molecules to singlet oxygen states through an electrical discharge.

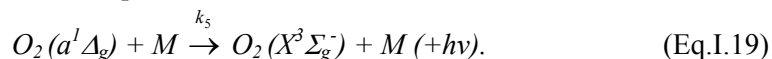
In combustion reaction with ground state triplet oxygen, various atoms and radicals are produced. Particularly, with hydrocarbons, combustion proceeds in a chained manner through various reactions such as hydrogen abstraction. In contrast, excited oxygen, being an electrophilic reactant, is prone to react with a substance having a greater electron donative characteristic. Accordingly, in contrast with triplet oxygen, which is liable to react with radicals, singlet oxygen is prone to induce two-electron reactions. For example, singlet oxygen is able to actively induce reactions which are difficult to induce by triplet oxygen, such as direct addition to a double bond and generation of dioxetane. In literature, Silver [108] showed that at a relative low temperature of 600 K, electronically excited oxygen reacts with hydrocarbons in reaction  $k_1$  at rates that are 10 to 20 times faster than quenching of the excited state ( $k_3$ ). The results show that electronically excited oxygen, O<sub>2</sub>( $a^1\Delta_g$ ), participates in cool flame combustion through a chain mechanism involving a manifold of electronically excited molecular species. The chain reaction mechanism proposed involves three processes :



The termination reactions are :



and the quenching of  $O_2(a^1\Delta_g)$  by a collision partner M, as :



Both termination processes can be either radiative processes or not.

This is an indication that the linear chain mechanism proposed above is a realistic and viable possibility for cool flame combustion processes

Finally, the other type of activation, which the oxygen can undergo is its excitation into higher vibrational levels, which are to be considered as metastable. Herzberg highlights the fact that the higher vibrational levels of a molecule must be regarded as metastable, and therefore, they too may be of importance in elementary chemical processes [109].

In the current study, we investigate nanosecond pulsed discharge enhancement of flame stability in a more complex partially-premixed flame configuration, burning methane. The approach is based on the fact that the excited atoms and molecules react much faster than the non-excited ones [33, 110] and this approach seems to be promising because of its potential higher efficiency compared to that initiated by ordinary heating.

## **I.4.4. Plasma assisted ignition**

### **I.4.4.1. ( $H_2$ /air), ( $CH_4$ /air) and ( $C_3H_8$ /air) systems**

The influence of non equilibrium plasma created by a pulsed discharge on the ignition thresholds of a combustible mixture at various pressures and temperatures has been studied by an installation consisting of a discharge cell connected to a shock-tube. It allows study of fast homogeneous ignition of supersonic flows [24]. In the study of Bozhenkov et al. [24], the ignition delay time decreases significantly in the case of the simultaneous action of the shock wave and the nanosecond discharge. Moreover, Klimov et al. [111] succeeded in ignition and stable burning of very lean propane/argon (1:9) mixtures in a supersonic air flow. A high frequency streamer discharge and a high frequency torch plasma discharge were used.

Authors of [24, 27, 92] studied the possibility of the acceleration of combustion (characterized by the ignition delay) by application of a nanosecond pulsed barrier discharge to ( $H_2$ /air), ( $CH_4$ /air) and ( $C_3H_8$ /air). The application of a discharge, which develops in the form of a fast ionization wave, in the system ( $H_2$ /air), is studied by Starikovskii [27]. In the case of the mixtures with 29.6% of  $H_2$  in air, a significant part of energy is spent for the direct dissociation of  $O_2$  and  $H_2$  by electronic impact, generating a great quantity of O and H atoms. The high degree of dissociation leads to a rapid development of ignition. Thus, the induction time until ignition is decreased under the action of the gas discharge. At high temperature (~2500 K), there is a difference by a factor 1.5 between a “thermal” and a “non equilibrium” ignition. This difference increases in a monotonous way with a temperature decrease. Also, experiments on ignition of nonflowing preheated hydrogen-air and hydrocarbon-air mixtures by a single-pulse fast ionization wave discharge demonstrate that it can substantially reduce ignition delay time [93]. In addition, the ignition threshold can be reduced by 300 K to 500 K with the pulsed discharge (high intensity and contribution of energy < 0.1 J/cm<sup>3</sup>).

It is worth noting that the most critical process for high voltage ignition is the atomic oxygen and atomic hydrogen production, which ensures the evolution of the flame.

Autoignition of ( $CH_4$ /air) mixtures non-diluted at high pressure ( $P \leq 500$  atm) is studied by Zhukov et al. [112] by shock-tube technique. The authors showed that in the process of ignition, initiated by the action of a pulsed discharge in  $CH_4$ /air at high temperature, its main role concerns the direct dissociation reactions of the gas by electron impact and the dissociative quenching of excited electronic states of  $N_2$  by oxygen. The production of additional “active centres” results from the acceleration of the chemical kinetic process.

An important characteristic is the proper organization of the energy deposited in the medium. Energy must be provided in the discharge space and be employed for the production of radicals (instead of the ionization of gas or the thermal heating) : the “streamer” discharge mode corresponds

well to these conditions. Indeed, the active particles are produced at the streamer "discharge head" (which measures typically 0.05 cm for voltages of 10-20 kV).

In addition, Chintala et al. [113] study experimentally the application of non equilibrium plasma created by a RF discharge, arc DC and "spark" in flows of CH<sub>4</sub>/air, C<sub>2</sub>H<sub>4</sub>/air and CO/air. For the CH<sub>4</sub>/air and C<sub>2</sub>H<sub>4</sub>/air stoichiometric flows, the flow rates ( $u$ ) and the studied pressures ( $P$ ) are :  $u \leq 4.3$  m/s,  $P \geq 350$  Torr and  $u \leq 6.3$  m/s,  $P \geq 240$  Torr, respectively. Results obtained with DC, arc and spark discharges, show that no ignition is obtained for pressures lower than 300 Torr for the CH<sub>4</sub>/air flows and below 200 Torr for C<sub>2</sub>H<sub>4</sub>/air and this for the same mass flow rate of 1.2 g/s.

Experiments show that the use of a RF discharge instead of a traditional ignition by arc or spark makes it possible to ignite flows of C<sub>2</sub>H<sub>4</sub>/air, CH<sub>4</sub>/air and CO/air, and this at higher flow rates and lower pressures.

Finally, recent experiments of Lou et al. [64] on ignition of premixed hydrocarbon-air flows using transverse RF discharge demonstrate that volume ignition can be produced at plasma temperature significantly lower than the autoignition temperature (300 – 400 °C). The propane dissociation by electron impact mechanism is described in [114].

2D images of OH emission under ignition of the propane-air mixture by a sequence of nanosecond pulses were obtained in [115] using an ICCD camera. The authors compared them with the ICCD images for ignition by conventional spark discharge. At the same energy deposited in the discharges (30 mJ) the emission from combustion initiated by the conventional spark is less intensive and the flame expansion rate for the conventional spark is slower too.

Mintousov et al. [89] consolidate the theory and the suggested model of the influence of radicals. According to their results, the main channels of production of the active particles (O, H, and OH) in the mixtures with air (N<sub>2</sub>/O<sub>2</sub>) are :

- the N<sub>2</sub> excitation by electronic impact, which generates the production of molecules in an excited electronic state ;
- the kinetics of the excited states, mainly the N<sub>2</sub>\* quenching on O<sub>2</sub> (N<sub>2</sub>\* + O<sub>2</sub>) with the formation of atomic oxygen O ;
- then the combustion of a new mixture with concentrations in highly non equilibrium radicals and with the production of new excited radicals (OH\*).

Finally, the authors of [116] replaced N<sub>2</sub> by Ar to remove the main channel of formation of active particles: the result is a deceleration of the flame speed.

#### **I.4.4.2. (C<sub>n</sub>H<sub>2n+2</sub>/air) systems (n>3)**

The excitation of molecular oxygen, its dissociation and its ionization entirely control the oxidation of alkanes, but also that of the reaction products and intermediates. Let us recall that the dissociation threshold of alkanes by electronic impact decreases by approximately 1eV with the increase of one carbon atom in the molecule [29].

Also, the steric factor increases proportionally with the quantity of carbon atoms of alkane. In the other hand, the  $[\text{alkane}]_{\phi=1}$  decreases proportionally to the quantity of C atoms. Thus, one expects that when one passes from a light alkane to a heavy alkane (at  $\phi=1$ ), the variation in  $[\text{alkane}]$  is compensated by the variation of the steric factor. However, with an increased number of C atoms, the dissociation threshold by electronic impact decreases ; therefore, one expects a faster oxidation of the heaviest alkanes.

The fuels used in internal combustion engines include HC of C8 to C16. The authors of [29] studied the oxidation of decane (C<sub>10</sub>H<sub>22</sub>) by a nanosecond discharge. The total oxidation time of the mixture {C<sub>10</sub>H<sub>22</sub>/O<sub>2</sub>} at various equivalence ratios is obtained from the intensities of the bands of CO emissions CO (B<sup>1</sup>Σ→A<sup>1</sup>Π). Conclusions previously made for smaller alkanes on the total oxidation time can be extended to heavier alkanes.

## I.5. Conclusion

Combustion processes impact a lot of aspects of modern life. It is of vital interest to maximize the efficiency of combustion processes to save fuel and reduce pollution. It is the object of this work, to significantly improve combustion and reduce pollutant emissions with plasma “activation”. Several studies demonstrate that the presence of a discharge significantly reduces the fuel/air ratio at which a flame could be maintained (spark and arc [87]).

The low-temperature plasma of a gas discharge is the most often and widely used for plasma-assisted processing. Production of active neutral particles in plasma (i.e. metastable atoms and radicals) is the key element. The main advantage of this technique is the fact that the main part of the energy introduced is used for the generation of highly energetic electrons leading to the production of reactive particles, minimising energy lost in the heating of the gas volume. Moreover, nonthermal plasmas have the advantage to be generated at pressures less or equal to atmospheric pressure, to be stable and reproducible.

Electric fields and non thermal plasmas have been widely studied in the context of changing the behaviour of flames. However, little work has been carried out on the non thermal plasma “activation” of fuels, oxidants, and/or fuel-oxidant mixtures for the purpose of enhancing combustion [114]. Regarding the present study, we will focus on **non-thermal plasma oxidizer activation**. In particular, electronically excited oxygen is expected to accelerate chemical reactions at low temperature. These additional active species are expected to influence the kinetics of combustion and significantly decrease the ignition delay, increase flame velocity and intensify combustion.

The following report is divided into four parts. The first section will present the oxygen molecule and particularly characteristics of electronically excited oxygen singlet delta  $O_2(a^1\Delta_g)$  and singlet sigma  $O_2(b^1\Sigma_g^+)$  states. Electronic configuration and emission spectra simulation are presented. Next, modelling results will be described and discussed. The fourth chapter will present the experimental generation and identification of excited species produced in the plasma and particularly, singlet sigma  $O_2(b^1\Sigma_g^+)$ . Finally, plasma assisted combustion experiments are presented.

# Chapter II : Identification of species and temperature measurement by emission spectroscopy

## Abstract

---

The knowledge of the various properties of molecules allows us to understand many of the physical and chemical properties of the gases under consideration. Observed molecular spectra in various kinds of electric discharges and flames show characteristic line spectra. The band spectra observed in the visible and ultra-violet regions of the spectrum obviously cannot be interpreted as simple rotation or rotation-vibration spectra, since their structure are generally more complicated. However, one explains these visible and ultra-violet band spectra as due to electronic transitions in molecules (in conformity to electronic transitions in atoms).

The subject of this chapter is not to give a detailed interpretation of molecular spectroscopy, but to present some theoretical backgrounds allowing to model synthetic emission spectra of molecules of interest. Excited states of molecules or atoms are generated by thermal excitation, absorption of radiation or chemical reactions (chemiluminescence). In our plasma medium, they are generated by electrical excitation.

Here, we focus on oxygen molecule and on the study of electronically excited oxygen singlet delta  $O_2(a^1\Delta_g)$  and singlet sigma  $O_2(b^1\Sigma_g^+)$  states. OH hydroxyl radical, molecular nitrogen and  $C_2$  were also investigated but are not presented here.

This modelling work will be later used to identify species created in the plasma and to measure the plasma rotational and vibrational temperatures.

A short description of suitable experimental techniques is proposed at the end of the chapter.

---

## II.1. Introduction

Determination of the electronic structure of  $O_2$  is important for our understanding of its role in various areas such as atmospheric physics, gaseous discharges, and plasmas.

Besides its more or less intense electronic systems in the ultraviolet spectral region, oxygen has two further systems in the near infrared and visible regions that are uncommonly weak. With absorbing substance in a sufficiently long path and with sensitive means of detection, bands in these systems exhibit well-developed rotational structure that reveal the symmetry of electronic states between which these transitions occur. The first works determining the gaseous molecular oxygen absorption spectra, were performed in 1885, when Egoroff announced in the “Comptes Rendus de l’Académie des Sciences” that he has found the doublet bands of A and B groups of the solar spectra in the gaseous oxygen absorption spectra examined at 6 atm pressure in 60 meters long tubes. A certain number of bands have been put in evidence by Janssen, Liweing and Dewar, Pihlblad and Audubert [117].

As discussed before, oxygen is important in its excited molecular states, singlet delta oxygen,  $O_2(a^1\Delta_g)$  and singlet sigma oxygen,  $O_2(b^1\Sigma_g^+)$ .

This sentence extracted from [30] “... So that the transition, with its 45 minutes mean lifetime at the limit of zero pressure is quite possibly the molecular transition that is most forbidden in nature” gives an illustration of the difficulty to observe these emissions. Therefore, one of the main goals of this work is to achieve significant yields of excited oxygen molecules, in nonequilibrium gas discharge oxygen plasmas at low temperatures; its identification and use for plasma temperature measurements by comparisons between experimental and simulated emission spectra. To reach these goals, we first give an overview of the particularity of molecular oxygen, as diatomic molecule; afterwards, simulation programs are developed in order to generate synthetic emission spectra. The point concerns the method allowing identifying emission fingerprint of excited oxygen and in that case estimating the

temperature of rotation. To explain the theoretical model, we shall develop the case of both transitions :  $O_2(a^1\Delta_g) \rightarrow O_2(X^3\Sigma_g^-)$  (0,0) and  $O_2(b^1\Sigma_g^+) \rightarrow O_2(X^3\Sigma_g^-)$  (0,0) emission bands of molecular oxygen.

## II.2. Spectroscopic description of oxygen molecule

### II.2.1. $O_2$ potential energy curves

#### II.2.1.1. Presentation

An additional feature of diatomic molecules is the internuclear distance of the two nuclei. The potential energy versus nuclear separation curves for the lower states of  $O_2$  is shown schematically in fig.II.1. One of the most accurate methods for generating potential energy curves is the Rydberg-Klein-Rees (RKR) Procedure [118, 119]. The RKR procedure is basically described by Albritton et al. in [120] and has been used extensively for many years to treat a very large number of diatomic molecular states.

Potential energy curves, as calculated by the RKR code for the  $X^3\Sigma_g^-$ ,  $a^1\Delta_g$ , and  $b^1\Sigma_g^+$  states of  $O_2$  are shown in Fig.II.1. The potential energy (in eV) is plotted against the separation of the two atoms bound in the diatomic oxygen molecule. It is worth noting that transitions between the ground state  $X^3\Sigma_g^-$  and the lowest excited state  $a^1\Delta_g$  have a lower energy than between some vibrational levels (for  $v' > 6$ ) of the ground state [121].

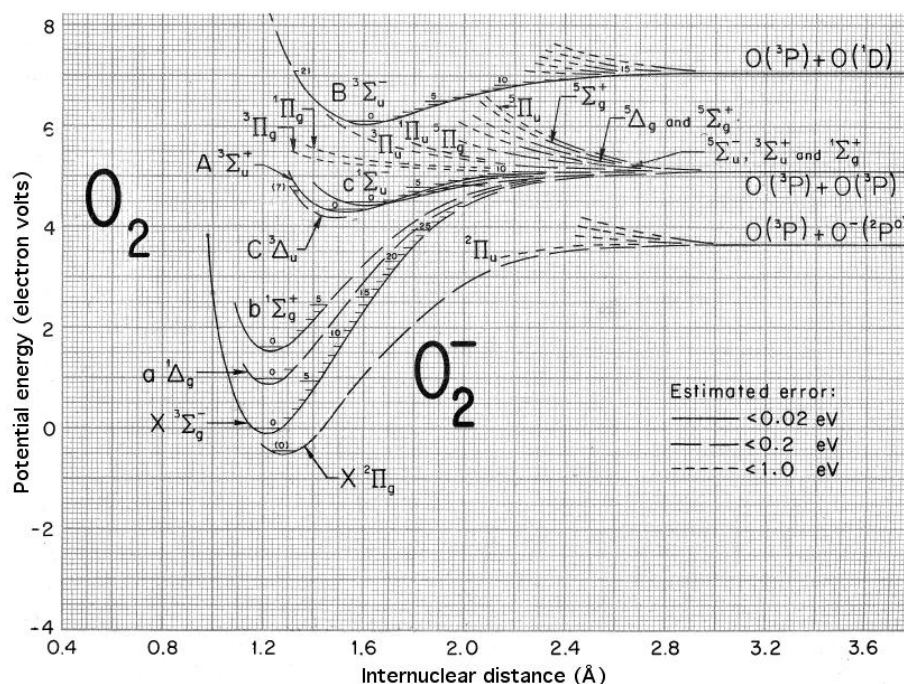


Fig.II.1.  $O_2$  Potential energy curves; reprinted from [122].

In the unified atom approximation for molecules, a main quantum number can be assigned. In molecules the energy levels are usually abbreviated by upper and lower case letters, where X is the ground state (as a rule). Electronic levels are named by Greek letters attributed for each electronic quantum number  $\Lambda$  :

$\Lambda$	0	1	2	3	4
spectral letter	$\Sigma$	$\Pi$	$\Delta$	$\Phi$	$\Gamma$

Table II.1. Spectral terms.

The ground electronic state  $X^3\Sigma_g^-$ , the two first excited electronic states ( $a^1\Delta_g$ ) and ( $b^1\Sigma_g^+$ ) are shown. The excited electronic states  $c^1\Sigma_u^-$ ,  $A^3\Sigma_u^+$  and  $C^3\Delta_u$ , close to each other in energy, known as “Herzberg states”, are also shown in Fig.II.1. For each state, some of the individual vibrational levels are indicated. Rotational levels are not shown; their spacing is much smaller than those of the vibrational energy levels. Actually, the vibrational motion is anharmonic, and the spacing between vibrational levels decreases with increasing energy, becoming vanishingly small at the dissociation energy at the top of each potential curve [123].

Moreover, one can observe that the curves for  $X^3\Sigma_g^-$ ,  $a^1\Delta_g$  and  $b^1\Sigma_g^+$ , all have roughly the same equilibrium radius ( $r_e$ ) and that they dissociate to the same products ( $O^3P + O^3P$ ). The  $a^1\Delta_g$  state lays roughly 0.98 eV above the  $X^3\Sigma_g^-$  ground state and  $b^1\Sigma_g^+$  state roughly 1.63 eV above it. Converting these energies to wavelengths, one can obtain the following relations :

$$\lambda_{O_2(a^1\Delta_g)} = \frac{1239.8 \text{ eV} \cdot \text{nm}}{0.98 \text{ eV}} = 1268 \text{ nm} \quad (\text{Eq.II.1})$$

$$\lambda_{O_2(b^1\Sigma_g^+)} = \frac{1239.8 \text{ eV} \cdot \text{nm}}{1.63 \text{ eV}} = 762 \text{ nm} \quad (\text{Eq.II.2})$$

Thus, singlet delta oxygen ( $a^1\Delta_g$ ) and singlet sigma oxygen ( $b^1\Sigma_g^+$ ) emission band are centred at 1.27  $\mu\text{m}$  and 762 nm respectively.

### II.2.1.2. Electronic configuration

The linear combination of atomic orbitals (LCAO) model leads to the following occupation of molecular orbitals in the ground state. The electron configuration for the diatomic oxygen molecule is:

$$(1\sigma_g)^2 (1\sigma_u)^2 (2\sigma_g)^2 (2\sigma_u)^2 (3\sigma_g)^2 (1\pi_u)^4 (1\pi_g)^2. \quad (\text{Eq.II.3})$$

The ground state of  $O_2$  is unusual because it is a triplet state; specifically the spectroscopic term for this state is  $X^3\Sigma_g^-$ . Because of its unique spin, this state is responsible for many of oxygen's unique characteristics. The electronic properties of oxygen are determined by the six electrons in  $\pi$  molecular orbitals. Moreover, the unpaired electrons in two different molecular orbitals account for the paramagnetism of  $O_2$ . The electron occupancy is described in Fig.II.2.

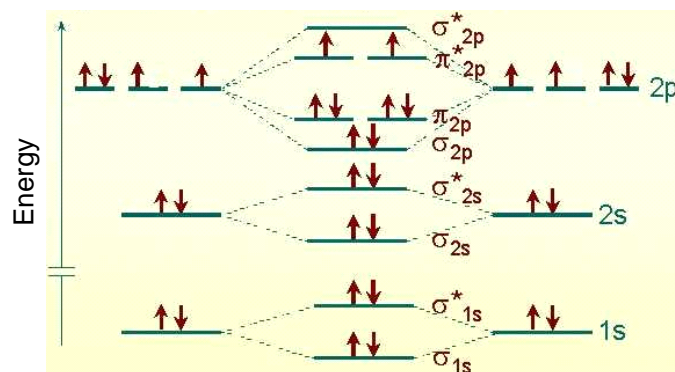


Fig.II.2. Molecular orbital diagram for  $O_2$  molecule <sup>3</sup>.

The most well known system of molecular oxygen is the Herzberg system. Since this system ( $A^3\Sigma_u^+ - X^3\Sigma_g^-$ ) was first observed by Herzberg in 1932, there have been many publications of a considerable interest. The Herzberg I bands consist of many sharp rotational structures. Absorption

<sup>3</sup> Master courses “Energy and Environment” : Spectroscopy of diatomic molecules, Orléans University.

intensity measurements were obtained by Hasson and Nicholls using photographic techniques in 1971. More recently, Huestis et al. [124] observed the A-X bands by the method of Cavity Ring-Down Spectroscopy (CRDS). Yoshino et al. [125] measured the Herzberg I bands of O<sub>2</sub> by Fourier transform spectrometry in the wavelength region 240-270 nm. Dieke and Babcock [126] discussed the 0-0, 1-0, 2-0 and 3-0 bands of O<sub>2</sub>.

In this study, we focus on the two lowest energy states of molecular oxygen. In 1948 at the Mont Wilson Observatory, Babcock and Herzberg [109] photographed seven absorption bands of the b<sup>1</sup>Σ<sub>g</sub><sup>+</sup> - X<sup>3</sup>Σ<sub>g</sub><sup>-</sup> red atmospheric band system of the oxygen molecule between the vibrational levels v''=0 and 1 of the X<sup>3</sup>Σ<sub>g</sub><sup>-</sup> state, and v'=0 through 3 of the b<sup>1</sup>Σ<sub>g</sub><sup>+</sup> state. This electric-dipole-forbidden transition was recorded with the Snow telescope using air absorption paths up to 100 km and in the laboratory with interferometric studies using 30 m air absorption paths. These original data have been reanalysed by several authors (Albritton et al. [127]; Kanamori et al. [128]) to produce a more consistent set of molecular parameters. More recently, Naus et al. [129, 130] investigated the oxygen A and B bands, corresponding to the (0-0) and (1-0) bands of the b<sup>1</sup>Σ<sub>g</sub><sup>+</sup> - X<sup>3</sup>Σ<sub>g</sub><sup>-</sup> system, using Cavity Ring Down laser Spectroscopy (CRDS). Ritter and Wilkerson obtained, by ultrahigh-resolution laser absorption for pressures up to 1 bar, a weak Einstein coefficient A(b-X) of 0.0887 s<sup>-1</sup>, corresponding to the radiative lifetime τ(b-X)=1/A(b-X) of 11.3 s [131]. Also, the (0,1) band of the (<sup>1</sup>Δ<sub>g</sub>→<sup>3</sup>Σ<sub>g</sub><sup>-</sup>) system of oxygen was first observed in the twilight airglow by Wallance Jones and Harrison [132]. According to [132], the (0,0) band of the (<sup>1</sup>Δ<sub>g</sub>→<sup>3</sup>Σ<sub>g</sub><sup>-</sup>) system is theoretically at least 10 times stronger than the (0,1) band but was not detected from the ground because of re-absorption by oxygen in the lower atmosphere.

The 0-0 band produces strong absorption in the solar spectrum at 1.27 μm. This absorption in the lower atmosphere makes it difficult to observe the 0-0 band in emission with ground-based instruments, but it was achieved by Noxon and Vallance Jones [133] from an aircraft at an altitude of about 13 km. Moreover, the most extensive and accurate measurements of the atmospheric oxygen bands are those by Dieke and Babcock [126], which were based on wavelengths obtained with interferometers by Babcock.

Concerning the a<sup>1</sup>Δ<sub>g</sub> - X<sup>3</sup>Σ<sub>g</sub><sup>-</sup> infrared band system of the oxygen molecule, transition of the O<sub>2</sub> dimer involving the [O<sub>2</sub>(<sup>1</sup>Δ<sub>g</sub>)v=0]<sub>2</sub> → [O<sub>2</sub>(<sup>3</sup>Σ<sub>g</sub><sup>-</sup>)v=0]<sub>2</sub> transition has been recorded near 632.6 nm by Biennier et al. [134] using Cavity Ring Down laser Spectroscopy. The interest of this oxygen dimer in atmospheric chemistry is that it may be involved in a new production channel of ozone in the stratosphere and may help to address the “ozone deficit problem” [134]. Moreover, in the stratosphere, O<sub>2</sub> is produced in the b<sup>1</sup>Σ<sub>g</sub><sup>+</sup> state by recombination of oxygen atoms and in a secondary reaction of photodissociation of ozone by solar ultraviolet radiation.

The O<sub>2</sub> a<sup>1</sup>Δ<sub>g</sub> and b<sup>1</sup>Σ<sub>g</sub><sup>+</sup> states arise from the ... (2pσg)<sup>2</sup>(2pπu)<sup>4</sup>(2pπ\*<sub>g</sub>)<sup>2</sup> electronic configuration which also gives rise to the ground X<sup>3</sup>Σ<sub>g</sub><sup>-</sup> state. The electron occupancy of the ground state and the two lowest excited states are described in figs.II.3 :

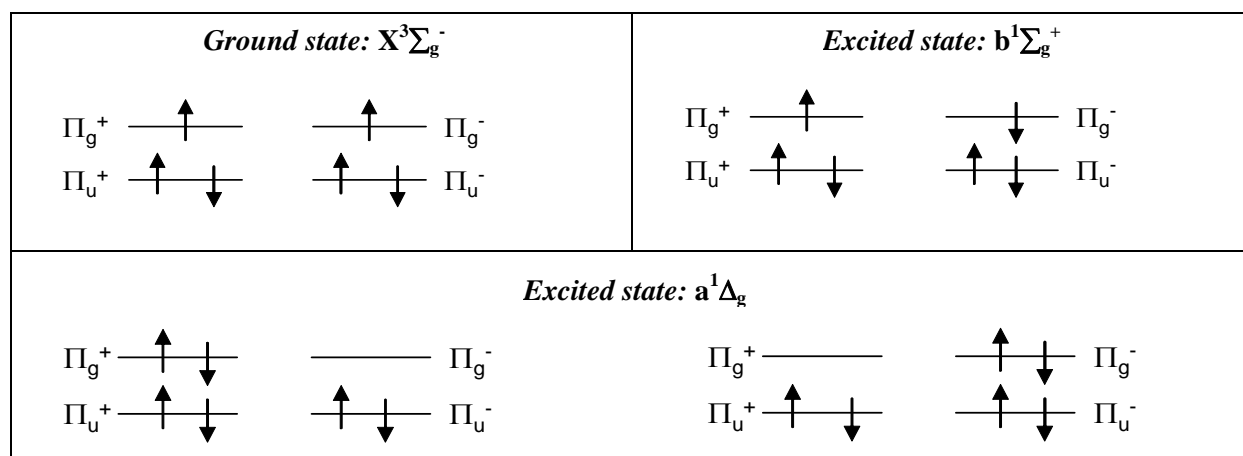


Fig.II.3. Occupation of molecular orbital (MO) in oxygen.

The electronic configuration shown in Fig.II.3 gives rise to three different electronic states,  $X^3\Sigma_g^-$ ,  $a^1\Delta_g$  and  $b^1\Sigma_g^+$  (two different electron occupancy for  $a^1\Delta_g$  state), each with its own sub-components, as shown in Table II.2. This table deals with the two electrons in the anti-bonding  $\pi_g$  orbital.

Orbital Assignment	Eigenvalue under		Components of state
	$L_z$	$S_z$	
$\pi_g^+\alpha \quad \pi_g^+\beta$	2	0	$a^1\Delta_g$
$\pi_g^+\alpha \quad \pi_g^-\alpha$	0	1	$X^3\Sigma_g^-$
$\pi_g^+\alpha \quad \pi_g^-\beta$	0	0	$X^3\Sigma_g^-, b^1\Sigma_g^+$
$\pi_g^+\beta \quad \pi_g^-\alpha$	0	0	$X^3\Sigma_g^-, b^1\Sigma_g^+$
$\pi_g^+\beta \quad \pi_g^-\beta$	0	-1	$X^3\Sigma_g^-$
$\pi_g^-\alpha \quad \pi_g^-\beta$	-2	0	$a^1\Delta_g$

Table II.2. Molecular oxygen configuration components.

An electron can have either the positively circulating probability of  $\pi^+$  or the negatively circulating probability of  $\pi^-$ . In addition, the electron can have spin up, marked  $\alpha$ , or spin down, marked  $\beta$ .

Table II.2 shows the six unique, allowed possibilities (out of 16) of + ; - ;  $\alpha$  and  $\beta$ , their corresponding Eigenvalues of  $L_z$  and  $S_z$ , and which state they make up [123].

## II.2.2. Branches and spectra

### II.2.2.1. Structure

The spectra of molecules are richer than those of atoms because the extra atoms add extra degrees of freedom. The simplest molecule, the homonuclear diatomic shown in fig.II.4 has  $3n = 6$  degrees of freedom ( $n$  being the number of atoms). Among these degrees of freedom are the centre of mass translation in ( $x, y, z$ ), one degree of freedom is vibration, one degree of freedom is rotation about an axis perpendicular to the centre of the internuclear axis, and the remaining one is rotation around the internuclear axis.

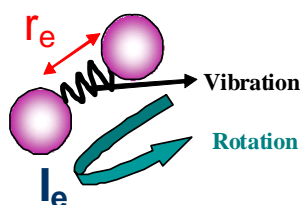


Fig.II.4. Schematic  $O_2$  homonuclear diatomic molecule : degrees of freedom.

Since the rotational energy of a diatomic molecule is much smaller than the vibrational energy (exception made for  $H_2$  diatomic molecule), there is a manifold of rotational lines for each vibrational level. Transitions between different vibrational levels are accompanied by changes in rotational quantum number as well.

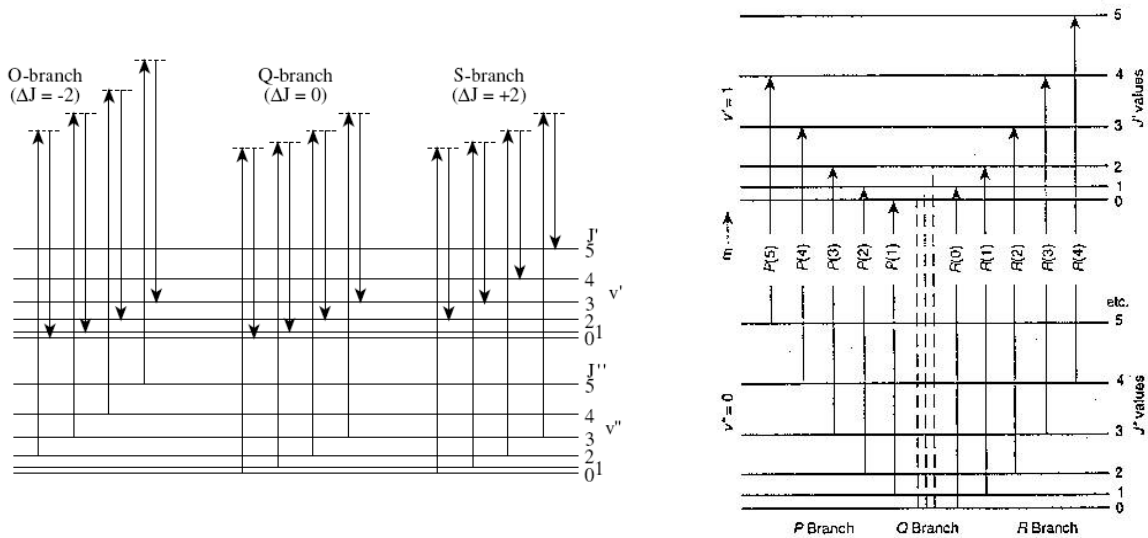


Fig.II.5. Rotational and vibrational levels [30].

The transitions with  $\Delta J = 0$  are called Q-branch transitions. The transitions with  $\Delta J = -2$  are called O-branch transitions and those with  $\Delta J = +2$  are S-branch transitions. P and R branches, corresponding to transitions with  $\Delta J = -1$  and  $\Delta J = +1$  respectively, are also presented in Fig.II.5.

### II.2.2.2. Cooperative emission bands

The importance of the oxygen dimer has been recently highlighted by kinetic studies relative to the ozone cycle [135]. In the chemical laser field, Yoshida et al. [136], observed an unexpected red fluorescence in a chemical oxygen iodine laser, corresponding to an excited metastable state of  $(O_2)_2$ . More recently, Biennier et al. [134] recorded  $O_2$  dimer emission involving two  $O_2(a^1\Delta_g)$  molecules near 632.6 nm by CRDS. The following figure sums up all the known radiative transitions bringing into play two molecules :

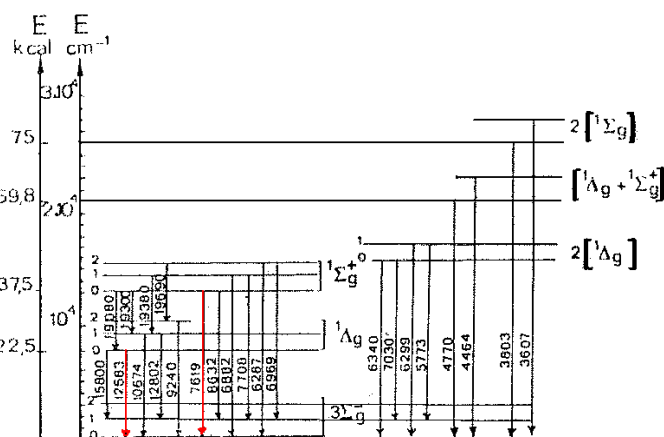


Fig.II.6. Observed radiative transitions of molecular oxygen  $O_2$  [137].

There are several simultaneous transitions of colliding singlet oxygen molecule pairs which cause a relaxation of the multiple selection rules. I.e., while the direct decay of  $O_2(a^1\Delta_g)$  to the ground state is forbidden, the emission of a single photon by a colliding pair is not. The photon wavelengths produced by various colliding molecule pairs are shown in Table II.3. This emission of a photon by a simultaneous transition has been called dimol emission in the past, but since no dimers of  $O_2$  exist at ordinary conditions, this nomenclature is incorrect and misleading.

The following table sums up all the most known important radiative transitions bringing into play two molecules (cooperative emission bands), and highlights in grey the photon wavelength corresponding to transitions of particular interest in this study.

Colliding Pair	Photon Wavelength (nm)
$(X^3\Sigma_g^-)(X^3\Sigma_g^-)$	No transition
$(a^1\Delta_g)(X^3\Sigma_g^-)$	1270
$(b^1\Sigma_g^+)(X^3\Sigma_g^-)$	762
$(a^1\Delta_g)(a^1\Delta_g)$	634
$(b^1\Sigma_g^+)(a^1\Delta_g)$	476
$(b^1\Sigma_g^+)(b^1\Sigma_g^+)$	381

Table II.3. Oxygen simultaneous transition wavelengths.

Emission spectrum of the afterglow of an oxygen discharge at 2 Torr pressure for the wavelength region 400-800 nm is presented by Findlay [49]. Observed emission bands are the following: at 632.1 nm, 703 nm and the (0,0) and (1,0) bands of the  $(^1\Sigma_g^+ - ^3\Sigma_g^-)$  system of oxygen at 762 and 690 nm. Three other bands appear in the spectrum at 478.4, 516.5 and 578.8 nm. Due to the weakness of these bands, it was not possible to obtain spectra at sufficient resolution to resolve any rotational structure.

The following spectrum extracted from an experimental study of Naumov [138] represents the emission spectrum of an oxygen/argon mixture in a crossed discharge. The characteristics of the crossed discharge are listed in the caption.

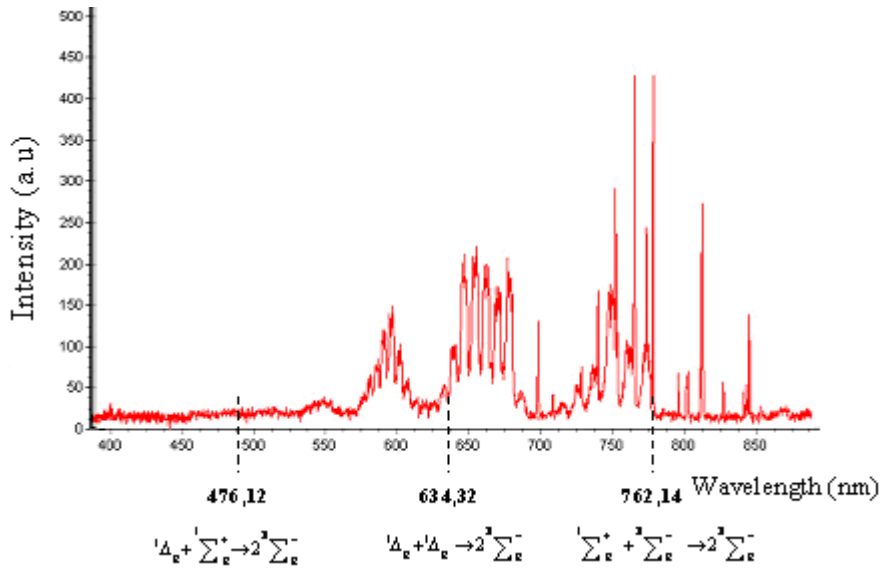
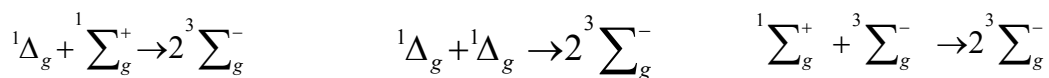


Fig.II.7. Emission spectra of a combined cross discharge in  $O_2$  (5%)/Ar mixtures at 50 Torr pressure. AC PS: 100 Hz, 7 kV ~ 1 W, DC PS: 800 V, 30 mA.

This experimental spectrum has been obtained in conditions of generation of non-self-sustained discharge. The three emission bands at 476.12, 634.32 and 762 nm are assigned to the following double electronic transitions of oxygen respectively :



The experimental generation of excited oxygen presented in further chapters will show that, contrary to literature results focussed on the generation of excited oxygen, in the present study, the acquired emission spectra are of high resolution. Thus, the rotational structure has been resolved.

We describe now the simulation of the atmospheric A-band and infrared band emission spectra of O<sub>2</sub> used later for identification and temperature measurements (determination of the gas temperature in nonequilibrium plasma from the emission spectra rotational structure).

## II.2.3. Selection rules

### II.2.3.1. Introduction

Considering the Born Oppenheimer approximation, the total energy of a molecule is the sum of electronic, vibration and rotation energies. A change of these energies is induced by an emission or by absorption of a photon.

The only possible transitions between two rotational levels from two different electronic states are described by selection rules.

### II.2.3.2. O<sub>2</sub> b<sup>1</sup>Σ<sub>g</sub><sup>+</sup> → X<sup>3</sup>Σ<sub>g</sub><sup>-</sup> transition

The Σ<sub>g</sub> → Σ<sub>g</sub> transition, though strictly forbidden as electric dipole radiation, is possible as magnetic dipole or electric quadrupole radiation. The observed branches of the red atmospheric oxygen bands can be explained only by the selection rules for magnetic dipole radiation [109] :

Selection rules	Forbidden transitions	Selection rules	Forbidden transitions
ΔJ = 0, ± 1	$J = 0 \xrightarrow{NO} J = 0$	ΔJ = 0, ± 1, ± 2	$J = 0 \xrightarrow{NO} J = 0$ $J = 1 \xrightarrow{NO} J = 0$
+ ↔ + - ↔ -		+ ↔ + - ↔ -	
	$- \xrightarrow{NO} +$ $+ \xrightarrow{NO} -$		$- \xrightarrow{NO} +$ $+ \xrightarrow{NO} -$

Table II.4. Selection rules for : left) magnetic dipole radiation ; right) electric quadrupole radiation.

Thus, in addition to the transitions allowed by the selection rules described before, under certain conditions transitions occur that contradict the selection rules discussed previously. They are called “forbidden transitions”. They can be observed in absorption by using very long absorbing paths (considerably longer than are necessary for the ordinarily allowed transitions) [127, 129, 130, 134, 139-142], mainly by absorption spectroscopy and Cavity Ring Down Spectroscopy, CRDS. In emission, they appear only under quite special conditions of excitation.

The occurrence of forbidden transitions may have one of the three following reasons :

- the selection rule that is violated may hold only as a first approximation ;
- the selection rule may hold strictly for dipole radiation but not for quadrupole radiation or magnetic dipole radiation ;
- the selection rule may hold only for the completely free and uninfluenced molecule and may be violated in the presence of external fields, collisions with other molecules.

Then, the well-known atmospheric oxygen bands which appeared in the red part of the solar spectrum are accounted for on the assumption that they represent an electric dipole <sup>1</sup>Σ<sub>u</sub><sup>-</sup> → <sup>3</sup>Σ<sub>g</sub><sup>-</sup> transition or that they represent a magnetic dipole <sup>1</sup>Σ<sub>g</sub><sup>+</sup> → <sup>3</sup>Σ<sub>g</sub><sup>-</sup> transition. In either case there are four branches observed. The other example is provided by the infrared atmospheric oxygen bands at 1.27 μm and 1.07 μm which represent a magnetic dipole <sup>1</sup>Δ<sub>g</sub> → <sup>3</sup>Σ<sub>g</sub><sup>-</sup> transition.

The following figure, extracted from [109] shows the different branches of a <sup>1</sup>Σ<sub>g</sub><sup>+</sup> → <sup>3</sup>Σ<sub>g</sub><sup>-</sup> transition.

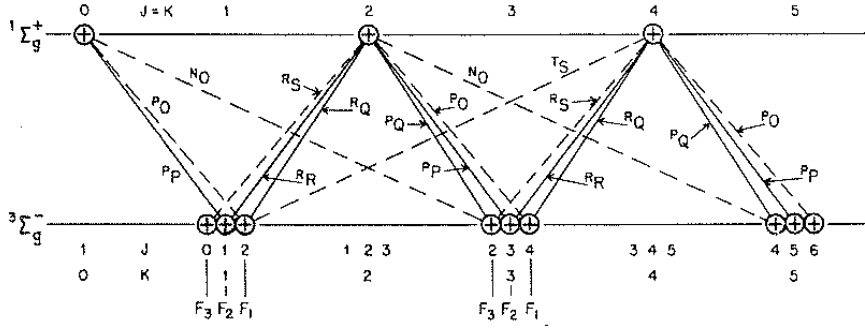


Fig.II.8. Combinations associated with branches of the  $b^1\Sigma \rightarrow X^3\Sigma$  system [109].

The three components of the  $X^3\Sigma_g^-$  oxygen ground state are designated by  $F_1$ ,  $F_2$  and  $F_3$ . The notation of all rotational lines of a transition between two levels ( $E'$ ,  $v'$ ) and ( $E''$ ,  $v''$ ) with the same values of  $\Delta N$  and  $\Delta J$  is written :

$$\Delta N \Delta J_{ij} \quad (\text{Eq.II.4})$$

Where  $i$  and  $j$  represent the subscripts of the higher and the lower states multiplicities, respectively. In our case  $i=1$  and  $j=1, 2$  and  $3$ .

Branches for which  $\Delta N = \Delta J$  are called "principal branches" and branches for which  $\Delta N \neq \Delta J$  are called "satellite branches". Notations of different branches are represented in table II.5 :

	<b>N</b>	<b>O</b>	<b>P</b>	<b>Q</b>	<b>R</b>	<b>S</b>	<b>T</b>
$\Delta J$			-1	0	1		
$\Delta N$	-3	-2	-1	0	1	2	3

Table II.5. Notation of different rotational branches.

Three different types of selection rules are considered :

- general selection rules, independent of the Hünd coupling<sup>4</sup> mode considered ;
- the selection rules common to (a) and (b) Hünd coupling mode but not valid for other case of selection ;
- the selection rules specific to Hünd (a) mode coupling, and the selections rules specific to Hünd (b) mode coupling.

For Hünd coupling cases (a) and (b), the quantum numbers  $\Lambda$  and  $S$  are both defined. One can observe for these both cases, the following selection rules :

$$\begin{aligned} \Delta \Lambda &= 0, \pm 1, \\ \Delta S &= 0. \end{aligned} \quad (\text{Eq.II.5})$$

Moreover, for a  $\Sigma \leftrightarrow \Sigma$  transition, we observe :

$$\begin{aligned} \Sigma^+ \leftrightarrow \Sigma^+, \Sigma^- \leftrightarrow \Sigma^- &: \text{allowed transitions,} \\ \Sigma^+ \leftrightarrow \Sigma^- &: \text{forbidden transitions.} \end{aligned} \quad (\text{Eq.II.6})$$

If both states of the transition belong to the Hünd case (a), then one observes the following selection rule (the quantum number  $\Sigma$  does not refer to the electronic spectral state  $\Sigma$  due to  $\Lambda=0$ ) :

$$\Delta \Sigma = 0. \quad (\text{Eq.II.7})$$

Taking into account the previous selection rules, we obtain :

<sup>4</sup> The movement of electrons, of molecule nuclei, the resultant spin and eventually the individual electron spins are not totally independent one from another. There are interactions between these movements. The different so-called Hünd coupling modes are presented in appendix 1.

$$\begin{aligned} \Delta\Omega=0, \pm 1, \\ \Delta J=0 \quad \text{forbidden for } \Omega=0 \leftrightarrow \Omega=0. \end{aligned} \quad (\text{Eq.II.8})$$

The state  $^1\Sigma$  can either be treated in the Hünd coupling case (a) or (b). The state  $^3\Sigma$  can only be treated in the case (b). In the case of both states belonging to the (b) Hünd mode, one observes the following selection rule:

$$\begin{aligned} \Delta N=0, \pm 1 \\ \Delta N=0 \quad \text{forbidden for } \Sigma \leftrightarrow \Sigma \text{ transition} \end{aligned} \quad \begin{aligned} (\text{Eq.II.9}) \\ (\text{Eq.II.10}) \end{aligned}$$

Now let us focus on the transition:  $b^1\Sigma_g^+ \rightarrow X^3\Sigma_g^-$

According to selection rules previously presented, we can determine the different branches present. First of all, according to  $\Delta J=J'-J''$ , one can have *P*, *Q* or *R* branches for  $\Delta J= -1, 0, \text{ and } +1$  respectively. Then, for satellite branches, one can have *N*, *O*, *P*, *Q*, *R*, *S*, *T* satellite terms for  $\Delta N=-3, -2, -1, 0, +1, +2, +3$  respectively (see table II.5)

However, in the case of both states in the (b) Hünd mode coupling, the selection rule (Eq.II.9) allows us to eliminate satellite terms *T*, *S*, *O* and *N*. Moreover, the selection rule (Eq.II.10) allows us to eliminate the satellite term *Q*. For a given level of rotation, the quantum number *J* takes the values :  $N + S \leq J \leq N - S$ , with  $\Delta N=N'-N''$  and  $\Delta S=S'-S''$  (for the  $b^1\Sigma_g^+$ ,  $S=0$  and for  $X^3\Sigma_g^-$ ,  $S=1$ ). According to selection rules, we obtain the following rotational bands :

$^1\Sigma \rightarrow ^3\Sigma$
$^R R$
$^P P$
$^P Q$
$^R Q$

Table II.6. Rotational branches for the transition  $b^1\Sigma_g^+ \rightarrow X^3\Sigma_g^-$ .

The corresponding transitions are indicated as follows: There is an  $^R R$  branch ( $\Delta J = +1, \Delta N = +1$ ), a  $^P P$  branch ( $\Delta J = -1, \Delta N = -1$ ), an  $^R Q$  branch ( $\Delta J = 0, \Delta N = +1$ ), and a  $^P Q$  branch ( $\Delta J = 0, \Delta N = -1$ ). In addition, branches  $\Delta J = \pm 2$  should occur.

To conclude, the oxygen atmospheric ‘A’ band, corresponding to the (0,0) band of the  $b^1\Sigma_g^+ \rightarrow X^3\Sigma_g^-$  system is a prominent feature in the absorption and emission spectrum of the terrestrial atmosphere. Nevertheless, these bands are very weak due to the strongly forbidden character of gerade-gerade and  $\Sigma^+ - \Sigma^-$  transitions, and it can only be observed via a magnetic dipole transition moment.

### II.2.3.3. $O_2 \ a^1\Delta_g \rightarrow X^3\Sigma_g^-$ transition

The relaxation of the singlet excited state to the triplet ground state by infrared electronic transitions is forbidden by several selection rules [123] :

$$\begin{aligned} g \neq g \\ \Lambda = 0, \pm 1 \quad (\text{not } \pm 2 \text{ as required by } \Delta \rightarrow \Sigma) \\ \Sigma^+ \neq \Sigma^- \end{aligned}$$

The  $O_2 \ a^1\Delta_g \rightarrow X^3\Sigma_g^-$  transition is electric-dipole forbidden, but can be induced by magnetic-dipole and electric quadrupole interactions. Investigations using electron paramagnetic resonance, emission spectroscopy and absorption spectroscopy led to a value of the Einstein coefficient of  $A(a-X)$  of  $2.3 \cdot 10^{-4} \text{ s}^{-1}$ , which corresponds to the extremely long radiative lifetime  $\tau(a-X)$  of 72 min [131]. Therefore, these two oxygen electronic transitions have weak Einstein coefficients and their emissivity should be weak.

Nevertheless, the experimental part of this study will reveal high signal/noise ratio emission spectra at high resolution.

To conclude, although all the transitions between these states are strongly prohibited, one observes :

- the transition  $O_2 (b^1\Sigma_g^+, v=0) \rightarrow O_2 (X^3\Sigma_g^-, v=0)$  said “atmospheric A-band” at 762 nm (Badger et al. 1965 [143]) ;
  - the transition  $O_2 (a^1\Delta_g, v=0) \rightarrow O_2 (X^3\Sigma_g^-, v=0)$  said “infrared band” at 1.27  $\mu\text{m}$  (Noxon, 1967 [144] and Miller et al. 1969 [145]) ;
  - the transition  $(b^1\Sigma_g^+, v=0) \rightarrow O_2 (a^1\Delta_g, v=0)$ , said “Noxon system” (Noxon, 1962 [133]).
- $(a^1\Delta_g, V'') \rightarrow (X^3\Sigma_g^-, V')$  and  $(b^1\Sigma_g^+, V'') \rightarrow (X^3\Sigma_g^-, V')$  transitions are allowed in the magnetic-dipole approximation.

## II.3. Structure and simulation of excited $O_2$ emission bands

### II.3.1. Presentation

A diatomic species has, besides its translation and electronic degrees of freedom, degrees of freedom of vibration and rotation. Energies of the different levels of vibration and rotation that a molecule can take can be rather simply expressed according to the quantum numbers of vibration  $v$  and rotation  $J$ . These expressions can be determined by solving the equation of Schrödinger for each case (vibration or rotation) [123].

The rotational structure (wavelength and associated intensity for every rotational peak) is perfectly determined for a given temperature (equilibrium temperature case). Presented in form of spectra and with a variable precision, which allows approaching at best the experimental spectral resolution, the results of these calculations are compared with recording; the best correspondence gives the temperature of rotation of the molecule. The method allowing in that case estimating the temperature of rotation consists of a theoretical simulation of the rotational structure of the studied band.

To explain the theoretical model, we shall develop the case of both transitions:  $O_2(a^1\Delta_g) \rightarrow O_2(X^3\Sigma_g^-)$  (0,0) and  $O_2(b^1\Sigma_g^+) \rightarrow O_2(X^3\Sigma_g^-)$  (0,0) emission bands of molecular oxygen. Let us point the fact that, experimentally, only the last band is observed in this work.

### II.3.2. Rotational structure

We are therefore going to study successively  $X^3\Sigma_g^-$ ,  $b^1\Sigma_g^+$  and  $a^1\Delta_g$  states.

$X^3\Sigma_g^-$  state presents a spin multiplicity equal to three and the projection  $\vec{\Lambda}$  of the electronic angular momentum of the molecule on the internuclear axis is null. This state belongs to case (b) of Hund.

#### II.3.2.1. Energy of a molecule

The energy of the electronic state, vibrational and rotational of a diatomic molecule can be written as :

$$E = E_e + E_v + E_r \quad (\text{Eq.II.11})$$

where  $E_e$  is the electronic energy of the state  $E_v$  is the energy of vibration and  $E_r$  is the energy of rotation. By introducing the spectral terms, expression (Eq.II.11) becomes :

$$E = hc[X_e + G(v) + F_v(J)] \quad (\text{Eq.II.12})$$

where  $h$  indicates the Planck constant,  $c$  the light velocity,  $X_e$  is the electronic spectral term,  $G(v)$  (or  $G_v$ ) is the vibrational spectral term and  $F_v(J)$  is the rotational spectral term.

### II.3.2.2. Vibration mode

One assumes in a first approach that the movement of vibration of the molecule is harmonic. Then by resolution of the equation of Schrödinger, one can obtain :

$$E(v) = \frac{h}{2\pi} \sqrt{\frac{k}{\mu}} \left( v + \frac{1}{2} \right) \quad (\text{Eq.II.13})$$

$k$  and  $h$  are usual constants described before and  $\mu$  is the systems reduced mass. The vibrational spectral term corresponds to :

$$G_v = \frac{E(v)}{hc} = \omega_e \cdot \left( v + \frac{1}{2} \right). \quad (\text{Eq.II.14})$$

However, in practice, movement of vibration is anharmonic, and upper orders are used to represent energies of each level of vibration. The energy of a level of vibration  $v$  is given by expression :

$$G_v = \omega_e \cdot \left( v + \frac{1}{2} \right) - \omega_e x_e \left( v + \frac{1}{2} \right)^2 + \omega_e y_e \left( v + \frac{1}{2} \right)^3 + \omega_e z_e \left( v + \frac{1}{2} \right)^4 + \dots \quad (\text{Eq.II.15})$$

where  $v$  is a quantum number having only the values  $v=0, 1, 2$ , etc. and  $\omega_e, \omega_e x_e, \omega_e y_e$  and  $\omega_e z_e$  are constants for a given electronic state ( $\omega_e \gg \omega_e x_e \gg \omega_e y_e \gg \omega_e z_e$ ).

The spacing of successive vibrational energy levels diminishes as the quantum number of vibration  $v$  increases (exception made for  $H_2$ ).

### II.3.2.3. Rotation mode

In the case of rotation, we have :

$$E(J) = \frac{h^2 J(J+1)}{8\pi^2 \cdot \mu \cdot r^2}. \quad (\text{Eq.II.16})$$

The rotational spectral term corresponds to :

$$F(J) = \frac{E(J)}{hc} = \frac{hJ(J+1)}{8\pi^2 c\mu \cdot r^2} = BJ(J+1) \quad (\text{Eq.II.17})$$

where  $R$  is the internuclear distance and  $B$  is a constant of rotation.

However, in practice, the movement of rotation is subjected to effects of centrifugal distortions, and the upper orders are used to represent energies of each level. The energy of a level of rotation  $J$  is given by expression :

$$F(J) = B(J(J+1)) - D(J(J+1))^2 + H(J(J+1))^3 \quad (\text{Eq.II.18})$$

where  $D$  and  $H$  are the centrifugal distortion constants.

Also, the spacing out of the successive levels of energy of rotation increases as the quantum number of rotation  $J$  increases.

In practice, the movements of vibration and rotation of a molecule occur simultaneously. And, when the molecule reaches higher levels of vibration  $v$ , its internuclear distance  $r$  increases comparing to its distance of equilibrium ( $r_e$ ) under the influence of effects of anharmonicity of vibration.

Also, as the constant of rotation  $B$  depends on internuclear distance ( $r$ ), it is therefore going to depend on the level of vibration  $v$  of the molecule and going to decrease for higher values of  $v$ . This is also true for constants  $D$  and  $H$ . Therefore, one can obtain the following expressions :

$$B_v = B_e - \alpha_e \left( v + \frac{1}{2} \right) + \gamma_e \left( v + \frac{1}{2} \right)^2 + \delta_e \left( v + \frac{1}{2} \right)^3 + \eta_e \left( v + \frac{1}{2} \right)^4 \quad (\text{Eq.II.19})$$

$$D_v = D_e + \beta_e \left( v + \frac{1}{2} \right) + \dots \quad (\text{Eq.II.20})^5$$

### II.3.2.4. Rovibronic structure

It is worth noting that electronic energy, vibration and rotation (i.e. rovibronic energy) of the molecule can be separated, and that the wave function of the molecule can be proportioned in three wave functions regrouping the electronic terms, that of vibration and that of rotation. The total energy of a given state of the molecule is then written :

$$E_{e,v,J} = E_{el} + E_{vib} + E_{rot}, \text{ with } E_{el} \gg E_{vib} \gg E_{rot} \quad (\text{Eq.II.21})$$

Or more in details :

$$\begin{aligned} E_{e,v,J} &= T(e) + G(v) + F_v(J) \\ &= T(e) + \omega_e \left( v + \frac{1}{2} \right) - \omega_e x_e \left( v + \frac{1}{2} \right)^2 + \omega_e y_e \left( v + \frac{1}{2} \right)^3 + \dots \\ &\quad + B_v(J(J+1)) - D_v(J(J+1))^2 + H_v(J(J+1))^3 \end{aligned} \quad (\text{Eq.II.22})$$

### II.3.2.5. Fine structure of quantum states: rotational terms

The phenomena of coupling between the movement of electrons and the movement of rotation have the effect of changing the position of the rotational energy levels in comparison with the quantum number of spin  $S$ . The expression of the rotational energy levels differs according to the degeneration of the spin: doublet states, triplet..., which correspond respectively to  $S=1/2, 1$ , etc.), but also the electronic quantum number  $\Lambda$  (states  $\Sigma, \Pi, \Delta$ , etc., respectively).

The various additional interactions resulting from these couplings are then introduced in the form of additional spectroscopic constants :

- interactions spin-orbit expressed by the spectroscopic constant  $A_v$  ;
- interactions spin-spin expressed by the spectroscopic constant  $\lambda_v$  ;
- interactions spin-rotation expressed by the spectroscopic constant  $\gamma_v$ .

For a singlet sigma state,  $^1\Sigma$  (for  $b^1\Sigma_g^+$ ), rotational term is written :

$$F(J) = B_v(J(J+1)) - D_v(J(J+1))^2 + H_v(J(J+1))^3 \quad (\text{Eq.II.23})$$

Moreover, rotational term of the state  $a^1\Delta_g$  ( $v=0$ ) is written :

$$F(J) = \nu_0 + B_0[J(J+1) - \Lambda^2] - D_0[J(J+1) - \Lambda^2]^2 \quad (\text{Eq.II.24})$$

with  $\Lambda = 2$  appropriate for this state.

Finally, for a triplet sigma state,  $^3\Sigma$  (for  $X^3\Sigma_g^-$ ), rotational term is written according to three terms :

$$\begin{aligned} ^3\Sigma_2(J \geq 2) &= B_v(J(J+1)) - D_v(J(J+1))^2 - (\lambda_v - B_v + \frac{1}{2}\gamma_v) \\ &\quad + [(\lambda_v - B_v + \frac{1}{2}\gamma_v)^2 + 4J(J+1)(B_v - \frac{1}{2}\gamma_v)^2]^{1/2} \end{aligned} \quad (\text{Eq.II.25})$$

<sup>5</sup> We realizes that a better agreement between simulated and experimental spectra is obtained when using the correct litteral expression of  $D_v$  in Eq.II.20. An error in the sign of  $\beta_e$  was done.

$${}^3\Sigma_1(J \geq 1) = B_v(J(J+1)) - D_v(J(J+1))^2 \quad (\text{Eq.II.26})$$

$${}^3\Sigma_0(J \geq 0) = B_v(J(J+1)) - D_v(J(J+1))^2 - (\lambda_v - B_v + \frac{1}{2}\gamma_v) + [(\lambda_v - B_v + \frac{1}{2}\gamma_v)^2 + 4J(J+1)(B_v - \frac{1}{2}\gamma_v)^2]^{1/2} \quad (\text{Eq.II.27})$$

where  $B_v$  is the rotational constant and  $D_v$  and  $H_v$  are the quartic centrifugal distortion and the sextic centrifugal distortion constants respectively.

The term  $H_v$ , which can be considered as a perturbation of rigid-rotor rotational energy levels, may be treated in diatomic molecules as follows :

$$H_v = \sum_{i=0,\dots} Y_{i3} \left( v + \frac{1}{2} \right)^i, \dots \quad (\text{Eq.II.28})$$

where  $Y_{i3}$  are Klein-Dunham coefficients. The use of Klein-Dunham coefficients (i.e. matrix form) prevents from the profusion of spectroscopic constants and potential notation errors.

Finally, neglecting the difference between  $H_v$  and  $H_e$ , one finds to a first approximation :

$$H_v \approx H_e = \frac{2D_e}{3\omega_e^2} (12B_e^2 - \alpha_e \omega_e) \quad (\text{Eq.II.29})$$

### II.3.2.6. Intensity of the molecular bands

$N(n', v', J')$  is the number of molecules stated in the upper level  $(n', v', J')$  and  $A_{n'',v'',J''}^{n',v',J'}$  is the probability of transition between states  $(n', v', J')$  and  $(n'', v'', J'')$ ; the emitted molecular band intensity is expressed as :

$$I_{n'',v'',J''}^{n',v',J'} = N_{n',v',J'} \times A_{n'',v'',J''}^{n',v',J'} \times h \times c \times \sigma \quad (\text{Eq.II.30})$$

where  $h \times c \times \sigma$  is liberated energy during the transition.

The transition probability is linked to the molecule dipole moment by the following relation:

$$A_{n'',v'',J''}^{n',v',J'} = \frac{64\pi^4 \cdot \sigma^4}{3h} \cdot \frac{\sum |R_{n'',v'',J''}^{n',v',J'}|^2}{g_{j'}} \quad (\text{Eq.II.31})$$

where  $g_{j'}$  is the degeneracy of the upper state and,

$$\sum |R_{n'',v'',J''}^{n',v',J'}|^2 = |R_e^{n',n''}|^2 \times |R_{vib}^{v',v''}|^2 \times S_{J',J''} \quad (\text{Eq.II.32})$$

where  $|R_{vib}^{v',v''}|$  is the overlap integral  $\int R_{v'} \times R_{v''} \times r^2 \times dr$  (Franck-Condon principle),

$|R_e^{n',n''}|^2$  is proportional to the electronic transition probability,

$S_{J',J''}$  is the Hönl-London factor (or band strength); this number without dimension determines the relating intensity of the different branches of a band.

The number of molecules in the electronic state  $n'$ , vibrational  $v'$ , and rotational  $J'$  is given by the high canonical group theory applied to Boltzmann statistics :

$$N_{n',v',J'} = \frac{N}{Q} \times (2 - \delta_{0,\Lambda'}) \times (2S'+1) \times (2J'+1) \times \exp\left(-\frac{h \cdot c \cdot (T_e' + G_{v'} + F_{v'}(J'))}{k_B \cdot T}\right) \quad (\text{Eq.II.33})$$

Where  $N$  represents the total number of considered molecules,  $k_B$  the Boltzmann constant,  $T$  the temperature and  $\delta_{0,n'}$  the Krönecker symbol :

$$\begin{aligned}\delta_{0,n'} &= 1 \text{ if } n'=0 \\ \delta_{0,n'} &= 0 \text{ if } n'=1\end{aligned}$$

$Q$  is the internal partition function of the molecule. A single temperature  $T$  is set, as one assume local thermodynamic equilibrium ( $T = T_r = T_v$ ) ; the outcome allows a single temperature to be attributed to the whole system.

For homonuclear molecules and in the hypothesis of the separation of movements, the partition function is written as :

$$\begin{aligned}Q &= Q_{el} \times Q_{vib} \times Q_{rot} \\ &= \sum_{n', \Lambda', \delta'} \frac{(2 - \delta_{0,\Lambda'}) \times (2\delta + 1) \times \exp\left(-\frac{h \cdot c \cdot T_{e'}}{k_B \cdot T}\right)}{2 \times \left(1 - \exp\left(-\frac{h \cdot c \cdot \omega_e}{k_B \cdot T}\right)\right)} \times \frac{k_B \cdot T}{h \cdot c \cdot B_e}\end{aligned}\quad (\text{Eq.II.34})$$

where  $Q_{el}$ ,  $Q_{vib}$ ,  $Q_{rot}$  indicate respectively electronic, vibration partition and rotation partition functions.  $\omega_e$  and  $B_e$  are mean vibrational and rotational constants, equal for any electronic terms.

By replacing expressions (Eq.II.34) and (Eq.II.31) in (Eq.II.30), the expression of the intensity of a molecular band becomes :

$$I_{n',v',J'}^{n'',v'',J''} = C \cdot N \cdot \sigma \cdot |R_e^{n',n''}|^2 \cdot |R_{vib}^{v',v''}|^2 \cdot S_{j',j''} \cdot \exp\left(-\frac{h \cdot c \cdot (G_{v'} + F_{v'}(J'))}{k_B \cdot T}\right)\quad (\text{Eq.II.35})$$

where  $C = \frac{64\pi^4 \cdot c}{3} \cdot \frac{1}{Q} \cdot (2 - \delta_{0,\Lambda'}) \cdot \exp\left(-\frac{h \cdot c \cdot T_{e'}}{k_B \cdot T}\right)$  is a constant at given temperature and for a given electronic state.

One will find below the expressions of band strengths and the Hönl-London factors for different transitions.

Both transitions studied here are forbidden transitions, so general expressions of Hönl-London factors are not possible as they depend on the nature of the perturbation making the transition allowed. As an added complication, the transitions are magnetic dipole, rather than quadripole. For the  ${}^1\Delta - {}^3\Sigma$  transition in molecular oxygen, it should be possible to derive approximate expressions as it seems that a single transition moment is adequate to model the transition. The net result will most likely end up similar to the formulas for a  ${}^3\Sigma$  to the  $\Omega=2$  component of a Hund's case (a)  ${}^3\Pi$  state.

It is worth noting that they will depend on the constants used in the lowest state (particularly the relative values of constants  $B$  and  $A$ , see later).

### II.3.3. $\text{O}_2$ ( $\text{a}^1\Delta_g$ ) (0,0) and $\text{O}_2$ ( $\text{b}^1\Sigma_g^+$ ) (0,0) emission spectra simulation

#### II.3.3.1. $\text{O}_2(\text{b}^1\Sigma_g^+, v=0) \rightarrow \text{O}_2(\text{X}^3\Sigma_g^-)$ and $\text{O}_2(\text{a}^1\Delta_g, v=0) \rightarrow \text{O}_2(\text{X}^3\Sigma_g^-)$ lines

We have developed a simulation program under Matlab<sup>®</sup> software. In this program, the three components of the  $\text{X}^3\Sigma_g^-$  ground state of oxygen are designated by F1X, F2X and F3X. The <sup>P</sup>P and <sup>R</sup>R branches of the red atmospheric bands correspond to transitions from the F2X component, the <sup>R</sup>Q and <sup>P</sup>Q branches to transitions from the F1X and F3X components, respectively [109].

Formulas for the intensities of rotational lines in transition  $b^1\Sigma_g^+ \rightarrow X^3\Sigma_g^-$  transition of diatomic molecular oxygen assuming the Hünd's case (b) behaviour of both the singlet and the triplet state are given by Watson [146]. In addition, in order to calculate the rotational line intensities, theoretical Höln-London factors [147] are integrated in the program.

The same procedure has been used for the  $O_2 \ ^1\Delta_g \rightarrow ^3\Sigma_g^-$  transition. Rotational terms of the state  $a^1\Delta_g$  ( $v=0$ ) are integrated.

Molecular constants for  $X^3\Sigma_g^-$ ,  $b^1\Sigma_g^+$  state of  $O_2$  of Babcock and Herzberg [109, 148] were employed. For  $a^1\Delta_g$  state, those of Western [149] were used. It is worth noting that molecular constants obtained by other researchers were used for comparisons. Table II.7 presents the molecular constants used.

Spectroscopic constants	$O_2 (X^3\Sigma_g^-)$	$O_2 (a^1\Delta_g)$	$O_2 (b^1\Sigma_g^+)$
Band origin ( $cm^{-1}$ )	0	7883.75224580137	13123.36
<b>B</b>	1.437676476	1.4178400247845	1.3912442
$\lambda_{SS}$	1.984751322		
$\gamma$	-0.00842539		
<b>D</b>	4.84256E-6	5.10664455622163E-6	5.3524E-6
<b>H</b>	2.8E-12		
$\lambda_D$	1.94521E-6		
$\gamma_D$	8.106E-9		
$\gamma_H$	-4.7E-14		

Table II.7. Rotational constants for  $O_2 (X^3\Sigma_g^-)$ ,  $O_2 (a^1\Delta_g)$  and  $O_2 (b^1\Sigma_g^+)$ .

$B$  is the rotational constant;  $D$ , the quartic centrifugal distortion;  $H$ , the sextic centrifugal distortion;  $\gamma_D$  and  $\gamma_H$  are the centrifugal distortions of gamma;  $\lambda_D$ , the centrifugal distortion of lambda. For  $S \geq 1$ ,  $\lambda_{SS}$  (the spin-spin coupling constant) may also be important.

The accuracies of the molecular parameters are a limiting factor. However, as discussed among published data for the (b-X) and (a-X) oxygen systems it is worth noting that there is a general agreement on the rotational constants [139, 141]. Although line positions of the A-band have been determined using improved techniques, the most extensive measurements of the band remains that of Babcock and Herzberg [109]. In that study, the accuracy of spectroscopic constants reported surpassed that for any other molecule at the time [142], even if many more recent studies on A-band show some disagreement concerning the absolute positions of the lines [139, 141, 150, 151]. These lines were recorded using high-resolution Fourier transform spectrometers [139, 141], or at high resolution using Intracavity Laser Spectroscopy (ILS) [109].

The program structure implemented in Matlab<sup>®</sup> is schematized in Fig.II.9.

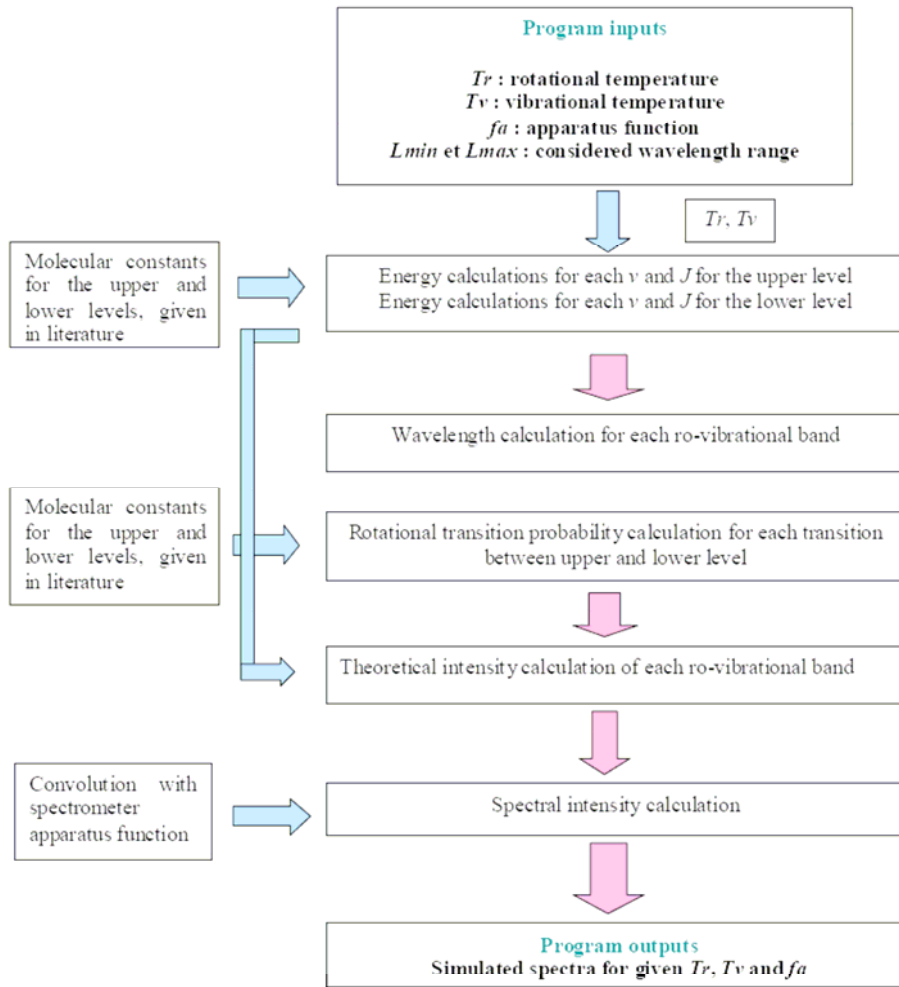


Fig.II.9. Simulation program structure.

### II.3.3.2. Emission spectra simulation

The emission spectrum is a spectral fingerprint of the studied gas and reveals information of the gas dynamical process itself like reaction intensity, stability, species concentration and temperature. The spectral analysis of the spontaneous emission, i.e. the detection of the signal as a function of wavelength, is called emission spectrum. The following figures present the considered atmospheric « A » band and infrared band emission spectra at different resolutions. The rotational temperature used for calculations is 365 K, a typical temperature for nonthermal plasma.

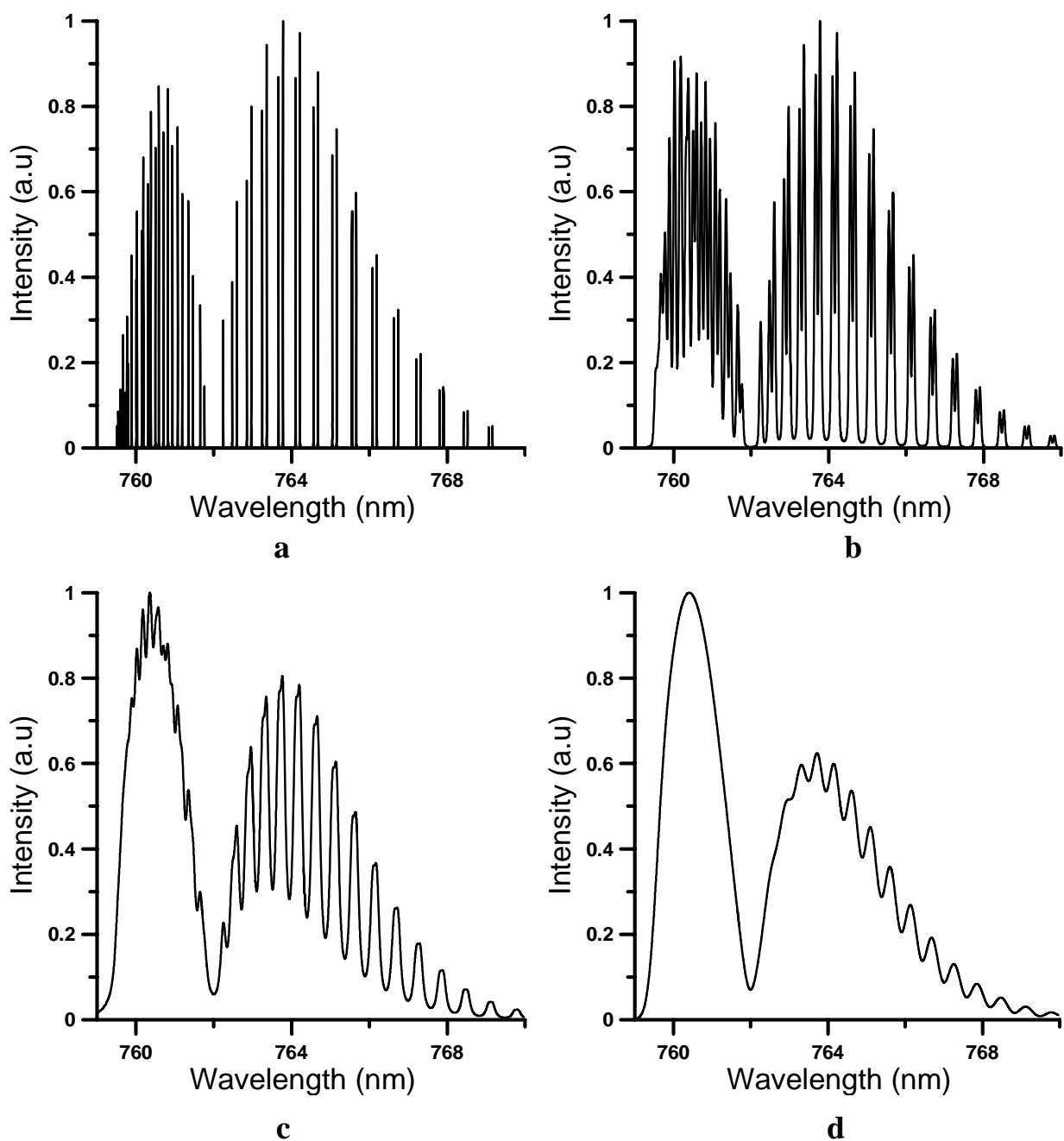


Fig.II.10. Simulated partially resolved emission spectra of gaseous  $^{16}\text{O}_2$  in the band  $b^1\Sigma_g^+(v=0) \rightarrow X^3\Sigma_g^-(v=0)$ , temperature 365K. Different resolutions are used : a) 0.05 Å, b) 0.5 Å, c) 2 Å and d) 5 Å.

The characteristic structure of the red atmospheric oxygen « A » band is an R-form branch forming a head and a P-form branch, separated from the former by a zero gap. Experimental singlet sigma emission will be identified using different spectrometers at different resolutions. The different cases will be clearly identified.

From these sets of spectra, it is now possible to predict accurately the transitions between these states. Our first test will be to compare between calculated and observed transitions and in a second time to measure the associated rotational temperature.

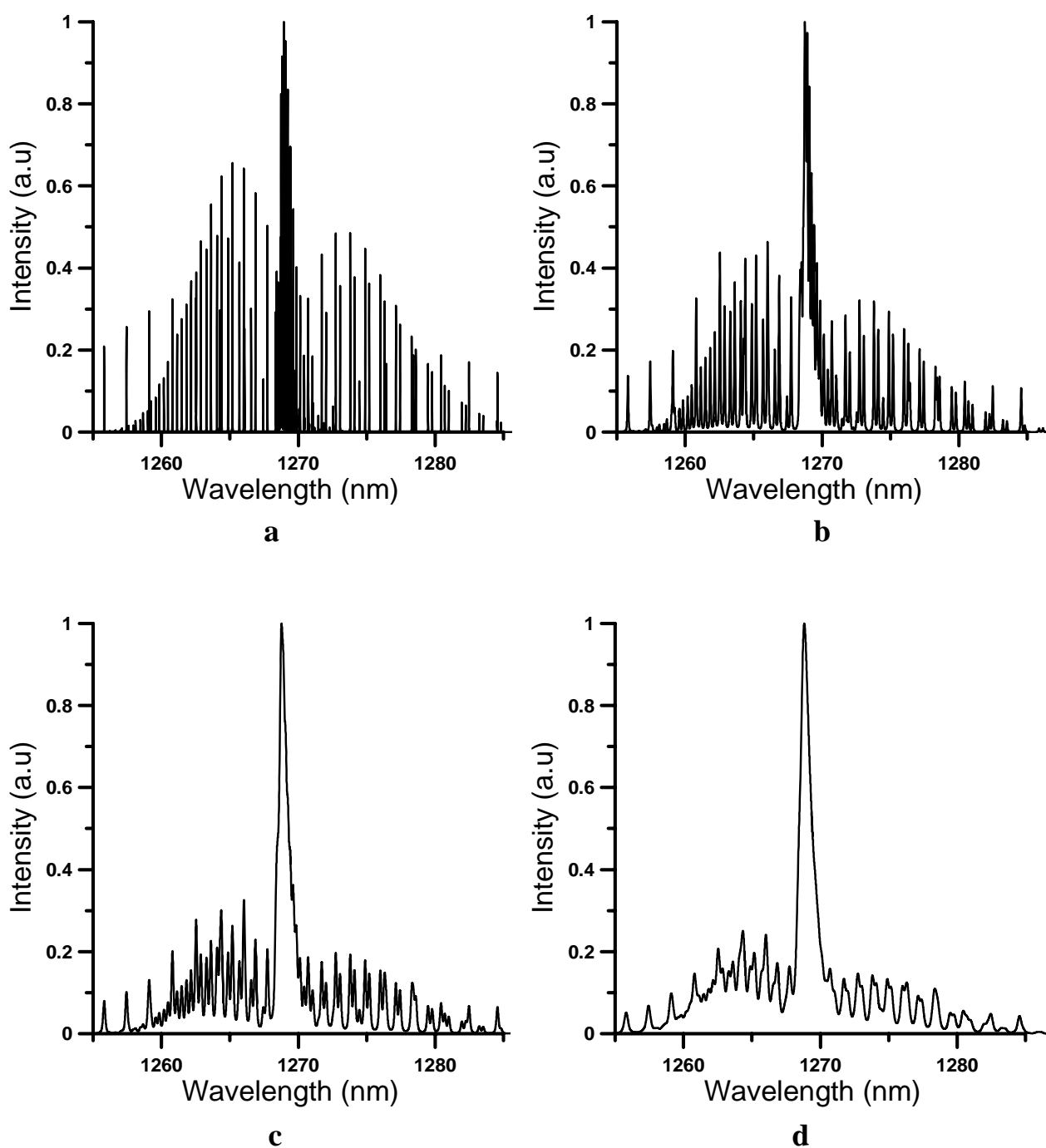


Fig.II.11. Simulated partially resolved emission spectra of gaseous  $^{16}\text{O}_2$  in the band  $a^1\Delta_g(v=0) \rightarrow X^3\Sigma_g^-(v=0)$ , temperature 365K. Different resolutions are used :  
 a) 0.05 Å, b) 0.5 Å, c) 2 Å and d) 5 Å.

The characteristic structure of the infrared band lets clearly appear the P, Q, and R branches at 1264 nm, 1269 nm, and 1274 nm. In analogy to the atmospheric “A” band emission, spectra at different resolution are presented. However, within this study, due to the fact that an infrared spectrometer was not available, experimental singlet delta emission will not be identified.

### II.3.3.3. Validation with other simulation codes

The program PGOPHER<sup>®</sup> [149] and the HITRAN<sup>®</sup> database were used and compared to our simulation program for both transitions  $O_2(a^1\Delta_g) \rightarrow O_2(X^3\Sigma_g^-)$  (0,0) and  $O_2(b^1\Sigma_g^+) \rightarrow O_2(X^3\Sigma_g^-)$  (0,0) of molecular oxygen. Briefly, PGOPHER<sup>®</sup> is general purpose program for simulating and fitting rotational spectra [149]. To perform a simulation, we have created an input file containing the rotational constants and other settings required. In addition, HITRAN<sup>®</sup> is a database and not a modelling code.

The development of our own code has been done in view to be more flexible not only for excited oxygen emission spectra simulation, but also for other molecules. Furthermore, vibrational spectra simulation, not possible using PGOPHER<sup>®</sup>, is then accessible with our own code.

A comparison, at different resolutions between spectra simulations performed using the program PGOPHER<sup>®</sup>, HITRAN<sup>®</sup> and our simulation program shows that the position of lines corresponds with a very good accuracy. For each line, we confirm the fact that a very satisfactory fit is observed using one program or the other (results are presented in appendix 2). The very slight systematic deviation between the two calculated values is probably due to the fact that the values of certain molecular constants, which have to be used in the determination of the lines positions, are not exactly the same. Also, the shape differences between spectra at the basis come from the convolution fitting (Lorentzian line shape to account for pressure broadening in the PGOPHER<sup>®</sup> program). This has no influence on the rotational temperature determination.

For temperature measurement by emission spectroscopy, whatever the retained method of determination, the resolution of the rotational structure on the experimental recording is necessary ; in particular if this method requires an excellent identification of all rotational peaks (Boltzmann diagram method for temperature determination). However, the spectra acquired in practice usually do not satisfy this requirement (fast acquisition time (OMA) being often incompatible with a good spectral resolution).

### II.3.3.4. Rotational temperature effect on $O_2 : b^1\Sigma_g^+ \rightarrow X^3\Sigma_g^-$ (0,0) spectra

Effects of rotational temperature on the emission spectra of this band are presented in Figs.II.12. Spectra at 365 K, 700 K and 1000 K are shown. The resolution taken of 0.5 Å corresponds to that of the high resolution spectrometer that will be used in the experimental work.

Furthermore, due to the fact that infrared band  $O_2 : a^1\Delta_g \rightarrow X^3\Sigma_g^-$  (0,0) will not be experimentally detected, analogous results showing the rotational temperature effects on emission spectra fingerprint of this band are not presented here.

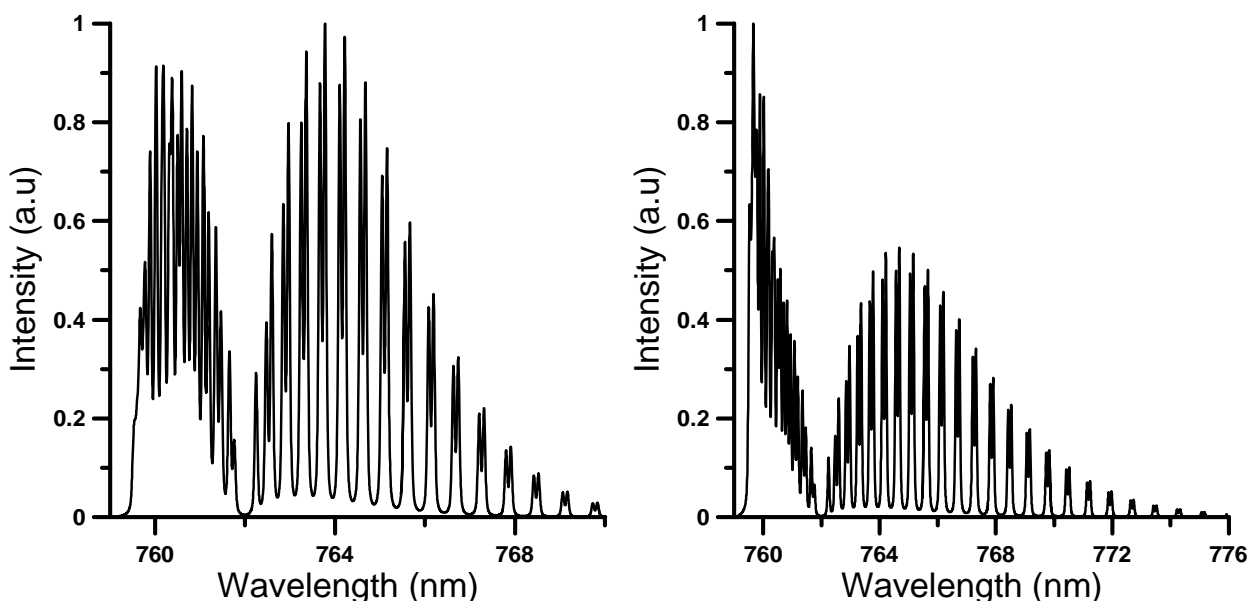


Fig.II.12. Simulated partially resolved emission spectra of gaseous  $^{16}\text{O}_2$  in the band  $b^1\Sigma_g^+(v=0) \rightarrow X^3\Sigma_g^-(v=0)$  at (left):  $T_{rot}=365\text{K}$  and (right):  $T_{rot}=700\text{K}$ .

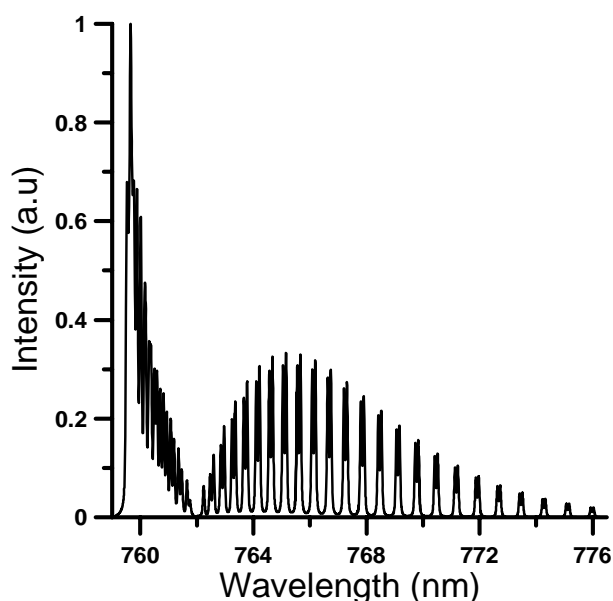


Fig.II.13. Simulated partially resolved emission spectra of gaseous  $^{16}\text{O}_2$  in the band  $b^1\Sigma_g^+(v=0) \rightarrow X^3\Sigma_g^-(v=0)$  at  $T_{rot}=1000\text{K}$ .

Characteristic structure of the red atmospheric oxygen « A » band: the R-form branches, the P-form branches and the separation zero gap is conserved with temperature variation. The quantities measured are a wavelength characterizing each line within the rotational fine structure of each band. Optical emission spectra are strongly influenced by the effect of temperature. An increase in the rotational temperature produces an increase of bands at higher rotational quantum numbers  $J$  compared to the bands of lower  $J$  numbers. Furthermore, the rotational structure is extended with the increase of temperature.

Finally, a band head phenomenon is a characteristic of the spectrum.

Results of our experiments consist of qualitative measurements of spectra of gaseous  $\text{O}_2$  in emission in the band  $b^1\Sigma_g^+(v=0) \rightarrow X^3\Sigma_g^-(v=0)$ . Because this system emission line strengths are so

weak [151], there are conspicuous experimental difficulties involved in undertaking these measurements. But comparison with further experimental results provides satisfactory confirmation of the accuracy of our approach, allowing a reliable species identification.

Finally, in this study, we have also simulated theoretical spectra of several atomic species of interest. Considerable material is available for the atomic emission lines [152]. The NIST atomic spectra database: <http://physics.nist.gov/PhysRefData/> was used as input file. The simulated theoretical spectra of helium (HeI), argon (ArI) and atomic oxygen (OI) were obtained thanks to the Matlab<sup>®</sup> program specifically developed for this use, but are not discussed further here.

### II.3.4. Temperature measurements

Apart from the role of identification of simulated spectra, this program will also be used to measure the rotational temperature. A method for temperature measurement is the fit of the computer simulation to the measured bands of O<sub>2</sub>.

However, rotational and vibrational bands of molecular nitrogen or its ion are much more commonly used in practice. In our case, nitrogen is not part of the gas mixture, but it is sufficient to add (just for diagnostic purposes) a small amount of nitrogen to the flow. Also, working at low pressure, a small leakage can provide small amount of N<sub>2</sub> from air. Since the energy distance between rotational levels in one vibrational state is usually very small, typically, much less than a tenth of electronvolt, the rotational population can be characterized by a rotational temperature  $T_{rot}$  (Boltzmann population).  $T_{rot}$  is obtained either from a Boltzmann plot or from a comparison of measured rovibrational bands with simulations of spectra based on molecular constants. This one is the method employed within this work.

Practically, the gas temperature in the plasma is determined from emission spectra of the N<sub>2</sub><sup>+</sup> first negative system: B<sup>2</sup>Σ<sub>u</sub><sup>+</sup> - X<sup>2</sup>Σ<sub>g</sub><sup>+</sup> (0-0) at 391.4 nm. The relative intensity of the emission bands characterizes a population on the rotational levels of the molecule at a given temperature [153].

Futhermore, visible emission spectra of the plasma (rotationally and vibrationally resolved bands of the N<sub>2</sub>(C<sup>3</sup>Π<sub>u</sub>→B<sup>3</sup>Π<sub>g</sub>) band system) have been used to infer the vibrational temperature in the plasma. For this, synthetic spectrum has been used, with accurate nitrogen molecular constants [154], rotational line intensities [147], and the experimentally measured slit function of the spectrometer. N<sub>2</sub> second positive system C<sup>3</sup>Π<sub>u</sub> - B<sup>3</sup>Π<sub>g</sub> is used for vibrational temperature measurement. The developed simulation program includes several subprograms edited in Matlab<sup>®</sup>. The simulation program, named "TRACESOPRA2" allows to call the emission spectra experimental file, to embed the wavelength of the main band head (first operation), then to cut out noise (second operation), and to normalize to 1 the maximum intensity (third operation). Once the experimental file is ready, the main program allows launching spectra simulation.

Figure II.14 shows a schematic of observed emission bands for N<sub>2</sub> second positive system: C<sup>3</sup>Π<sub>u</sub> - B<sup>3</sup>Π<sub>g</sub>, Δv = +1.

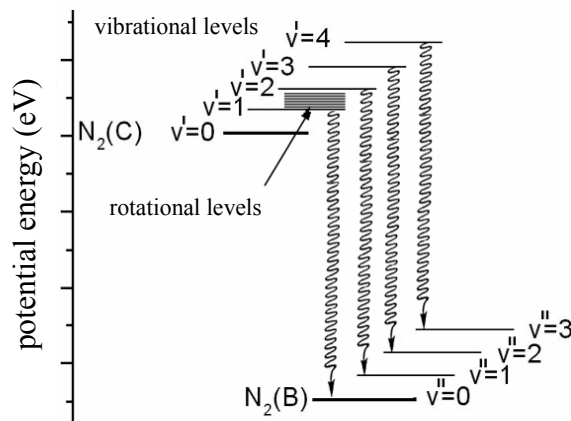


Fig.II.14. Simplified scheme of vibrational energy levels of N<sub>2</sub>(C) and N<sub>2</sub>(B) electronic states.

The wavy arrows indicate the observed transitions between the different vibrational levels. In order to simplify the scheme, rotational levels are represented only for the  $N_2(C, v'=1)$  level. The determination of vibrational temperature from the vibrational bands of molecular nitrogen  $v' - v''$  with  $\Delta v = -1, 0$  and  $+1$  corresponding to the electronic transition  $C^3\Pi_u - B^3\Pi_g$ , (called the second positive system of nitrogen) will be shown in the experimental part.

## II.4. Species identification

### II.4.1. Singlet oxygen detection techniques

The so-called oxygen atmospheric ‘‘A’’ band, corresponding to the (0,0) band of the  $b^1\Sigma_g^+ \rightarrow X^3\Sigma_g^-$  system is a prominent feature in the absorption and emission spectrum of the terrestrial atmosphere. Nevertheless, these bands are very weak due to the strongly forbidden character of gerade-gerade (g-g) and  $\Sigma^+ - \Sigma^-$  transitions, but are allowed in the magnetic dipole approximation (selection rules, as discussed previously). In the late 1970s and early 1980s, the direct spectroscopic detection of  $O_2(a^1\Delta_g)$  became possible due to the development of NIR-sensitive photomultipliers and Ge diodes, first in Russia and then in the United States.

The first time-resolved detection of  $O_2(a^1\Delta_g)$  singlet oxygen in solution was achieved by Krasnovsky in 1976, using the  $a \rightarrow X$  phosphorescence at 1.27  $\mu\text{m}$ . Badger et al. [143] observed the absorption at 1.27  $\mu\text{m}$ , due to the doubly forbidden  $^1\Delta_g \rightarrow ^3\Sigma_g^-$  transition of oxygen. Although this transition is extremely weak, it was possible to measure the absolute intensity and the transition probability. The absorption spectrum of pure oxygen at 4 atm and 32 m path allowed them to observe a discrete line band characteristic of the  $^1\Delta_g \rightarrow ^3\Sigma_g^-$  system at 1.27  $\mu\text{m}$  and at 1.065  $\mu\text{m}$  for (0,0) and (1,0) regions respectively. The Einstein coefficient of the (0,0) band was calculated equal to  $2.58 \cdot 10^{-4} \text{ s}^{-1}$ .

Due to the outstanding importance of singlet oxygen in numerous photobiological processes, it is expected that a great deal of future research will be devoted to  $O_2(a^1\Delta_g)$  detection in biological environments. However, the currently used technology has important limitations which need to be overcome in order to make quantitative studies in these complicated and strongly deactivating media. During the past 30 years, the 1.27  $\mu\text{m}$  singlet oxygen luminescence has been detected mainly with cryogenic germanium diodes, the sensitivity of which is often insufficient to provide quantitative information.

Different techniques have recently been employed to improve the sensitivity with semiconductor detectors. For example, Kakinuma and co-workers [155] used a dual charge integrating amplifier coupled to two InGaAs/InP pin photodiodes for the investigation of enzyme-catalyzed production of  $O_2(a^1\Delta_g)$  in aqueous solution under physiological conditions.

Another important advance has been made with the introduction of near infrared photomultipliers (NIR-PM), whose sensitivity in the 1.27  $\mu\text{m}$  region was reported to be about an order of magnitude larger than that of Ge diodes. Measurements of  $O_2(a^1\Delta_g)$  near-infrared (NIR) luminescence at 1.27  $\mu\text{m}$  in biological environments is done by a NIR-sensitive photomultiplier tube [156]. The measurements of  $O_2(a^1\Delta_g)$  have been performed by King et al. [53] using a thermoelectrically-cooled germanium photodiode, filtered by a coherent IR narrow bandpass filter.

Optical methods enjoy the widest use as non-intrusive diagnostics of plasmas, and are in principle able to provide all the informations required. Three main types of techniques can be used: absorption measurements [49] and in particular tunable diode laser techniques and Cavity Ring Down Spectroscopy (CRDS), with their high spectral resolution. Emission studies are far more common [22, 25, 29, 45, 112, 157-159]. It is worth to highlight that the emission is characteristic of the excited species, usually in an electronically excited state, but it is the ground state, which is present in far higher concentration, dominates the chemistry. The third technique, which produces emission, but measures the ground state concentration, is laser induced fluorescence (LIF) in plasmas. Of course, the species to be observed by this technique must fluoresce, and many, particularly polyatomic radicals and molecules, do not [160]. The standard observation technique of  $O_2(a^1\Delta_g)$  are the chemiluminescence and the spontaneous emission of the forbidden transition at 1.27  $\mu\text{m}$ .

Raman spectroscopy has been used to measure oxygen for a long time, but has more recently been used to measure singlet oxygen as well. Recently work has been done with both spontaneous and coherent Raman spectroscopy for mapping  $O_2(^1\Delta_g)$  concentrations in oxygen iodine lasers.

A flash lamp-pumped tunable pulsed dye laser operating near the head of the  $O_2$  atmospheric B band at 688 nm is used by Lawton et al. [161] to excite the  $v=1$  vibrational level of the  $b^1\Sigma_g^+$  state. The time dependence of the density of  $b^1\Sigma_g^+$  molecules is determined by monitoring photoluminescence near 762 nm.

Vacuum ultraviolet absorption spectroscopy is used by Touzeau et al. [162] to determine the kinetic temperature ( $T_g$ ). Furthermore,  $O_2(^1\Delta_g)$  concentration is measured by absorption of the resonance oxygen line at 130 nm emitted by a microwave lamp source, working in flowing oxygen. Another study of Vialle et al. [11] uses VUV absorption spectroscopy in the positive column of a DC oxygen glow discharge. The investigated range of pressures is 0.2-2 Torr. Also, the concentrations of ground state oxygen molecules  $O_2(X^3\Sigma_g^-)$ , metastable singlet molecules  $O_2(a^1\Delta_g)$  and  $O_2(b^1\Sigma)$  ozone molecules and  $T_g$  were measured. It is worth noting that the absorption cross section of  $O_2(a^1\Delta_g)$   $\sigma_a=5.5 \cdot 10^{-19} \text{ cm}^2$  has to be taken into account.

A tunable dye laser was used by Martin et al. [32] for direct excitation of  $O_2(b^1\Sigma_g^+)$  at 762.8 nm. The oxygen was kept flowing through the cell at  $100 \text{ cm}^3/\text{s}$  and the working pressure is 1 atm. Pulses of 762.8 nm radiation, 20  $\mu\text{J}$  energy, 10 ns long, 2 per second, were supplied by the dye laser.

Intercavity laser Spectroscopy (ICLS) is used by Cheskis and Kovalenko [163]. This technique is based on a dye laser pumped by an argon-ion laser. It is important to underline that in the ICLS spectra, four lines represent transitions  $^1Q_9(629.846 \text{ nm})$ ;  $^1P_9(629.923 \text{ nm})$ ;  $^1Q_{11}(630.2 \text{ nm})$  and  $^1P_{11}(630.277 \text{ nm})$  of the 2-0 band of the  $b^1\Sigma_g^+ \rightarrow X^3\Sigma_g^-$  system of molecular oxygen.

Besides, under some conditions, CRDS has been used for quantitative diagnostics of atomic and molecular oxygen species [134]. CRDS was first demonstrated by O'Keefe and Deacon in 1988. In CRDS, a laser pulse is stored in a high-finesse optical cavity containing the sample, and the pulse decay is monitored with the aid of a detector that measures the intensity of light transmission through one of the mirrors.

Furthermore, Integrated Cavity Output Spectroscopy (ICOS) based on laser absorption spectroscopy coupled with the sensitivity cavity enhanced absorption spectroscopy can be used to achieve the precision and accuracy necessary to provide relevant measurements of extremely scarce trace gas species (e.g. electronically excited oxygen present in the atmosphere). The sensitivity of ICOS comes from coupling coherent light into a high-finesse optical cavity composed of two high-reflectivity mirrors. The ICOS technique differs from its precursors in that instead of monitoring the decay of light from a pulsed source, the steady state power emitted from the cavity is measured as the frequency of the laser is scanned. ICOS has been used to quantitatively detect the ( $a^1\Delta_g$ ) state of molecular oxygen generated in a variety of discharges [164-168]. It has been demonstrated that several lines belonging to the Q and P branch of the band could be detected and scanned, which enabled accurate evaluation of the rotational temperature.

Moreover, Coherent anti-Stokes Raman spectroscopy (CARS) is a well known technique for measuring rotational and vibrational populations. Typical spectra of the vibrational bands of  $O_2(a^1\Delta_g)$  and  $O_2(X^3\Sigma_g^-)$  states are presented in [162].

Another approach to singlet oxygen detection is based on electron paramagnetic resonance (EPR). EPR is known as one of the most sensitive and informative methods in the studies of various magnetic species. EPR spectroscopy is a type of absorption spectroscopy in which molecules containing unpaired electrons (typically transition-metal ions and organic radicals) absorb microwave radiation. It is based on the Zeeman splitting of the electron states with uncompensated magnetic moments. EPR is a non-optical technique in which energy transfer between the intrinsic magnetism of unpaired electrons and an external magnetic field is measured with a sensitive microwave detection system. Excited oxygen ( $a^1\Delta_g$  and  $b^1\Sigma_g^+$ ) is a non magnetic molecule and cannot be detected directly by EPR. However, the reaction of singlet oxygen with a stable molecule can generate a moderately long-lived free radical. For instance, Falick et al. [10] detected and analysed the paramagnetic resonance spectrum of  $a^1\Delta_g$  molecules in discharged oxygen and established a method for determining their absolute concentration. The studied pressure is 0.3-0.5 Torr. Furthermore, Cupitt et al. [33] use also an EPR spectrometer technique to detect  $O_2(a^1\Delta_g)$ , atomic oxygen, OH and H generated by

microwave discharge of pure oxygen and O<sub>2</sub>/Ar binary mixtures. It is worth noting that the minimum concentration of O<sub>2</sub>(a<sup>1</sup>Δ<sub>g</sub>) that could be observed was ~3.10<sup>13</sup> cm<sup>-3</sup>.

Slanger and Black [169] use a reaction cell, where O<sub>2</sub> is photodissociated by a 147 nm Xe resonance lamp, to produce O(<sup>1</sup>D) and by reaction with O<sub>2</sub> is converted into O<sub>2</sub>(b<sup>1</sup>Σ<sub>g</sub><sup>+</sup>) and O(<sup>3</sup>P). A 761.8 nm narrow band interference filter is used to monitor O<sub>2</sub>(b<sup>1</sup>Σ<sub>g</sub><sup>+</sup>) emission.

Let's highlight also the study of the O<sub>2</sub>(<sup>1</sup>Δ<sub>g</sub>→X<sup>3</sup>Σ<sub>g</sub><sup>-</sup>) (0,1) band at a wavelength of 1.58 μm by the mean of a scanning Fabry-Perot system, in the evening twilight airglow. Also, the formation of the O<sub>2</sub>(a<sup>1</sup>Δ<sub>g</sub>) state by three body recombination of atomic oxygen explained the observed emission at a wavelength of 1.27 μm [170].

Tachibana and Phelps [171] determine the excitation coefficients for the (a<sup>1</sup>Δ<sub>g</sub>) metastable state of O<sub>2</sub> by low energy electrons in O<sub>2</sub>/Ar mixtures using a drift tube technique. These excitation coefficients are given as a function of *E/n*. Moreover, rate coefficients for excitation of the (b<sup>1</sup>Σ<sub>g</sub><sup>+</sup>) state of O<sub>2</sub> have been measured using the same drift tube technique by Lawton and Phelps [172]. The absolute intensity of the 762 nm radiation emitted by the O<sub>2</sub>(b<sup>1</sup>Σ<sub>g</sub><sup>+</sup>) molecules excited by electrons drifting are measured under the influence of a uniform electric field. Indeed, the 762 nm band was isolated from the background radiation at the photomultiplier by an interference filter with 64% peak transmission at 762 nm and a 10 nm FWHM.

Mass spectrometry allows the detection of all neutral and ionic species. However, it is an intrusive technique that can't allow spatial resolution. It is relevant to note that mass spectrometric detection of O<sub>2</sub>(a<sup>1</sup>Δ<sub>g</sub>) molecules can also be performed [33]. The authors of [173] studied gaseous mixtures used for the development of thin layers or surface treatment (N<sub>2</sub>/CH<sub>4</sub>; Ar/H<sub>2</sub>; Ar/N<sub>2</sub>/SiH<sub>4</sub>).

In the literature, emission spectroscopic techniques are applied to determine the space-time structure of discharges and to analyze the kinetics of plasmas in nanosecond discharges [25, 157, 174]. The visible and close UV emission spectroscopy is used in the study of Castel et al. [174] to characterize the low pressure glow discharge plasma. The studies of Luo et al. [157], Gouda and Massines [22], Chintala et al. [113] and Starikovskaia et al. [92] use emission spectroscopy to follow the excited species in low temperature and atmospheric pressure plasma.

Although these technologies look extremely promising, both time-resolved and spatially resolved methods suffer from weak signals, and a quantitative detection of very small amounts of O<sub>2</sub>(a<sup>1</sup>Δ<sub>g</sub>) is currently difficult to obtain in any medium ; exception made for Integrated Cavity Output Spectroscopy (ICOS) and Cavity-Ring Down Spectroscopy (CRDS) (i.e. long path absorption spectroscopy based techniques) where it has been used to quantitatively detect very small concentrations of the (a<sup>1</sup>Δ<sub>g</sub>) state of molecular oxygen generated in a variety of discharges [165-167]. Two different approaches have been proposed to make such observations. Both rely on the introduction of fluorescent probes, which are either (i) non fluorescent molecules that become fluorescent after reaction with singlet oxygen or (ii) molecules that fluoresce strongly upon energy transfer from singlet oxygen.

## II.4.2. Spontaneous emission spectroscopy

Optical emission spectroscopy (OES) is one of the most established and oldest diagnostic tools in astrophysics and plasma physics (see for example [6, 175]). Radiating atoms, molecules and their ions provide an insight into plasma processes and plasma parameters and offer the possibility of real-time observation. Emission spectra in the visible spectral range are easy to obtain with a quite simple and robust experimental set-up. The method itself is non-invasive, which means that the plasma is not affected. For our study, spontaneous emission is used as diagnostics for both, plasma and flame characterisation. In flames, the species observed are intermediate reaction products like OH\*, CH\*, C<sub>2</sub>\*, etc. (the asterisks indicate electronically excited states). OES is our first step to investigate unknown species in emitting plasma. In a second step, based on OES results, more sophisticated laser technique (e.g. LIF) may be applied to gain more insight of the process under investigation.

The optical diagnostics setups will be described later within this report. Globally, emitted light from the plasma or flame is collected with an appropriate convergent lens system or fiber optics and focussed at the entrance slit of a spectrometer or on the photosensitive screen of a camera. The light is then dispersed by a grating, and detected by a detector.

To conclude, spontaneous emission spectroscopy will allow us :

- to verify the presence of singlet oxygen ;
- to follow the evolution of its concentration when changing the experimental parameters ;
- and to measure the rotational and vibrational temperatures of the plasma.

For illustration, the following figs.II.15 presents the partially resolved emission spectra of  $O_2(b^1\Sigma \rightarrow X^3\Sigma)$  emission for a (10% $O_2$ /90%He) mixture at P=120 Torr [41, 48].

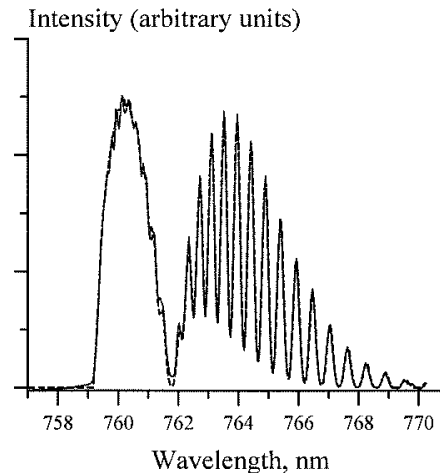


Fig.II.15. Experimental and synthetic emission spectra for  $O_2(b^1\Sigma \rightarrow X^3\Sigma)$  : simulation (dashed line); measurement (continuous line) [41, 48].

Since three different spectrometers will be employed in this work, we now define precisely the equipment chosen to collect and detect the emitted radiation, including their characteristics and calibration.

#### II.4.2.1. Low resolution spectrometer

The low resolution spectrometer is a Spectral Products SM-240 Spectrometer. The SM240 is a compact CCD spectrometer for use with a PC via USB port. It is a compact system, with flexible optical input direct to a fiber. It allows measurements up to a 750 nm window, between 150 nm and 900 nm. The durable aluminium housing that encloses the SM240 provides stable optical bench operation over a wide range of temperatures.

We can obtain a spectrum without discharge and with the same integration time as discharge experiment; and subtract it during spectra analysis. A background noise subtraction is also performed. The spectrometer is calibrated with a helium lamp using the emission lines of helium present in the literature and especially those at 587.5 nm (NIST) ; 667.8 nm ; 501.57 nm and 492.19 nm. The minimum spectral resolution of this setup is 1 nm.

#### II.4.2.2. Medium resolution spectrometer

A SpectraPro-2300i spectrograph from Acton Research Corporation, including a triple grating turret for three gratings, is used for some experiments. It is a 300 mm focal length, Czerny-Turner type with polished aspheric mirrors (the angle of the grating is changed by a stepper motor controlled through the acquisition and processing software Davis 7.1).

A LaVision intensified CCD camera with 1024 \* 1280 pixels (the pixel size is 14.5  $\mu\text{m}$  x 14.5  $\mu\text{m}$ ) is directly mounted to the exit of the monochromator for detection. Through acquisition it allows real-time data detection with the computer. This arrangement and the wavelength window of about 90 nm for the 600 lines/mm grating provided by the monochromator, give a minimum spectral resolution for this setup of about 0.7 nm.

### II.4.2.3. High resolution spectrometer

The aim of using a high resolution spectrometer is to correctly resolve atomic bands and the rotational structure of diatomic molecules. A SOPRA F1500 monochromator with a grating of 1800 grooves/mm is used. The angle of the grating is changed by a stepper motor controlled through a computer program called PI-IRIO, also allowing the wavelength calibration (calibration done with a mercury lamp). An optical multi-channel array (OMA) of 1024 pixels is directly mounted to the exit of the monochromator for detection and allows data detection with the computer. The Peltier effect cooled CCD OMA is flushed with nitrogen ( $-30^{\circ}\text{C} \pm 0.04^{\circ}\text{C}$ ). This triple stage cooling system allows decreasing the noise.

The wavelength calibration of the detection system was checked before and after each series of measurements. Indeed, the emission intensity recorded in the region of the spectrum was calibrated with a mercury lamp. The resolution of the spectrometer is  $0.5 \text{ \AA}$ . When necessary, especially for  $\text{O}_2(\text{b}^1\Sigma_g^+)$ , to improve the signal-to-noise ratio, the signal has been integrated over a time period of 1 s. Spectra of the plasma discharge were recorded by emission spectroscopy in the wavelength range of 153-980 nm.

Finally, one problem encountered, was the appearance of signal noise due to the high pulse frequency. The solution was to ground both the CCD camera and the controller of the spectrometer.

### II.4.2.4. Wavelength calibration

An important issue is the calibration of the spectroscopic system. One part is the calibration of the wavelength axis, done by using spectral lamps in combination with wavelength tables (NIST database). Groups of lines with various distances between each other (wavelength axis) are very well suited to determine the spectral resolution of the system and the apparatus profile. In this case, line broadening mechanisms must be excluded, for example, by using low pressure discharge lamps.

The experimental setups are calibrated using a low pressure mercury light source (MS-416) mercury spectral lamp from Lot-Oriel<sup>®</sup>. It produces narrow, intense lines from the excitation of mercury. The great advantage of this lamp is its temperature insensitivity. This allows to calculate the apparatus function and to determine the minimum resolution. For this calibration the spectral lamp is placed directly in front of the monochromator, which allows the calibration by optimizing the alignment of monochromator and camera. The atomic lines of mercury and argon are observed and used for calibration. For high resolution, a doublet and a triplet line can be observed for calibration. A doublet appears around 313 nm and 580 nm and a triplet-line around 366 nm.

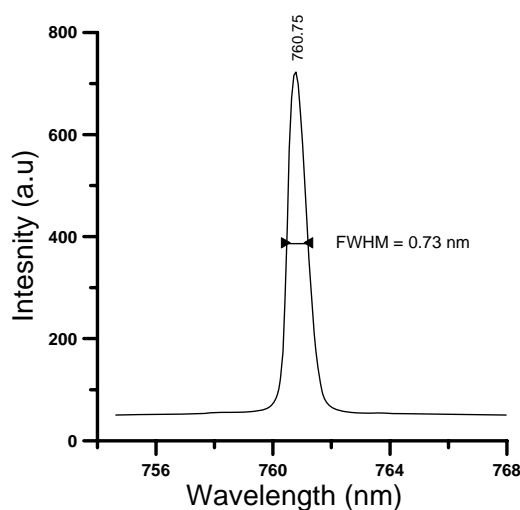


Fig.II.16. Hg/(Ar) lamp emission line at 760.75 nm.

The emission line in Fig.II.16 corresponds to Ar (I) transition theoretically at 763.51 nm. The significant measure for the apparatus function is the width of the peak at medium height. For the given

spectral line a resolution of 0.73 nm is found which is not far from the minimum resolution. An additional check with a He emission band at 587.562 nm and at 781.61 nm gives the same result. Much more effort is needed for the calibration of the intensity axis, which can be either a relative or an absolute calibration. A relative calibration takes into account only the spectral sensitivity of the spectroscopic system along the wavelength axis. On the other hand, an absolute calibration provides in addition the conversion between measured signals (voltage or counts) in  $W/(m^2.sr)$  or to photons/ $(m^3.s)$ . However, the mercury lamp is not adapted for such calibration, and therefore the intensity calibration has not been carried out.

### II.4.2.5. Optics

The experimental plasma facility detailed in chapter IV is designed for the use of spectroscopic diagnostics. In particular, the low pressure tank has three optical access  $CaF_2$  windows, as shown in fig.II.17.

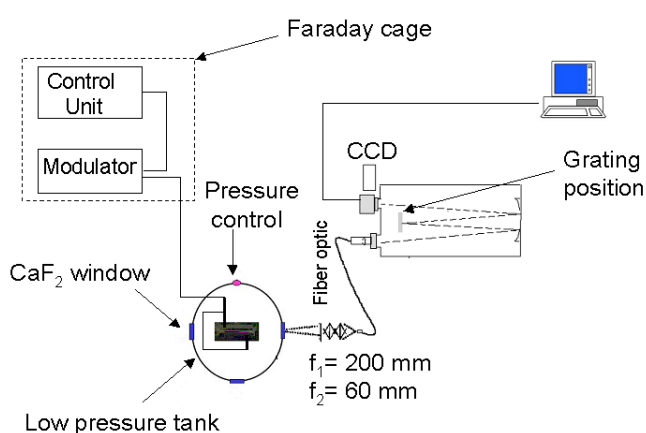


Fig.II.17. (Left) diagram of apparatus used for optical emission spectroscopy in the visible range and (right) UV-VIS high resolution SOPRA Czerny–Turner type spectrometer used in this study.

1 : Spectrometer ; 2 : CCD detector ; 3 : optical table ; 4 : controller.

The spectrometer is equipped with a CCD detector. The light source is either imaged by an imaging optics onto the entrance slit or coupled by fibres to the slit. The latter is very convenient, particularly when direct access to the plasma light is difficult. The cone of convergence is of great importance for the dimensions of the optical fibre. The optical focus arrangement has then been optimized. The adapted matching solution was to use convergent lenses with 200 mm and 60 mm focal length.

### II.4.3. Direct visualization by ICCD camera

Spontaneous emission of the flame has been investigated, as detailed in chapter V. Species identification can get complicated due to the presence of emission from many molecules (see Appendix 3). This can be avoided by using suitable filters.

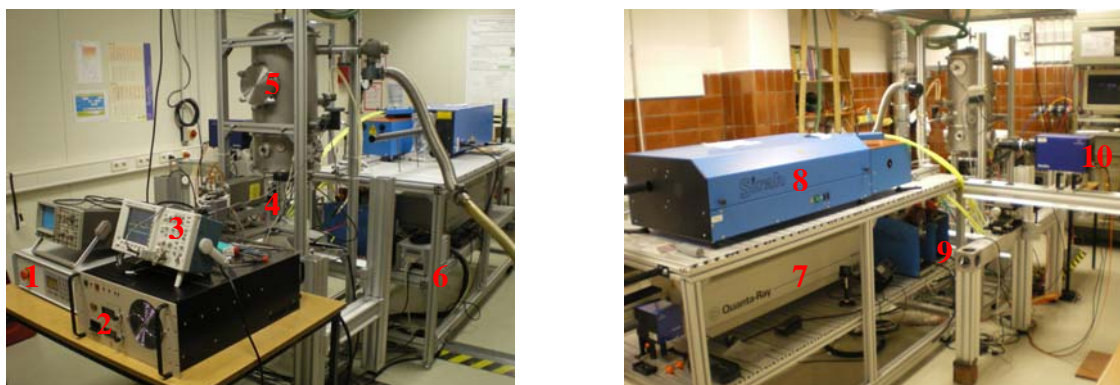
The digital image is recorded via an ICCD camera with high resolution and high sensitivity. An intensified CCD (ICCD) camera is a CCD detector coupled with an image intensifier. The image intensifier itself consists of a vacuum tube with three main components (a photocathode, a micro channel plate and a phosphor screen). The combination of a CCD and an image intensifier allows a better sensitivity (it is possible to measure single photons), allows to operate at UV extended spectral sensitivity (the camera spectral range covers the wavelength range from 190 nm to 900 nm), and to obtain an extremely short shutter time of a few nanoseconds.

The camera is linked to a PC via a fiber optic with SC connectors. A 105 mm focal objective is used. The CCD has an active image area of 1280 x 1024 pixels with a pixel size of 14.5  $\mu\text{m}$  x 14.5  $\mu\text{m}$ . The CCD pixel is subject to electronic noise. The major part of noise is generated thermally. Therefore, the CCD sensors are air-cooled down to -11 degrees Celsius. The acquisition and processing software used is Davis 7.1.

## II.4.4. Laser Induced Fluorescence

Laser induced fluorescence is a widely used method for flame analysis [176, 177]. In contrast to emission spectroscopy, a direct access to ground state densities is possible with LIF. Besides densities, also temperatures of atoms and molecules can be obtained from the measured spectral profile. Further advantages are a high spatial resolution and, depending on the laser source, fast measurements.

In our study, a preliminary study for Planar Laser-Induced Fluorescence (PLIF) imaging of OH radicals has been carried out, to qualitatively understand the flame structure modification in the presence of plasma. Pictures of the experimental arrangement are shown in Fig.II.18 :



1 : HVPPS ; 2 : HVDCPS ; 3 : oscilloscope ; 4 : pulser (high voltage unit) ; 5 : low pressure tank ; 6 : laser shutter ; 7 : Nd:YAG laser ; 8 : dye laser ; 9 : dye solution ; 10 : ICCD camera.

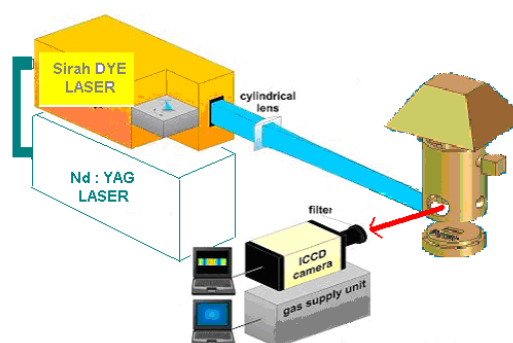


Fig.II.18. Pictures and schematic of apparatus used for OH Laser Induced Fluorescence experiments.

We have decided to excite the isolated band Q1(5) of OH (see Fig.II.19). The excitation laser system is composed of a Spectra Physics Nd:YAG laser pumping with its third harmonic and a Sirah dye laser whose output beam is doubled in frequency, in order to reach the selected excitation band at 282.66 nm. An appropriate dye solution (1.6 g/l of coumarin 153 diluted in ethanol) has been chosen. The Nd: YAG laser gives, at a frequency of 10 Hz, laser pulses of 10 ns duration and a mean energy of 280 mJ for the third harmonic at 355 nm.

The doubling crystal placed after the dye laser generates a beam at a wavelength near 283 nm. We have finally obtained UV laser pulses presenting a mean energy of 5 mJ.

An energy monitor is used for measurements of the laser pulse energy. The simultaneous acquisition of camera images and laser energy allows the correction of the measurements.

During the experiences of fluorescence, the verification of the excitation wavelength must be accomplished. This is performed by comparing the experimental LIF excitation spectra of OH radical with that theoretical calculated by LIFBASE [209]. Therefore, by identifying the different bands of the molecule, one can establish the calibration in wavelength of the laser. The figure II.19 represents the experimental LIF excitation spectra, obtained by varying the excitation wavelength from 282.5 nm to 283.5 nm by increments of 0.002 nm. The different bands of the OH molecule can be observed. The Q1(5) lines is highly emissive and well isolated from the others so a good selection of the LIF excitation line can be achieved. Also, as we choose to detect the emission lines around 262.68 nm, this Q1(5) line can be very efficiently separated.

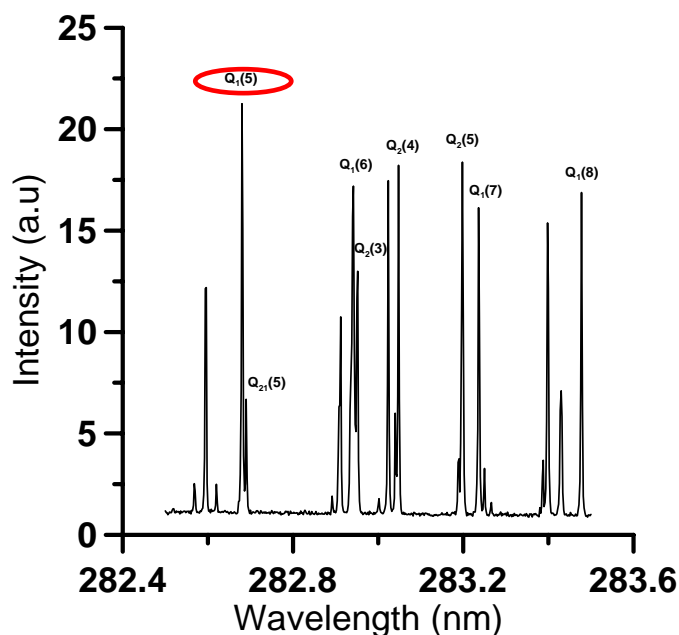


Fig.II.19. Experimental LIF excitation spectra of OH radical.

## II.5. Conclusions

The  $b^1\Sigma_g^+ \rightarrow X^3\Sigma_g^- (0,0)$  electric dipole and spin forbidden electronic transition of  $O_2$ , long designated the atmospheric A-band and the  $a^1\Delta_g \rightarrow X^3\Sigma_g^- (0,0)$ , designated the infrared band have been the subject of a literature spectroscopic study and synthetic spectra modelling.

We have performed such simulations to help diagnostics and give us useful information concerning plasma parameters (i.e. temperature measurements by comparison between experimental and simulated emission spectra).

Simulations are performed using three different programs: one especially developed for this study (MATLAB<sup>®</sup> program), PGOPHER<sup>®</sup> and HITRAN<sup>®</sup> simulation programs. Intensities of spectral lines as well as frequencies of emission are calculated by the simulation programs and the final spectrum is determined by choosing a rotational temperature. A Lorentzian line shape (to account for the pressure broadening) and an instrumental Gaussian line shape are used.

These simulated emission spectra are analyzed for getting information about the plasma characteristics. Indeed, presented in form of spectra with different resolutions, which allows approaching at best the experimental spectral resolution, the results of these calculations will be compared with experimental recordings ; the best correspondence will give information about the temperature of rotation of the molecule.

The next chapter will focus on modeling work :

- first, electron energy calculations, in order to optimize the production of singlet oxygen ;
- then, calculations of the effects of singlet oxygen on flame fundamental parameters.

# Chapter III : Modelling work

## Abstract

---

In a first part, we focus on the study of electron energy distribution function in binary mixtures containing oxygen. This modelling work will be used to identify the needed electron energy for optimal singlet oxygen species production and to discuss the effect of diluent addition. Energy input calculations have shown that optimal excitation of excited oxygen occurs at low reduced electric field. In order to significantly improve the efficiency of singlet oxygen generation in the discharge, we should operate in a narrow window. This important result will be taken into account in experimental development of plasma reactor, in which we can adjust the electric field close to the optimum for excitation of singlet oxygen molecules, to increase the production yield.

The promoting action of electrical discharges on combustion processes results in reduction of the ignition delay, improvement of flame stability as well as extension of the flammability limits. These features are key technical issues for combustion improvement. One particularly promising approach consists of plasma-enhanced activation of the oxidizing substance, such as when transforming molecular oxygen into its electronically excited singlet delta  $O_2(a^1\Delta_g)$  and singlet sigma  $O_2(b^1\Sigma_g^+)$  states. The second part, as a complement for further experimental results, will concern the numerical study of ignition and combustion in subsonic flows of diluted hydrogen-air mixtures including electronically-excited  $O_2$  molecules, as they appear in the experiments. In contrast with non-excited reactants, singlet oxygen molecules display a higher chemical activity and can affect reaction kinetics due to a decrease of the energy barrier associated with endoenergetic reactions. All computations rely on a detailed reaction scheme implemented within the package CHEMKIN 4<sup>®</sup> [178]. The reaction mechanism involves the excited species  $O_2^*$  ( $= O_2(a^1\Delta_g)$ ),  $O^*$  ( $= O(^1D)$ ) and  $OH^*$  ( $= OH(^2\Sigma^+)$ ). Results show that in the presence of excited oxygen in the initial mixture, a reduction of the ignition delay and of the minimum temperature for inflammation is observed, together with an increase of the laminar flame speed, the thermal flame thickness and of the maximum concentration of all main radicals. The extinction strain rate increases with oxygen excitation.

---

## III.1. Plasma modelling: electron energy distribution function

### III.1.1. Introduction

When a gas is subjected to an electrical field, accelerated electrons collide with neutral species and excite or ionize them. If the mean free path of charged species is small (i.e. high pressure), these acquire kinetic energy between two inelastic collisions; kinetic energies of different plasma particles are in the same order of magnitude; the medium is then in thermodynamic equilibrium.

If the pressure is weak or the electric field high enough, the mean kinetic energy of charged species is higher than kinetic energy of neutrals; one is in presence of non equilibrium plasma. Non thermal plasmas are weakly ionized plasmas associated with low ionization degree.

Bolsig plus<sup>®</sup> [179, 180] is a code for the numerical solution of the Boltzmann equation for electrons in weakly ionized gases and in steady-state, uniform fields. This code was especially designed to generate electron and transport data in pure gases or gas mixtures over a wide range of values of reduced electric field  $E/n$ .

## III.1.2. Boltzmann equation resolution in the case of a discharge

It is through the electrons that electrical energy is principally coupled to the plasma (the ions and the gas). Speeds of the various electron-oxygen reactions depend on the reduced electric field parameter  $E/n$ , by the intermediate of the electron energy distribution function  $f(u)$ . The reduced electric field is expressed in Townsend (1 Td= $10^{-17}$  V.cm<sup>2</sup>).

The normalization chosen is [137] :

$$\int_0^{\infty} \sqrt{u} \cdot f(u) \cdot du = 1 \quad (\text{Eq.III.1})$$

The usual first order development of the Boltzmann equation leads to the following classical equation [137] :

$$-\frac{1}{3} \left( \frac{E}{n} \right)^2 \frac{d}{du} \left[ \frac{u}{\sum_j \delta_j Q_{ej}} \cdot \frac{df}{du} \right] = 2m \cdot \sum_j \delta_j \frac{Q_{ej}}{M_j} \cdot \frac{d}{du} \cdot [u^2 \cdot f] \quad (\text{Eq.III.2})$$

$$- \sum_{jk} \delta_j \cdot (u \cdot f \cdot Q_{jk}) \quad (\text{Eq.III.3})$$

$$+ \sum_{jk} \delta_j [(u + u_{jk}) \cdot f(u + u_{jk}) \cdot Q_{jk}(u + u_{jk})] \quad (\text{Eq.III.4})$$

$$+ 2u \frac{d}{du} \left[ u^2 Q_{ee} \left( f \int_0^u u' \cdot f(u') du' + \frac{2}{3} \frac{df}{du} \cdot \left( \int_0^u u'^{3/2} \cdot f(u') du' + u^{3/2} \cdot \int_0^{\infty} f(u') du' \right) \right) \right] \quad (\text{Eq.III.5})$$

$$+ \frac{2m}{M_i} \cdot \alpha \cdot Q_{ei} \cdot \frac{d}{du} \cdot [u^2 f] \quad (\text{Eq.III.6})$$

In this equation, the left term (Eq.III.2) corresponds to the energy contribution due to the electric field (Joule heating). In the right-hand term, the first line corresponds to energy transfer by elastic collisions (Eq.III.2); the second line corresponds to inelastic collisions (Eq.III.3), the third one to super-elastic collisions (Eq.III.4), the fourth line to electron-electron collisions (Eq.III.5) and the last one to electron-ion collisions (Eq.III.6). It appears, in addition to the main parameter  $E/n$ , other parameters like the ionization degree  $\alpha$  and the proportion of a species  $j$ ,  $\delta_j$ . The distribution function, once known, allows to calculate the macroscopic parameters like the drift velocity, the diffusion coefficient, the reaction rates and energy loss fraction [137].

## III.1.3. Simulations

### III.1.3.1. Cross sections

The determination of cross sections for electron-impact excitation, ionization and dissociation of electronic states of molecular oxygen has been the object of numerous studies. For example, the development and initial results of a method for the determination of differential cross sections for electron scattering by molecular oxygen are described in [121]. The following calculations are performed using a set of cross sections integrated in Bolsig plus<sup>®</sup> [179, 180]. Data of cross-sections used in this work are in [121].

### III.1.3.2. Energy electron distribution function

The distribution of electron energy is Maxwellian, i.e. the electron translational energy levels follow a Boltzmann distribution. It is worth noting that at atmospheric pressure a gas usually has a

Maxwellian distribution of kinetic energy because of the high density of particles. In the case of air with electron density  $n_e \ll 10^{15} \text{ cm}^{-3}$ , it has a strong deviation from Maxwellian distribution. If there is no electric field applied and if the energy levels of the species interacting with electrons follow a Boltzmann distribution at a single temperature  $T_g$ , then statistical mechanics shows that the steady-state electron energy distribution will be the Maxwellian distribution at temperature  $T_g$  :

$$F(\varepsilon) = \frac{2}{\sqrt{\pi}} (k_B T_g)^{-3/2} \cdot \varepsilon^{1/2} \cdot e^{-\varepsilon/k_B T_g} \quad (\text{Eq.III.7})$$

The energy distribution  $f$  is defined as:  $f = \frac{1}{n_e} \cdot \frac{dn_e}{d\varepsilon}$  and is subject to the normalization :

$$\int_0^{\infty} f(\varepsilon) d\varepsilon = 1 \quad (\text{Eq.III.8})$$

One often uses the reduced electron energy distribution function defined as :

$$f_0(\varepsilon) = \frac{f(\varepsilon)}{\varepsilon^{1/2}} \quad (\text{Eq.III.9})$$

In the Maxwellian case,  $f_0$  is equal to :

$$f_0(\varepsilon) = \frac{2}{\sqrt{\pi}} (k_B T_g)^{-3/2} \cdot e^{-\varepsilon/k_B T_g} \quad (\text{Eq.III.10})$$

$f_0$  is conveniently linear in a log-linear plot :

$$\log f_0(\varepsilon) = \log\left[\frac{2}{\sqrt{\pi}} (k_B T_g)^{-3/2}\right] - \frac{\log(e)}{k_B T_g} \varepsilon \quad (\text{Eq.III.11})$$

When an electric field is applied (i.e. in an electrical discharge), a new source term appears in the electron energy equation, since electrons are accelerated and gain energy between collisions. The field increases the average electron energy, and the solution of the Boltzmann equation is usually different from the Maxwellian distribution at temperature  $T_g$ . Electron-electron collisions tend to “Maxwellianize” the electron energy distribution, for a given electric field. If the rate of electron-electron collisions is high enough (i.e. depending on high electron density and collision cross-sections), then any disturbance to the Maxwellian distribution is quickly smoothed out by electron collisions, and the distribution remains Maxwellian. If the distribution is not found or assumed to be Maxwellian, it cannot have the same temperature as the gas, because that would imply no energy transfer between electrons and heavy species. Energy transfer from electrons to heavy species is needed when the electron energy equation is in steady-state, because the input energy on the electron gas by the field is not zero. The system is a two-temperature plasma, with a gas temperature  $T_g$  and an electron temperature  $T_e$ .

The electron energy distribution function (EEDF) in a gas discharge is a good indicator of the state of the plasma. Chemical kinetics is especially sensitive to the EEDF and the electron population plays a central role in coupling power into the desired reactions. In molecular gases, the situation is complicated through the wide variety of species (and energy states within each one); but the distribution of electron energies is still an important indicator of what processes have or could have taken place.

Figure III.1 shows results obtained with Bolsig plus<sup>®</sup> for the EEDF in 10%O<sub>2</sub>/90%He plasma, for different values of  $E/n$ .

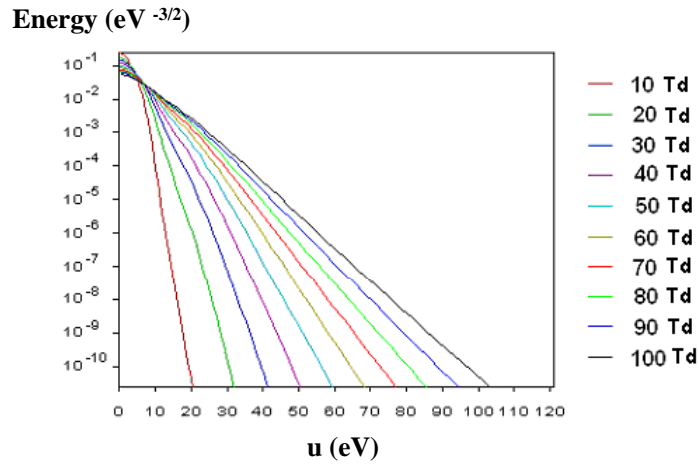


Fig.III.1. Energy distribution function for several values of reduced electric fields in Td (see colour legend) for a mixture 10%O<sub>2</sub>/90%He. The ionization level is set null.

The y axis corresponds to a logarithmic plot of part of the EEDF, which conveniently shows Maxwellian distributions as straight lines.

### III.1.3.3. Energy loss fractions for different processes including electronically excited oxygen

The electron energy distribution in non-equilibrium discharges plays the most important role in defining the plasma chemistry. It is through electron impact excitation and ionization that the charged particles, excited species, and radicals are produced.

Once the electron energy distribution function is known, it is possible to calculate macroscopic parameters of plasma. The present section focuses on the energy loss fraction for different processes including electronically excited oxygen production.

An important parameter for the discharge is the value of the reduced electric field (which is related to the electronic temperature). The Boltzmann solver calculates the energy electron distribution function in the plasma as well as the gas dissociation and the electronic excited states population, and provides the resultant electron impact process rate coefficients as a function of ( $E/n$ ).

Figure III.2 shows the dependence of specific energy deposited to excite O<sub>2</sub> in its first and second singlet states (O<sub>2</sub>(a<sup>1</sup>Δ<sub>g</sub>) and O<sub>2</sub>(b<sup>1</sup>Σ<sub>g</sub><sup>+</sup>)), to excite the vibrations (v=1) and for O<sub>2</sub> dissociation, according to ( $E/n$ ), first for pure O<sub>2</sub> :

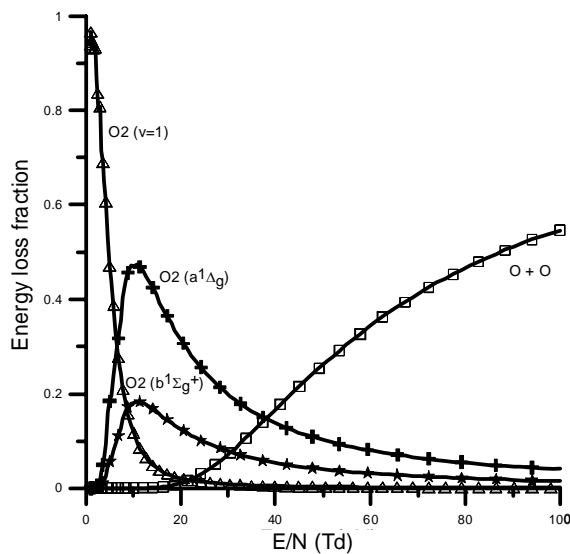


Fig.III.2. Fractional energy losses of electrons in pure O<sub>2</sub> against reduced electric field ( $E/n$ ) for excitation of the vibrations  $v=1$  ( $E_{exc}=0.19$  eV), excitation of a<sup>1</sup>Δ<sub>g</sub> ( $E_{exc}=0.98$  eV), excitation of b<sup>1</sup>Σ<sub>g</sub><sup>+</sup> ( $E_{exc}=1.63$  eV) and O<sub>2</sub> dissociation O<sup>3</sup>P + O<sup>1</sup>D ( $E_{diss}=8.4$  eV).

The processes considered in the model are : rotational, vibrational and electronic excitation processes, ionization process and attachment processes. They are listed below :

- Elastic momentum transfer ;
- Two body and three body attachment processes ;
- Rotational excitation process at energy level  $E = 0,02$  eV ;
- Vibrational excitation processes (resonance energy loss) at different energy levels  $O_2 + e \Rightarrow O_2(v) + e$  :
  - o  $O_2$  (v=1) with  $E = 0,19$  eV,
  - o  $O_2$  (v=2) with  $E = 0,38$  eV,
  - o  $O_2$  (v=3) with  $E = 0,57$  eV,
  - o  $O_2$  (v=4) with  $E = 0,75$  eV
- Electronic excitations :
  - o  $O_2 + e \Rightarrow O_2(a^1\Delta_g) + e$  (E = 0,98 eV)
  - o  $O_2 + e \Rightarrow O_2(b^1\Sigma_g^+) + e$  (E = 1,63 eV)
  - o  $O_2 + e \Rightarrow O_2^* + e$  (E = 4,5 eV)
  - o  $O_2 + e \Rightarrow O_2c + e$  (electronic sum :  $c = B^3\Sigma + A^3\Sigma + C^3\Delta + c^1\Sigma$ ) (E = 6 eV)
- Electronic impact dissociation :
  - o  $O_2 + e \Rightarrow O(^3P) + O(^3P) + e$  (E = 6,12 eV)
  - o  $O_2 + e \Rightarrow O(^3P) + O(^1D) + e$  (E = 8,4 eV)
  - o  $O_2 + e \Rightarrow O(^1D) + O(^1D) + e$  (E = 9,97 eV)
- Electron impact ionization :  $O_2 + e \Rightarrow O_2^+ + 2e$  (E = 12,06 eV)
- Two-body attachment (dissociative attachment) :
  - o  $O_2 + e \Rightarrow O + O^-$

The gas-phase chemistry in the oxygen plasma is relatively complex. A more detailed reaction kinetic model for oxygen that includes the basic kinds of charged and neutral particles is presented in appendix 4.

The electron energy balance is simulated as a function of reduced electric field strength. It is calculated by solving the steady-state space-uniform electron Boltzmann equation. The figure III.2 shows calculations made for pure  $O_2$ , with all molecules in the ground state (the ionization degree is set to zero and so electron-electron collisions are neglected).

One can observe that the energy fraction spent in the direct excitation of  $O_2(a^1\Delta_g)$  is quite high, approaching a maximum of 47% at  $E/n \sim 11$  Td. For  $O_2(b^1\Sigma_g^+)$ , the maximum of 18% is approached at  $E/n \sim 10$  Td. These results are similar with those found by Napartovich et al. [40] who found a percentage of 43% at  $E/n = 8.7$  Td for the direct excitation of  $O_2(a^1\Delta_g)$  and 17% at  $E/n = 8$  Td for  $O_2(b^1\Sigma_g^+)$ .

The following graphs show the dependence of specific energy deposited to excite  $O_2$  diluted in helium in its first and second singlet state as a function of the reduced electric field ( $E/n$ ).

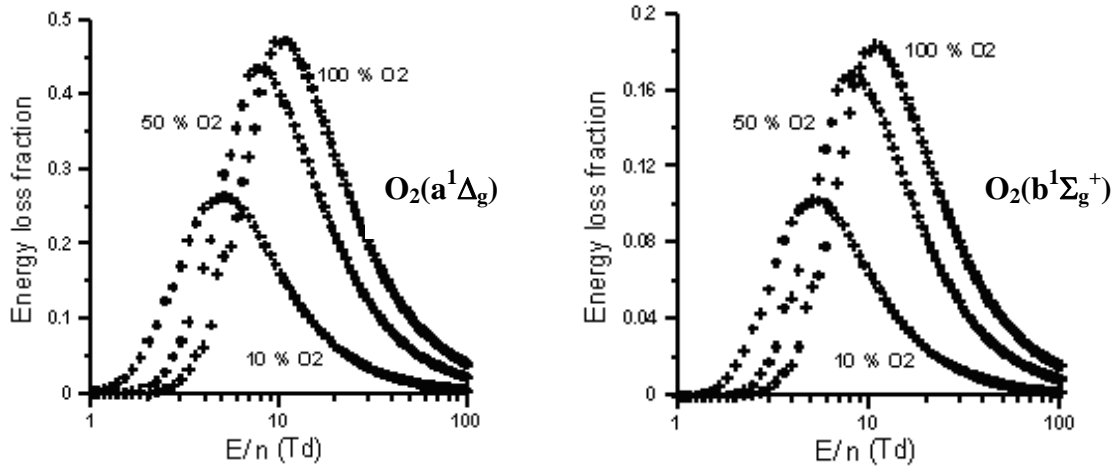


Fig.III.3. Fractional energy losses of electrons in pure  $O_2$  against reduced electric field ( $E/n$ ) for excitation of  $a^1\Delta_g$  ( $E_{exc}=0.98eV$ ) (left), and  $b^1\Sigma_g^+$  ( $E_{exc}=1.63eV$ ) (right), and for different percentages of  $O_2$  in binary mixtures  $O_2/He$ .

One can observe from fig.III.3 that the maximal efficiency of  $O_2(a^1\Delta_g)$  and  $O_2(b^1\Sigma_g^+)$  excitation decreases with helium dilution. In the same time, the optimal ( $E/n$ ) corresponding to the maximum singlet oxygen excitation decreases with He dilution (10 Td, 7.5 Td and 5 Td for pure  $O_2$ , 50%  $O_2$  and 10%  $O_2$  diluted in helium respectively). It is worth noting that this  $E/n$  value is considerably lower than those achieved in self-sustained nonequilibrium electric discharge. These results are in agreement with literature results [25, 33, 40, 41, 43, 181]. Indeed, recent investigations on electric discharge production of  $O_2(a^1\Delta_g)$  consisted on engineering the ( $E/n$ ) nearer to the optimum value for  $O_2(a^1\Delta_g)$  production. In pure oxygen, the optimal value of  $\sim 10$  Td can be obtained.

To conclude, in order to optimize the  $O_2(b^1\Sigma_g^+)$  and  $O_2(a^1\Delta_g)$  yield in the plasma, the discharge should operate at  $E/n$  values where the energy input into the target states is maximum. These numerical results confirm that the transition to a non-self-sustained mode can significantly improve the efficiency of singlet oxygen generation in the discharge and are in agreement with results of Napartovich et al. [40]. For that reason, a double discharge plasma-chemical reactor has been developed. In this crossed discharge, short high voltage DBD pulses produce ionization while a comparatively low electric field supports the electric current between ionizing pulses. This allows adjusting the electric field close to the optimum for excitation of singlet oxygen molecules and increases the production yield. The description of this combined discharge will be the object of chapter IV.

### III.1.3.4. Diluent effect

In a general way, we can expect that the fraction of electron energy intended for the direct excitation of  $O_2(a^1\Delta_g)$  and  $O_2(b^1\Sigma_g^+)$  decreases when diluents are added. Numerical simulations were performed for different percentages of dilution of  $O_2$ , particularly in helium, argon, nitrogen, neon and xenon. The following figures show the results for binary mixtures  $O_2$ /diluent, focussing on electronic excitations:  $O_2 + e^- \rightarrow O_2(a^1\Delta_g) + e^-$  and  $O_2 + e^- \rightarrow O_2(b^1\Sigma_g^+) + e^-$  (vibrational excitation:  $O_2 + e^- \rightarrow O_2(v=1) + e^-$  and oxygen dissociation :  $O_2 + e^- \rightarrow O + O + e^-$  have also been studied but are not shown here).

### III.1.3.4.1. Effects of helium diluent

Effect of helium dilution on the calculation of fractional energy losses of electrons against reduced electric field ( $E/n$ ) for excitation of singlet oxygen is presented in figure III.4.

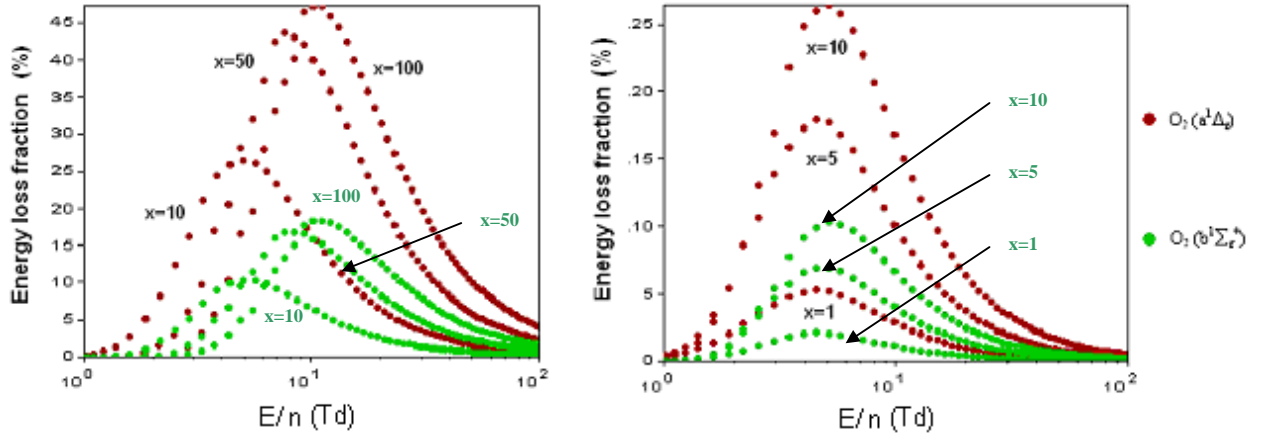


Fig.III.4. Fractional energy losses of electrons in pure  $O_2$  against reduced electric field ( $E/n$ ) for excitation of  $a^1\Delta_g$  ( $E_{exc}=0.98$  eV) (red), and  $b^1\Sigma_g^+$  ( $E_{exc}=1.63$  eV) (green) and for different percentages  $x$  of  $O_2$  in binary mixtures  $O_2/He$ .

The right figure corresponds to high dilution levels ( $x$  is the percentage of  $O_2$  in the mixture). One can observe that diluting with helium changes the electron energy balance. When increasing the dilution percentage, the maximal efficiency of  $O_2(a^1\Delta_g)$  and  $O_2(b^1\Sigma_g^+)$  excitation is significantly reduced. For pure oxygen and 1% of  $O_2$  diluted in helium, the maximum energy loss fraction decreases from 47% to 5% respectively. For  $O_2(b^1\Sigma_g^+)$ , it decreases from 18% to 2%, respectively. Moreover, the optimal reduced electric field  $(E/n)_{opt}$  decreases with helium dilution.

### III.1.3.4.2. Effects of argon diluent

Effect of argon dilution on the calculation of fractional energy losses of electrons in pure  $O_2$  against reduced electric field ( $E/n$ ) for excitation of singlet oxygen is presented in figure III.5.

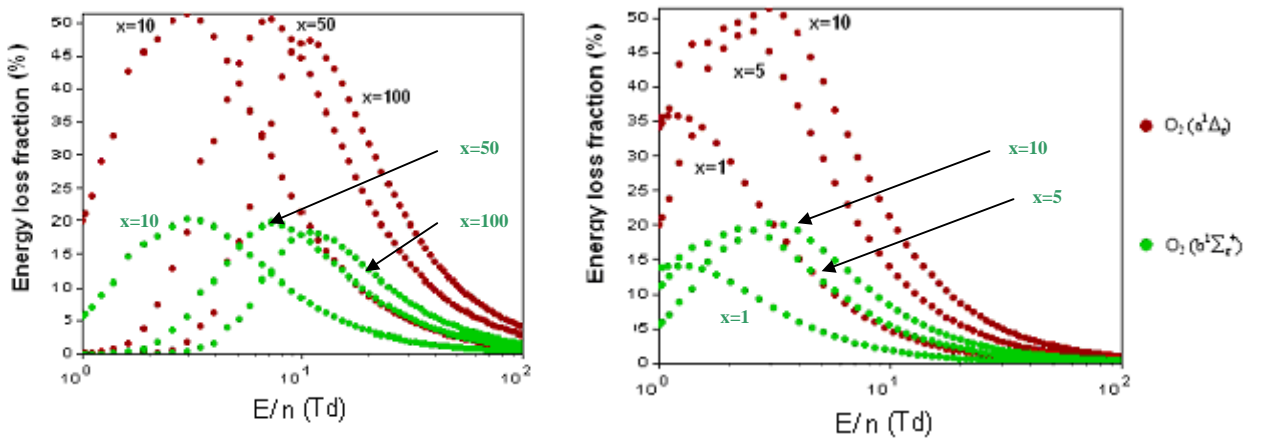


Fig.III.5. Fractional energy losses of electrons in pure  $O_2$  against reduced electric field ( $E/n$ ) for excitation of  $a^1\Delta_g$  ( $E_{exc}=0.98$  eV) (red), and  $b^1\Sigma_g^+$  ( $E_{exc}=1.63$  eV) (green) and for different percentages  $x$  of  $O_2$  in binary mixtures  $O_2/Ar$ .

From pure  $O_2$  (i.e.  $x=100\%$ ) to 10% of oxygen in binary mixtures ( $O_2/Ar$ ), one can observe that diluting with argon, the maximum fractional energy losses for excitation of  $O_2(a^1\Delta_g)$  and  $O_2(b^1\Sigma_g^+)$  increases from 47% to 51% and from 16% to 20%, respectively. Even at high argon dilution, the

maximal efficiency of  $O_2(a^1\Delta_g)$  excitation does not change very much (i.e. electron energy balance remains slightly modified). On the other hand, the optimal reduced electric field  $(E/n)_{opt}$  decreases strongly with argon diluting.

The electron energy balance as a function of the reduced electric field strength is of high importance for the optimization of one of the different existing processes. We can see from this simulation that the energy fraction spent in the direct excitation of  $O_2(a^1\Delta_g)$  and  $O_2(b^1\Sigma_g^+)$  is quite high at low  $E/n$  values. Therefore, it is expected that the presence of  $O_2(a^1\Delta_g)$  in the gas will have a significant influence on the electron energy distribution function and energy balance. Finally, with  $E/n$  increasing, the excitation goes on as follows (not shown here) : vibrations  $\rightarrow$  electronic state excitation  $\rightarrow$  dissociation  $\rightarrow$  ionization of  $O_2$ . In other words, at high  $E/n$ , the maximal fractional energy loss (i.e. in percentage) is shifted to vibrational excitation. In the same time, the lowest fractional energy goes to ionization.

### III.1.3.4.3. Effects of nitrogen diluent

Effect of nitrogen dilution on the calculation of fractional energy losses of electrons in pure  $O_2$  against reduced electric field  $(E/n)$  for excitation of singlet oxygen is presented in figure III.6.

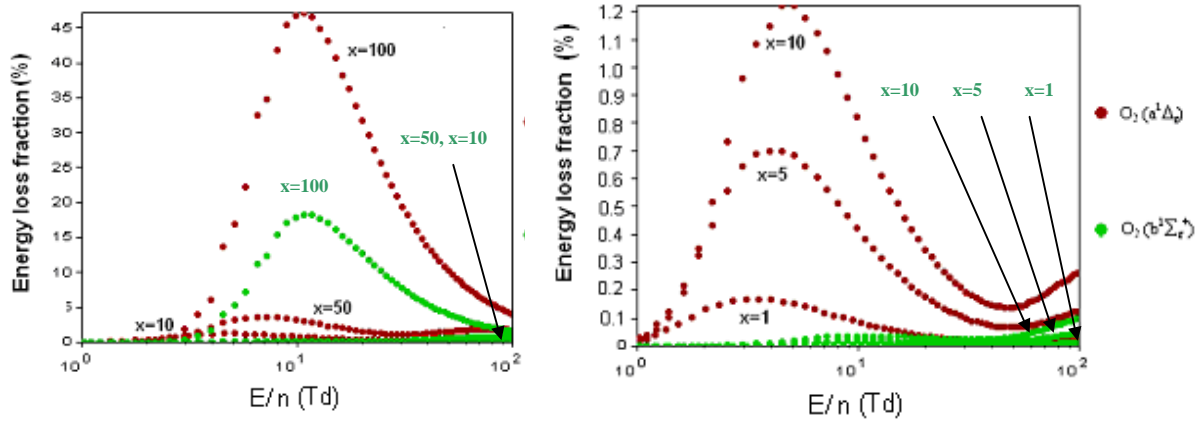


Fig.III.6. Fractional energy losses of electrons in pure  $O_2$  against reduced electric field  $(E/n)$  for excitation of  $a^1\Delta_g$  ( $E_{exc}=0.98$  eV) (red), and  $b^1\Sigma_g^+$  ( $E_{exc}=1.63$  eV) (green) and for different percentages  $x$  of  $O_2$  in binary mixtures  $O_2/N_2$ .

Diluting with nitrogen dramatically changes the electron energy balance even for small  $N_2$  addition.  $N_2$  can capture a large part of electron energy, thus defavouring oxygen electronic excitation. Moreover, it is worth noting that the maximal efficiency of  $O_2(a^1\Delta_g)$  and  $O_2(b^1\Sigma_g^+)$  excitation dramatically falls down with  $N_2$  dilution. In the case of  $N_2$ , the optimal reduced electric field  $(E/n)_{opt}$  decreases again with  $N_2$  dilution.

As for argon and helium dilution, the electron energy balance as a function of the reduced electric field strength is of high importance for the optimization of one of the different existing processes. We can see from this simulation that the energy fraction spent in the direct excitation of  $O_2(a^1\Delta_g)$  and  $O_2(b^1\Sigma_g^+)$  is weak but higher at low  $E/n$  values (i.e.  $E/n = 10$  Td and lower). Finally, with  $E/n$  increasing, the fractional energy losses of electrons is dominated by the following processes respectively : first,  $O_2$  vibrations (i.e. the specific energy deposited to vibrational excitation dominates the kinetics) and followed by  $O_2$  electronic states excitation, then  $N_2$  vibrations,  $N_2$  electronic state excitation,  $O_2$  dissociation and ionization of  $O_2$ . In other words, at high  $E/n$ , the maximal fractional energy loss (i.e. in percentage) is shifted to vibrational excitation. In the same time, the lowest fractional energy goes to ionization.

### III.1.3.4.4. Effects of neon diluent

Other diluent gases were also used for our calculations. They show interesting results concerning excitation efficiency. Effect of neon dilution on the calculation of fractional energy losses of electrons in pure O<sub>2</sub> against reduced electric field ( $E/n$ ) for excitation of singlet oxygen is presented in figure III.7.

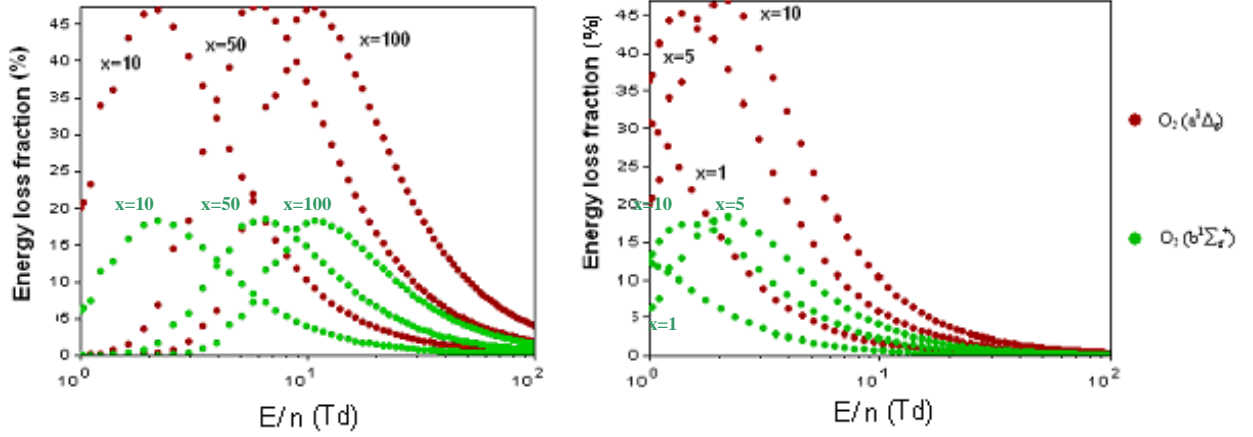


Fig.III.7. Fractional energy losses of electrons in pure O<sub>2</sub> against reduced electric field ( $E/n$ ) for excitation of  $a^1\Delta_g$  ( $E_{exc}=0.98$  eV) (red), and  $b^1\Sigma_g^+$  ( $E_{exc}=1.63$  eV) (green) and for different percentages  $x$  of O<sub>2</sub> in binary mixtures O<sub>2</sub>/Ne.

One can observe that the energy fraction spent in the direct excitation of O<sub>2</sub>( $a^1\Delta_g$ ) is almost insensitive to dilution up to 95% of Ne, approaching a maximum of 47%. For O<sub>2</sub>( $b^1\Sigma_g^+$ ), the maximum of 18% is approached at  $E/n \sim 10$  Td for pure O<sub>2</sub>. At 99% dilution, it reaches 31% and 13% respectively. However, the choice of neon as diluent agent in our experiments was not kept for cost reasons.

### III.1.3.4.5. Effects of xenon diluent

Effect of xenon dilution on the calculation of fractional energy losses of electrons in pure O<sub>2</sub> against reduced electric field ( $E/n$ ) for excitation of singlet oxygen is presented in figure III.8.

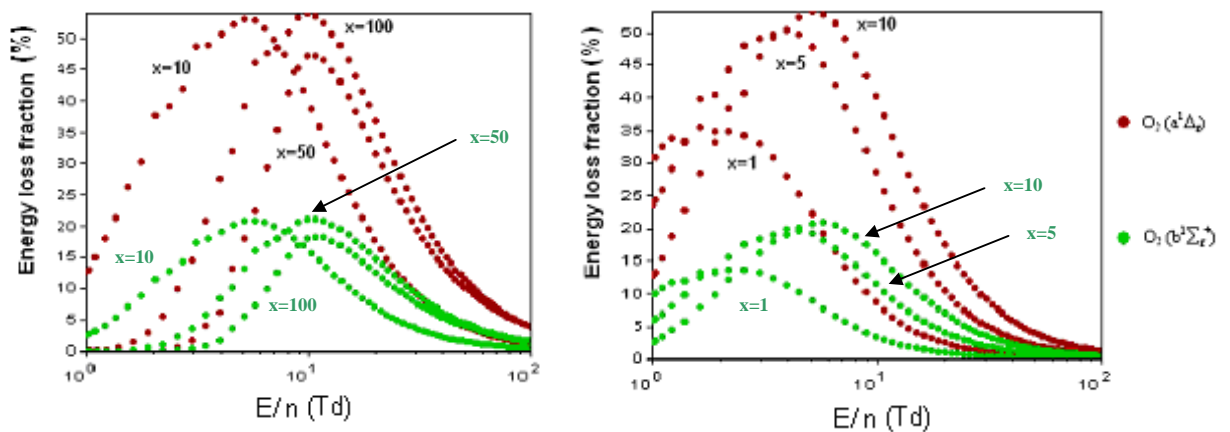


Fig.III.8. Fractional energy losses of electrons in pure O<sub>2</sub> against reduced electric field ( $E/n$ ) for excitation of  $a^1\Delta_g$  ( $E_{exc}=0.98$  eV) (red), and  $b^1\Sigma_g^+$  ( $E_{exc}=1.63$  eV) (green) and for different percentages  $x$  of O<sub>2</sub> in binary mixtures O<sub>2</sub>/Xe.

As for neon dilution, an interesting energy deposition efficiency is observed. But, once again, the choice of xenon as diluent agent in our experiments was not kept for cost reasons.

### III.1.3.5. Interpretation of dilution effects on discharge

The replacement of pure oxygen by oxygen/diluent gas mixtures has been discussed in the bibliography chapter I (section I.3) and we concluded that contradictions exist on the beneficial effects of diluents for singlet oxygen generation. Experimentally, an inert diluent such as helium is often added to the  $O_2$  to reduce the temperature rise in the discharge and support the gas dynamics by increasing pressure. Moreover, the presence of a diluent also reduces the amount of flow expansion caused by  $O_2$  dissociation, which in turn increases the residence time and leads to higher specific energy deposition and so a consequent rise in yield [44]. In our specific case (excited oxygen generation), in order to optimize the  $O_2(b^1\Sigma_g^+)$  and  $O_2(a^1\Delta_g)$  yield in the plasma, the discharge should operate at reduced electric field values, where the energy input into the target states is maximum. The addition of an inert gas such as helium may promote higher  $O_2(a^1\Delta_g)$  yield by allowing the discharge to operate at a more favourable  $E/n$  than does pure  $O_2$ .

The question raised here concerns the choice of diluent for experiments. Therefore, taking into account costs by rejecting expensive rare gases (xenon and neon), a competition between argon, helium and nitrogen gases is instigated. Molecular nitrogen being a strong quencher of electronically excited oxygen, we decide to dismiss it and therefore we will centre our attention in a choice between helium and argon. The question raised is whether argon is a better diluent than helium or not. The first argument favourable for dilution of oxygen with helium is that the binary He/ $O_2$  mixtures provide the lowest flow temperature. But, according to numerical results presented in previous section, the first argument favourable for dilution of oxygen with argon is that the binary Ar/ $O_2$  mixtures provide higher yields of  $O_2(a^1\Delta_g)$  and  $O_2(b^1\Sigma_g^+)$  states. This result can be explained by the facts that :

- Elastic losses to low atomic weight helium pump energy out of  $O_2(a^1\Delta_g)$ .

- Argon is beneficial because it has a higher atomic weight and hence its elastic losses are lower. However, experimental difficulties are highlighted in the literature concerning the input of energy in argon-containing gas mixtures.

In the framework of these first statements, it is clear from previous figures that argon diluent provides a significant benefit. A deeper analysis of dilution effects is presented in Fig.III.9, where it shows the maximal  $O_2(a^1\Delta_g)$  and  $O_2(b^1\Sigma_g^+)$  excitation efficiency ( $\eta$ ) in percent in argon, helium and nitrogen gas mixtures.

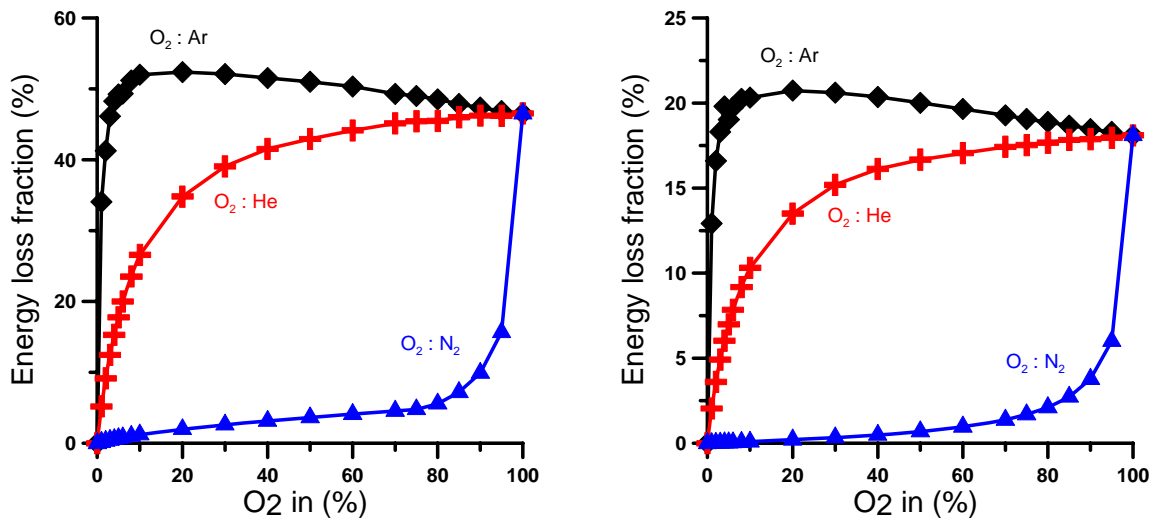


Fig.III.9. Maximal (left)  $O_2(a^1\Delta_g)$  and (right)  $O_2(b^1\Sigma_g^+)$  excitation efficiency in different gas mixtures.

One can observe that calculated maximal singlet oxygen excitation efficiency in different gas mixtures follows the same trend. Diluting with argon gives the best results. Energy loss fraction does not change significantly from 0 to 90% dilution. Even at high argon dilution,  $O_2$  receives most electron energy. In the case of helium, one can observe a more significant change in the energy balance, associated with a decrease of the maximal excitation efficiency when increasing the dilution.

In the case of nitrogen, dilution with  $N_2$  (even small dilution) dramatically decreases the maximum excitation efficiency, which means a change in the electron energy balance. Even at small addition,  $N_2$  receives most electron energy. It is worth noting that in presence of nitrogen in discharges, the EEDF can show significant depletion around 2 – 5 eV where there is a large cross-section for vibrational excitations of the  $N_2$  molecule.

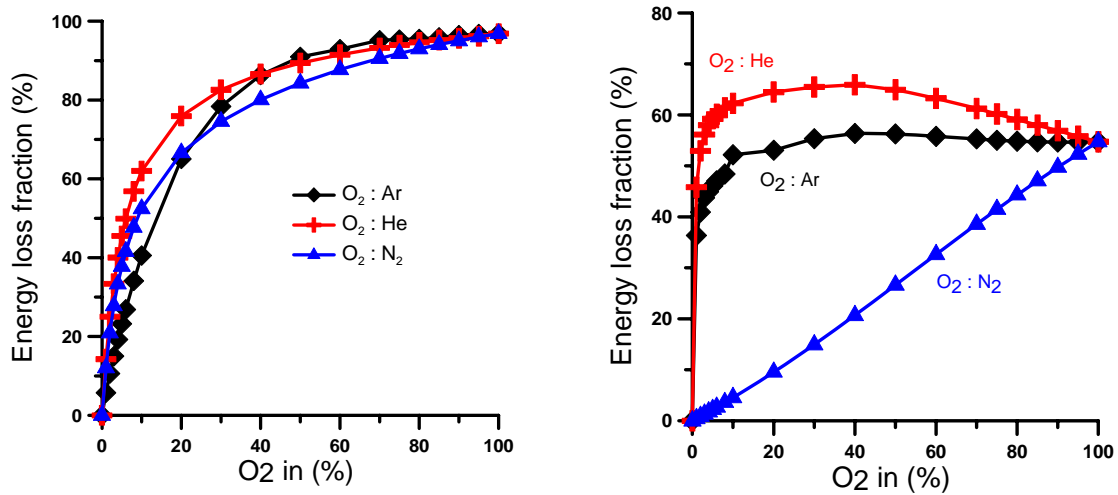


Fig.III.10. Maximal (left)  $O_2(v=1)$  and (right)  $O_2$  dissociation ( $O + O$ ) efficiency in different gas mixtures.

One can observe in Fig.III.10 that calculated maximal  $O_2(v=1)$  vibrational excitation efficiency in different gas mixtures evolve in a similar curve. Diluting with argon, helium or nitrogen gives a significant decrease of the energy loss fraction. Two linear evolutions with two different slopes can be observed. The first one, from 0 to 20% of  $O_2$  and the second one, less abrupt, from 20 to 100%  $O_2$ .

In addition, the  $O_2$  dissociation efficiency is shown in Fig.III.10. Contrary to the previous case of electronic excitation, the dilution with helium gives higher dissociation efficiency in the entire range of  $O_2$  percentage. In the case of nitrogen, dilution induces a linear decrease of the maximum dissociation efficiency within the entire gas mixtures range.

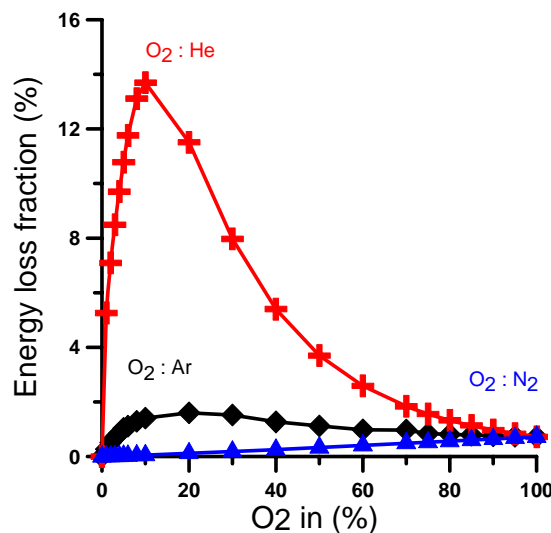


Fig.III.11. Maximal ionization efficiency in different gas mixtures.

Finally, Fig.III.11 shows the maximal ionization efficiency in the different gas mixtures and diluents. An important observation concerns the net difference between helium and other considered diluents. An optimal ionization efficiency of 14% appears around 10%  $O_2$  in He. The values are ~2% and < 1% for argon and nitrogen diluents, respectively.

The development of a plasma discharge begins by dissipating power in a gas mixture. In our particular case, the diluent allows reducing the amount of flow expansion caused by O<sub>2</sub> dissociation, which in turn increases the residence time in discharge region. In turn, the increased residence time leads to higher specific energy deposition with a consequent rise in yield. Also, the diffusion losses of both excited states and charged particles are reduced.

It has been suggested that the addition of an inert diluent such as argon and helium may promote higher singlet oxygen yields by allowing the discharge to operate at a more favourable  $E/n$  for its production [40, 41, 43]. Adding helium to an O<sub>2</sub> discharge does reduce the quasi-steady-state reduced electric field. The quasi-steady  $E/n$  is approached as the rate of ionization balances the rate of loss by diffusion to the walls, attachment and recombination. In the experiment we choose to maintain the partial pressure of O<sub>2</sub> constant and to vary only He partial pressure so that a portion of the reduction in  $E/n$  reflects reduced charged particle loss by diffusion.

For pure O<sub>2</sub>, the maximum power dissipated into O<sub>2</sub>\* occurs near 10 Td, but the discharge could operate at higher values. As helium is added, the  $E/n$  at which the O<sub>2</sub>\* excitation is a maximum decreases as does the operating  $E/n$  while the fraction of power dissipated into O<sub>2</sub>\* decreases. The reduction in operating  $E/n$  made possible by the addition of helium does not fully counteract the decrease in the fraction of power dissipated in O<sub>2</sub>\* excitation. Therefore, for these conditions the addition of He actually decreases the efficiency of electron impact excitation of O<sub>2</sub> to O<sub>2</sub>\*.

Below 10 Td, at high helium fractions the singlet oxygen density is high enough so that more electron impact events remove power from O<sub>2</sub>\* by superelastic collisions [43] compared to the power added by direct electron impact, resulting in negative power fractions to singlet oxygen. Helium addition reduces the rate of direct electron impact reaction with O<sub>2</sub>. Moreover, due to the increase in heat capacity and thermal conductivity that occurs with helium addition, the peak gas temperature decreases with He addition.

In our experimental work, we finally observed that adding helium to oxygen leads to better results than with argon dilution. Indeed, we have observed that input of energy is more difficult in the latter case and discharge constrictions are easily obtained with argon dilution. Furthermore, the choice of xenon or neon as diluent agent in our experiments was not kept for cost reasons. Finally, diluting with nitrogen dramatically changes the electron energy balance even for small N<sub>2</sub> addition. N<sub>2</sub> can capture a large part of electron energy, thus defavouring oxygen electronic excitation and this is the reverse of desired effect.

Finally, other factors can be responsible and affect directly the singlet oxygen yield. Apart from electron energy consideration, the power supply used has to be optimized for a given plasma reactor (i.e. power supply with load matching) to prevent or limit the main power of the high voltage to be dissipated back to the generator. It is worth noting that the dilution is the dominant effect.

In table III.1, a comparative table is presented where helium and argon advantages (marked with (+)) and drawbacks (marked with (-)) for optimal singlet oxygen generation are presented.

<b>Helium as diluent</b>	<b>Argon as diluent</b>
(+) Detection of O <sub>2</sub> (b <sup>1</sup> Σ <sub>g</sub> <sup>+</sup> )	(+) Diluting with Ar does not change significantly the electron energy balance. (+) Maximal efficiency of O <sub>2</sub> (a <sup>1</sup> Δ <sub>g</sub> ) excitation does not change very much; only at very high dilution
(+) He/O <sub>2</sub> mixtures provide the lowest flow temperature	(+) Argon is beneficial because it has a higher atomic weight and hence its elastic losses are lower
(-) Maximal efficiency of O <sub>2</sub> (a <sup>1</sup> Δ <sub>g</sub> ) and O <sub>2</sub> (b <sup>1</sup> Σ <sub>g</sub> <sup>+</sup> ) excitation decreases with He diluting	(-) No Detection of O <sub>2</sub> (b <sup>1</sup> Σ <sub>g</sub> <sup>+</sup> ) Suggestion: emission intensity is at least a factor 30-50 lower than in O <sub>2</sub> -He mixture

(-) Elastic losses to low atomic weight helium rob power to $O_2(a^1\Delta_g)$ .	(-) $O_2(b^1\Sigma_g^+)$ may be rapidly quenched in resonance energy transfer collisions with Ar atoms (-) $O_2(a^1\Delta_g)$ and $O_2(b^1\Sigma_g^+)$ states are more quickly relaxed by energy resonant transfer quenching by collisions with Ar atoms than with He atoms (Hicks et al. 2005 [41])
--	---

Table III.1. Diluent addition effects. Comparison between argon and helium.

In the Boltzmann equation solver for the electron energy distribution, the main collisional processes involved in  $O_2/He$  and  $O_2/Ar$  gas mixture are taken into account (elastic collisions including the energy exchange and thermal motion of the gas, inelastic collisions such as rotational, vibrational and electronic excitations, attachment and ionization, and also superelastic collisions). However, the gas-phase chemistry in the oxygen plasma is more complex and for a detailed plasma simulation, a kinetic model for argon-oxygen and helium-oxygen mixtures that includes charged and neutral particles should be developed. The main kinetic processes responsible for excitation and quenching of singlet oxygen should be taken into account in the model. The chemical species of interest include 18 particles, charged and neutral,  $O_2(X^3\Sigma_g^-)$ ,  $O_2(a^1\Delta_g)$ ,  $O_2(b^1\Sigma_g^+)$ ,  $O(^3P)$ ,  $O(^1D)$ ,  $O_3$ , electrons, ions negative ( $O^-$ ,  $O_2^-$ ,  $O_3^-$ ), positive ions ( $O^+$ ,  $O_2^+$ ,  $O_3^+$ ,  $O_4^+$ ),  $Ar^+$ ,  $Ar_2^+$ ,  $He^+$  and  $He_2^+$ . The model would also incorporate a number of electron impact processes in the nonequilibrium plasma, such as ionization, dissociation, electronic excitation, and dissociative attachment. And reaction rate coefficients for processes involving electrons are found by solving the electron Boltzmann equation as functions of the reduced electric field, which is re-calculated when plasma parameters changed [41]. This approach should solve space and time variations of the electric field coupled with continuity and momentum transfer equations. In this manner, more accurate predictions could be obtained.

### III.1.4. Conclusions on excitation

These conclusions take into account the theoretical results presented here, but also the experimental observations detailed in chapter IV.

Although the dominant effect of helium addition is to increase the residence time, the gas density also increases relative to the pure  $O_2$  case. Both the reduction in temperature and the net increase in density influence many of the rates in the reaction mechanism, which on the average increases  $O_2(a^1\Delta_g)$  yield. On the other hand, argon dilution causes difficulties to input of energy into the gas. It is clear from previous statements that helium diluent provides a significant benefit. Besides, molecular nitrogen has to be banned or at least highly reduced due to its extreme negative effect on oxygen electronic excitation

Energy input calculations have shown that optimal excitation of excited oxygen is at low reduced electric fields (lower than 10 Td) and preliminary experimental results of optical emission spectroscopy of pulsed dielectric barrier discharge will show that electron energy must be controlled to excite oxygen at 762 nm. In this sense, the next chapter will concern the design and engineering of a plasma chemical reactor capable of reaching optimal electron energy for excitation of molecular oxygen in its singlet electronic states  $O_2(a^1\Delta_g)$  and  $O_2(b^1\Sigma_g^+)$  by means of a non-thermal electric discharge, at reduced pressure until atmospheric pressure.

For a better accuracy, a more complete plasma simulation including the space and time variations of the electric field and neutral and charged particle densities should be solved. The analysis of the calculated electric field together with the ion, neutral and electron densities would help to explain the discharge mechanisms involved and to analyze the best conditions to achieve the most effective way to excite oxygen. We will demonstrate in chapter IV the feasibility to electronically excite molecular oxygen. In preparation for experiments of plasma-assisted combustion, the rest of this chapter is devoted to the numerical modelling of flame properties in the presence of excited oxygen, as it will appear in the experiments.

## III.2. Modelling of plasma-assisted combustion

### III.2.1. Introduction

The ultimate object of this work is to significantly improve combustion efficiency and reduce pollutant emissions using oxidizer “activation” by nonthermal plasma. For this purpose, the experimental production of excited species is essential and has been discussed previously. It is now important to support further experimental findings by a numerical analysis. In order to describe numerically the influence of excitation on the reaction process, appropriate kinetic schemes must be employed. The ignition and combustion of hydrogen fuel have been extensively studied. Detailed kinetic schemes have been developed to describe the ignition and combustion of hydrogen, e.g. Li et al. [182], O’Conaire et al. [183] and Konnov [184] mechanisms. At present, relatively little is known about the possible influence of electronically-excited species on oxidation kinetics. If present in critical concentrations, they may in particular reduce ignition delay time [185]. Numerical models including excited species have demonstrated that pulsed corona discharges may be used for NO removal at low temperature and atmospheric pressure [186]. A kinetic model that can describe the removal of NOx with pulsed corona discharges is proposed in [187, 188].

The computations have been done using complex chemistry with the CHEMKIN 4 package [178]. A detailed reaction mechanism describing H<sub>2</sub>/Air combustion is used. It is composed of Ibraguimova et al. [189] mechanism where an “excited block”, including O<sub>2</sub>\* (=O<sub>2</sub>(a<sup>1</sup>Δ<sub>g</sub>)), O\* (=O(<sup>1</sup>D)) and OH\* (=OH(<sup>2</sup>Σ<sup>+</sup>)) is integrated in the final mechanism.

### III.2.2. Numerical modelling

This study considers only laminar combustion processes involving diluted hydrogen - oxygen. To compute the structure of such flames different modules available in the package CHEMKIN 4 are employed [178]. A variety of models and parameters are needed to carry out the computations :

- A full reaction mechanism based on individual reactions modelled using modified Arrhenius laws and including the influence of excited species is needed.
- Thermodynamic data for all (neutral as well as excited) species must be available. For the excited species O<sub>2</sub>\*, OH\* and O\*, the corresponding thermodynamic parameters have been determined prior to the flame computations using the GAUSSIAN software [190].
- Finally, transport data are requested, in particular diffusion coefficients. For the present study the excited species are considered to behave identically with their non-excited counterparts, as predicted by the kinetic theory of gases [191].

In the absence of electronic excitation, complete reaction schemes describing hydrogen oxidation are well established. There have been a very large number of measurements made. These include flame speed measurements, burner stabilized flames in which species profiles are recorded, shock tube ignition delay times, and concentration profiles in flow reactor studies. For example, Li and co-workers [182] validated their mechanism over the temperature range 298-3000 K, at equivalence ratios of 0.25 < Φ < 5.0 and pressures of 0.3 to 87 atm. Very good agreement of the model predictions with the experimental measurements demonstrate that their updated comprehensive mechanism has excellent predictive capabilities for different experimental systems. Unfortunately, excited species are usually not included in these schemes.

In the framework of an INTAS collaboration, a recent kinetic model describing reaction pathways in diluted H<sub>2</sub>-O<sub>2</sub> mixtures including electronically-excited O<sub>2</sub>\* molecules has been developed and is used in the present work. Evaluated kinetic data for high temperature gas phase reactions obtained when taking into account O<sub>2</sub>(a<sup>1</sup>Δ<sub>g</sub>), O(<sup>1</sup>D) and OH(<sup>2</sup>Σ<sup>+</sup>) rely on the data published in [189]. Data on the rate constants for the reactions with excited molecules are estimated and included in the model. Rate constants concerning chemical reactions with singlet oxygen are known from precise kinetic measurements and modelling in atmospheric chemistry, photochemistry and plasma chemistry. However, information about rate parameters of these reactions in conditions relevant to combustion is

insufficient, and considerable efforts are still required for an adequate modeling of complex combustion chemistry in this case.

Electronically excited species are treated as chemical reagents with their own thermodynamic properties, and corresponding electronic energy exchange and quenching processes are considered as usual chemical reactions. Also, translational, rotational, and vibrational degrees of freedom of molecules are assumed to be in quasi-Boltzmann distribution and not disturbed by chemical reactions. Rate constants for reactions with normal oxygen are based on compilations of the updated data from the CODATA Task Group (Baulch et al. [192]), IUPAC Subcommittee (Atkinson et al. [193]), NASA Panel (Sander et al. [194]), NIST chemical kinetics database (Mallard et al. [195]), CHEMKIN collection [178], GRI mechanism (Smith et al. [196]), Leeds mechanism [197], Konnov's mechanism (Konnov [184]), LLNL (Westbrook et al. [198]), O'Conaire et al. [183], Marinov et al. [199]), Li et al. [182] and others.

Moreover, rate constants for reactions with singlet oxygen, governing hydrogen oxidation, are based on the review of data from Starik and Titova [200] and AFRL kinetic database (Carroll et al. [201]). Finally, some specific reactions with electronically excited species were obtained from Skrebkov and Karkach [185] as far as they were validated by Shatalov et al. [202].

This mechanism (later called MSU kinetic model) includes 14 species ( $H_2$ ,  $O_2$ ,  $H$ ,  $O$ ,  $O_3$ ,  $OH$ ,  $HO_2$ ,  $H_2O_2$ ,  $H_2O$ ,  $O(^1D)$ ,  $O_2(a^1\Delta_g)$ ,  $OH(^2\Sigma)$ ,  $N_2$ ,  $Ar$ ,  $He$ ) and 142 elementary reactions (Table A2.1, see Appendix 5). It is worth noting that  $N_2$ ,  $Ar$  and  $He$  are considered as diluent in the reaction mechanism (i.e. collision partner). The chemical reaction rates ( $k_i$ ) are modeled by a modified Arrhenius law ( $k_i = A T^n \exp(-E_a/RT)$ ), where the preexponential factor  $A$  is the coefficient factor expressing the empirical relationship between temperature and rate coefficient and related to the gas kinetic collision frequency. It depends on how often molecules collide and on whether the molecules are properly oriented when they collide.  $E_a$  is the activation energy and  $T$ , the temperature. The reaction rates including  $N_2$  and  $He$  as collision partner are deduced from that with  $Ar$  specie, using a multiplication factor ( $\times 0.875$  for  $N_2$  and  $\times 0.98$  for  $He$ ). The full model can be consulted in Appendix 5.

The numerical analysis carried out in this work considers in particular the influence of excited  $O_2$  molecules ( $a^1\Delta_g$  state) on  $H_2/O_2$ (air) combustion under subsonic conditions. The first computational step consists in achieving a converged solution for prescribed boundary and initial conditions. This is very easy for well-established standard reaction schemes. But, as soon as excited species are taken into account and due to large reaction rates, convergence is hardly reached. As a consequence, a lot of effort has been necessary before obtaining converged solutions with CHEMKIN4<sup>®</sup>.

A detailed numerical analysis of the influence of singlet oxygen excitation on the most important flame characteristics (laminar flame speed, auto-ignition delay, flame structure) is presented now.

### III.2.3. Flame properties without excited species

#### III.2.3.1. Laminar flame speed

For a validation of the MSU kinetic scheme, diluted  $H_2$ - $O_2$  laminar premixed flames without excited species are first considered. For such conditions, a wealth of experimental results can be found in the literature. The evolution of laminar premixed flame speed with hydrogen mole fraction is presented in Fig.III.12.

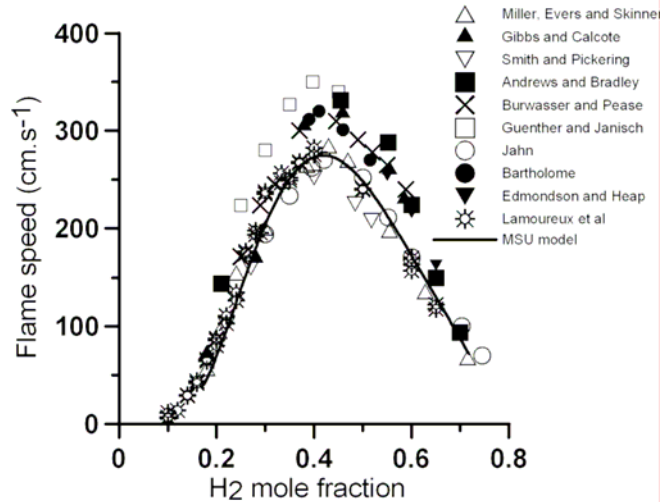


Fig.III.12. Laminar flame speed at  $P = 1$  atm for  $H_2$ - $O_2$  oxidation (ratio  $O_2:N_2 = 1:3.76$ ). Continuous line: MSU model. Symbols: various experimental results from the literature (see [203, 204]).

Only freely propagating atmospheric flames at ambient temperature are considered here. The experimental measurements of the various research groups are in good agreement. The numerical predictions obtained with the MSU model coincide very well with the experimental values, demonstrating that this scheme is able to describe standard premixed flames with good accuracy.

### III.2.3.2. Influence of dilution

As explained previously, the generation of excited species always takes place using diluted oxygen. Various diluting species can be employed experimentally to promote or prevent excitation. Therefore, the employed kinetic scheme must be able to correctly take into account the impact of high dilution levels. The variation of the laminar flame speed for different diluents (nitrogen, argon, helium) and different dilution levels are now considered by comparison with the experiments of Kwon and Faeth [205] at atmospheric pressure (Fig.III.13).

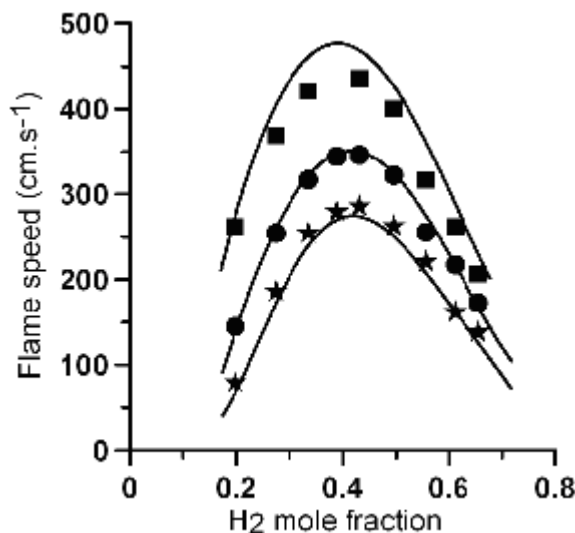


Fig.III.13. Laminar flame speed for atmospheric  $H_2/O_2$  flames diluted with either ( $\star$ ):  $N_2$ , ( $\bullet$ ):  $Ar$  or ( $\blacksquare$ ):  $He$  (ratio  $O_2:N_2 = O_2:Ar = O_2:He = 1:3.76$ ). Solid lines: MSU model. Symbols: experiments [205].

The observed good agreement of the model predictions with the experimental measurements demonstrate that the MSU kinetic model presents excellent predictive capabilities for the influence of

dilution in non-excited flames. Nevertheless, a small overprediction is obtained for helium dilution. It is worth noting that the dilution with helium leads to a higher flame velocity than with Ar, while Ar dilution leads again to a higher flame velocity than N<sub>2</sub>.

These variations can be readily explained by the classical thermal theory, first proposed by Mallard and Le Châtelier in 1883. In its simplest form, this theory leads finally to a flame velocity proportional to  $(\lambda/C_p)^{1/2}$  where  $\lambda$  is the thermal conductivity and  $C_p$  the mixture specific heat capacity at constant pressure. The different thermal conductivities and heat capacity of nitrogen, helium and argon are sufficient to explain the observed variations.

As a first conclusion it has been demonstrated that the employed kinetic scheme can reproduce with an excellent accuracy the evolution of the laminar flame speed for H<sub>2</sub>/O<sub>2</sub> combustion, taking into account different diluting species and for an equivalence ratio varying between  $\Phi = 0.5$  and 5. Globally, good agreement with experimental data is obtained.

### III.2.3.3. Auto-ignition delays

In shock tube studies the auto-ignition delay is typically defined as being the time interval between the passage of the reflected shock wave ( $V_{OCR}$ ), where the gas mixture is instantaneously placed at high temperature and high pressure, and the time associated with 50 % of the maximum of the OH\* emission signal. Excited OH\* radicals return to the fundamental state quasi instantaneously (the life time of OH\* lies typically around 1  $\mu$ s), by emitting light in UV at 306 nm. The OH radical is a typical marker of the hydrogen flame front. It is also particularly interesting for optical combustion diagnostics, since it is relatively easy to detect [206]. The numerical estimations of the auto-ignition delays rely on the closed homogeneous batch reactor module of CHEMKIN [178].

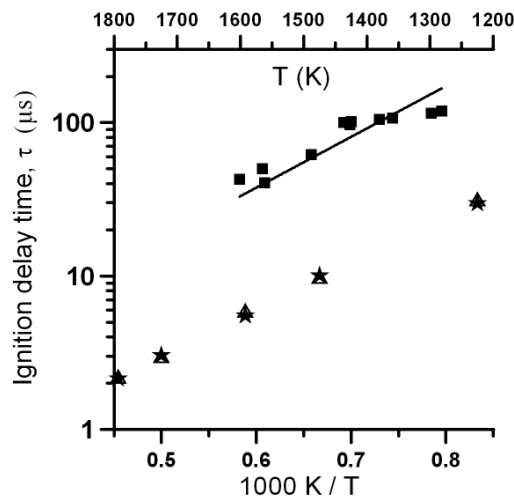


Fig.III.14. Auto-ignition delay times determined numerically from either (★): fundamental OH or from (Δ): excited OH\* radicals using MSU kinetic model at  $P = 1$  atm and for H<sub>2</sub>:O<sub>2</sub>:N<sub>2</sub> = 2:1:3.76 mixture. Comparison between experimental data (■, [207]) and numerical results (MSU model, solid line) both at  $P = 3$  atm for H<sub>2</sub>:O<sub>2</sub>:Ar = 1:1:98 mixture. The ignition delay time is defined when reaching 50% of the maximum OH concentration.

Comparisons presented in Fig.III.14 have shown that it is possible to consider the same definition as in the experiments, following the temporal evolution of either fundamental or excited OH species. On the other hand, the final OH concentration is noticeably smaller when taking into account excited radicals (not shown), as expected. In what follows non-excited OH radicals are considered to define ignition delay.

Figure III.14 shows also the ignition delay times for a H<sub>2</sub>-O<sub>2</sub>-Ar mixture at 3 atm. A good agreement between experiments and simulations is achieved using the MSU model. The general trend is reproduced throughout the entire temperature range, with only a very slight overprediction (at low

temperature) or underestimation (at high temperature). The numerical model best coincides with the experiments at intermediate temperatures (roughly 1300 to 1650 K).

Thus, it has been demonstrated that the employed kinetic scheme can reproduce with excellent accuracy the main properties of laminar flames without excitation for a large domain of equivalence ratio, temperature and dilution level. It is now possible to consider the influence of excitation on the corresponding laminar flame properties.

## III.2.4. Flame properties with excited oxygen species

### III.2.4.1. Influence of $O_2^*$ on ignition delay

Ignition delays of an  $H_2$ -air mixture at an equivalence ratio  $\Phi=0.5$  are first considered numerically, taking into account the presence of a varying percentage of excited oxygen in the initial mixture. Pressure levels of 0.1, 0.5 and 1 atm are considered, with an initial temperature range  $1000 < T < 2000$  K. For all upcoming figures, up to 5 % of excited oxygen is considered in the initial mixture. This amount corresponds typically to the maximum amount of excited  $O_2$  that can be achieved experimentally today as documented in the literature [58].

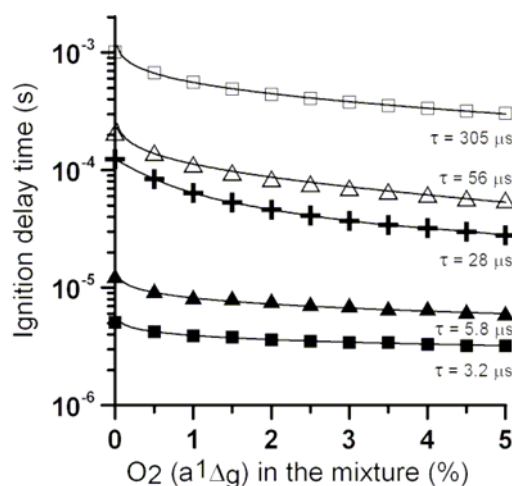


*Fig.III.15. Influence of excited oxygen on ignition delay time of a  $H_2:O_2:N_2$  mixture for  $\Phi=0.5$ , at a pressure of 0:1 ( $\square$ ), 0:5 ( $\Delta$ ) and 1 atm (+) and at an initial temperature of 1000 K. Also at  $P=1$  atm for an initial temperature of 1000 (+), 1500 ( $\blacktriangle$ ) and 2000 K ( $\blacksquare$ ). The ignition delay corresponds to reaching 50% of peak OH concentration.*

The ignition time decreases rapidly when adding even a small amount of excited oxygen into the initial mixture (Fig. III.15, note the log scale on the y-axis). The magnitude of this effect depends on initial pressure and temperature. At atmospheric pressure and high initial temperature ( $T=2000$  K), there is already a factor 1.6 speedup between a pure thermal ignition (no excited species) and a case with 5 % of  $O_2^*$ . This factor increases in a monotonous way when decreasing initial temperatures and reaches a factor of 4.5 for an initial temperature of 1000 K (Fig.III.15). Regarding pressure, the reduction of the ignition delay decreases in a monotonous way when decreasing pressure, still amounting to a factor 3.3 at 0.1 atm and 1000 K. Also, excitation of  $O_2$  molecules significantly decreases the self-ignition temperature. At atmospheric pressure with no excitation, the computations lead to an ignition temperature threshold of 860 K. It is decreased by 50 K and 170 K when using 1% and 5% of  $O_2^*$  respectively in the initial mixture.

### III.2.4.2. Influence of $O_2^*$ on laminar flame speed

The influence of exciting  $O_2$  molecules on the  $a^1\Delta_g$  state in a subsonic flow of a diluted  $H_2-O_2$  mixture is now considered. Corresponding simulations rely on the freely propagating flame module of CHEMKIN [178].

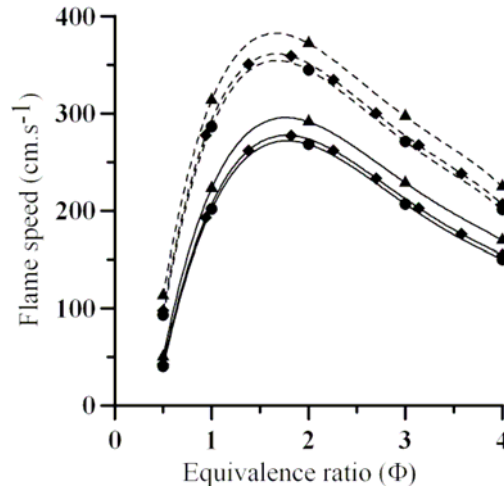


Fig.III.16. Influence of excited oxygen ( $\bullet$ : 0%,  $\blacklozenge$ : 1%,  $\blacktriangle$ : 5%) on flame speed as a function of the equivalence ratio. Solid lines:  $O_2:N_2=1:3.76$  at 1 atm and  $T=298$  K. Dashed lines:  $O_2:Ar=1:3.76$  at 1 atm and  $T=298$  K.

One can observe from Fig.III.16 that the maximum laminar flame speed increases by up to 15% when adding excited oxygen into the fresh gas mixture. This increase is observed at all equivalence ratios but is particularly visible for rich flames. As observed previously without excitation, argon dilution systematically leads to a higher flame speed.

Singlet oxygen has a higher energy than ground-state oxygen and all its electron spins are paired, so that it is much more reactive towards common organic molecules. For example, hydrogen will very effectively absorb energy from singlet oxygen and convert it back into the unexcited ground state. Considering further values of the initial  $O_2^*$  percentage, also above the experimentally achieved limit of 5% one finds an exponential increase of the laminar flame speed with the  $O_2^*$  percentage (see later Fig.III.22). This demonstrates the possibility of intensifying considerably the combustion (characterized here by the laminar flame speed) when feeding a burner with excited molecular oxygen, as later performed in experiments.

### III.2.4.3. Influence of $O_2^*$ on laminar premixed flame structure

The next investigation concerns possible modifications of the laminar flame structure when using excited oxygen in the gas mixture. The variations of the species mole fractions as well as temperature and heat release along the axial direction are compared with or without excited species in the initial mixture for a one-dimensional, laminar premixed flame. Since it is impossible to show results for all possible conditions, the presentation of the results is restricted to an equivalence ratio of  $\Phi=0.5$  (lean flame),  $\Phi=1$  (stoichiometry) and  $\Phi=2$  (rich flame).

The mole fraction profiles of reactants, non-excited intermediates (H, O, OH), excited intermediates ( $O^*$ ,  $OH^*$ ,  $O_2^*$ ), temperature and heat release are plotted in what follows. Figure III.17 shows the comparison of the ground state and excited H, O and OH concentration profiles in the presence of excited molecular oxygen in the fresh gas mixture with those obtained without excited species. As previously, up to 5% of the total  $O_2$  mole fraction is considered to be excited initially. The computed profiles for H show globally a similar profile with or without excited species, but with a large increase in maximum concentration (+23.5%). Similar considerations hold for the O and OH radicals (+18% and +12.4% increases in maximum concentration respectively).

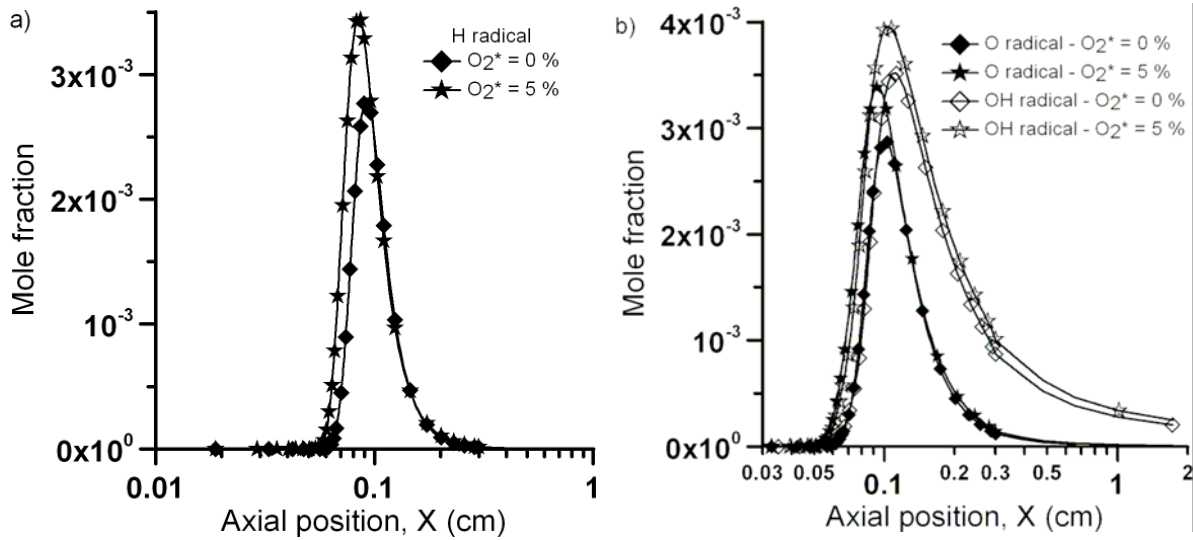


Fig.III.17. Computed a) H, b) O and OH radical profiles in a  $H_2$ -Air mixture at  $\Phi=0.5$ ,  $P=1$  atm and  $T=298$  K.

As confirmed by the next figures, one can observe that when increasing the percentage of  $O_2^*$  in the initial mixture, the width of the flame and of all radical species profile increase considerably. The slope of the gradients on the fresh gas side (left) becomes steeper. Simultaneously, the peak radical concentration values increase, typically by 12 up to 28%. Due to these very noticeable modifications of the laminar flame structure, optical diagnostics should be able to detect the influence of excited species on the flame structure [206]. These structural modifications show that electronically excited oxygen in metastable singlet state can accelerate formation of chemically active atoms O, H and radical OH due to a reduction in the activation barrier of endoenergetic reactions. This leads indirectly to an intensification of the chain branching mechanism of hydrogen oxidation, explaining the observed reduced ignition delays and auto-ignition temperatures.

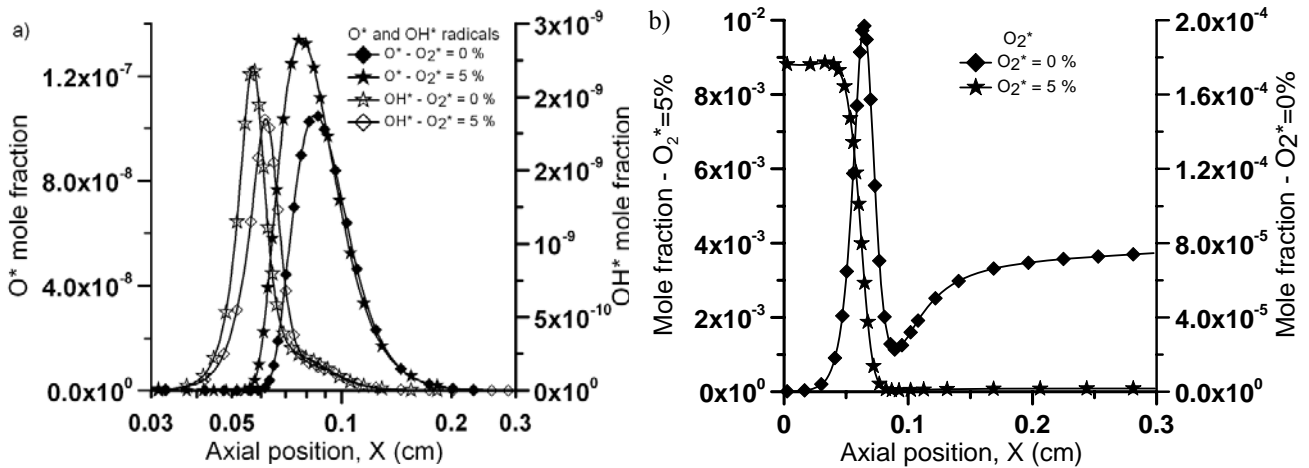


Fig.III.18. Computed a)  $OH^*$ ,  $O^*$  and b)  $O_2^*$  profiles in an  $H_2$ -Air mixture at  $\Phi=0.5$ ,  $P=1$  atm and  $T=298$  K.

Concerning the excited  $OH^*$  radical (Fig.III.18a), adding excited oxygen leads to a considerable thickening of the active reaction zone. Nevertheless, it must be kept in mind that the associated values are very small (peak mole fraction below  $3 \cdot 10^{-9}$ ). One can again observe a steeper slope and higher maximal concentration when increasing the  $O_2^*$  percentage in the initial mixture, while the peak moves further into the fresh gases. When increasing further the  $O_2^*$  percentage above 5%, a bimodal structure appears for  $OH^*$  with a large peak on the fresh gas side and a secondary,

lower peak on the burnt gas side (not shown here, but later Fig.III.21b). Such a bimodal structure is also observed at high  $O_2^*$  concentrations for O and OH.

The bimodal structures observed for some species in premixed flames are usually traced back to two separate chemical pathways, one at low, one at high temperatures. Here, a first fast rise in the  $OH^*$  radical can be observed. It is situated in a low temperature zone of the flame front ( $\sim 600$  K). The second maximum is situated in the high temperature zone ( $\sim 1200$  K). It was shown that reactions  $H_2 + HO_2 = H_2O + OH^*$  and  $O^* + H + M = OH^* + M$  are the main contribution in production of the electronically-excited radicals  $OH(^2\Sigma^+)$  [185]. Similar modifications are observed for the excited oxygen  $O^*$ , but only a single peak is always observed for this species. More complex is of course the evolution of the  $O_2^*$  profile itself (Fig.III.18b) since it is modified due to the varying fresh gas composition (left side). The mole fraction appears to be roughly constant over the first 0.5 mm of the computation. Afterwards, the peak value increases with the excitation level (note the two different y-scales for the two conditions).

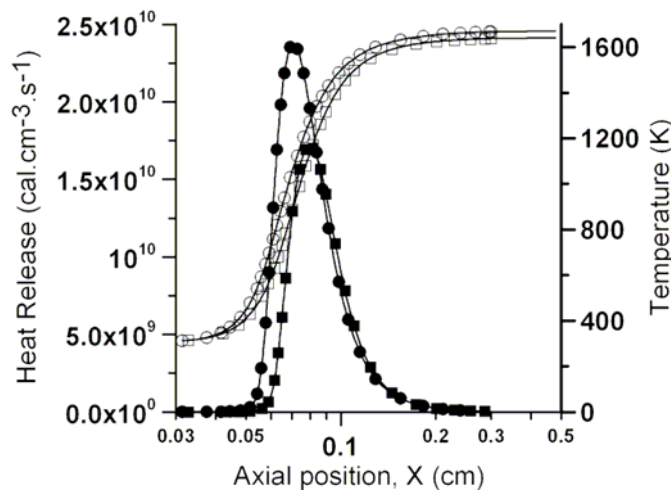
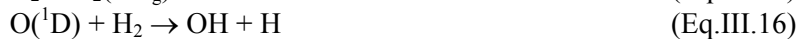


Fig.III.19. Computed heat release (filled symbols) and temperature (empty symbols) profiles in an  $H_2$ -Air mixture at  $\Phi = 0.5$ ,  $P = 1$  atm and  $T = 298$  K. Influence of  $O_2^*$  (square: 0 %, circle: 5 %) mole fraction in the fresh gas mixture.

The modification of the heat release due to the presence of  $O_2^*$  is presented in Fig.III.19. The peak value is increased by 38.4% when adding 5% excited oxygen in the fresh gases. Simultaneously, the profile becomes steeper on the fresh gas side and the reaction zone is again thicker. Coupled with the increase of heat release a relatively slight temperature increase (8%) is observed. These modifications corroborate the previously observed reduction of the ignition delays and result from the intensification of the chain reactions in the  $H_2$ - $O_2$  oxidation process, owing to the presence of electronically excited oxygen molecules in the initial flow. Hydrogen oxidation relies on chain reactions with the formation of intermediate active species, in particular H, O, and OH around  $T \sim 1000$  K. The principal source of these species is the following ramification reaction :



When considering oxygen excitation, new pathways of the chain can appear, in particular :



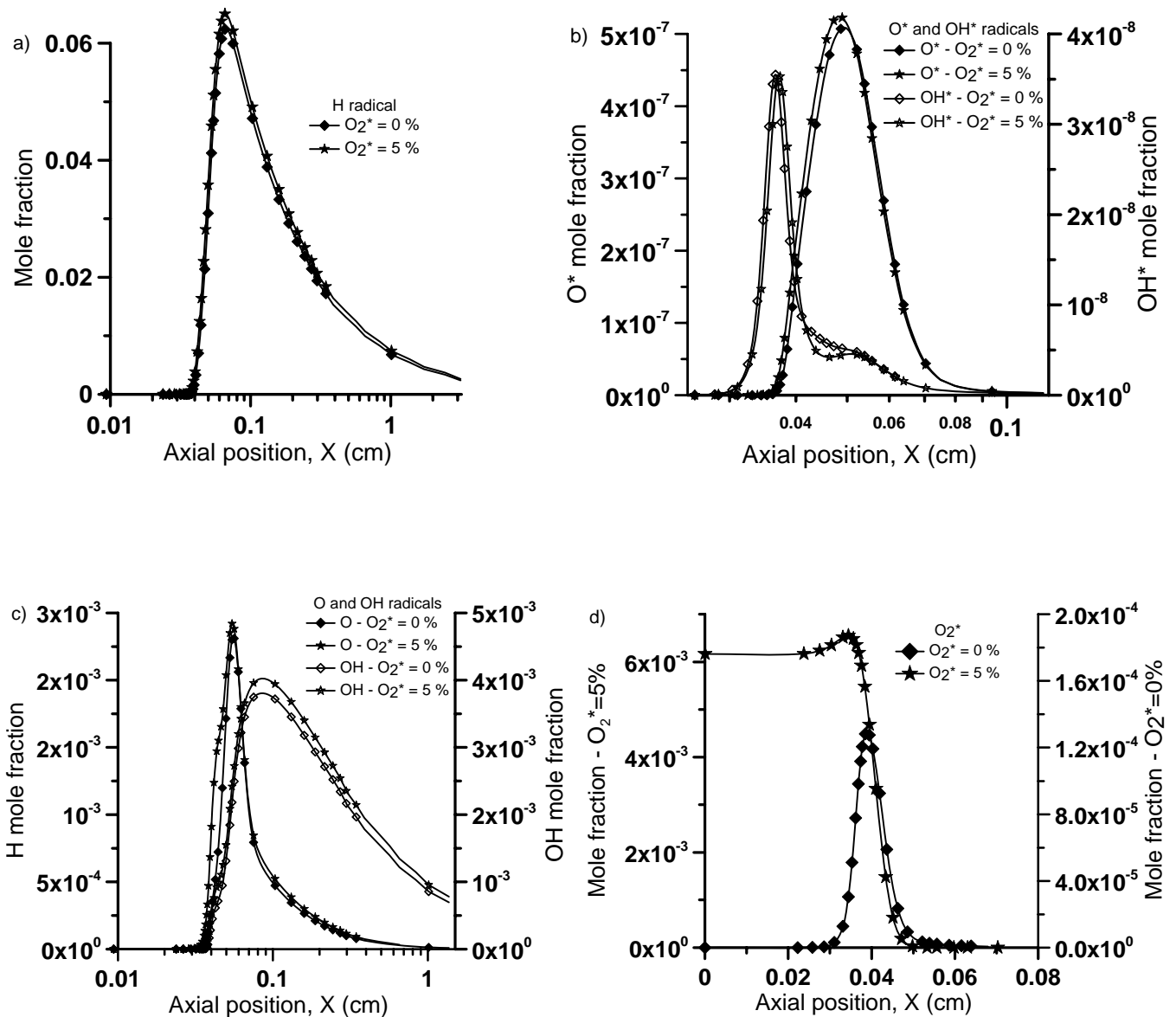
thus favoring additional formation of OH, O, and H species, essential for initiation of hydrogen-oxygen combustion [200].

Using a nonthermal plasma in a gas mixture containing  $O_2$  and a diluent, it is possible to generate active species by the excitation and dissociation of  $O_2$  by electronic impact, and thus to reduce the energy threshold of chemical reactions. The resulting production of additional active centers leads to the acceleration of the chemical kinetic process. This explains the increase in flame speed, the reduction of ignition delays and auto-ignition temperatures. As a consequence electronically excited  $O_2^*$  appears to be a very efficient way to promote hydrogen oxidation.

### III.2.4.4. Influence of $O_2^*$ on laminar premixed flame structure at other equivalence ratios

#### III.2.4.4.1. Equivalence ratio $\Phi = 2$

As previously, up to 5% of the total  $O_2$  mole fraction is excited initially. The computed profiles for this rich flame are shown in Figs.III.20.



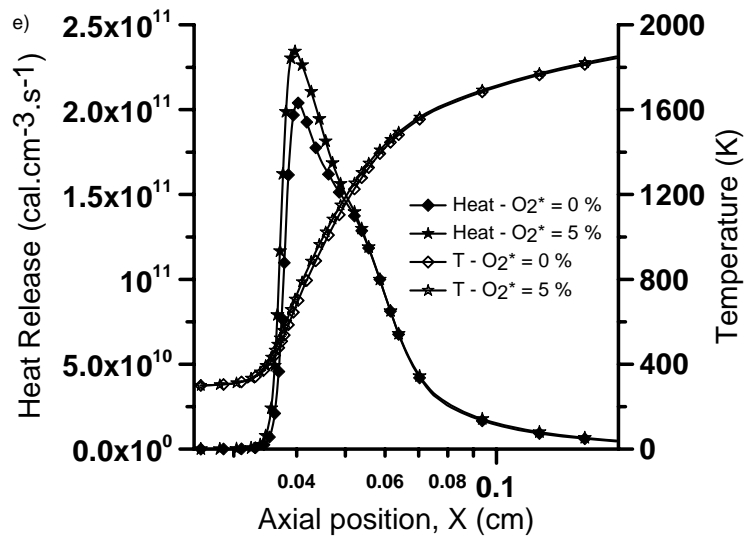


Fig.III.20. Computed a) H, b) OH\*, O\*, c) O, OH, d) O<sub>2</sub>\* profiles and e) computed heat release and temperature profiles in an H<sub>2</sub>-Air mixture at  $\Phi=2$ ,  $P=1$  atm and  $T=298$  K. Influence of O<sub>2</sub>\* (diamond : 0 %, star : 5 %) mole fraction in the fresh gas mixture.

The computed profiles for H show globally a similar profile with or without excited species, with only slight modifications (maximum 8% increase for the H radical). Globally, one can observe that when increasing the percentage of O<sub>2</sub>\* in the mixture, the flame width increases. The slope on the fresh gas side becomes steeper. Simultaneously, the maximum values increase. A similar tendency is observed for the O and OH profiles.

Concerning the excited OH\* radical, the model predicts a bimodal distribution for almost all conditions. One can observe a steeper slope and higher maximal concentrations for both peaks when increasing the O<sub>2</sub>\* percentage in the initial mixture, while the first peak moves further into the fresh gases. As for the other radical profiles the global width is increased when increasing O<sub>2</sub>\* mole fraction. Thus, using some amount of excited oxygen clearly leads to a wider flame.

Similar results are observed for the excited oxygen O\*, but only a single peak is always observed for this species. The mole fraction of O<sub>2</sub>\* appears to be constant over the first 2-3 millimetres of the computation. Afterwards, the peak value increases of course when increasing the excitation level and the profile becomes simultaneously steeper.

The modification of the heat release due to the presence of O<sub>2</sub>\* is also presented in fig.III.20. The peak value is increased by a factor exceeding 15% when adding 5% excited oxygen in the fresh gases. Simultaneously, the profile becomes steeper and the flame is thicker. The increase of heat release is associated to a slight (up to 5%) temperature increase.

### III.2.4.4.2. Equivalence ratio $\Phi = 1$

Flame structure calculations of a stoichiometric H<sub>2</sub>/air flame are presented in figs.III.21. Globally, one can observe that when increasing the percentage of O<sub>2</sub>\* in the mixture, the flame modifications are similar to that previously described for other equivalence ratios, but even more pronounced (steeper slope on the fresh gas side, much higher peak concentrations and wider flame).

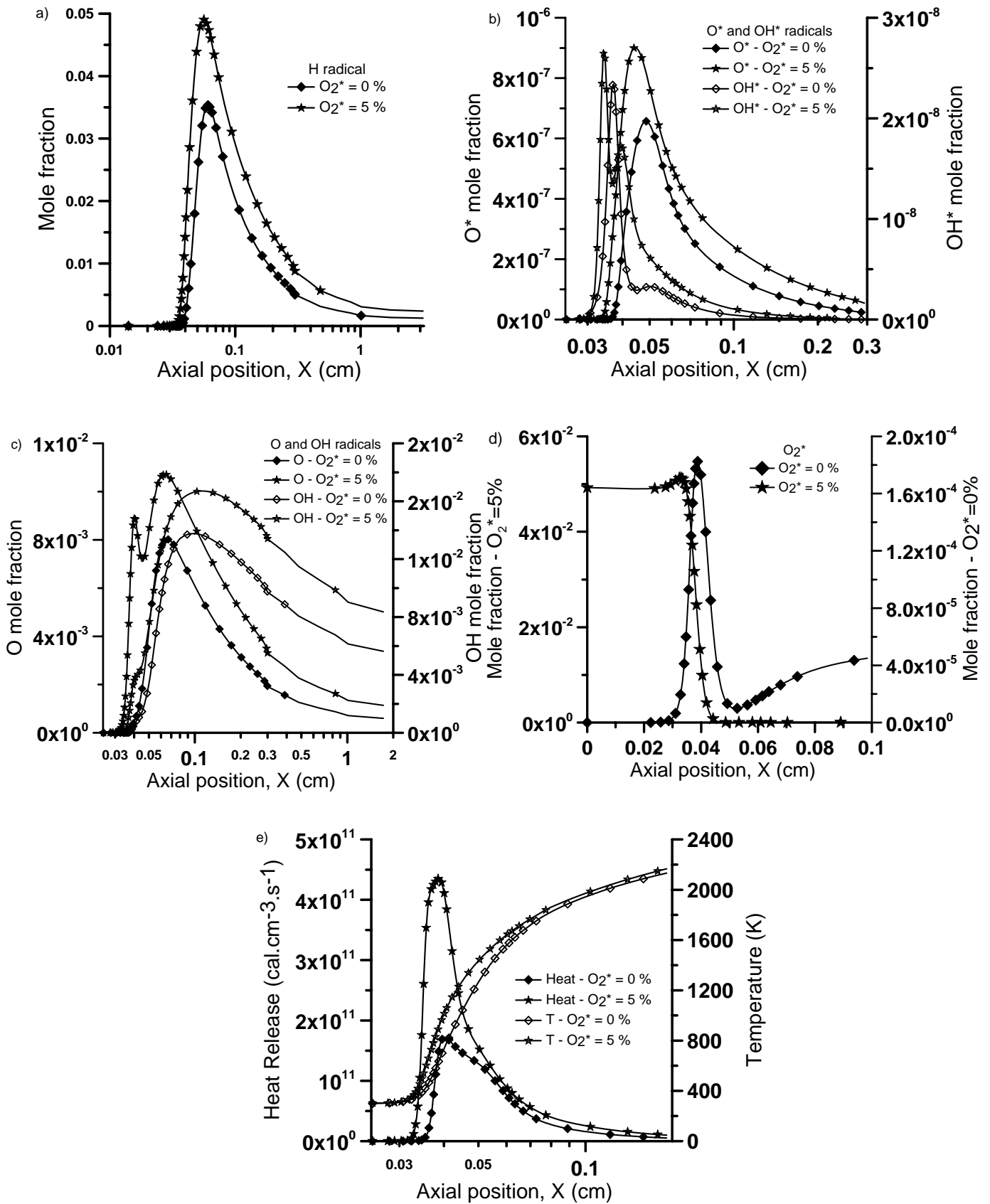


Fig.III.21. Computed a) H, b)  $OH^*$ ,  $O^*$ , c) O, OH, d)  $O_2^*$  profiles and e) computed heat release and temperature profiles in an  $H_2$ -Air mixture at  $\Phi=1$ ,  $P=1$  atm and  $T=298$  K. Influence of  $O_2^*$  (rhombus: 0%, star: 5%) mole fraction in the fresh gas mixture.

A bimodal distribution is observed for OH and OH\* radicals (and also to some extent for O), with a first, very high peak appearing progressively on the fresh gas side. Concerning the excited OH\* radical, the model predicts a bimodal distribution (fig.III.21b) for almost all conditions. This observation, for OH and OH\*, supports the observed reduction of the ignition delays. Nevertheless, it must be kept in mind that the associated values are very small (peak mole fraction below  $3 \cdot 10^{-8}$ ). Finally, the heat release is more than doubled when injecting 5% excited oxygen.

### III.2.4.5. Influence of a high percentage of O<sub>2</sub>\* on laminar premixed flame

As explained before, for all figures presented up to now, up to 5% of excited oxygen has been considered in the initial mixture, a value corresponding to known experiments. In Fig.III.22, we investigate what would be the effect of a much higher quantity of excited oxygen, in case this could be realized in the future.

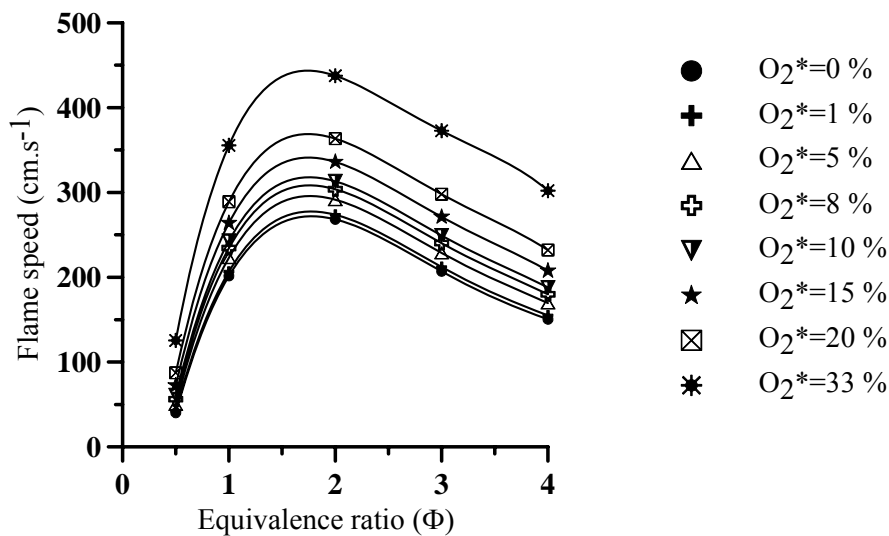


Fig.III.22. Influence of excited oxygen (up to 33 %) on laminar flame speed as a function of the equivalence ratio for an O<sub>2</sub>:N<sub>2</sub>= 1:3.76 mixture at 1 atm and T= 298 K.

The laminar flame speed is strongly increased under the action of oxygen excitation. There is a difference by a factor 1.5 in flame speed between a "non excited" (O<sub>2</sub>\*=0%) and an "excited" (O<sub>2</sub>\*=33%) initial mixture. It is worth noting that this difference increases in an exponential way with the O<sub>2</sub>\* percentage for Φ= 1. This increase is observed to be similar at other equivalence ratios (not shown).

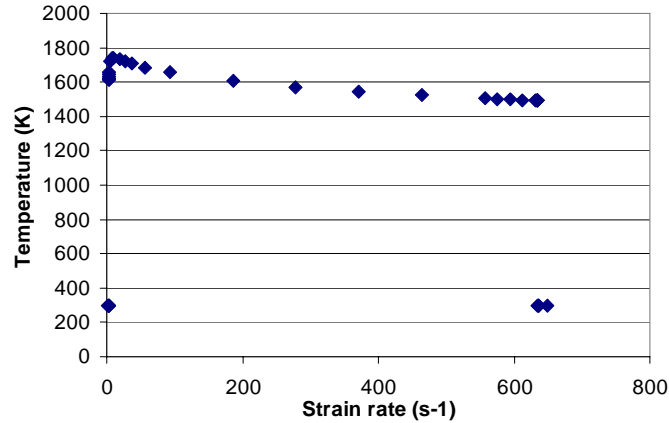
### III.2.4.6. Influence of O<sub>2</sub>\* on laminar non-premixed counterflow flame structure

The extinction limit of counterflow diffusion flames of diluted hydrogen and air is now investigated using the opposed-flow flame module of CHEMKIN [178]. The equal injection velocities of fuel and oxidizer are increased gradually (by 0.1 mm/s), while keeping all other parameters fixed. The fuel stream is composed of 2.5% H<sub>2</sub> and 97.5% N<sub>2</sub> (by mass), the oxidizer being air. The distance between the two burner exits is 2 cm. A direct approach was employed to obtain extinction strain rates for a given mixture, by slowly increasing the fuel and oxidizer exit velocities until the solver delivers a nonburning solution. The velocity at which the flame first extinguishes is converted to an extinction strain rate  $\epsilon_e$  using the expression proposed by Seshadri and Williams [208] :

$$\epsilon = (2 \cdot V / d) \times \sqrt{\rho_f / \rho_o} \quad (\text{Eq.III.17})$$

where  $V$  is the velocity of the fuel and oxidizer flows,  $d$  is the separation distance,  $\rho_f$  is the density of the diluted fuel and  $\rho_o$  is the oxidizer density.

The following figure shows the extinction curve for a diluted  $H_2$  (mass fraction of  $H_2$  in  $N_2$  is 2.5 %) counter-flow diffusion flame. The relation between maximum flame temperature and strain rate shows a typical curve :



*Figs.III.23. Maximum flame temperature of  $H_2/N_2$  : Air counter-flow diffusion flame as a function of strain rate.*

When the strain rate is large, the maximum flame temperature decreases with an increase of the strain rate. In addition, when the strain rate is small, the maximum flame temperature decreases with the decrease of the strain rate. By following both directions, strain extinction limit induced by strain (i.e. upper limit) and low extinction limit induced by radiative heat loss are defined. In the present simulations, one can observe that the flame can be ignited in a wide range of global strain rates, varying from 1.54 to 635.3 s<sup>-1</sup>. Experimentally, the low limit strain rate should be at higher values, due to destabilization of the flames by buoyancy effects.

The effect of excited oxygen on extinction curves for diluted hydrogen flames can be found in Fig.III.24, showing the relation between maximum flame temperature (K) and strain rate  $\epsilon$  obtained in the simulation.

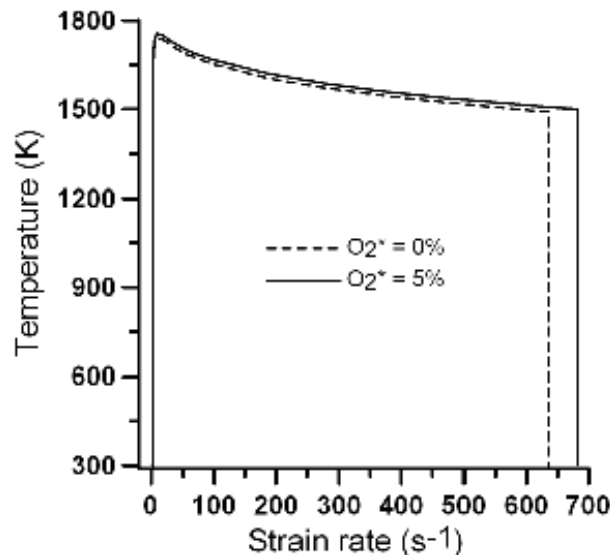


*Fig.III.24. Maximum flame temperature of a  $H_2/N_2$  : Air counterflow diffusion flame as a function of strain rate in s<sup>-1</sup>.*

Figure III.24 shows that the flame can sustain a maximum strain rate of 635 s<sup>-1</sup> without any excitation. The addition of electronically excited oxygen allows stable flames to be obtained at

considerably higher strain-rates. When considering 5% of excited oxygen in the oxidizer mixture, as previously, the extinction strain rate  $\varepsilon_e$  is increased by 7%. The critical injection velocity moves from 342 cm/s to 368 cm/s. The introduction of excited oxygen does not noticeably increase the flame temperature for stable burning conditions. The maximum difference remains below 15 K. Calculations demonstrating modifications of the non-premixed flame structure have also been performed but will not be shown here.

### III.2.4.7. Counter-flow methane diffusion flame modelling

Numerical computations of a counterflow methane diffusion flame have also been performed without excited species using the same approach, in order to investigate an experiment described later. Results focussed mainly on OH, CH and temperature profiles, as presented in Fig.III.25.

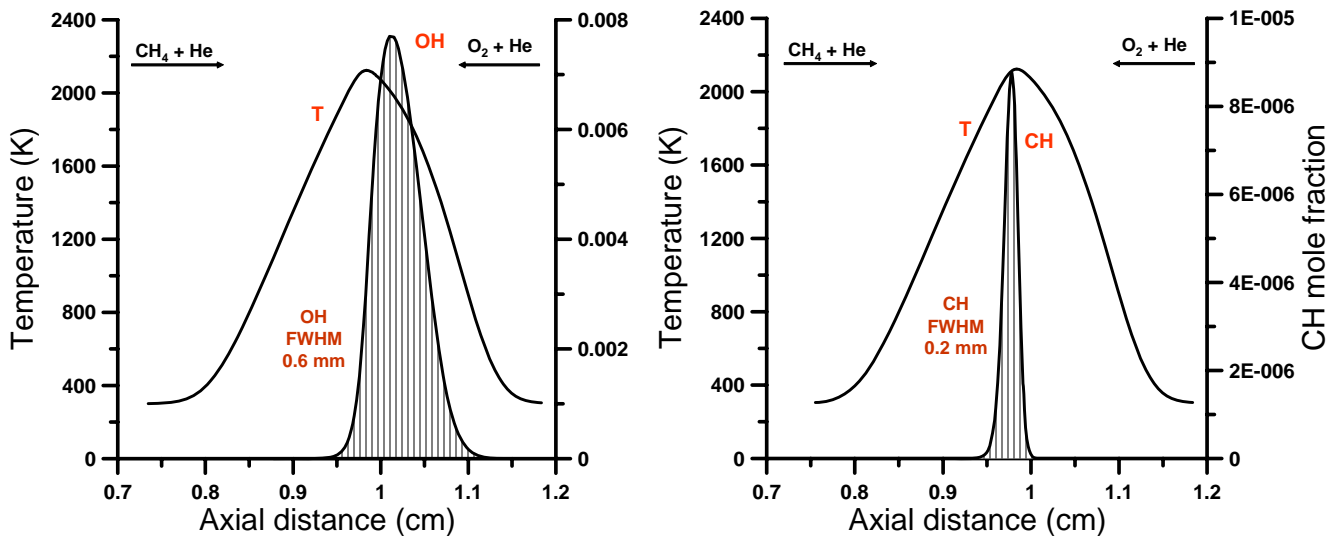


Fig.III.25. Counterflow flame structure for  $CH_4/He$  ( $=35/65$ ) –  $O_2/He$  ( $=21/79$ ) and strain rate  $\varepsilon = 200 s^{-1}$ .

The numerical modelling of this flame ( $\Phi = 4.5$ ,  $\varepsilon = 200 s^{-1}$ ), allows to observe that the OH concentration profile is approximately three times wider than that of CH (0.6 mm FWHM and 0.2 mm FWHM respectively). Thus, it appears that the temperature does not significantly vary through the CH zone and is almost equal to the peak temperature. Therefore, one can consider that the temperature is constant in the CH region and can be described by a “single” temperature. In further experimental study of counter flow configuration flame, these results will allow us to use CH emission spectra to determine the flame temperature.

Experimental determination of the rotational temperature is performed by two bands belonging to  $CH^*$  molecule emission spectra. Fig.III.26 shows a comparison between experimental and simulated  $CH^*$  emission spectra (LIFBASE<sup>®</sup> [209]) (related experiments will be described in chapter V).

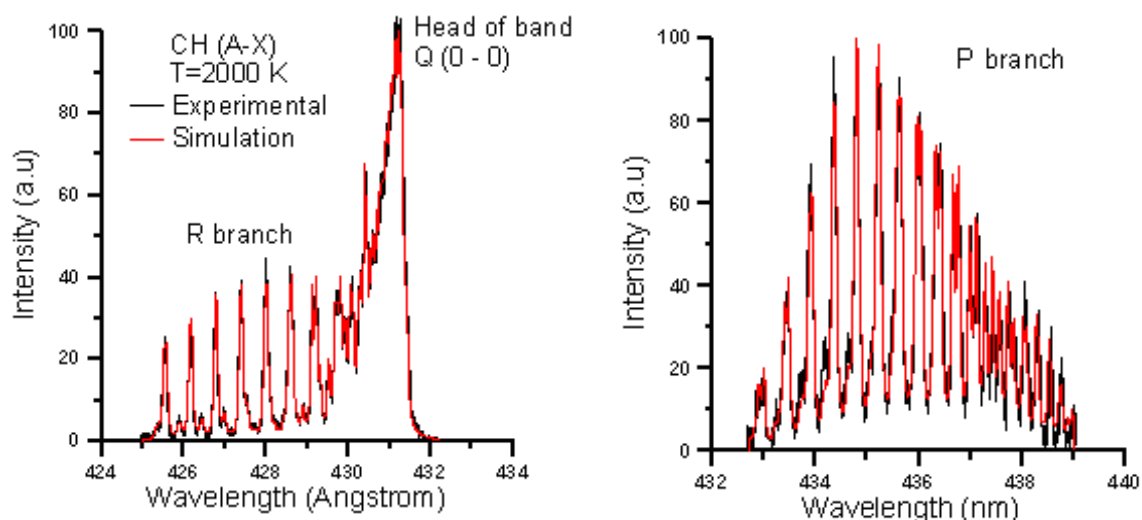


Fig.III.26. Comparison between experimental (black) and simulated (red) spontaneous emission spectra of (left):  $A^2\Delta - X^2\Pi$  transition of R-branch CH radical and (right): P-branch. Both in a counter flow diffusion flame ( $CH_4$ ) / ( $O_2+He$ ).

Temperature determination was performed as a result of an excellent fit between experimental and simulated spectra, for both branches and transitions considered ( $B^2\Sigma^- - X^2\Pi$ ) and ( $A^2\Delta - X^2\Pi$ ). A temperature of  $2000\text{ K} \pm 50\text{ K}$  was obtained. This value seems reasonable for this flame, giving us confidence that the temperature can indeed be quantified in this manner.

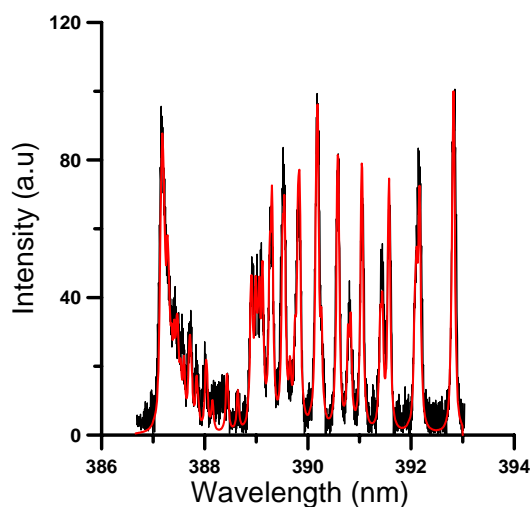


Fig.III.27. Comparison between experimental (black) and simulated (red) spontaneous emission spectra of  $B^2\Sigma^- - X^2\Pi$  transition of CH radical in a counter flow diffusion flame ( $CH_4$ ) / ( $O_2+He$ ).

### III.2.5. Conclusions on plasma-assisted combustion modelling

The combustion of diluted hydrogen plays a prominent role in fundamental research as well as in a variety of applications, from fire safety to energy conversion and propulsion. The present numerical study supports the interest of our later experimental work. Flame structures and properties obtained when burning excited oxygen have been investigated numerically. The laminar flame speed, the auto-ignition delay and the evolution of radicals and flame parameters have been determined from simulations relying on a complete reaction scheme. The kinetic mechanism has been first validated by simulating the combustion of diluted H<sub>2</sub>-O<sub>2</sub> mixtures without excited species, before investigating the influence of electronically excited species. The ignition and combustion of diluted hydrogen-oxygen mixtures containing up to 5% of electronically excited oxygen O<sub>2</sub>\* have been calculated. It is found that preliminary oxidizer excitation substantially enhances combustion intensity and thus flame speed, while reducing ignition delay and increasing flame thickness. The excitation of oxygen molecules to the a<sup>1</sup>Δ<sub>g</sub> and b<sup>1</sup>Σ<sub>g</sub><sup>+</sup> states with vibrational quantum number v' = 0 results in a significant promotion of the formation of highly reactive atoms O, H as well as OH radicals. The corresponding effect increases when increasing the percentage of excited oxygen. This can be explained by an intensification of chain reactions in the H<sub>2</sub>-O<sub>2</sub> mixture. Finally, the global extinction strain rate of H<sub>2</sub>-air counterflow diffusion flames increases when the percentage of electronically excited molecular oxygen in the initial oxidizer mixture is increased.

The last chapters of the manuscript will present experimental work concerning the generation of excited oxygen and plasma-assisted combustion experiments at atmospheric and reduced pressures.

### III.2.6. Further remarks

Mainly due to safety issues the flames investigated later burn methane and not hydrogen. Unfortunately, there is at present no information available in the literature concerning reaction rates involving methane oxidation with excited species. It is therefore impossible to carry out computations similar to those described in III.2 for methane flames. As a consequence, it will be unfortunately impossible to compare quantitatively the simulations of section III.2 (hydrogen flames) with the experiments of chapter V (methane flames). Qualitative evolutions may be compared.

During this Ph.D work, a coupled simulation of the plasma and of the reacting flow in the flame has been attempted using the commercial multi-physics software COMSOL<sup>®</sup>. In spite of first promising results, it was finally impossible to get a converged solution due to huge computer memory requirements. The available PC with 2 Gigabytes of RAM was insufficient for that purpose. As a consequence, no results are shown.

Both issues open clear perspectives for future studies.



# Chapter IV : Experimental generation of electronically excited oxygen species

## Abstract

---

Nonequilibrium plasmas, which have a relatively high electron temperature and low gas temperature, have many attractive characteristics. Energetic electrons produce excited species, free radicals, and ions as well as additional electrons through electron-impact dissociation, excitation, and ionization of background gas molecules [22, 210]. The present experimental chapter provides a method of converting a portion of the triplet oxygen molecules into singlet oxygen molecules, which are expected to induce combustion intensification. Among different possible techniques, electrical discharges are retained for exciting triplet oxygen to singlet oxygen. The previously described plasma modelling of energy input in the discharge allows making important decisions on plasma reactor optimization for generation of electronically excited oxygen species.

In a first part, the experimental study of diluted oxygen plasma, generated by a pulsed dielectric barrier discharge is presented. A second part will focus on the crossed discharge reactor. After a detailed description of the different developed experimental facilities, the spectroscopic study of the generated plasma is presented at atmospheric and reduced pressure. Measurements of visible emission spectra in the discharge region show the different species evolution when varying several experimental parameters (discharge power, pulse repetition rate, O<sub>2</sub> fraction in the flow). Results using low (5 Å) and high resolution (0.3 Å) spectrometers are shown. Finally, rotational temperatures deduced from these spectra are determined.

---

## IV.1. Pulse dielectric barrier discharge (DBD) plasma facility

### IV.1.1. Introduction and characteristics

A discharge that occurs in an electrode system under the condition that at least one electrode is covered by dielectric material, is called a dielectric barrier discharge (DBD) [210]. Sometimes it is referred to as either a silent discharge, since it operates noiselessly [162], or a corona discharge with dielectric [162] according to the physics of the process.

Some of the drawbacks of the DBDs are their relatively low electron energies and densities, which limit their use in several applications that require a richer chemical environment. Amongst these is plasma-assisted combustion. So, a mean by which a control over chemistry is possible concerns the application of short high voltage pulses [211]. Indeed, increasing the electron number density and their energy translates to an increase in the production of reactive species. To achieve this increase of ionization and to extend the electron energy distribution to higher values, short high voltage pulses are used. Using short duration pulses has the added advantage of keeping a low average power and does not substantially increase the gas temperature. Limiting the gas temperature is an important asset as elevated temperature and temperature gradients can be at the origin of instabilities that makes the discharge unstable (i.e. unsteady diffuse regime).

Moreover, it is particularly difficult to create non thermal plasma in molecular gases containing substantial concentrations of oxygen, even with non-self-sustained techniques. This is due to the rapid removal of the free electrons by their attachment to oxygen. To maintain conductivity, the ionizer source power requirement can be very large indeed. However, nonequilibrium excitation methods can be used to reduce oxygen attachment [212]. Therefore, to maintain any level of ionization, a high voltage electric field can be repetitively pulsed [41, 217].

## IV.1.2. AC against pulse power supply

Use of high voltage pulsed power supply for generation of the barrier discharge preionization can be explained qualitatively considering the basic parameters of a barrier discharge. Let us consider two quantities:  $\tau_s$ , a lifetime of an isolated streamer; and  $U_b$ , a breakdown voltage. The time  $\tau_s$  is determined by the electron kinetics and it is of the order of 10 ns (depending on pulse duration). Exception made for streamer breakdown mechanism, the breakdown voltage  $U_b$  depends mainly on gas mixture properties and distance between the electrodes (in accordance with Paschen law [213]). However, it also depends on electrode surface properties, the residual ionization degree in the gas between pulses and other parameters that are defined by the discharge regime. The main difficulty to achieve homogeneous barrier discharge while using classical sinusoidal power-supply is linked to the slow voltage growth rate. In order to increase the number of filaments (or quasi-homogeneous discharge) using a sinusoidal power supply, the homogeneity of emission properties of electrode surfaces has to be increased and a power supply should enable charge  $Q$  transfer during time  $\tau_s$  [214]. These conditions cannot be easily fulfilled. These problems are, however, resolved for pulse generators with steep voltage front e.g. often in the order of  $\sim 1$  ns. The fast voltage growth, when compared to  $\tau_s$  and a capacity to generate the required charge within this time, are extremely important for such pulsed power supply. Both mentioned characteristics of pulsed power supply are mutually related, i.e. when the required charge is not provided, the voltage will not grow fast enough. Moreover, fast voltage growth with amplitudes much higher than  $U_b$  creates conditions for streamers. The application of sinusoidal power supply instead of pulsed power supply with steep front (rise and fall front) results in completely different plasma-chemical evolution, especially, in the region of low voltage  $U < U_b$ . In the case of sinusoidal power supply, the charged particles decay not only due to recombination but also due to drift in slowly decreasing and later increasing field. As a result, shortly before voltage reaches again the threshold value  $U_b$ , residual ionization degree of a gas-medium is low. In pulsed excitation regime, voltage drops “immediately” to zero and plasma decay is only due to recombination [41]. This means that charge decay is significantly slower than in the sinusoidal power supply case, the residual ionization being higher. In the case of pulsed power supply, voltage and frequency can be varied independently and lead to power growth. For these reasons we have chosen to work with a pulsed power supply for our application.

At last but not least, one main advantage of pulse power is its low average energy consumption, making this solution economically more viable.

## IV.1.3. Experimental set-up for the pulsed dielectric barrier discharge

As a rule, a dielectric barrier discharge can be generated in either a plane-to-plane or a coaxial geometry where one or both electrodes are covered with dielectric. Within this study, a new plasma facility has been developed, which is specifically designed for excited oxygen production. The geometry of the DBD is composed of two parallel electrodes, both covered by a dielectric alumina ceramic ( $\text{Al}_2\text{O}_3$ ). The dielectric layer above each electrode plays the role of capacities in series with the gas discharge gap. The gap in which the plasma is produced is typically varied from 4 to 10 mm wide. The design of our plasma chemical reactor using DBD is given in Fig.IV.1.

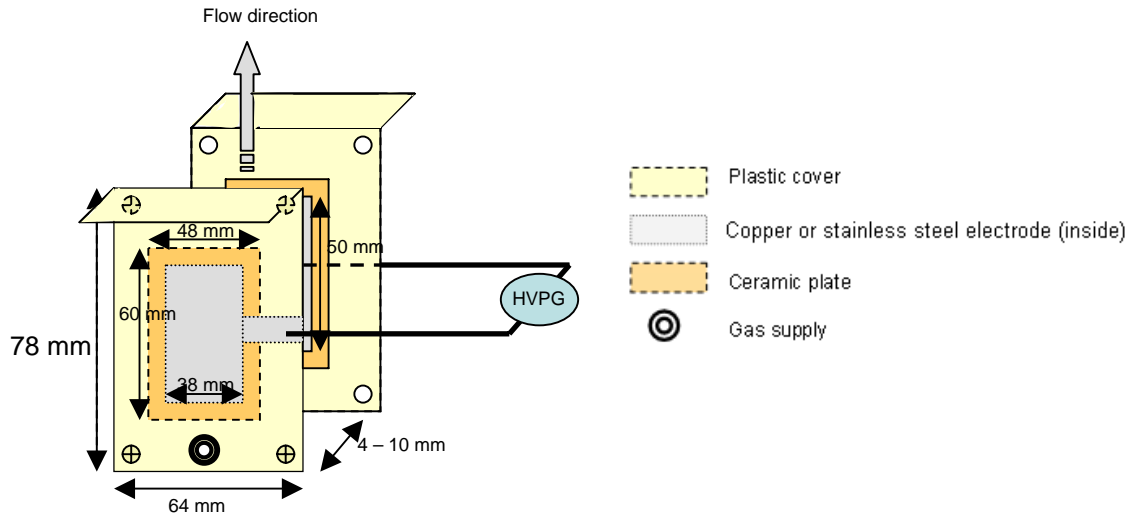


Fig.IV.1. Pulsed dielectric barrier discharge in plane/plane configuration.

The dimensions of the ceramic plates ( $\text{Al}_2\text{O}_3$ , with a dielectric permittivity of 9) are :  $60 \times 48 \times 1 \text{ mm}^3$ ; that of the copper or stainless steel electrodes are :  $\sim 50 \times 38 \times 0.5 \text{ mm}^3$ .

Initiation of the discharge with an abrupt slope of voltage (about  $1 \text{ kV/ns}$ ) at intermediate gas densities is of great interest. Modern high voltage generators (pulse amplitudes of tens and hundreds of kV, voltage rise time of units and tens of ns, pulse durations of tens and hundreds of ns and repetitive frequencies up to tens of kHz) make it possible to create a spatially uniform discharge, up to gas densities of  $(6 - 8) \times 10^{12} \text{ m}^{-3}$  [1]. A new generation of high voltage pulse generator (i.e. using magnetic compression of pulses) is used. The power supply used within the experimental study is described in Appendix 6.

The electrodes are connected to the pulsed power supply, which allows one to vary the input voltage from 0 to 20 kV and the frequency,  $f$ , up to 100 kHz.

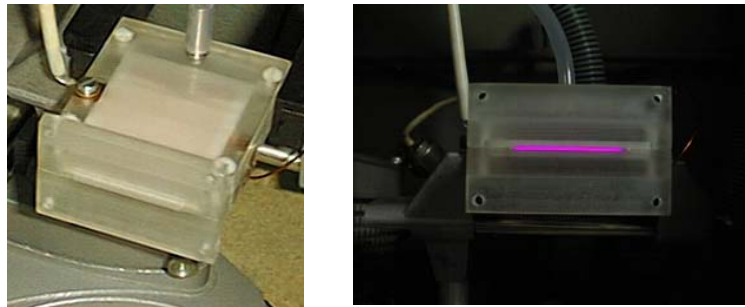


Fig.IV.2. Discharge cell for a dielectric barrier discharge – two copper electrodes covered by  $\text{Al}_2\text{O}_3$  plates. (Left) : Plasma off and (Right) : Plasma in air at atmospheric pressure.

Figures IV.2 show the discharge cell made of Plexiglas and integrating the barrier electrodes. The first investigations performed on electrical discharges in air and binary mixtures of  $\text{O}_2/\text{Ar}$  and  $\text{O}_2/\text{He}$  concerned pulsed dielectric barrier discharges.

For our experimental objectives, this type of discharge gives a priori several important advantages, particularly the fact that the volume occupied by the discharge DBD can be made compatible with the section of a burner slot.

The discharge will be characterized by emission spectroscopy and electrical measurements. In our experimental configuration ( $\text{He}/\text{O}_2$  binary mixture), this discharge is a homogeneous one in the sense that no filaments are observed.

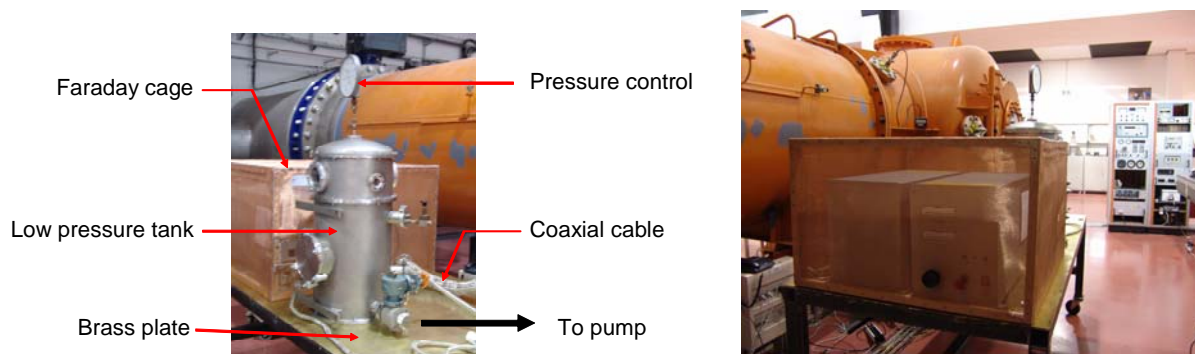
Before investigating the discharge, the electromagnetic compatibility of the DBD with the surrounding equipment must first be checked.

All electrical and electronic devices generate electromagnetic interference, and are sensitive to it. The ability of a device to operate within the limits of interference immunity and suppression is known as electromagnetic compatibility. The experimental difficulties of these particular discharges are obvious. The nanosecond pulsed discharge requires on one hand an equipment with nanosecond temporal resolution, and on the other hand, they generate a high electromagnetic noise [25]. In most cases, the pulse power supply circuit radiates unacceptable amounts of noise or is too susceptible to incoming radiated interferences. Obviously, both radiative processes and high frequency parasitic interference propagation take place through cables. Moreover, there exist disturbances in the distribution of the electric fields, especially when the values of the discharge intensity are high. For that, several authors underline that using pulsed discharges, there is an electromagnetic compatibility problem of the strong power high voltage source with the equipment around (Napatovich [5], Hicks et al. [48] and Chintala et al. [113]). They use several techniques to reduce the generated electromagnetic interferences.

In our experimental work, to place side by side high frequency pulse power supply with apparatuses of high sensitivity asks for a certain number of precautions. Usually the source of such electro-magnetic interference is the load. To prevent interference of the high voltage pulse generator with the diagnostic equipment, the entire test section assembly (HVPG) is shielded by a copper Faraday cage and connections by ferrites and filtered connections (Fig.IV.3). Within the conductive shielding, the high frequency electromagnetic field is going to induce a high frequency current. This current, if no energy is dispelled by Joule effect, induces in turn a field, which will oppose exactly to the inductive field. The resulting field outside the cage will be zero.

A good quality electrical grounding plan (in zero potential) is imperative to avoid electrical interference problems. One mass point is located on the brass plate of the table and all connections of the different elements to ground are connected at that point. The differences in electrical conductivity of aluminium and brass (i.e. copper and zinc alloy) materials used explain our choice. The percentage of electrical conductivity of a material is often given relative to copper, which is considered to be 100% conductive (this does not, of course, mean that copper has no resistance, but rather that it is the standard by which other materials are measured). Therefore, aluminium is 61% as conductive as copper and brass is only 28% as conductive as copper<sup>6</sup>.

The different parts of this electrical safety set-up are shown in Fig.IV.3.



<sup>6</sup> Electrical conductivities are : brass :  $16.2 \times 10^6$  S/m ; aluminium :  $37.7 \times 10^6$  S/m and copper :  $59.6 \times 10^6$  S/m.

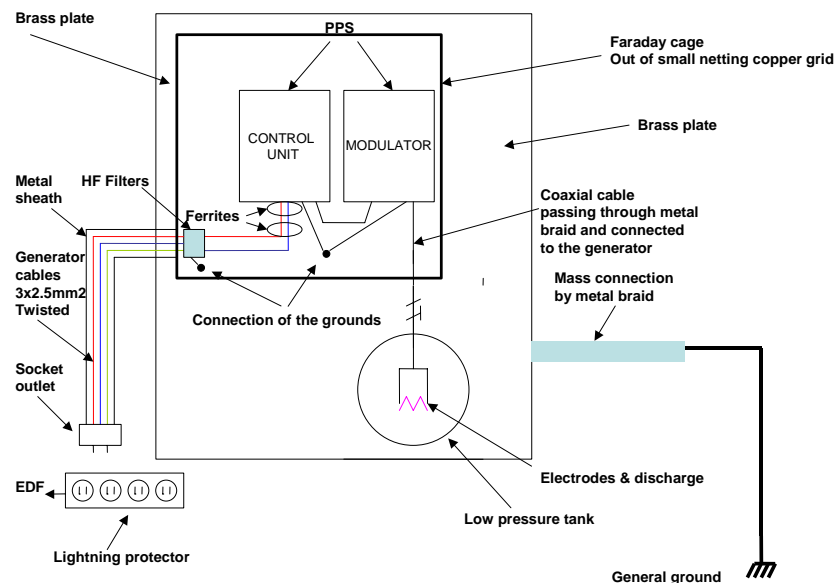


*Fig.IV.3. Electrical set-up of the DBD.*

A 40 litres cylindrical stainless steel tank is used to allow working at low pressure (Fig.IV.3). The main dimensions are ~30 cm in diameter and ~1 m high. The upper and lower parts are composed of a removable bridle integrating the pressure control system. A large CaF<sub>2</sub> window (10 cm diameter) is situated on the front face of the reactor and three additional 4 cm CaF<sub>2</sub> optical access allow optical diagnostics under reduced pressure.

Working pressure is measured by an MKS Portray127 Baratron gauge. After introduction of the DBD into the low pressure tank, a primary vacuum pumping is carried out until a residual pressure of 0.1 Torr is reached, then a binary mixture of helium and oxygen (O<sub>2</sub>, Airlaz purity from Air Liquide) is introduced, raising the pressure to atmospheric pressure. The continuous flow rate is controlled by Rosemount mass flow meters, calibrated by the constructor. The desired operating pressure is finally set by adjusting the valve between the vacuum chamber and the pump.

The effects of applied voltage, pulse repetition rate, flowrate, gas composition (helium and oxygen/helium) and pressure are first studied by emission spectroscopy.

## **IV.1.4. Characterization of the dielectric barrier discharge**

### **IV.1.4.1. Electrical characteristics**

The discharge is initiated only after high voltage exceeds the breakdown voltage. This produces ionization in the test section. In the present experiments, stable repetitively pulsed discharges in O<sub>2</sub>-He flows were maintained at test section pressures up to P= 760 Torr.

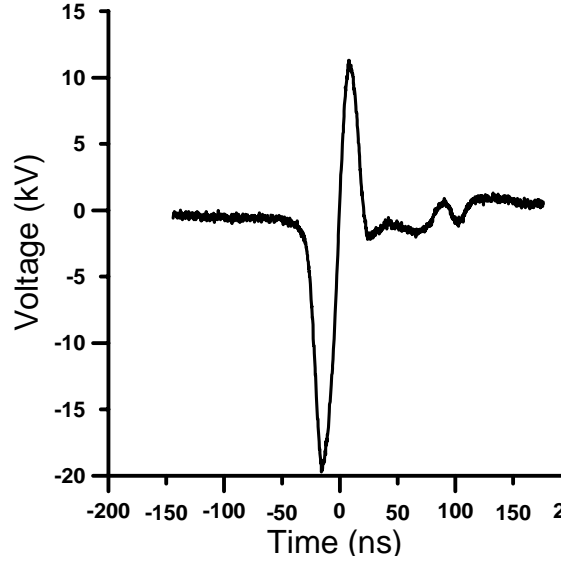


Fig.IV.4. Typical oscillogram of a single high voltage pulse.

Fig.IV.4 shows a typical oscillogram of a single high voltage pulse in a 10% O<sub>2</sub> – 90% He flow, at atmospheric pressure and at a volumetric flow rate equal to 10 l/min. It can be seen that the pulse peak voltage is 20 kV with negative polarity, with the pulse full width at half maximum of about 25 ns. The pulse repetition rate is 20 kHz. A so called “overshoot” is observed in the oscillogram before reaching stabilization.

At atmospheric pressure and temperature of 300 K, the reduced electric field  $E/n$  can be estimated :

$$\frac{E}{n} = \frac{2 \times 10^4}{2.45 \times 10^{19}} \approx 0.8 \times 10^{-15} \text{ V.cm}^2 = 80 \text{ Td}$$

For an interelectrode distance of 1 cm and 20 kV, and in the pressure and temperature conditions mentioned above, the estimated reduced electric field is 80 Td.

#### IV.1.4.2. Optical emission spectroscopy

Optical emission spectroscopy is largely used in this study. Analysis of emission spectra obtained when varying experimental parameters such as oxygen addition, injected power and pulse repetition rate are presented in the experimental chapters. Since the energy of a transition is a characteristic of the particle species, the wavelength is an identifier for the radiating particle. The observed wavelength range is 280-950 nm. The observed emission bands are attributed to helium, molecular nitrogen and atomic oxygen. In fact, even at low pressure and even if present in small amounts, nitrogen bands are detected. This is due to the high emissivity of molecular nitrogen experimental test bench may have a negligible but existing leak rate, allowing very small quantities of molecular nitrogen from surrounding air to penetrate the test section.

Analysis of the emission spectra of our DBD flow, by comparison with simulated O<sub>2</sub>(b<sup>1</sup>Σ<sub>g</sub><sup>+</sup>) (0,0) band emission spectra, shows that we have not been able to detect excited molecular oxygen O<sub>2</sub>(b<sup>1</sup>Σ<sub>g</sub><sup>+</sup>). In the same manner, the O<sub>2</sub> emission at 632 nm assigned to the double electronic transition is not detected. The emission band detected corresponds to a molecular system, degrading towards the blue region and assigned to N<sub>2</sub> (C<sup>3</sup>Π<sub>u</sub>→B<sup>3</sup>Π<sub>g</sub> (0,2)).

During the modelling of the O<sub>2</sub> discharge (presented in chapter III), we have seen that nitrogen is an effective quencher but the presence of good nitrogen emission spectra will allow us to measure the plasma temperature. Once temperature is measured, in order to remove nitrogen, we have then worked with a fully leak-proof system as well as with higher purity gases.

The rotational temperature is determined from rotationally-resolved  $N_2^+$  first negative system spectra of this band as explained in chapter II. The head (0-0) of this band system can be found in the near ultraviolet at 391.44 nm (Fig.IV.5).

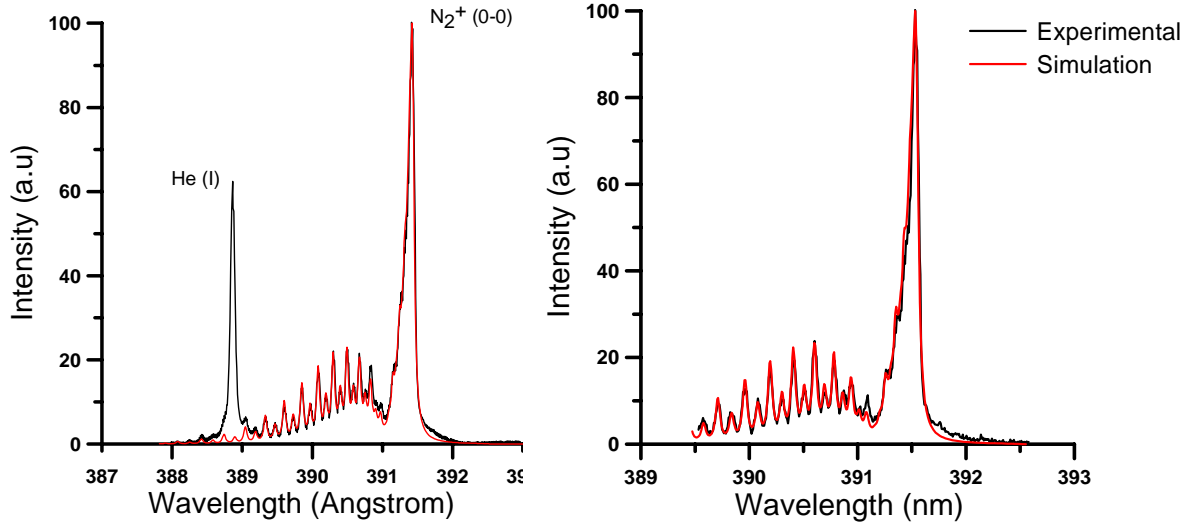


Fig.IV.5. Comparison between experimental and simulated spectra of  $N_2^+$  in the discharge at  $P=120$  Torr and acquisition time=1s, for He at 10l/min, and  $f=10$  kHz. (Left) :  $I=5.4$  mA and  $U=1.28$  kV ( $P=7$  W) ; (right) :  $I=6$  mA and  $U=2$  kV ( $P=12$  W).

The resolution is set to  $0.5 \text{ \AA}$ . A rotational temperature of 365 K is found with an uncertainty of  $\pm 10$  K. Therefore the expected low temperature characteristic of the plasma is experimentally confirmed. An increase of applied power from 7 to 12 W, leads to a slight increase of 5 K in the rotational temperature. This temperature is the temperature during the pulse that could increase afterwards. This could have been checked by the use of an optical emission spectroscopy diagnostic temporally resolved, unfortunately not possible within the framework of this study.

To conclude, an experimental test bench has been developed and the plasma discharge obtained by pulsed dielectric barrier has been analysed. The results of an investigation of singlet oxygen production by application of a dielectric barrier discharge in diluted  $O_2$  mixtures have shown that we have not been able to produce excited molecular oxygen  $O_2(b^1\Sigma_g^+)$  and  $O_2(a^1\Delta_g)$  by excitation of gas phase oxygen at atmospheric and reduced pressure. To optimize the  $O_2(b^1\Sigma_g^+)$  and  $O_2(a^1\Delta_g)$  yield in the plasma, the discharge should operate at reduced electric field values where the energy input into the target states is maximum. We have therefore decided to cross the simple pulse dielectric barrier discharge with a DC component.

## IV.2. Crossed discharge reactor (CDR)

### IV.2.1. Non self sustained discharge

We have shown in chapter III that, in order to optimize the fractional power dissipated in the electron impact production of  $O_2(a^1\Delta_g)$  and  $O_2(b^1\Sigma_g^+)$  :



the reduced electric field  $E/n$  should be near or below 10 Td. This reduced electric field corresponds to an electron temperature of  $T_e \approx 1.2$  eV. Unfortunately, self-sustained discharges in He/ $O_2$  mixtures operate at higher values of reduced electric field, roughly corresponding to the peak in oxygen dissociation. To obtain an optimal reduced electric field, the approach used now employs two overlapping discharges in a rectangular geometry, a repetitively pulsed discharge and a DC sustainer

discharge. The DC voltage, which can be tailored to maximize the energy input into the  $O_2(a^1\Delta_g)$  state, couples power to the plasma. The duration of the high power pulse should be just long enough for the electron temperature spike to cause a large increase in ionization by avalanching the electron density. After the high power pulse, the background power level is applied to moderately heat the electrons. By definition, a discharge and an electric current, which survives only when one external ionizing agent is applied to it is said to be in a non-self-sustained regime.

This method, first demonstrated by Hill [215] has been previously used to develop a high-power, fast flow  $CO_2$  laser [214-216]. Works of Hicks et al. [48, 56, 217] showed that this approach produces stable and diffuse plasmas in  $O_2$ -He flows for DOIL (discharge oxygen odine laser) applications. Singlet delta oxygen yield was up to 5.0%–5.7% [56]. Hill developed a controlled avalanche process method (CAP) whereby short, high voltage pulses ionize the gas while a lower electric field sustains the discharge between the pulses [218]. He obtained 16%  $O_2(a^1\Delta_g)$  yield. This CAP has also been investigated by Verdeyen et al. [42].

## **IV.2.2. Characterization of crossed discharge reactors**

### **IV.2.2.1. Introduction**

The collaboration with the Heat and Mass Transfer Institute in Minsk allowed working on the development of a new generation of high voltage pulse power supply and on crossed discharge reactors for excited  $O_2$  generation. Experiments with different discharge cells were performed at the Heat and Mass Transfer Institute (HMTI, Minsk), at ICARE Institute (Orléans, France) and at LSS (Magdeburg, Germany). After a description of the experimental set-up, results of the crossed discharge characterization will be presented and discussed.

### **IV.2.2.2. Motivation**

Non equilibrium gas plasmas are weakly ionized molecular gases, with typical ionization fractions of  $\sim 10^{-6}$ . With pressures  $\sim 1$  atm, it is possible to maintain such plasmas in steady state, with their translational/rotational external mode temperature quite low, but with some of the internal energy modes highly energetic, and with the energy of free electrons quite high,  $\sim 1$  eV or more [219-221]. With gases at low pressure ( $\sim 0.01$  atm), a stable plasma can be created in rather large volumes, with electron production in the plasma volume balanced by volume and wall recombination and diffusion. These are familiar glow discharges, which indeed have a low external mode temperature and high free electron energies. However, at higher pressures and in extended volumes, such non thermal plasmas are impossible to maintain. The discharge current path contracts, the ionization fraction rapidly increases and the plasma thermalizes into an arc discharge [214].

To create the desired glow-plasma-like non thermal environment in large volumes and at high gas pressures, it is necessary to separate the task of creating volume ionization of the gas from the task of supplying energy to the internal modes (non-self-sustained discharge). This can be done by using some external source of ionization, for example an electron beam, a radiation source, or a high voltage electric field, together with a second electric field that drives the current and maintains the internal mode excitation by electron-molecule inelastic collision [215]. Optimization of discharge parameters and modification of the discharge cell design compared to [48] allows us to operate at elevated pressures (up to atmospheric) and enlarge specific electric energy input (up to 10 eV/molecules), keeping good discharge uniformity.

### **IV.2.2.3. Experimental set-up for combined discharge reactor**

A schematic of the experimental set-up is presented in Fig.IV.6. The discharge equipment consists of the crossed discharge reactor (CDR) ; a high voltage pulse generator (HVPG) (described in Appendix 6) used for the preionization by the pulse barrier discharge and a high voltage direct current power supply (HVDCPS) used for the excitation by the direct current discharge ; two inductance

chokes (in order to separate the two circuits : the DC and pulse power supply circuits) ; two oscilloscopes with special probes for energy input measurements. The HVPG basic characteristics are the following: maximum voltage, 30 kV ; frequency is adjusted from 1 up to 100 kHz, maximum pulse energy, 10 mJ ; power is up to 1 kW.

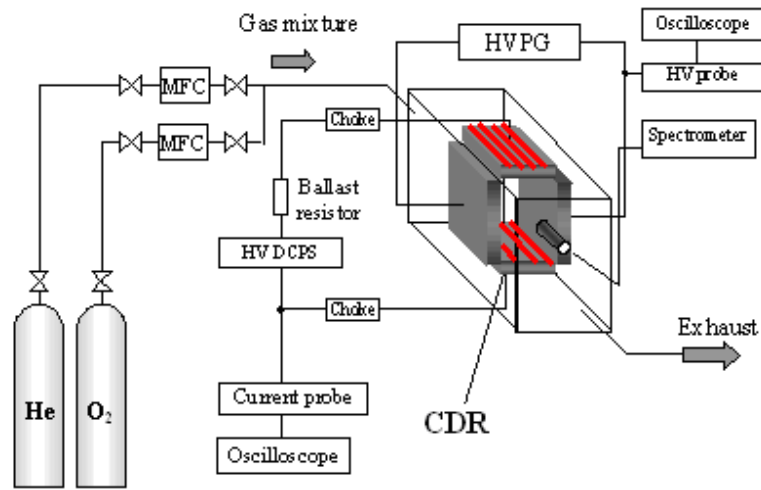


Fig.IV.6. Schematic of the plasma facility.

CDR - crossed discharge reactor, MFC – mass flow controller, HVPG – high voltage pulse generator, HV DCPS – high voltage direct current power supply.

The adjustable high-power ballast resistors (0-10 k $\Omega$ ) are connected in series with the DC power supply to limit the maximum sustainer current. High resistance of the external circuit prevents the current from reaching a large value. In the present experiments, the ballast resistance is set to 940  $\Omega$ .

Current and voltage in the pulsed discharge are measured using a fast-response Lecroy PPE 20 KV high voltage probe and a home made low-capacitance resistive current probe. The current and voltage waveforms are analysed by a 1 GHz Tektronix TDS5034B digital phosphor oscilloscope. DC current is measured using a Tektronix TCP202 current probe. This probe is placed just after the ballast resistors. It is worth noting that ferrite rings are placed at the extremities of each cable of electrical measurement probes, such as to limit the electromagnetic interferences.

A scheme of the crossed discharge and external electrical circuit is presented in Fig.IV.7.

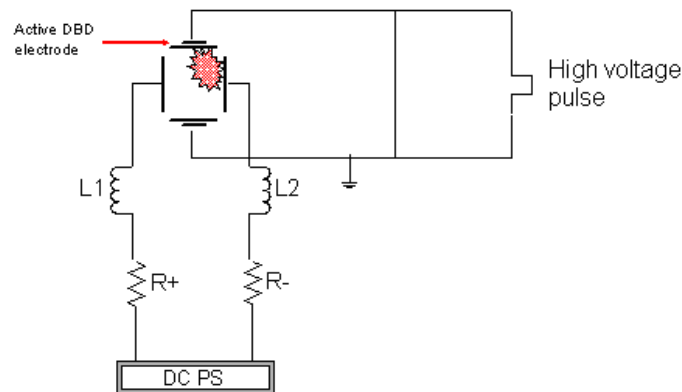


Fig.IV.7. Schematic of the crossed discharge reactor and external electrical circuit (chokes and ballast resistor).

In the absence of chokes, the plasma would concentrate between the active pulse DBD electrode and the ground DC electrode (see Fig.IV.7). The role of the external chokes is to avoid such configuration and to get a homogeneous plasma discharge. In this case,  $R_{ballast} \gg R_L = \omega \times L$ , where  $\omega$  is the frequency. During the pulse,  $R_L \gg R_{ballast}$ , therefore there is no discharge between pulsed and

DC electrodes. Moreover, these two chokes aim to separate two circuits : the DC and pulse power supply circuits. In such a manner, pulse reflection back to the power supply is limited.

In the experiments, the typical operating pulse repetition rate is 20-25 kHz. At working frequency of 25 kHz and a pulse FWHM of 50 ns, the duty cycle of the repetitively pulsed discharge is :

$$Duty\_cycle = \frac{pulse\_duration}{periode} = \frac{50ns}{40\mu s} = \frac{1}{800} \quad (Eq.IV.3)$$

It can be seen that the voltage duty cycle is extremely low. This low voltage duty cycle greatly improves the discharge stability and helps sustaining diffuse, uniform, and volume filling nonequilibrium plasma.

Final energy input in the cross discharge at atmospheric pressure (gas mixture He/O<sub>2</sub>) was more than 2 J/cm<sup>3</sup>. The reduced electric field applied within the DC electrodes can also be estimated by the relation :

$$U = U_{PS} - 2*I*R - 2*L*di/dt \quad (Eq.IV.4)$$

where  $R$  is the ballast resistance in Ohms ( $= 2*470$  Ohms),  $L$  is the chokes inductance in Henry ( $= 2*3.65*10^{-4}$  H) and  $U_{PS}$  is a constant DC power supply voltage. The sustainer voltage can be written  $U$ . From current intensity and voltage measurements, the reduced electric field  $E/n$  can be evaluated, based on the flow number density at room temperature and the cathode voltage fall in the sustainer discharge. The cathode voltage fall has been estimated from the x-axis intercept of the linear slope of the current voltage characteristic by [48] to an amount of  $U_c = 360 \pm 50$  V for 10% O<sub>2</sub> in He at 100 Torr.

#### IV.2.2.4. First crossed discharge reactors

On the way toward achieving optimal conditions, two first simple crossed discharge reactors have been developed and characterized. Presence of singlet oxygen within the discharge slit has been registered in oxygen/helium mixtures at atmospheric and reduced pressure. Optical emission spectra analysis revealed well-defined peaks of emission of O<sub>2</sub>(b<sup>1</sup>Σ<sub>g</sub><sup>+</sup>) at 762 nm. Measurements of the O<sub>2</sub>(b<sup>1</sup>Σ<sub>g</sub><sup>+</sup> → X<sup>3</sup>Σ<sub>g</sub><sup>-</sup>) emission in the discharge volume, show that concentration of O<sub>2</sub>(b<sup>1</sup>Σ) increases with the power of the continuous discharge and increases with the decrease of the molar fraction of O<sub>2</sub> in the flow. Concerning the effect of the sustainer DC power on O<sub>2</sub>(b<sup>1</sup>Σ<sub>g</sub><sup>+</sup>) excitation efficiency, He:O<sub>2</sub> mixtures reveal an increase of O<sub>2</sub>(b<sup>1</sup>Σ<sub>g</sub><sup>+</sup>) concentration with the increase of supporting discharge power. The same tendency is observed for excited atomic oxygen and helium emissions.

These two crossed discharge reactors could not be easily integrated as part of a plasma burner. Moreover, it appeared unfeasible to obtain excited oxygen outside of the discharge volume at atmospheric pressure. Indeed, although the radiative lifetime for O<sub>2</sub>(a<sup>1</sup>Δ<sub>g</sub>) and O<sub>2</sub>(b<sup>1</sup>Σ<sub>g</sub><sup>+</sup>) molecules is unusually long, ~ 3900 s and ~ 14 s respectively, collisions with other molecules (collisional deexcitation) and diffusion to the electrodes may of course induce a much shorter lifetime. Nevertheless, a considerable lifetime (at least several milliseconds) has been observed in practical experiments at low pressure. The final experimental study has been performed with an improved crossed discharge reactor, targeting singlet oxygen generation at relatively low pressure (~100 Torr).

#### IV.2.3. Finally retained CDR

Details of the power supply for this crossed discharge reactor are shown in Appendix 6. The body of the CDR is executed from Peek plastic. The test section static pressure can be varied from 10 to 760 Torr. This makes the experimental facility suitable for studies both in low and intermediate pressure flows. A schematic of the crossed discharge reactor (3D design) is presented in Fig.IV.8 :

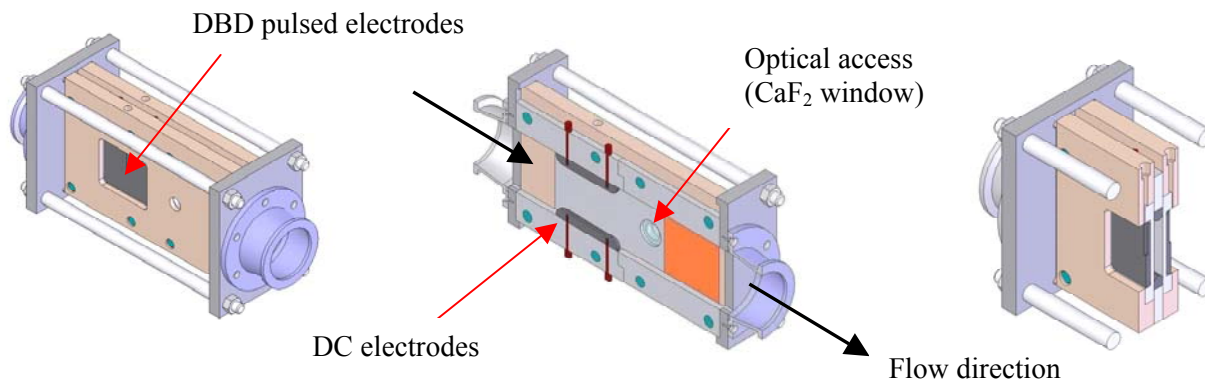


*Fig.IV.8. Crossed discharge for excited oxygen generation. The flow is from left to right.*

The flow enters and passes between two electrode blocks. Both electrodes ( $36 \times 24 \text{ mm}^2$ ) of the pulse barrier discharge (Pulse DBD electrodes) are covered by dielectric Macor ceramic of 1 mm thickness; the gas gap (Pulse gap) is 6.5 mm. Thickness of the pulse electrodes is 0.15 mm. Open DC electrodes have been executed from stainless steel; their sizes are  $40 \times 6.5 \text{ mm}^2$ . Contrary to atmospheric pressure, at low pressure, constrictions at the cathode surface due to overheating of the gas is not observed, therefore working with two same DC electrode sizes is convenient. Edges of open electrodes were rounded with curvature radius of about 3.5 mm. The electrodes are rounded at the edges to prevent high electric field concentration and “hot spot” formation in the plasma near the edges. Also their surfaces were polished and are exposed to the flow. These electrodes have been machined according to a so called “Rogowsky” profile (i.e. rounded electrode shape following electric field potential lines) in order to reduce high electric field concentration at boundaries. To prevent corona discharge formation in the air pockets between the acrylic block, the stainless steel electrodes, and the ceramic plates, this space is filled by a self-hardening dielectric compound (silicon rubber).

### IV.2.3.1. Characterization of the discharge

Four  $\text{CaF}_2$  glass windows are used to provide optical access to the discharge and post-discharge regions (at 1.3 cm downstream of the discharge). A schematic of the experimental set-up is presented in Fig.IV.9 :

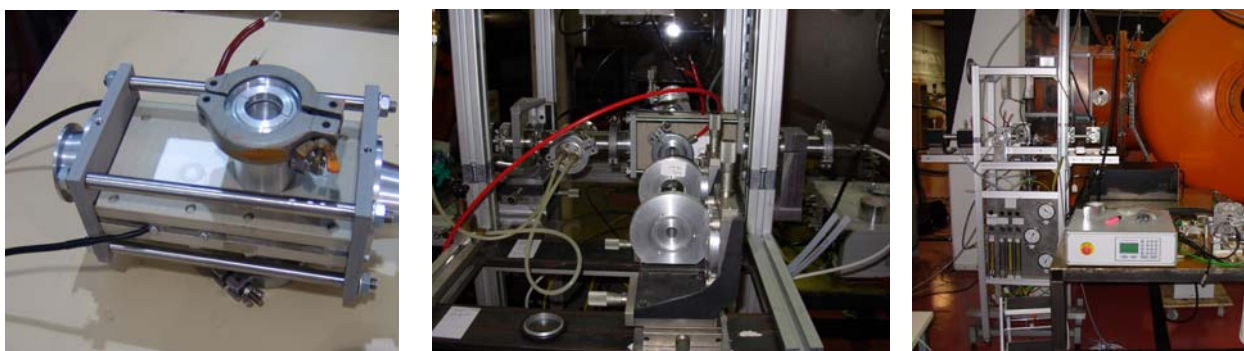


*Fig.IV.9. Crossed discharge reactor – Optical diagnostic with lens systems– Experimental set-up.*

For all measurements reported now, the pulser was operated at the pulse repetition rate of 20 kHz. At such high frequency, the typical run time with the crossed discharge turned on was from 3 to 5 seconds. On one hand, this time limitation is sufficient for data acquisition and on another hand limits the heating of the electrodes and the walls of the discharge cell so that they are destroyed less rapidly ; allowing a longer use between there replacement. The optical diagnostics described in chapter II allow measurements inside the discharge zone.

After stabilization of the test section pressure the DC sustainer voltage is first turned on. At these conditions, no breakdown is produced in O<sub>2</sub>/He flows since the maximal applied DC voltage is set under the breakdown value. The crossed discharge is initiated only after starting the pulse generator.

Fig.IV.10 shows typical oscillograms of a single high-voltage pulse in He 18 l/min + 10%O<sub>2</sub> at 120 Torr pressure. It can be seen that the negative polarity pulse peak voltage is 17 kV, with the pulse full width at half maximum of about 25 ns. The discharge stability was also verified by checking the sustainer current oscillograms. The appearance of “ripple” in the sustainer current means discharge instabilities. The discharge always terminates as soon as the pulser was turned off.

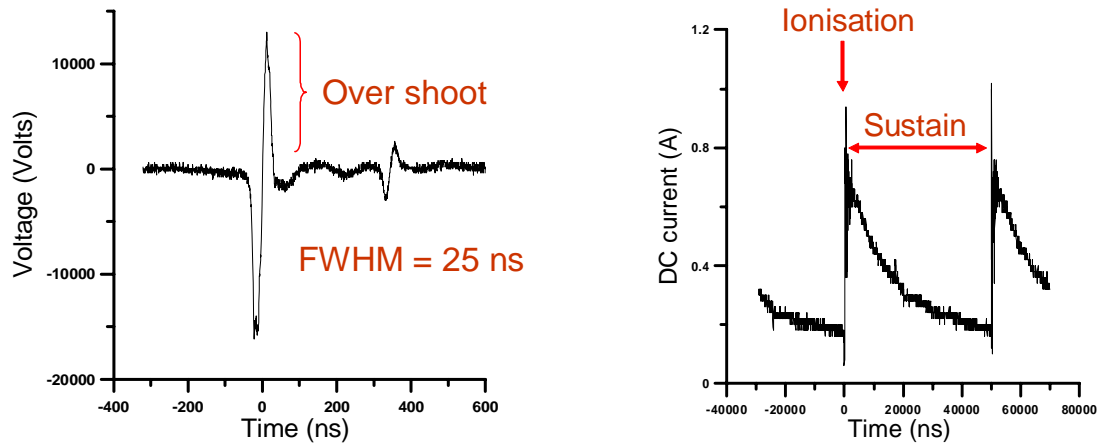


Fig.IV.10. (Left) : Typical single-pulse oscillogram in 10 % O<sub>2</sub> – helium flow at P = 120 Torr. The pulse peak voltage is 17 kV (negative polarity). (Right) : DC current temporal profile.

On one hand, the high reduced electric field  $E/n$  during pulses makes possible efficient ionization and dissociation of O<sub>2</sub> by electron impact. Also, the short pulse duration, the high frequency and the associated low duty cycle greatly improve plasma stability. The positive part of the voltage corresponds to the reflected power, which goes back to the generator. To prevent any damage, it is absorbed by a resistor in parallel with the electrical discharge.

Output voltage and current of our pulse generator are significantly dependent on the load. Figure IV.11 shows how output waveforms (voltage and current) of the high voltage pulse generator will be distorted. On the oscillograms, the red curve is current, the black one is voltage, and the blue one is calculated power = voltage  $\times$  current.

Current and voltage in the pulsed discharge are measured using a fast-response Lecroy PPE 20 KV high voltage probe and a home made low-capacitance resistive current probe. The phase shift between the voltage and current signals, shift due to the probe and connections impedances at the high frequencies contained in the signals, is measured by using a non inductive carbon flat resistance.

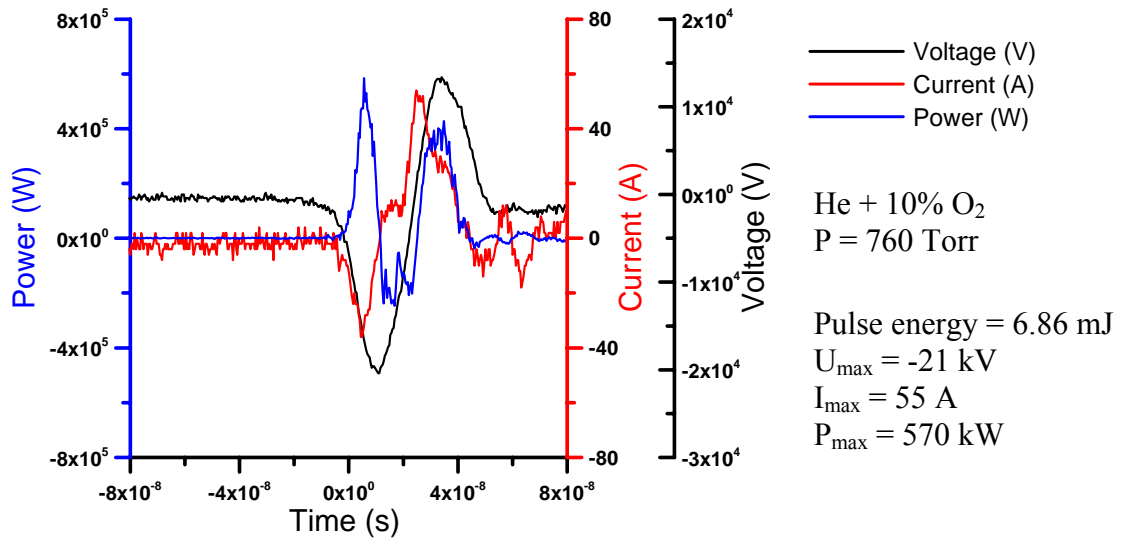


Fig.IV.11. Crossed discharge load typical single-pulse oscillograms : voltage, current and calculated power for single pulse in He + 10 % O<sub>2</sub> at atmospheric pressure.

One can observe from these electrical measurements that we have two peaks of high voltage output ; one negative and one positive. The second one (reflected power back to generator) leads to a high negative power of ~250 kW. The measured output maximum voltage, current, power and pulse energy are 21 kV, 55 A, 570 kW and 6.86 mJ, respectively.

Pulsed non-equilibrium discharges exhibit very interesting characteristics that can be quite different from that of those driven by conventional means, such as AC voltages. Using nanosecond pulses, short pulses with low duty cycles can sustain stable plasmas at relatively low power budgets and without contributing to a temperature increase of the heavy species. The power consumption is low in comparison with the consumption of plasma with the same electron density created by a DC electric field. The energy provided to the discharge is ~7 mJ (hybrid burner discharge load), corresponding to an average power of 140 W at 20 kHz repetition frequency respectively.

On the other hand, the direct current DC voltage only moves electrons and does not ionize the medium. Indeed, when the DC voltage is applied alone, no discharge occurs. The relatively low sustainer voltage current across the test section between the pulses is decreasing because electron density is decaying due to electron recombination and attachment.

Let us remind that the main advantage of this procedure is a possible independent adjustment of DC reduced electric field  $E/n$  in order to optimize energy input into desired target species.

The following Fig.IV.12 shows photographs of different modes of a repetitively pulsed crossed discharge, produced in the test section for a He 18 l/min + 10% O<sub>2</sub> at P=120 Torr, at a pulse peak voltage of 17 kV and frequency of 20 kHz. DC power supply is set to U<sub>DC</sub> = 1 kV.

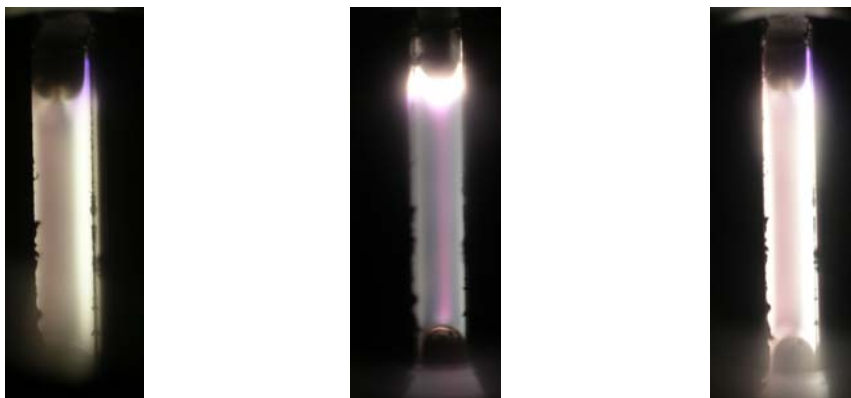


Fig.IV.12. Photographs of different modes of the discharge section in operation, O<sub>2</sub> + He: 10% - 90%, P=120 Torr, and pulse repetition rate 20 kHz :

Left : cathode layer mode, middle: transitional mode, right : diffuse glow mode.

The right pulsed DBD electrode is connected to the high voltage output of the pulser, and the left electrode is grounded. Experiments conducted in such a crossed discharge showed that it allows producing stable and diffuse plasma at higher pressures and much higher energy loadings compared with self-sustained discharges.

Different discharge modes can be observed in fig.IV.12. In all three cases, the crossed discharge appeared diffuse and stable. In the middle, intermediate mode can be observed. It is a discharge regime known as "transitional mode". This mode is characterized by the existence of a line between DC electrodes [214]. Light and dark parts can be observed, that correspond to the cathode layer and the positive column.

The results demonstrate that operation with sustainer discharge powers of 1500 W is possible. The reduced electric field in the positive column of the sustainer discharge varies from 5 to 8 Td ( $0.5 \times 10^{-16}$  to  $0.8 \times 10^{-16}$  V·cm<sup>2</sup>), which is significantly lower than the reduced electric field achieved in self-sustained discharges and close to the theoretically predicted optimum value for singlet oxygen excitation.

### IV.2.3.2. Electronically excited oxygen species production in He/O<sub>2</sub> binary mixture

The evidence of singlet sigma oxygen production in our electrical discharge is confirmed experimentally by spectroscopy and by comparison with corresponding synthetic emission spectra.

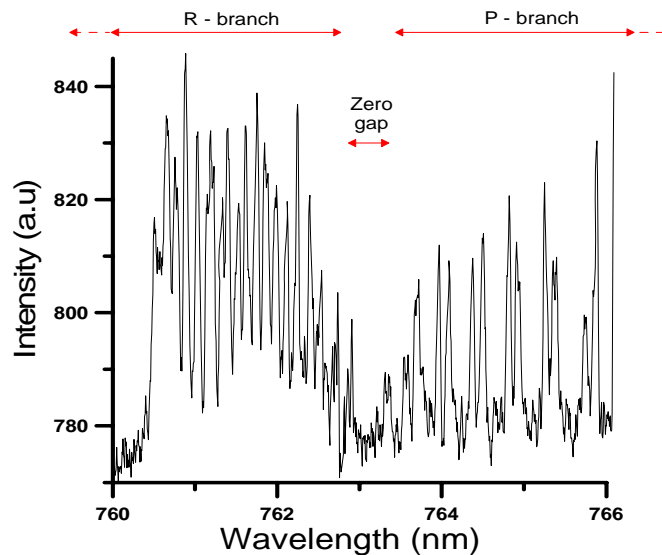


Fig.IV.13. Experimental  $O_2(b^1\Sigma_g^+)$  emission spectrum recorded at  $P = 120$  Torr ; pulse repetition rate of 20 kHz ;  $U_{DC} = 1.3$  kV for 12 l/min He+10% $O_2$ . The integration time is 1s.

A low pressure analysis of the plasma emission spectra shown in Fig.IV.13 revealed well-defined and resolved peaks of excited oxygen  $O_2(b^1\Sigma_g^+)$  centred at 762 nm. This assertion is consolidated by the spectra simulations performed in chapter II. The characteristic structure of the atmospheric oxygen «A» band is observed. And at such high resolution (i.e. 0.5 Å), the rotational structure of the R-branch and the doublets of the P-branch are clearly seen.

In order to evidence the transition to non self sustained discharge, associated with production of singlet oxygen, optical emission spectra have been acquired as a function of time. Three different steps can be visualized and are denoted as follow :

- no discharge ;
- first stage with only pulsed DBD preionization ;
- pulsed DBD + DC combined discharge stage.

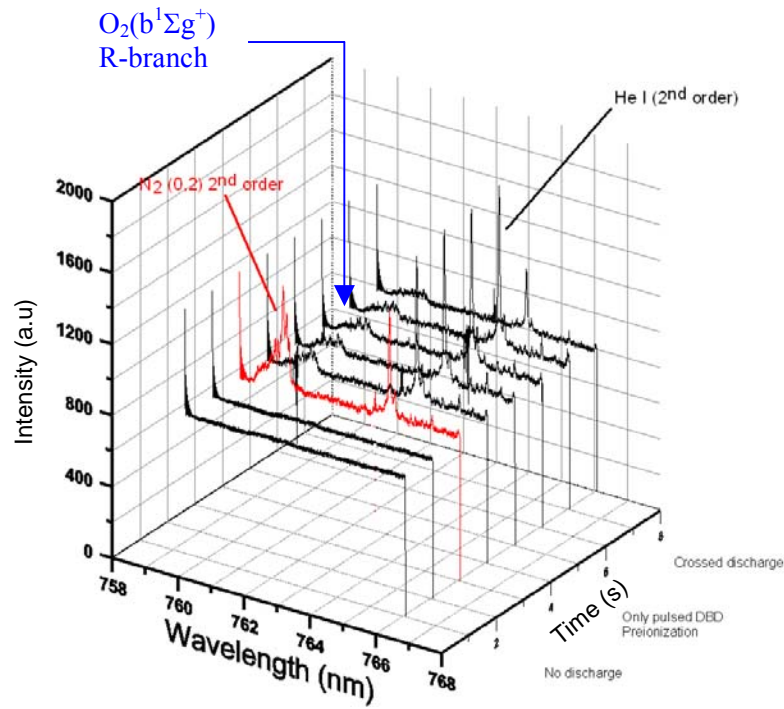


Fig.IV.14. Time resolved emission spectroscopy for He + 5 % O<sub>2</sub>, flow at 120 Torr, 20 kHz and U<sub>DC</sub> I= kV.

Fig.IV.14 allows distinguishing three different stages, temporally resolved: before discharge ignition no signal is observed. The second stage corresponds to the duration of the high power pulse, where we can observe emission spectra assigned to N<sub>2</sub> (C<sup>3</sup>Π<sub>u</sub>→B<sup>3</sup>Π<sub>g</sub> (0,2)). After the 25 ns pulse is applied it is followed by a 50 μs (20 kHz) delay before the next pulse. At this third stage, there will be an extended period where the reduced electric field falls below the self-sustaining value, allowing optimization of E/n to produce O<sub>2</sub>(b<sup>1</sup>Σ<sub>g</sub><sup>+</sup>). Indeed, fig.IV.14 allows to differentiate different characteristic emission spectra of second order N<sub>2</sub> (0,2) and O<sub>2</sub>(b<sup>1</sup>Σ<sub>g</sub><sup>+</sup>) (0,0).

Table IV.1 summarises the experimental tested cases, associated with emission bands of interest:

Emission bands	DBD 20 kHz		DBD 20 kHz + DC	
	He	He + 2% O <sub>2</sub>	He	He + 5% O <sub>2</sub>
O <sub>2</sub> (b <sup>1</sup> Σ <sub>g</sub> <sup>+</sup> )	No	No	No	Yes
N <sub>2</sub> (0-2) (2 <sup>nd</sup> order)	Yes	Yes	Yes	No
He I (2 <sup>nd</sup> order)	Yes	Yes	Yes	Yes

Table IV.1. Emission spectra identification according to plasma regime.

This set of experiments in a non-self-sustained discharge sustained by DC current suggested that it can be successfully used for efficient generation of singlet delta oxygen at reduced pressure.

The effect of frequency and DC sustainer voltage on emission spectra O<sub>2</sub>(b<sup>1</sup>Σ<sub>g</sub><sup>+</sup>) (0,0) centered at 762 nm is analysed in the following figure :

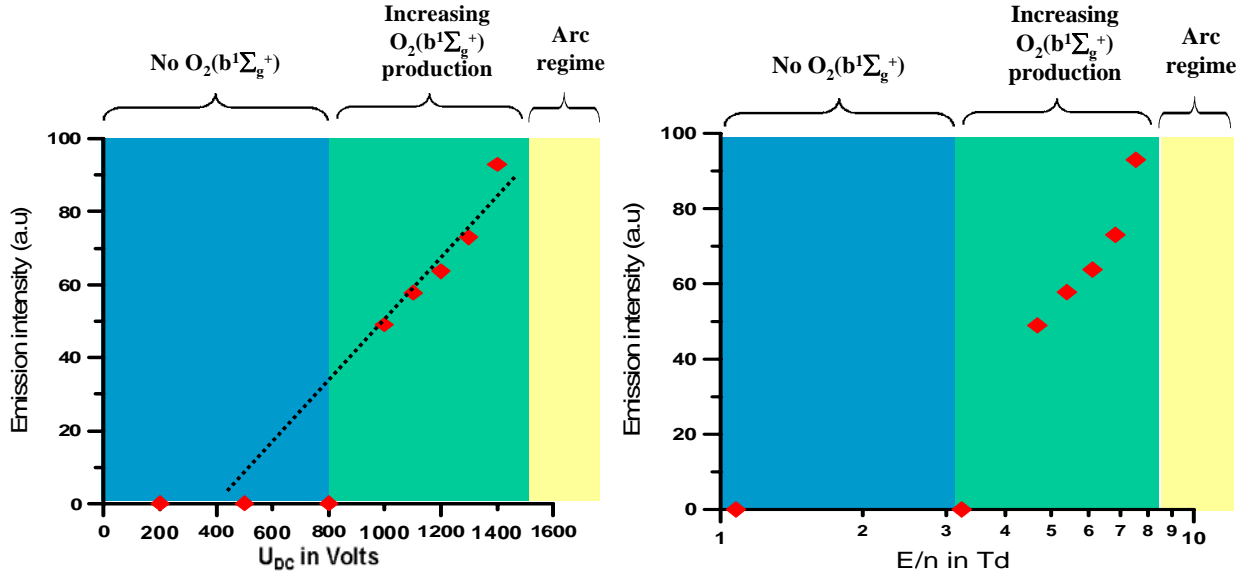


Fig.IV.15. Dependence of  $O_2(b^1\Sigma_g^+)$  emission band intensities on sustainer DC voltage (left) and  $E/n$  (right). Binary mixture : He 12 l/min + 6%  $O_2$ ; pulse repetition rate of 20 kHz and  $P = 120$  Torr.

Experimental conditions of He (12 l/min) + 6%  $O_2$  at pulse repetition rate of 20 kHz at 120 Torr pressure are used. A set of experiments has been performed keeping the experimental parameters constant. The DC sustainer voltage ( $U_{DC}$ ) was independently varied from 0 V to 1600 V. These experiments aimed to maximise the energy input into electron impact excitation of singlet sigma oxygen. From current intensity and voltage measurements, the reduced electric field  $E/n$  can be evaluated, based on the flow number density at room temperature and the cathode voltage fall in the sustainer discharge. The parameters used for the reduced electric field calculations ( $E/n$ ) (see Fig.IV.15 right) are :

- The cathode voltage fall is set to  $U_c = 350 \text{ V}^7$  ;
- The density  $n = 3.86 \times 10^{18} \text{ cm}^{-3}$  ;
- The interelectrodes gap  $d = 3.6 \text{ cm}$ .

One can see in fig.IV.15 left that there exists an observable emission intensity of  $O_2(b^1\Sigma_g^+)$  beginning from  $U_{DC} \approx 800 \text{ V}$ . This is partly explained by the cathodic voltage drop ( $U_c$ ) and the experimental sensitivity of the optical diagnostic. Thereafter, a quasi linear increase of  $O_2(b^1\Sigma_g^+)$  emission intensity as  $U_{DC}$  (i.e.  $P_{DC}$ ) increases is observed. This tendency evolves to an arc regime after  $U_{DC} = 1400 \text{ V}$ . Finally, when reducing the pulse frequency, the minimum value of  $U_{DC}$  requested to reach the presence of excited oxygen (2<sup>nd</sup> zone in Fig.IV.15) increases.

Calculations presented in Fig.III.3 show that the maximal efficiency of  $O_2(b^1\Sigma_g^+)$  excitation is obtained for  $E/n = 5 \text{ Td}$  for 10%  $O_2$  diluted in helium. The observed good agreement of the model predictions with the experimental measurements (see Fig. IV.15 right) demonstrate that the plasma kinetic model (i.e. the simplified kinetic model used for oxygen plasma simulations) presents good predictive capabilities for the optimal operating window and for the influence of dilution. Nevertheless, a small discrepancy obtained with experimental results presented in Fig.IV.15 right (i.e. higher values of  $E/n$ ) may be explained by the possible underestimation of voltage cathode fall that slightly shifts the curve towards higher values of  $E/n$ .

Moreover, the characteristic “bell” curve obtained numerically is partly observed (Fig. IV.15 right, note the log scale on the x-axis for comparison with Fig.III.3). The general trend is reproduced throughout the entire studied experimental  $E/n$  range. The slope of the curve on the low  $E/n$  side is well reproduced. The excited oxygen concentration peak value should be reached around 9-10 Td. To

<sup>7</sup> The cathode voltage fall has been estimated from the x-axis intercept of the linear slope of the current voltage characteristic by [48] to an amount of  $U_c = 360 \pm 50 \text{ V}$  for 10%  $O_2$  in He at 100 Torr.

completely corroborate the previously simulation of energy loss fraction against reduced electric field, one should have increased even more the DC sustainer voltage (i.e.  $E/n$ ). Experimentally, the limitation comes from the fact that at high DC sustainer voltage (i.e.  $U_{DC} > 1.4$  kV), the discharge current path contracts and the plasma thermalizes into an arc discharge regime.

Finally, it is worth reminding that the conception of crossed discharge reactor aiming at independently varying electron energy to maximize the energy input into electron impact excitation of singlet oxygen is fully justified and practically feasible.

The characteristic multiple line O (I) ( $\lambda=777$  nm) which comes from the emission ( $^5S-^5P$ ) is also measured at 20 kHz and the effect of applied power is shown in Fig.IV.16.

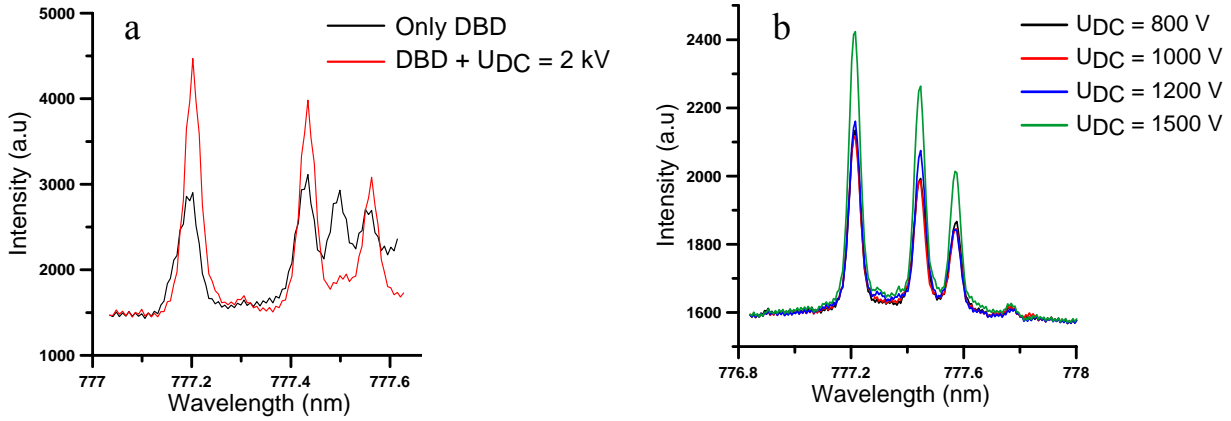


Fig.IV.16. Atomic oxygen emission spectra at  $P=120$  Torr, He 12 l/min + 6%  $O_2$ , a) :  $f = 20$  kHz and integration time is 3 s, b) :  $f = 10$  kHz and integration time is 3 s.

A clear fingerprint of triplet atomic oxygen O(I) emission spectra at 777 nm is observed. In the crossed discharge configuration, an increase of emission intensity is observed for all studied cases. Thus, a higher dissociation occurs when increasing the DC sustainer voltage. Let us note that at low frequency (1 kHz), triplet atomic oxygen has also been recorded, but as a weak signal. The effect of DC sustainer voltage and corresponding reduced electric field ( $E/n$ ) on emission spectra OI(777 nm) triplet at 777 nm is analysed and reproduced in figure IV.17.

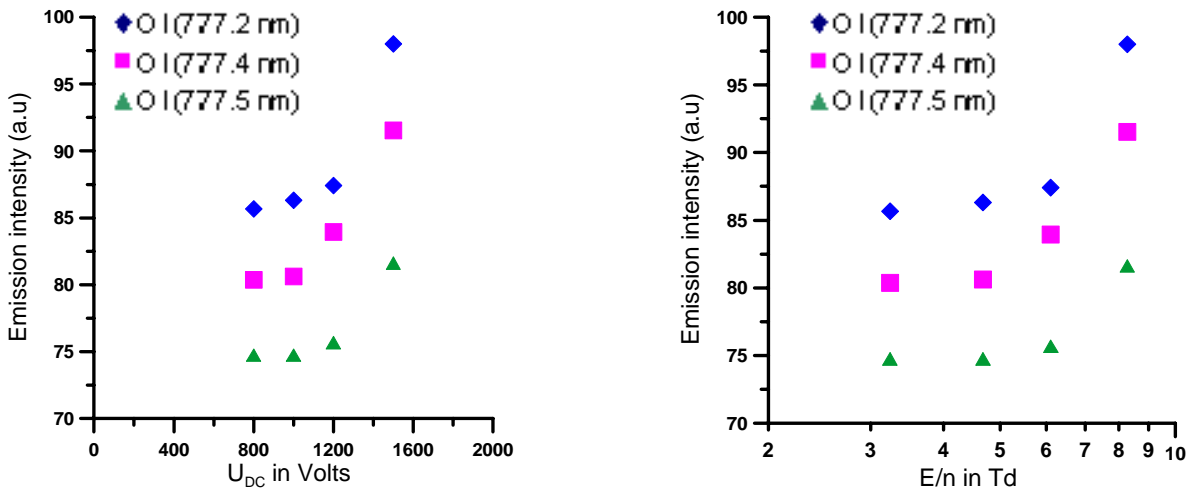


Fig.IV.17. Dependence of OI (777 nm) emission band intensities on sustainer DC voltage (left) and  $E/n$  (right). Binary mixture : He 12 l/min + 6%  $O_2$ ; pulse repetition rate of 10 kHz and  $P = 120$  Torr.

Contrary to  $O_2(b^1\Sigma_g^+)$  emission, the quasi linear increase of  $O_2(b^1\Sigma_g^+)$  emission intensity as  $U_{DC}$  increases is not observed for O I (777 nm). At higher  $U_{DC}$  ( $> 1$  kV), the emission intensity evolves

exponentially until reaching the arc regime. Moreover, with only pulsed DBD, O I(777 nm) emission is also observed.

Large amounts of O atoms are produced in the discharge, mainly by electron impact dissociation of molecular oxygen, considering the following key reactions :  $O_2 + e^- \Rightarrow O + O + e^-$  and by dissociation of excited  $O_2$ .

At the same time, we also measured the excited  $O^*$  atom line emission at 615 nm and 844 nm to estimate the dependence of the oxygen dissociation fraction on the discharge power. The same tendency is observed. It is worth noting that high O atom concentrations can adversely affect  $O_2^*$  yield.

Furthermore, at constant discharge power, triplet O 777 nm population decreases as a function of  $O_2$  percentage in the mixture (not presented here). This result suggests that the oxygen dissociation fraction in the low  $O_2$  percentage mixtures may be significantly higher than in flows with significant oxygen fractions.

### IV.2.3.3. $O_2(b^1\Sigma_g^+)$ generation in helium versus argon diluents

Besides helium, the possible generation of excited oxygen when diluting with argon has been checked experimentally. Though possible, this generation was always associated with conditions less favourable than for helium (see tables below). As a consequence, argon will not be considered for further experiments.

The following tables IV.2 and IV.3 list experimental cases where  $O_2(b^1\Sigma_g^+)$  has been identified at low pressure in two different binary mixtures :

- He 12 l/min + 6%  $O_2$  gas flow at frequency of 20 kHz and varying the pressure and the DC sustainer voltage (Table IV.2) ;
- Ar 36 l/min + 6%  $O_2$  gas flow at 120 Torr and varying the frequency and the DC sustainer voltage (Table IV.3).

$U_{DC}$ (V)	P = 20 Torr	P = 100 Torr	P = 300 Torr
100	No	No	No
200	No	No	No
300	No	No	No
400	Yes	No	No
500	Yes	No	No
600	Yes	No	No
700	Yes	No	No
800	Arc	No	No
900	Arc	No	No
1000	Arc	Yes	No
1100	Arc	Yes	No
1200	Arc	Yes	No
1300	Arc	Yes	No
1400	Arc	Yes	No
1500	Arc	Yes	No
1600	Arc	Arc	No
1700	Arc	Arc	No
1800	Arc	Arc	Yes
1900	Arc	Arc	Yes
2000	Arc	Arc	Arc

Table IV.2. Presence of excited molecular oxygen as a function of pressure and DC sustainer voltage in helium-oxygen mixture.

$U_{DC}$ (V)	f = 5 kHz	f = 10 kHz	f = 20 kHz	f = 30 kHz
100	No	No	No	No
200	No	No	No	No
300	No	No	No	No
400	No	No	No	No
500	No	No	No	No
600	Arc	No	No	No
700	Arc	No	Yes	No
800	Arc	No	Yes	Yes
900	Arc	Yes	Yes	Yes
1000	Arc	Yes	Yes	Yes
1100	Arc	Arc	Yes	Arc
1200	Arc	Arc	Yes	Arc
1300	Arc	Arc	Arc	Arc
1400	Arc	Arc	Arc	Arc
1500	Arc	Arc	Arc	Arc
1600	Arc	Arc	Arc	Arc
1700	Arc	Arc	Arc	Arc
1800	Arc	Arc	Arc	Arc
1900	Arc	Arc	Arc	Arc
2000	Arc	Arc	Arc	Arc

Table IV.3. Presence of excited molecular oxygen as a function of frequency and DC sustainer voltage in argon-oxygen mixture.

To conclude, the crossed discharge in oxygen-helium mixtures remained quite stable in the entire range of non arcing experimental conditions tested (pressure, mass flow rate, frequency). When using argon as diluent, sustainer discharge instabilities occurred frequently.

Differing diluent species yielded considerably different behaviours not only on the  $O_2(b^1\Sigma_g^+)$  production, but also on the discharge behaviour. In the case with argon as diluent, the plasma thermalizes into small arc discharge and surface discharge. This is partly explained by the higher argon electronegativity (i.e. electron affinity) and by the rapid removal of free electrons.

Moreover, at a given frequency (i.e. 20 kHz in tables IV.2 and IV.3), the maximal allowed DC power injected safely (before arcing) is higher in the helium dilution case. Furthermore, in given experimental conditions, although excited oxygen is detected in argon dilution case, the emission signal intensity is considerably weaker than with helium case. It is explained by the fact that the  $O_2(b^1\Sigma_g^+)$  state is highly quenched in resonance energy transfer collisions with argon atoms.

$U_{DC}$ (V)	$O_2/Argon$	$O_2/Helium$
700	Yes	No
800	Yes	No
900	Yes	No
1000	Yes	Yes
1100	Yes	Yes
1200	Yes	Yes
1300	Arc	Yes
1400	Arc	Yes
1500	Arc	Yes

Table IV.4. Presence of excited molecular oxygen as a function of DC sustainer voltage in argon-oxygen and helium/oxygen mixtures at 100 Torr and frequency of 20 kHz.

Previous results (Fig.IV.15) showed an increase of singlet sigma oxygen concentration as  $P_{DC}$  (i.e.  $U_{DC}$ ) increases. Experiments presented in Table IV.4 allows evidencing that Helium dilution permits working at higher DC sustainer voltage, which means a higher  $O_2(b^1\Sigma_g^+)$  production under these conditions.

#### IV.2.3.4. Electronically excited oxygen production in He/O<sub>2</sub>/NO ternary mixture

As explained before, a major quenching channel of singlet oxygen is its reaction with atomic oxygen. The idea of reducing its concentration by incorporation of NO in the studied gas mixture is experimentally investigated now.

Various methods have been investigated in the literature to optimise the reduced electric field  $E/n$ . This part will deal with the addition of components with low ionization threshold (e.g. NO). Other additives such as H<sub>2</sub>, CO may also be used to increase the net rate of ionization [34, 37] Finally, another method of oxygen atom removal is the coating of the discharge region (DBD electrodes) by HgO [222].

Atomic oxygen in the ground state  $O(^3P)$  produced in the discharge strongly quenches singlet oxygen. Therefore, in the present study, the possibility to scavenge  $O(^3P)$  by NO is investigated. For that, we measured  $O_2(b^1\Sigma_g^+ \rightarrow X^3\Sigma_g^-)$  line emission and at the same time, the excited O atom line emission at 777 nm and different nitrogen line emissions to estimate the dependence of singlet oxygen production and oxygen dissociation fraction on the discharge power with pressure and with admixture of some quantities of NO gas. A sequence of experiments has been performed where no nitric oxide is present in the mixture, and then in the presence of increasing amounts of NO.

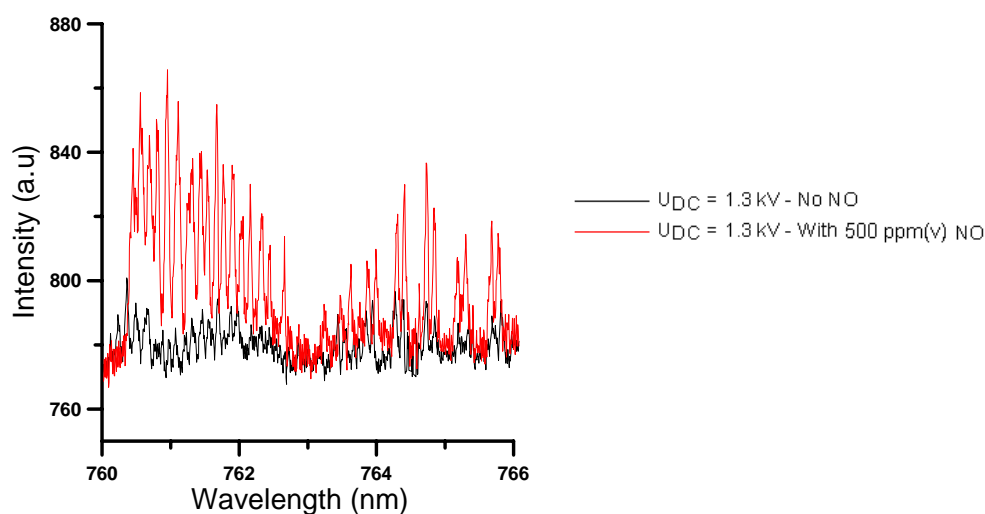
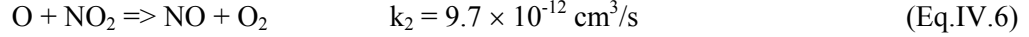
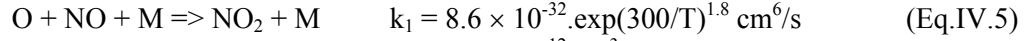


Fig.IV.18. Effects of NO addition on electronically excited oxygen emission spectra (arbitrary units) in a mixture of (He/O<sub>2</sub>/NO) at  $P = 120$  Torr, pulse repetition rate of 20 kHz and  $U_{DC} = 1.3$  kV. Interferential filter centred at 762 nm is used.

Figure IV.18 shows that when maintaining a non-self-sustained discharge in oxygen gas mixtures with adding NO (up to 500 ppm(v)), the efficiency of singlet sigma oxygen production can be increased by 10%.

It is worth to note that electron impact cross section data and kinetic modelling calculations suggest that both singlet oxygen states (lower molecular oxygen electronic energy states) are most efficiently excited at rather close  $E/n$  values (same optimal operating window, cf. chapter II). Therefore, one could expect the  $O_2(b^1\Sigma_g^+)$  and  $O_2(a^1\Delta_g)$  generation to scale in a similar way.

The influence of NO can be explained as follows, considering the following key reactions :



The effect of NO addition results in  $\text{O}(^3\text{P})$  decreasing. As a consequence, the role of the three body quenching reaction proposed in [46, 223] :  $\text{O}(^3\text{P}) + \text{O}_2(\text{a}^1\Delta_g) + \text{O}_2 \Rightarrow \text{O}(^3\text{P}) + 2\text{O}_2$  is highly reduced. In the case of  $\text{O}_2/\text{He}/\text{NO}$  mixture, the decrease of  $\text{O}(^3\text{P})$  concentration in the discharge is significant. As a result, at the same energy input, the singlet oxygen concentration is expected to increase. Atomic oxygen triplet at 777 nm has also been visualised, and the effects of NO and  $U_{\text{DC}}$  on the emission intensity have been observed.

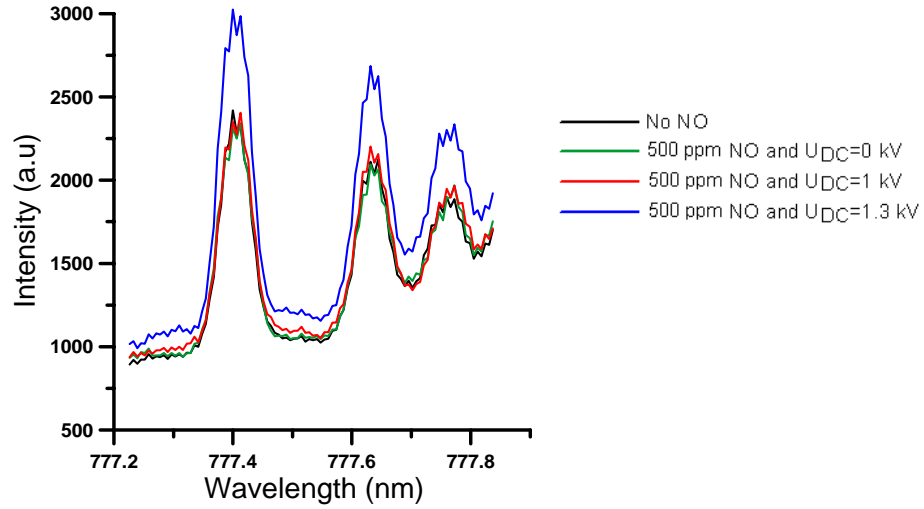


Fig.IV.19. Effects of NO addition and  $U_{\text{DC}}$  (kV) on excited atomic oxygen triplet at 777 nm emission spectra (arbitrary units) in mixture of ( $\text{He}/\text{O}_2 + 500 \text{ ppm NO}$ ) at  $P = 120 \text{ Torr}$ , pulse repetition rate of 20 kHz. Interferential filter centered at 777 nm is used.

The net increase that should have been noticed of the emission of the triplet O at 777 nm is inhibited by the presence of NO. We can effectively observe an increase of triplet O 777 nm triplet emission for  $U_{\text{DC}}=1.3 \text{ kV}$ , but not as high as it has been observed without NO in the initial mixture (see before Fig.IV.16).

It was previously demonstrated experimentally that, when increasing DC power, singlet oxygen emission intensity increases. The addition of NO into the gas mixture  $\text{O}_2/\text{He}$  enabled us to enhance the maximum electric field strength in the discharge. Indeed, the maximal DC sustainer voltage before arc formation can be increased by  $\sim 30\%$  in presence of 500 ppm of NO. Therefore, the specific input energy per molecular components of the mixture increases.

Also, the experiments demonstrated that the addition of NO gives the possibility to considerably enhance the stability of the discharge in oxygen gas mixtures. In addition, the discharge production of  $\text{O}_2(\text{b}^1\Sigma_g^+)$  was enhanced by the addition of a small proportion of NO. This can be paradoxical to the fact that the enhanced production of electronically excited oxygen is due to less quenching, but NO addition has a positive chemical effect (see Eq.IV.5 and IV.6). Moreover, NO has a lower ionization threshold than  $\text{O}_2$  and He, thus the addition of NO enhances the production of electrons, which increases the conductivity of the plasma, which reduces the electric field needed to sustain the plasma and, consequently, the requested  $E/n$  is reduced.

These results agree with experimental results of Carroll et al. [50]. They produced  $\text{O}_2(\text{a}^1\Delta_g)$  by an RF electric discharge at low pressure (5-15 Torr). By addition of a small proportion of NO, an increase of  $\text{O}_2(\text{a}^1\Delta_g)$  yield was obtained.

Concerning the dependence of the relative emission intensities of  $\text{O}_2(\text{b}^1\Sigma_g^+)$  on the oxygen percentage in the mixture it is observed that  $\text{O}_2(\text{b}^1\Sigma_g^+)$  decreases with the increase of the molar fraction of  $\text{O}_2$  in the flow. The  $\text{O}_2(\text{b}^1\Sigma_g^+)$  yield for a mixture with 12% of  $\text{O}_2$  in helium is approximately 1/2 of the yield for a mixture with 6% of  $\text{O}_2$ .

Moreover, the emission intensity of atomic excited oxygen at 777 nm decreases with the increase of the fraction of O<sub>2</sub> in the flow (not presented here), which suggests a lower dissociation of O<sub>2</sub> under these conditions.

The effect of increasing pressure is presented in Fig.IV.20.

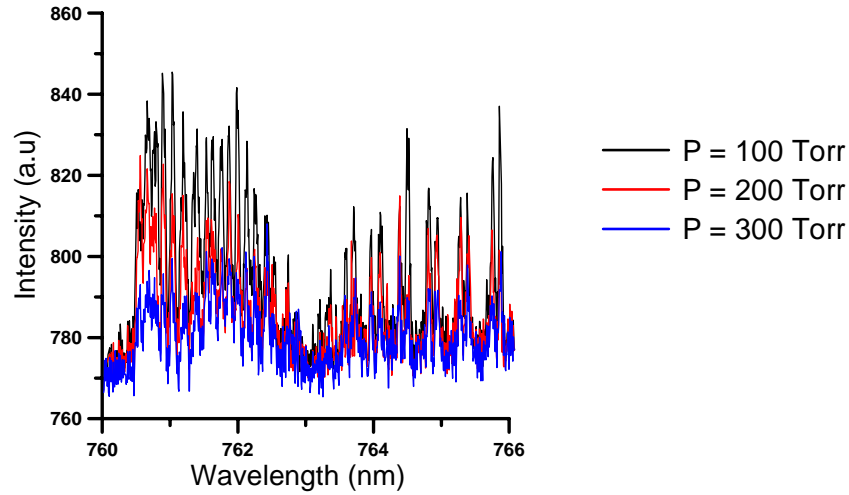


Fig.IV.20. Effects of absolute pressure on electronically excited oxygen emission spectra (arbitrary units) in a mixture of (He/O<sub>2</sub>/NO), frequency of 20 kHz and  $U_{DC} = 1.3$  kV.

One feature which is immediately apparent from these data is that the emission intensity of O<sub>2</sub>(b<sup>1</sup>Σ<sub>g</sub><sup>+</sup>) is decreased by 8% when the pressure increases by a factor 3. Moreover, it is worth to underline that the rate constants for quenching of O<sub>2</sub>(b<sup>1</sup>Σ<sub>g</sub><sup>+</sup>) are three or four orders of magnitude larger than for quenching of O<sub>2</sub>(a<sup>1</sup>Δ<sub>g</sub>). This greater sensitivity of O<sub>2</sub>(b<sup>1</sup>Σ<sub>g</sub><sup>+</sup>) to collisional deactivation may be understandable in terms of the previous considerations.

#### IV.2.3.5. Conclusions on oxygen excitation

Using a CDR allows to target the optimal value of ( $E/n$ ), leading to a noticeable production of excited oxygen. The present investigations consider the electronically excited state O<sub>2</sub>(b<sup>1</sup>Σ<sub>g</sub><sup>+</sup>), produced by a non-self sustained discharge at low pressure (100-300 Torr), using molecular oxygen diluted in helium. The effects of pressure, DC sustainer voltage, O<sub>2</sub> concentration as well as admixture of small quantities of NO on excited oxygen species evolution have been investigated. Measurements of visible emission spectra O<sub>2</sub>(b<sup>1</sup>Σ<sub>g</sub><sup>+</sup> → X<sup>3</sup>Σ<sub>g</sub><sup>-</sup>) in the discharge show the O<sub>2</sub>(b<sup>1</sup>Σ<sub>g</sub><sup>+</sup>) emission intensity to increase with the sustainer discharge power and to decrease as the O<sub>2</sub> fraction in the flow is increased.

Effect of addition of small quantities of NO additives in the gaseous mixture in the O<sub>2</sub>(b<sup>1</sup>Σ<sub>g</sub><sup>+</sup>) features is clear. An increase of the emission intensity by more than 10% is observed. The discharge production of O<sub>2</sub>(b<sup>1</sup>Σ<sub>g</sub><sup>+</sup>) was enhanced by the addition of a small proportion of NO to lower the average ionization threshold and thereby also lower the sustaining value of  $E/n$  of the gas mixture. Indeed, NO has a lower ionization threshold than O<sub>2</sub> and He, thus the addition of NO enhances the production of electrons, which increases the conductivity of the plasma, which reduces the electric field needed to sustain the plasma and, consequently,  $E/n$  is reduced. Finally, another receivable explanation on the effect observed when adding NO is that it reduces the ionization potential of the gas, thus changing the value of  $E/n$ , and particularly reducing it.

Results show that the electronically excited oxygen production mainly depends on the specific energy input (eV/molecule) on the oxygen molecule. Parameters favourable for increasing yield of excited oxygen are :

- reduced pressure ;
- high DC sustainer voltage (until arcing) ;

- reduced molar fraction of O<sub>2</sub> in the flow ;
- dilution with helium and not with argon.

Moreover, addition of small quantities of nitric oxide allows to increase the singlet oxygen production yield considerably.

## IV.2.3.6. Temperature measurements

### IV.2.3.6.1. Rotational temperature measurements

Measurements of the gas temperature in the crossed discharge are of key importance for interpretation of later plasma-assisted combustion experiments. In particular, they would help isolating the effect of excited oxygen species production on the combustion and flame characteristics, as opposed to a “trivial” effect of the flow preheating by the crossed discharge. The (0,0) band at 762 nm of O<sub>2</sub> ( $b^1\Sigma_g^+ \rightarrow X^3\Sigma_g^-$ ) and the  $v''=0 \rightarrow v'=0$  (0-0) at  $\lambda_{the} = 391.44$  nm of N<sub>2</sub><sup>+</sup> ( $B^3\Sigma_u^+ \rightarrow X^2\Sigma_g^+$ ) are used for rotational temperature measurement. The procedure relies on a comparison with synthetic emission spectra, described in chapter II.

Very small amount of nitrogen is added to the mixture. Its highly emissive characteristics allow studying energy transfers in the plasma.

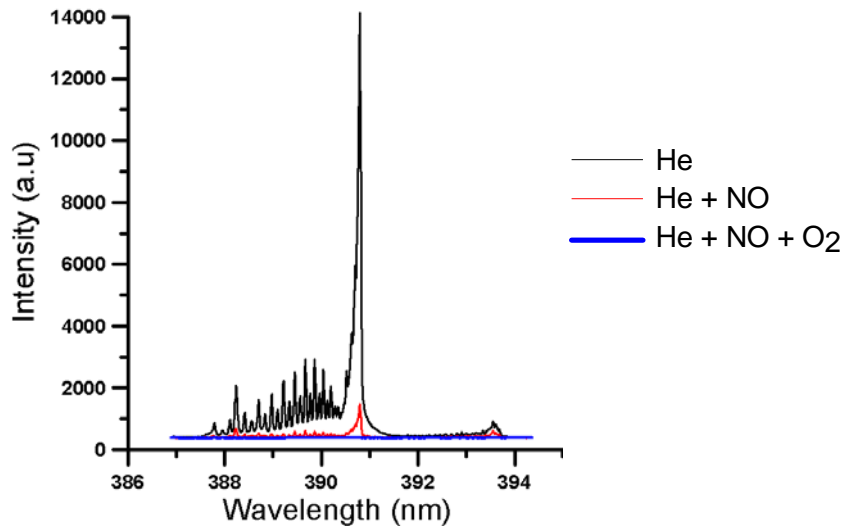


Fig.IV.21. Effects of gas mixture on molecular nitrogen ion ( $N_2^+$ ) emission spectra (arbitrary units) in mixtures based on He, O<sub>2</sub> and NO at  $P = 120$  Torr, pulse repetition rate of 20 kHz,  $U_{DC} = 0.8$  kV. No interferential filter is used. Integration time is 200 ms.

In Fig.IV.21, the black curve represents the emission spectrum of N<sub>2</sub><sup>+</sup>. For that a very small amount of N<sub>2</sub> (0.5%) is added to He ; the red curve is the one for (He+NO) and the blue curve for (He+NO+O<sub>2</sub>) mixtures. The influence of NO and O<sub>2</sub> addition on the N<sub>2</sub><sup>+</sup> first negative system:  $B^2\Sigma_u^+ - X^2\Sigma_g^+$  (0-0) is clearly seen. One can observe a significant decrease by a factor 9.3 on the emission intensity when adding NO in the mixture. The addition of O<sub>2</sub> leads to a complete extinction of this band.

The observed effect can be explained by a charge transfer (CT) reaction  $N_2^+ + O_2 \rightarrow N_2 + O_2^+$ . In contrast, electron transfer to N<sub>2</sub><sup>+</sup> occurs and it leads to O<sub>2</sub><sup>+</sup> with large exothermicity. Different mechanisms of electron transfer exist according to the electronic state of N<sub>2</sub><sup>+</sup>. This reaction path contributes to the vibrational deactivation of N<sub>2</sub><sup>+</sup>. Related characteristics of the reaction dynamics are discussed in [224].

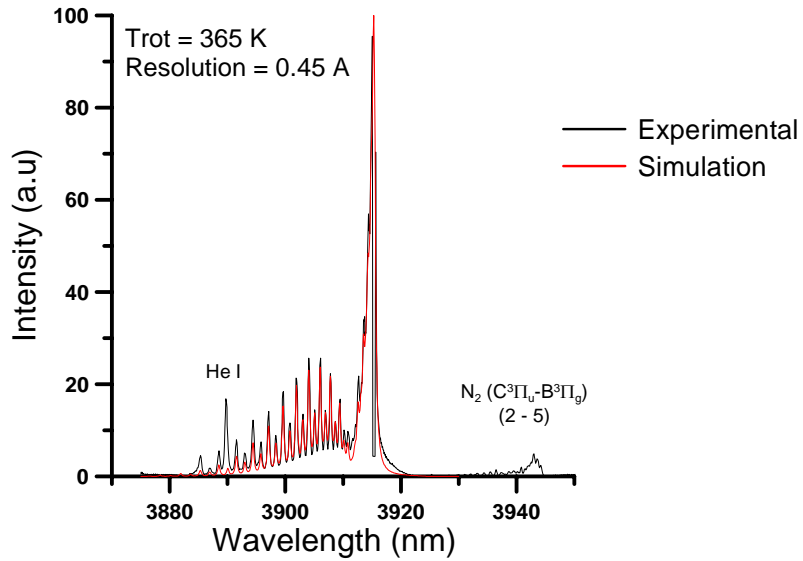


Fig.IV.22. Comparison between experimental and simulated spectra of  $N_2^+$  in the discharge at  $P= 120$  Torr, for He at 10l/min,  $f=20$  kHz and  $U_{DC}= 800$  V.

The gas temperature is obtained from the fit of the computer simulation (red curve, LIFBASE<sup>®</sup> [209]) to the measurement of  $N_2^+$  ( $B^2\Sigma_u^+ - X^2\Sigma_g^+$ ) (0-0) emission band (black curve),  $T_{rot}$  being the fit parameter in the simulation. The inferred rotational temperature is 365 K, based on the  $N_2^+$  spectra (Fig.IV.22). The uncertainty of rotational temperatures inferred from the synthetic spectra is  $\pm 10$  K.

Gas temperature is also determined from the best fit of our computer simulation (red curve) and the measurement of  $O_2(b^1\Sigma_g^+)$  (0-0) emission band (blue curve).

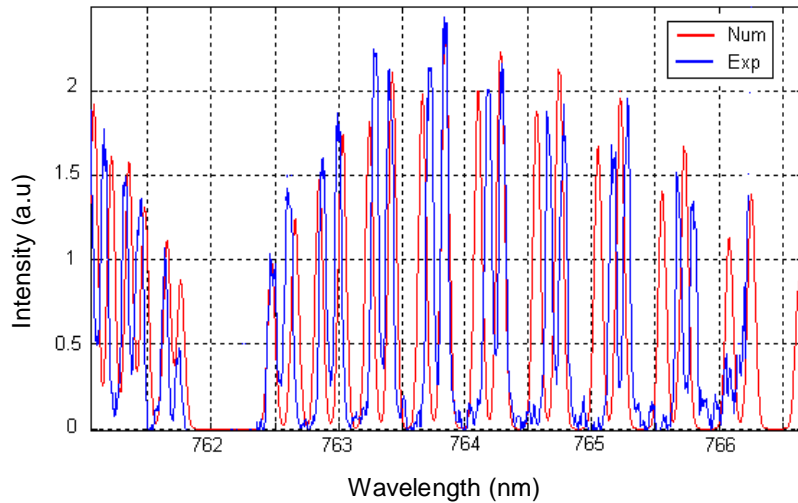


Fig.IV.23. Comparison between experimental and simulated  $O_2(b^1\Sigma_g^+)$  emission spectra in the discharge at  $P= 120$  Torr. Experimental conditions are :  $f= 20$  kHz,  $U_{DC}= 800$  V, in helium/10%  $O_2$  gas mixture.

The gas temperature of the oxygen flow entering the reactor is an important factor that might influence methane combustion. To measure temperatures at the discharge cell outlet, the spectra with the resolved rotational structure of P- and R-branches of the  $O_2(b^1\Sigma_g^+ \rightarrow X^3\Sigma_g^-)$  spontaneous emission band are recorded using the higher resolution spectrometer. The inferred rotational temperature is 370 K, based on the  $O_2$  spectra.

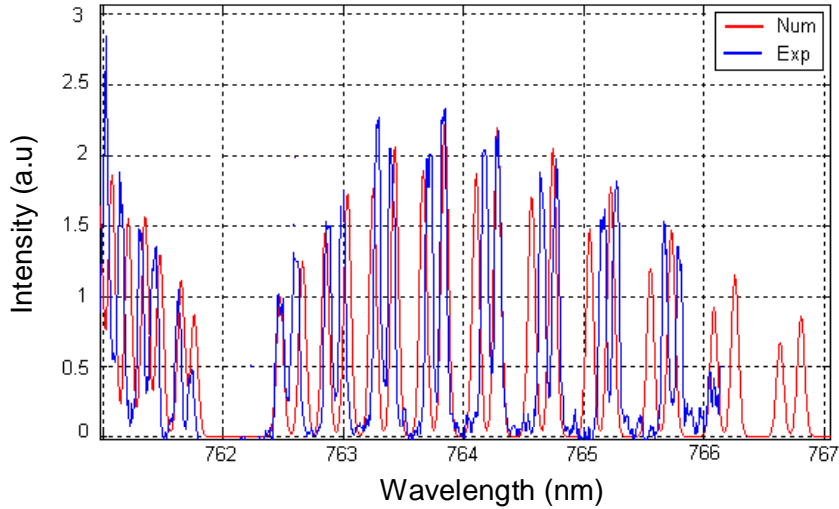


Fig.IV.24. Comparison between experimental and simulated  $O_2(b^1\Sigma_g^+)$  emission spectra in the discharge at  $P= 120$  Torr. Experimental conditions are :  $f= 20$  kHz,  $U_{DC}= 800$  V, in helium/10% $O_2$  with 500 ppm NO addition.

One can observe in figure IV.24 the effect of NO addition on the rotational temperature. In the presence of 500 ppm of NO, the inferred rotational temperature is 430 K, based on  $O_2$  spectra, compared to 370 K without NO (Fig.IV.23).

For both cases (Figs. IV.23 and IV.24), a good agreement is obtained between experimental and simulated spectra. However, figures show some disagreement concerning the absolute positions of the lines, which can be explained by the accuracy of spectroscopic constants used in the simulation program.

To conclude concerning rotational temperature measurements, the gas temperature rise in the discharge did not exceed  $\Delta T \sim 65$  K without NO addition (this point will be discussed in the plasma/flame experimental results interpretation). The measured rotational temperature is  $\sim 365$  K with an uncertainty of 10 K. This is an important result demonstrating that thermal effects can be neglected for the low pressure crossed discharge. However, the beneficial effect of NO addition for electronically excited oxygen generation will lead us to use it in later plasma-flame experiments. Experimental care should be taken to determine the oxidizer flow temperature in the crossed discharge part of the hybrid burner in the presence of NO, since an increase of  $T_{rot}$  by 120 K is observed when adding NO to the  $O_2$ /helium binary mixture. This temperature rise is due to energy release during exothermic conversion of NO to  $NO_2$  in the plasma.

#### IV.2.3.6.2. Vibrational temperature measurements

Vibrationally resolved bands of the  $N_2(C^3\Pi_u \rightarrow B^3\Pi_g)$  band system have been used to infer the nitrogen vibrational temperature  $T_{v(N_2)}$  from nitrogen emission bands in the plasma. Among the identified vibrational bands  $v' - v''$  with  $\Delta v = -1, 0$  and  $+1$ , the second positive system:  $C^3\Pi_u - B^3\Pi_g$ ,  $\Delta v = +1$  is shown here. Better characterization of plasma temperatures is then obtained (Fig.IV.25) for different experimental conditions. The rotational structure of each vibrational band is not clearly observed. Here, the resolution is insufficient to better distinguish them.

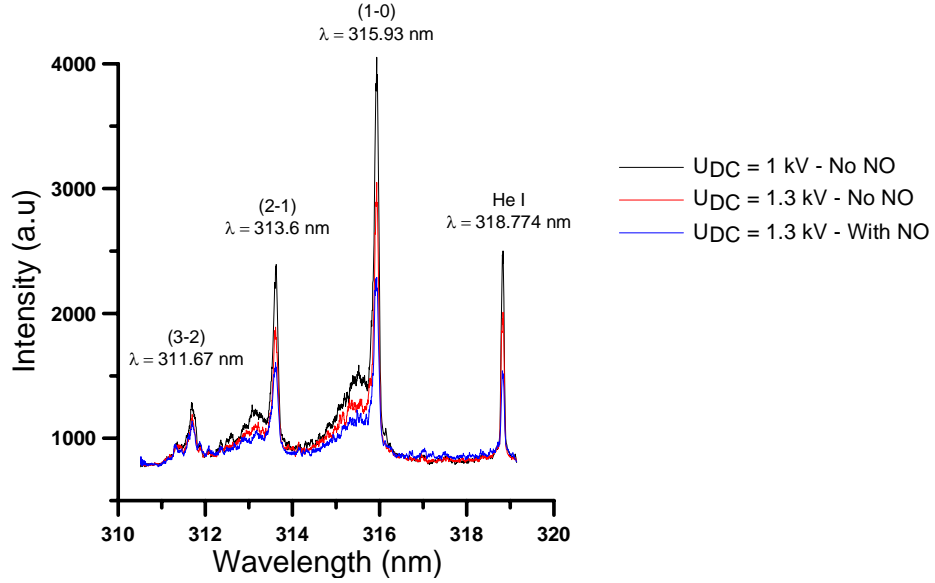


Fig.IV.25. Effects of NO addition and DC sustainer voltage on  $N_2$  second positive system :  $C^3\Pi_u - B^3\Pi_g$ ,  $\Delta v = +1$  emission spectra (arbitrary units) in mixtures based on He,  $O_2$  and NO at  $P = 110$  Torr, pulse repetition rate of 20 kHz.

The spectra presented in figure IV.26 show the  $C^3\Pi_u - B^3\Pi_g$ ,  $\Delta v = +1$  observed experimentally and compared to the corresponding adjusted simulated ones at 0.1 nm resolution. Within this wavelength range, three vibrational bands are considered.

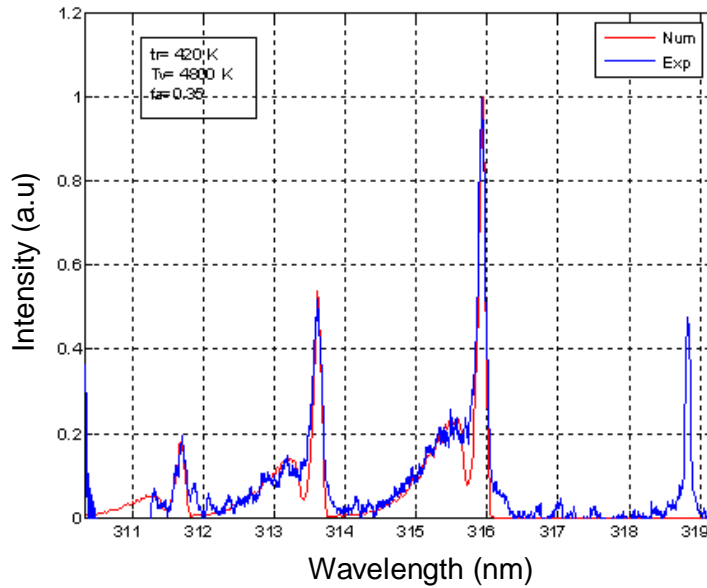


Fig.IV.26. Comparison between experimental (blue) spectra ( $U_{DC} = 1.3$  kV with NO) and simulated (red) spectra. The best fit obtained gives a rotational temperature  $T_r = 420$  K and a vibrational temperature  $T_v = 4800$  K.

In Fig.IV.26, the determined rotational temperature for an apparatus function of  $0.35 \text{ \AA}$  is 420 K and the vibrational temperature is 4800 K. One can observe that the first two bands have a form that is nicely reproduced by the simulation. This allows one to observe low temperature variations from spectra to another.

Let us notice that a sensible increase of the vibrational temperature is observed with NO addition.

In addition, emission spectra corresponding to the  $N_2$  second positive system  $C^3\Pi_u - B^3\Pi_g$ ,  $\Delta v = -1$  and  $\Delta v = 0$  are observed experimentally. Within the corresponding wavelength ranges, vibrational bands (presented in table IV.5) are detected.

Vibrational bands	$\Delta v = -1$			$\Delta v = 0$	
	(0,1)	(1,2)	(2,3)	(0,0)	(1,1)
Wavelength head of band (nm)	357.69	353.67	350.05	337.13	333.89

Table IV.5. Observed vibrational bands of  $C^3\Pi_u - B^3\Pi_g$  second positive system of  $N_2$ .

Thanks to these, confirmation of the vibrational temperature measurements is obtained.

To conclude, the experimental determination of temperature shows that the flow temperature rise in the discharge is rather modest, in the order of 60 to 120 degrees. An increase of the rotational temperature is observed in the presence of nitric oxide. A rotational temperature of 365 K is found with an uncertainty of  $\pm 10$  K without NO, and 420 K in the presence of NO. Therefore, excited species and radicals produced by the discharge can only be the result of chemical excitation by the discharge, heating effects being negligible.

## IV.2.4. Presence of excited oxygen in the post-discharge zone

### IV.2.4.1. Introduction

For successful plasma-assisted combustion, the influence of the discharge must still be measurable several millimetres/centimetres after leaving the CDR. Therefore the present section concerns the post-discharge spectroscopic characterization, as a function of distance. The medium resolution spectrometer (600 lines/mm grating) coupled with an intensified CCD camera is used for these optical diagnostics. In all experiments carried out, due to the NO addition benefit on the production of  $O_2(b^1\Sigma_g^+)$ , He/ $O_2$ /NO gas mixtures are studied. Experiments were conducted at 120 Torr and the pulse frequency is fixed at 20 kHz.

### IV.2.4.2. Spontaneous emission of $O_2(b^1\Sigma_g^+)$ and OI (777 nm)

An example image recorded by the ICCD camera coupled with the spectrometer in an  $O_2$ /He/NO binary mixture with He ( $0.65 \text{ m}^3/\text{h}$ ) +  $O_2$  ( $0.04 \text{ m}^3/\text{h}$ ) + NO ( $3.3 \cdot 10^{-4} \text{ m}^3/\text{h}$ ) at  $P=120$  Torr,  $U_{DC}=1$  kV and frequency= $20$  kHz is presented in Fig.IV.27.

The spectral emission of singlet sigma oxygen and atomic oxygen, in the 758 – 780 nm range has been recorded in the gas mixture. The flow velocity is  $\sim 55$  cm/s, corresponding to a residence time of the flow in the discharge region of approximately 0.09 seconds. This means, each gas sample experiences 1800 discharge pulses within the plasma reactor.

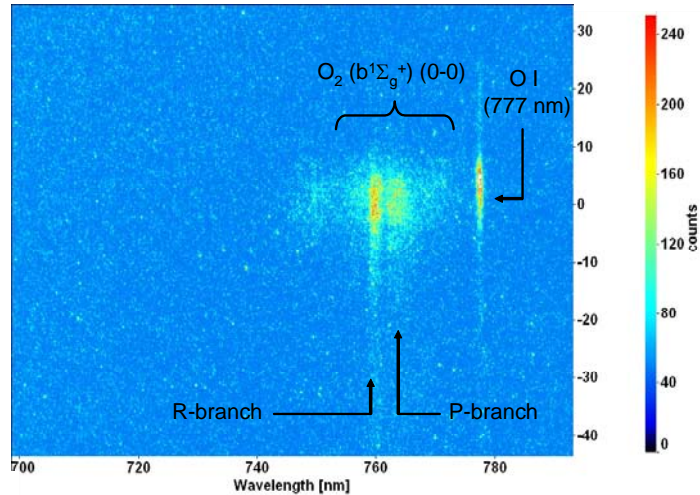


Fig.IV.27. Image recorded by ICCD camera coupled with spectrometer. He 0.65 + O<sub>2</sub> 0.04 m<sup>3</sup>/h with 500 ppm NO and U<sub>DC</sub> = 1 kV.

Analysis of Fig.IV.27 reveals a well-defined spectrum of excited oxygen O<sub>2</sub>(b<sup>1</sup>Σ<sub>g</sub><sup>+</sup>) centred at 762 nm. The R-form branch forming a head and the P-form branch separated from the former by a zero gap is apparent. Also, an emission feature at 777 nm corresponding to the excited atomic oxygen O I triplet at 777 nm can be seen. Due to the experimental resolution used here, the triplet cannot be resolved. In previous experiments, the triplet excited oxygen at 777 nm has been clearly observed at high resolution and confirms the present identification. This band will indicate the degree of dissociation of O<sub>2</sub>.

Post-processing of the ICCD images allows us to obtain typical emission spectra plots. Results of the intensity behaviour without (black curve) and with (red curve) 500 ppm NO admixture, at 20 kHz for He 0.65 m<sup>3</sup>/h + O<sub>2</sub> 0.04 m<sup>3</sup>/h and U<sub>DC</sub> 1 kV is shown in Fig.IV.28. Both, electronically excited molecular, and atomic oxygen are detected in the same plot. It can be observed that the admixture of 500 ppm of NO in the He/O<sub>2</sub> mixture leads to a significant decrease by 23% of excited O atom generation, which is pooled with a net increase of 10% in electronically excited O<sub>2</sub> (b<sup>1</sup>Σ<sub>g</sub><sup>+</sup>).

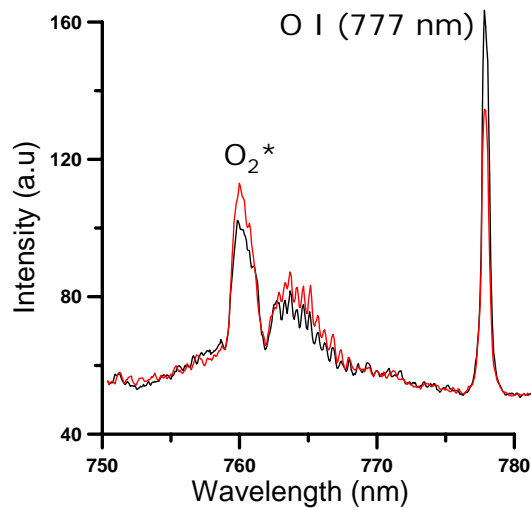


Fig.IV.28. NO addition effect on excited species emission intensities. Black curve : without NO, red curve : with 500 ppm NO. He 0.65 + O<sub>2</sub> 0.04 m<sup>3</sup>/h, and U<sub>DC</sub> = 1 kV.

At constant DC voltage of 1 kV, Fig.IV.29 presents the effects of higher NO concentrations. A negative effect of NO addition is observed when using concentrations higher than 500 ppm.

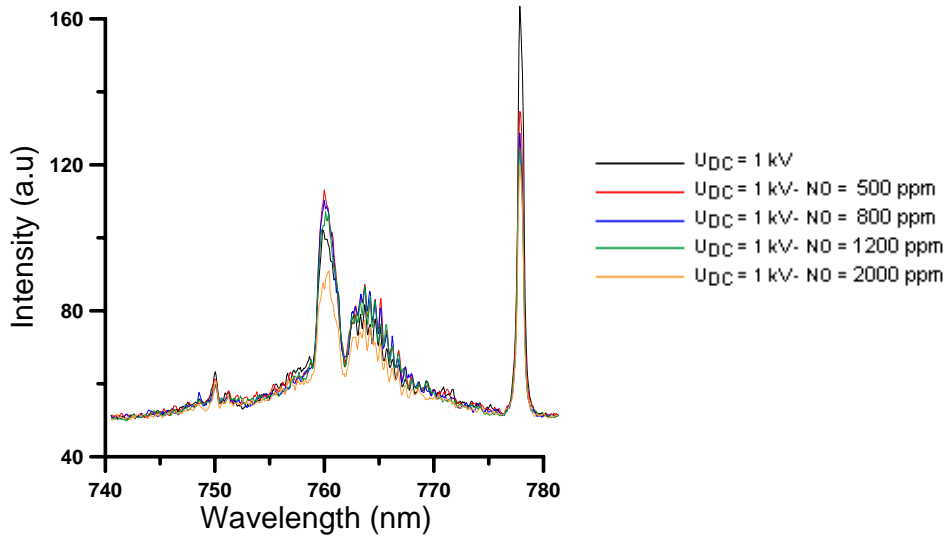


Fig.IV.29. Effect of NO concentration in the mixture at fixed 1 kV DC sustainer voltage. He 0.65 + O<sub>2</sub> 0.04 m<sup>3</sup>/h, and  $f = 20$  kHz.

In subsequent experiments, we varied the DC sustainer voltage and fixed the added NO concentration in the mixture to change the energy input into the flow. The effect of applied DC sustainer voltage at fixed NO concentration is shown in Fig.IV.30. It is then possible to estimate the dependency of the oxygen dissociation fraction on the discharge power in the post discharge and in presence of NO. The previous statements concerning this parameter are confirmed for the post-discharge. In the presence of 500 ppm of NO in the mixture, an increase of O<sub>2</sub> ( $b^1\Sigma_g^+$ ) by almost 90% is observed when passing from 1 kV to 1.3 kV DC sustainer voltage. Within the same conditions, the associated increase of excited atomic oxygen is 46%. For O<sub>2</sub> ( $b^1\Sigma_g^+$ ), the increase rate is much higher than without NO presence and the increase rate of atomic oxygen is highly reduced compared to the case of He/O<sub>2</sub> binary mixtures.

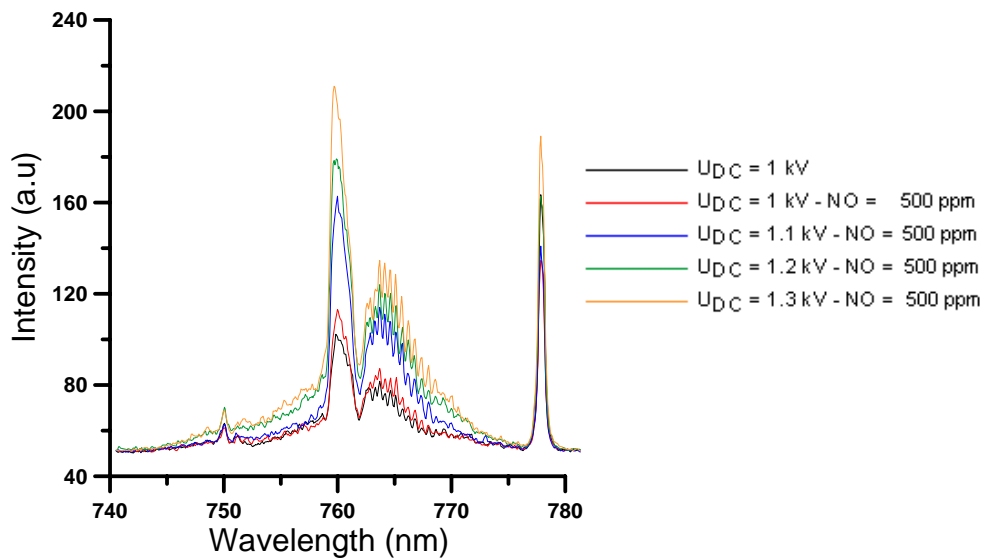


Fig.IV.30. DC sustainer voltage effect in the presence of 500 ppm of NO in the mixture, He 0.65 + O<sub>2</sub> 0.04 m<sup>3</sup>/h flow and  $f = 20$  kHz.

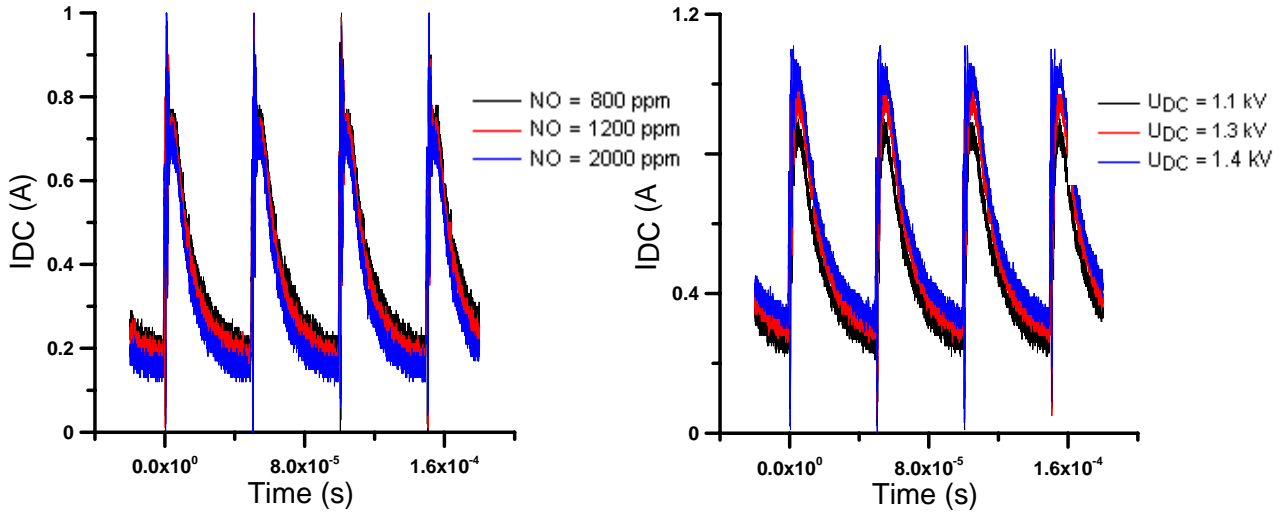


Fig.IV.31. Left) : Effect of NO concentration in the mixture on DC sustainer current time profiles. Right) : Effect of applied DC sustainer voltage in the mixture on DC sustainer current time profiles.

The associated DC current oscillograms in the crossed discharge are presented in Fig.IV.31. One can observe a decrease of DC sustainer current when adding some amount of NO. Also, an interesting result is that in presence of NO, we are able to inject 30% more DC sustainer voltage before apparition of parasitic arc discharges.

It is worth noting that, when increasing NO, the lifetime of charged species in between pulses decreases. Indeed, one can see that for a given time, the  $I_{DC}$  is decreased.

The dependency of the relative emission intensities of O I (777 nm) and  $O_2(b^1\Sigma_g^+)$  on oxygen percentage in the binary mixture ( $O_2/He$ ) is shown in Fig.IV.32a and IV.32b. The signal has been collected over a time period of 400 ms ( $10\text{ ms} \times 40$  accumulations).

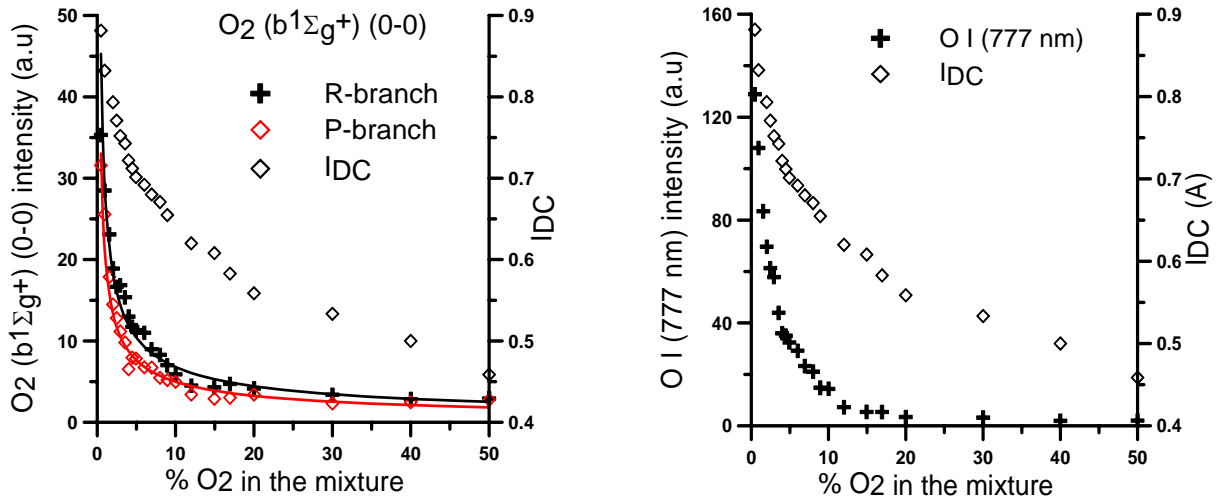


Fig.IV.32. a)  $O_2(b^1\Sigma_g^+)$  (left) and b) O I (777 nm) (right) emission intensities (a.u) and  $I_{DC}$  (A) as a function of  $O_2$  percentage in the mixture at 20 kHz and gas pressure of 120 Torr.

One can observe a decrease of the emission intensity of singlet sigma oxygen by a factor 10 when passing from 0.25 to 10%  $O_2$  in the binary mixture  $O_2/He$ . This means that the  $O_2(b^1\Sigma_g^+)$  concentrations in both mixtures are different. The  $O_2(b^1\Sigma_g^+)$  concentration in the 0.25%  $O_2$  mixture, defined as the fraction of all available oxygen molecules in the  $b^1\Sigma_g^+$  state, is nearly 10 times that in the 10%  $O_2$  mixture. Within the same range, there is a reduction in the DC sustainer current by a factor

1.4. Considering percentages of O<sub>2</sub> ranging from 10 to 30 %, the decrease of the emission intensity of singlet sigma oxygen reaches a factor 1.5 and the DC sustainer current, a factor 1.2. From 20% O<sub>2</sub>, for DC sustainer current, the decrease is quasi linear.

The decrease of the DC current when the fraction of molecular oxygen in the mixture is increased can be explained by the electronegativity of molecular oxygen. When increasing the percentage of oxygen in the mixture, the removal process of the free electrons by their attachment to oxygen is increased. The electron attachment to molecular oxygen is described by the reaction (dissociative or not) :



thus resulting in lower gas mixture conductivity. The attachment process considers that the reaction of a molecule O<sub>2</sub> with an electron occurs through the intermediate resonant state O<sub>2</sub><sup>-</sup>. From this state, according to the lifetime of specie O<sub>2</sub><sup>-</sup>, two reaction channels are possible. In the case where the lifetime is short, the electron will detach, keeping the O<sub>2</sub> molecule in a vibrational excited state. Although O<sub>2</sub><sup>-</sup> is a stable species, for longer lifetimes, the O<sub>2</sub><sup>-</sup> complex will dissociate into O<sup>-</sup> + O according to the following reaction : O<sub>2</sub><sup>-</sup> + e<sup>-</sup> => O<sup>-</sup> + O(<sup>3</sup>P) [41].

In the case of excited atomic oxygen, it is worth noting that the decrease rate within the range 0.25-10% is higher than that of excited molecular oxygen. This result suggests that the oxygen dissociation fraction in the low O<sub>2</sub> percentage mixtures may be significantly higher than in flows with significant oxygen fractions, which may well reduce O<sub>2</sub>(b<sup>1</sup>Σ<sub>g</sub><sup>+</sup>) yield at these conditions. To conclude, it is observed that a growth of O<sub>2</sub> concentration in the range 0.25 to 50% results in a significant decrease of atomic oxygen and singlet molecular oxygen emission intensities. One can observe that both species follow the same trend.

A parameter of high importance for the plasma-flame experiments concerns the distance travelled by excited species out of the CDR before total quenching. For that, a set of experiments have been carried out varying the distance above the discharge outlet. Fig.IV.33a and IV.33b plot the O<sub>2</sub>(b<sup>1</sup>Σ<sub>g</sub><sup>+</sup>→X<sup>3</sup>Σ<sub>g</sub><sup>-</sup>) emission intensity, which is proportional to the O<sub>2</sub>(b<sup>1</sup>Σ<sub>g</sub><sup>+</sup>) concentration, as well as the O atom line emission intensity against the distance above the CDR discharge slot, for O<sub>2</sub>-He mixtures at P=120 torr.

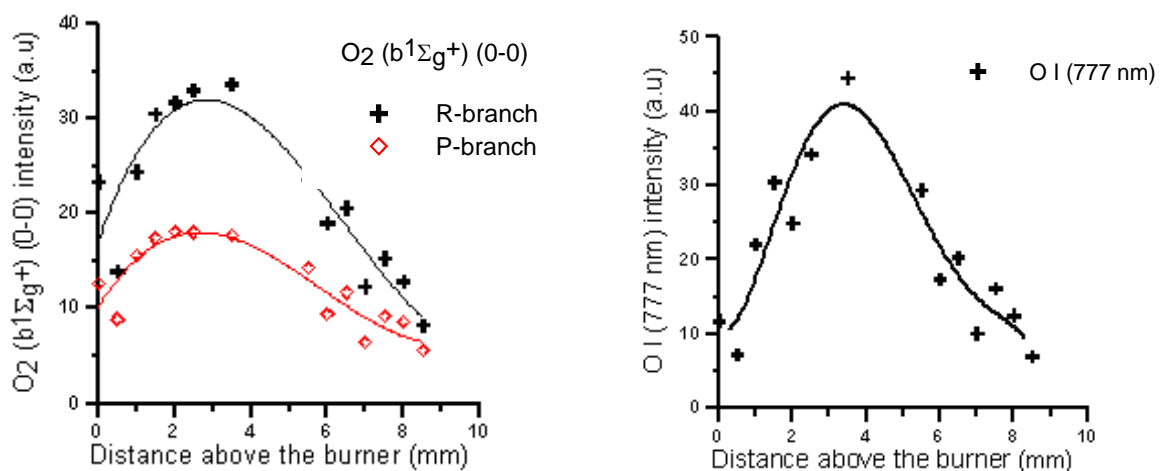


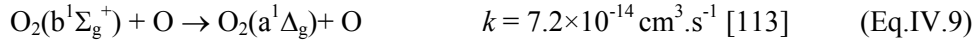
Fig.IV.33.a) O<sub>2</sub>(b<sup>1</sup>Σ<sub>g</sub><sup>+</sup>) (left) and b) O I (777 nm) (right) emission intensities (a.u) as a function of distance above the burner at 20 kHz and gas pressure of 120 Torr.

It can be seen from Fig.IV.33a that the O<sub>2</sub>(b<sup>1</sup>Σ<sub>g</sub><sup>+</sup>) population (R and P branches) evolves in three steps. First, the O<sub>2</sub>(b<sup>1</sup>Σ<sub>g</sub><sup>+</sup>) population grows approximately linearly as a function of the distance above the burner (both R-branch and P-branch), then reaches a maximum, and finally decreases. Note that the first increase stage is faster than the decrease stage. The curve is not symmetric. This characteristic structure will be confirmed during plasma-flame experiments.

The maximum of this curve corresponds to a distance above the burner called optimum position for excited oxygen production, which lies at 3 to 4 mm above the burner exit.

Fig.IV.33b plots the excited O atom line emission intensity, which is proportional to the atomic oxygen concentration, against the distance above the burner discharge slot. The characteristic “bell” form of this plot, as for electronically excited oxygen, is again observed. In this case, the symmetry of the plot is more pronounced. Also, compared to the previous curve, the optimum position for excited atomic oxygen production is similar to that of excited molecular oxygen at 3.5 mm above the burner.

In the discharge zone, the  $O_2(b^1\Sigma_g^+)$  density initially rises due to electron impact excitation. It reaches a plateau after the O density becomes large enough so that the rate of quenching by O atoms balances the rate of excitation. This is not necessarily a problem as the product of the quenching is dominantly  $O_2(a^1\Delta_g)$ , illustrated by the following reaction, where  $k$  is the rate coefficient at 300 K :



In the post-discharge zone, production of  $O_2(b^1\Sigma_g^+)$  is mainly done by the following pooling reaction:  $O_2(a^1\Delta_g) + O_2(a^1\Delta_g) \rightarrow O_2(b^1\Sigma_g^+) + O_2$ . Its quenching is also determined by the reaction with atomic oxygen and ozone.

Collisional de-excitation is an important removal channel for our excited species. The present part describes the behaviour with the increase of pressure.

The most important process in this type of plasma is electron-neutral collisions, due to the important kinetic energy of electrons acquired under the effect of the applied electric field. Electrons are accelerated according to :

$$a = \frac{e \cdot E}{m_e} \quad (\text{Eq.IV.10})$$

where  $a$  is the acceleration,  $e$  the electron charge,  $E$  the electric field and  $m_e$ , the electron mass.

The electron speed, thus their kinetic energy, will then increase, up to collision with other species. The distance travelled by the electron between two collisions is called the mean free path  $\lambda$ . If the pressure increases in the reactor, the density of neutral species increases and the mean free path decreases. Therefore, the energy acquired by electrons will be lower. One has therefore a possibility of varying the energy of electrons in the discharge by modification of pressure.

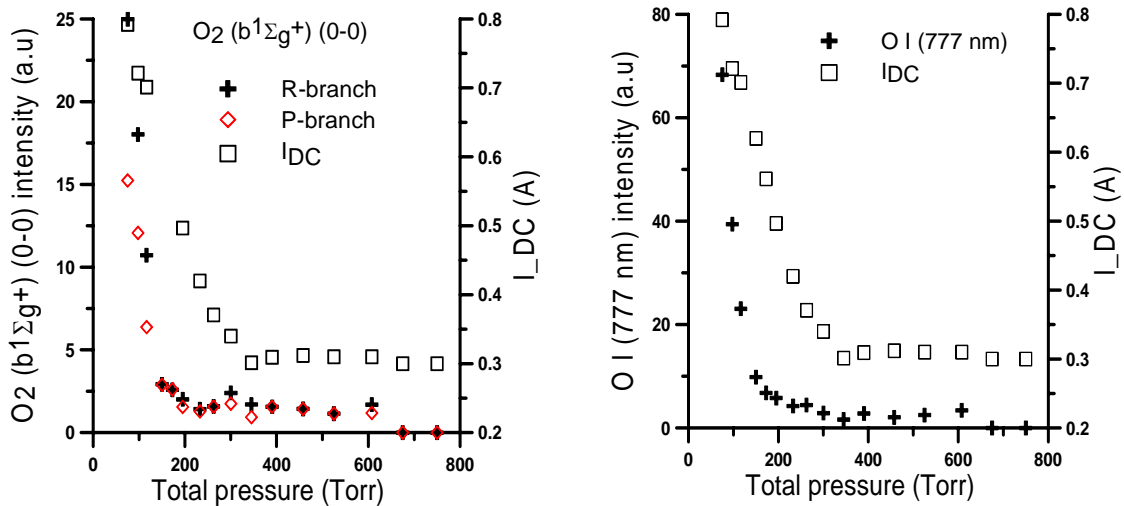


Fig.IV.34. a)  $O_2(b^1\Sigma_g^+)$  (left) and b)  $O I(777 \text{ nm})$  (right) emission intensities (a.u) and  $I_{DC}$  (A) as a function of total pressure at 20 kHz.

It is seen from Fig.IV.34a that increasing the absolute pressure results in a rapid decrease of the electronically excited oxygen concentration. The discharge parameter ( $pd$ ) ( $p$ -pressure,  $d$ -inter electrode distance) increases with the pressure increase, at fixed  $d$ . Moreover, let us recall the

importance of operating the discharge at reduced electric fields  $E/n$ . When increasing the total pressure  $p$ , the number density  $n$  increases, thus resulting in a decrease of the reduced electric field. Furthermore these results can be explained by the fact that quenching mechanisms by collisional de-excitation are of great importance at higher pressure.

Figure IV.34b shows atomic oxygen emission intensity as a function of total pressure at same conditions as in figure IV.34a. An additional remark is that the present non-self-sustained crossed discharges remain stable and diffuse at high pressures, contrary to self-sustained discharges.

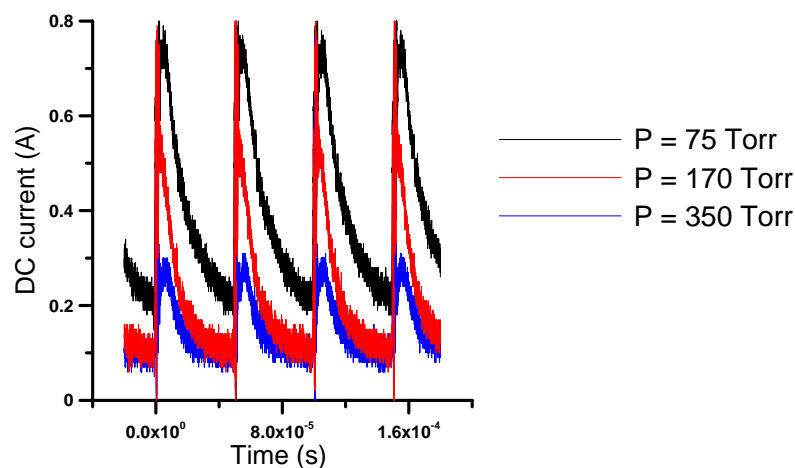


Fig.IV.35. Effect of pressure on DC sustainer current (A) at 20 kHz pulse repetition rate.

In Figure IV.35, the DC sustainer current decay between ionizing pulses is shown for three different pressures. In the three cases, one can observe that between the pulses the decaying plasma remains positive. On one hand, when increasing pressure from 75 Torr to 350 Torr, the maximum DC current is significantly reduced (by a factor 2.5); on the other hand, the DC current is more rapidly decreased. In such conditions, we could expect that electron density is decaying due to electron recombination and attachment.

At high pressure conditions, in order to increase the sustainer discharge energy loading and to maximize the energy input into the singlet oxygen states, the pulse repetition rate should be sufficiently increased to avoid complete plasma decay between the high-voltage pulses.

### IV.3. Conclusions

The study of the electronically excited state  $O_2(b^1\Sigma_g^+)$  in a non-self sustained crossed discharge at relatively low pressure (100-300 Torr) allows detecting noticeable quantities of  $O_2(b^1\Sigma_g^+)$ . The discharge and post-discharge characterization by analysing the effects of pressure, DC sustainer voltage,  $O_2$  concentration as well as admixture of small quantities of NO on excited oxygen species evolution have been realized, allowing us to optimise the experimental conditions to maximize excited oxygen yield :

- one should work at reduced pressures (typically up to 120 Torr) ;
- one should consider highly diluted mixtures of  $O_2$  in helium (a few percent of  $O_2$  in the mixture) ;
- one should add at most 500 ppm NO to the mixture ;
- one should maximize DC voltage but of course avoid arcing conditions.

In this manner, excited species are still visible up to 1 cm outside of the CDR.

The post-discharge reveals the same trends. Temperature calculations show that the flow temperature rise in the discharge is rather modest, in the order of 10 to 60 degrees without NO, while 120 K is found with NO admixture in the  $O_2/He$  gas mixture. Therefore, in the presence of NO, careful experiments should be done to distinguish the chemical and the heating effects of the discharge. It is now time to describe applications of excited oxygen species in plasma-assisted combustion experiments.



# Chapter V : Hybrid burner development for combustion intensification

## Abstract

---

Plasma-enhanced combustion is an innovative concept for improving the ignition, efficiency and stability of combustion. We have demonstrated that a crossed discharge non thermal plasma reactor combining pulsed DBD and DC discharges is an efficient way to generate electronically excited oxygen species. Experimentally, singlet oxygen generation has been performed in O<sub>2</sub>/helium mixtures, from reduced pressure up to atmospheric conditions and for different discharge parameters. It is now possible to produce a detectable quantity of O<sub>2</sub>(b<sup>1</sup>Σ<sub>g</sub><sup>+</sup>) (and a fortiori O<sub>2</sub>(a<sup>1</sup>Δ<sub>g</sub>)), as theory indicates that O<sub>2</sub>(a<sup>1</sup>Δ<sub>g</sub>) concentrations should be 4 to 10 times the O<sub>2</sub>(b<sup>1</sup>Σ<sub>g</sub><sup>+</sup>) concentrations [41]) molecules at atmospheric pressure. On the other hand, it has been shown numerically that the ignition delay time and the ignition temperature can be significantly reduced in the presence of electronically excited oxygen in the fresh gas mixture. Also, it has been numerically demonstrated that the flame speed can be considerably increased and that the main radical H, O and OH concentrations are increased.

The aim of this chapter is to study experimentally how combustion processes change in the presence of excited oxygen species that, in turn, are expected to react faster with hydrocarbon molecules and intensify combustion. Two specific burners (1- counterflow diffusion burner working at atmospheric pressure; 2- partially-premixed burner working at reduced pressure) have been developed. The same plasma reactor as described in previous chapters is used in these hybrid burners. The detection of excited radicals such as CH\*, C<sub>2</sub>\*, OH\*, as well as O\* atoms and O<sub>2</sub>\* has been performed using optical emission spectroscopy, in order to demonstrate combustion changes resulting from the presence of the excited species in the discharge.

This chapter describes the experimental set-ups. Spectroscopic and imaging results, at atmospheric and low pressure, for the flame with and without plasma enhancement are presented and discussed.

---

## V.1. Atmospheric pressure counter-flow diffusion flame

At first, we will briefly describe what is a counter-flow diffusion flame and the interest that brings this type of flame in the general context of research in combustion. Afterwards, we will present the experimental plasma burner prototype developed for such a flame configuration.

Finally, we will present the emission spectroscopy in the on/off discharge conditions and discuss about the choice of a new plasma burner prototype.

### V.1.1. General description of the counter-flow configuration

The counterflow flame configuration is a well-defined configuration where flames are stabilized between opposing flows of fuel and oxidizer. By sending a jet of oxidizer against a fuel jet and by lighting the mixture near the stagnation plane of these two jets, one obtains a so called counterflow nonpremixed (or diffusion) flame (Fig.V.1).

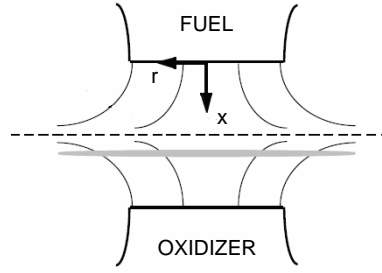


Fig.V.1. Schematic configuration of the counter flow burner.

Such a flame, with e.g. air as oxidant and methane as fuel is a stable and flat flame, characterized by a reaction zone near the stagnation plane. The opposed-flow geometry is an attractive experimental configuration, because the flames are flat, allowing for detailed study of the flame chemistry and structure. Moreover, the stability of such flames and their reproducibility allows experimental studies that can be compared to theoretical ones. One further advantage of such flame configurations is an easy optical access allowing application and development of optical diagnostics. Therefore, this configuration has been retained for the first experiments.

The equivalence ratio of a non-premixed laminar flame  $\Phi$  is defined as :

$$\Phi = \frac{(Y_{combustible} / Y_{oxidizer})_{mixture}}{(Y_{combustible} / Y_{oxidizer})_{stoichio}} \quad (\text{Eq.V.1})$$

where  $Y$  is the mass fraction of combustible or oxidizer and stoichio means stoichiometric values.

To calculate the equivalence ratio, we have to calculate the mass flow rates:

The volumetric flow rate is equal to  $(S \times v)$  and the mass flow rate to  $(\rho \times S \times v)$ , where  $S$  is the slot surface in  $\text{m}^2$  and  $v$  is the injection speed in  $\text{m.s}^{-1}$ .

Also, the perfect gas law has to be considered. The volumetric mass of  $\text{O}_2$  and  $\text{CH}_4$  are calculated as follows :

$$\rho_i = \frac{P \times M_i}{R \times T} \quad (\text{Eq.V.2})$$

where  $i$  designate  $\text{O}_2$  and  $\text{CH}_4$  respectively and  $P$ , the absolute pressure.

The strain rate  $\varepsilon$ , is defined [208] :

$$\varepsilon = \frac{2v}{d} \times \sqrt{\frac{\rho_f}{\rho_o}} \quad (\text{Eq.V.3})$$

where  $v$  is the identical injection velocity of the fuel and oxidizer flows,  $d$  is the burner separation distance,  $\rho_f$  is the density of the diluted fuel and  $\rho_o$  is the oxidizer density.

This counterflow configuration seems at first perfectly suitable for the study of the interaction between excited species produced by the plasma generator and the reaction zone of the flame. Moreover, in order to identify fundamental properties of the flame, it is interesting to work with such a configuration, where the parameters influencing the flame structure are easily controlled and their effects easily measurable. The flame is situated nearby the stagnation plane, far from all boundaries; thus, the use of non intrusive optical diagnostics is possible. One can observe with good accuracy the effects of the plasma oxidizer activation on the fine flame structure.

## V.1.2. Hybrid burner configuration

The technological solution for the insertion of excited oxygen species generated by the crossed discharge plasma reactor is shown in Figs.V.2 and V.3. A dedicated counter-flow burner has been conceived, into which the generated excited oxygen is injected.



Fig.V.2. From left to right : counter-flow diffusion flame burner (lower burner fitted with the discharge cell) ; direct view of the  $O_2$  injection cross-section.

This counter-flow diffusion burner consists essentially of two identical parts: the upper part is for the fuel, while the bottom one is for the oxidizer. Each of these consists of a rectangular injection slit (6.5 mm wide and 48 mm long), through which the gases are injected. They are surrounded by a larger slit, used to inject a nitrogen flow shield. This nitrogen flow prevents the flame from influences by the surrounding atmosphere. Besides, it allows for perfectly controlling the quantities of combustible and oxidizer, injected into the reaction zone and limits the velocity gradient around the main flow, that could lead to instabilities and perturbation of the reacting flows. For the oxidizer section the corresponding slit walls consist of the two electrodes, placed 6.5 mm from each other. Figure V.2 shows a photograph of this burner configuration. The right picture of fig.V.2 presents details of the oxidizer/helium injection. The screws visible in the right figure allow to change the distance between the fuel and oxidizer injection heads (usually placed at 1 or 2 cm from each other). Fitting directly the oxidizer injector on the discharge electrodes allows working with the largest possible quantity of excited oxidizer. It leads to the smallest time for excited molecules to reach the flame front.

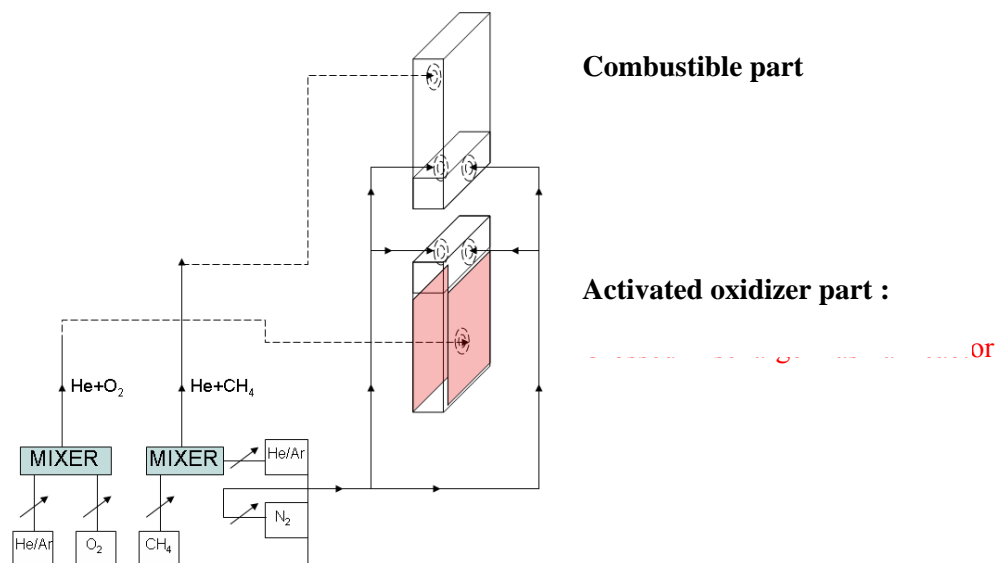


Fig.V.3. Schematic of the counterflow burner and gas feeding installation.

The scheme presented in Fig.V.3 shows the installation and gas feeding network for the counterflow diffusion flame generation. Oxygen and methane are injected to respective mixers with helium as diluting agent. One goes to the upper combustible part of the burner and the other to the lower oxidizer part. For the nitrogen shield, the flow is splitted at the exit of the flowmeter into two parts, one for the upper part, and the other for the lower part. In each burner part, stainless steel grids and 2 mm diameter glass balls are used to get a homogeneous gas flow.

The oxidizer part of the counterflow burner integrates the crossed discharge plasma chemical reactor described in chapter IV. The body of the CDR is executed from Peek plastic and Plexiglas. Both electrodes of the pulse barrier discharge are made of copper and are insulated from the flow by dielectric of 1 mm thickness made of 99.9 % purity  $\text{Al}_2\text{O}_3$  (dimension: planar  $60 \times 48 \times 1 \text{ mm}^3$ ); the gas gap is 6.5 mm (pulse gap). Perpendicular to these electrodes, two stainless steel DC electrodes with a rounded edge profile are mounted. In this section, all presented experiments have been conducted at atmospheric pressure, with a pulse generator frequency fixed at 10 kHz and with a discharge power of 100 W.

An important step of the project has been the determination of the best, stable burning conditions for the flame. For this purpose, we ignite with pure methane and an air-like oxidizer, i.e. with the corresponding percentage of oxygen in the  $\text{O}_2/\text{He}$  mixture, using a global equivalence ratio of 6.8 and a strain-rate  $\varepsilon = 180 \text{ s}^{-1}$  (for a distance between burners of 1 cm). Due to buoyancy, the initial flame is displaced upwards. Finally, the air flow rate and the distance between the oxidizer and fuel injectors are adapted in order to stabilize the resulting flame. After reaching stabilization of the flame, the oxygen content in the  $\text{O}_2/\text{He}$  mixture can be modified easily. A typical flame obtained with such a procedure is shown in fig.V.4.

The diffusion flame establishes nearby the counterflow stagnation plan. This flame is flat (see fig.V.4), has a unidimensional structure in its central part and is subject to convection effects at the boundaries; the hot gases going up, bend the flame.

The flow rates of  $\text{O}_2$  and  $\text{CH}_4$  are controlled by Rosemount flow-meters. For the results shown here, the final methane flow-rate is 0.52 l/min and the oxygen flow rate is 0.155 l/min. A  $\text{N}_2$  coflow of 20 l/min is injected from both sides. These flows result in ejection velocities of  $30 \text{ cm.s}^{-1}$ , which leads to a strain rate of  $180 \text{ s}^{-1}$  and an equivalence ratio of 6.8. All gases are injected at room temperature and atmospheric pressure.

The gas feeding is performed from 200 bar bottles. Considerable care is taken to ensure cell cleanliness and  $\text{O}_2$  purity. Oxygen with a purity better than 99.99% is used (Airlaz). Gas pressures are measured with a Bourdon type pressure gauge.

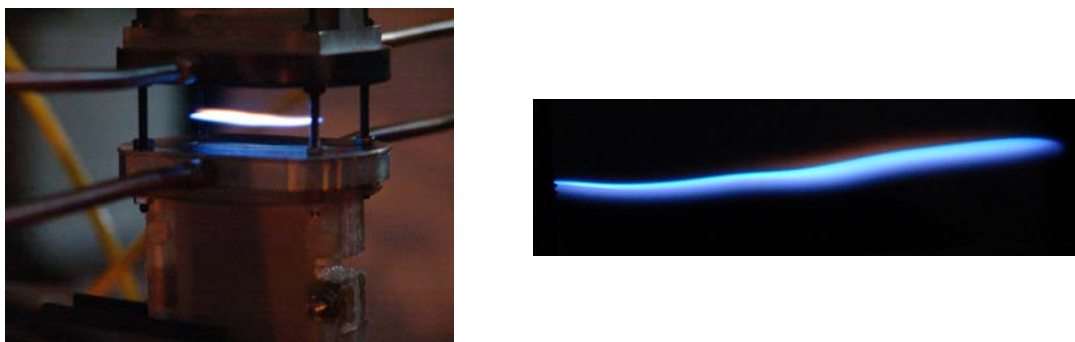


*Fig.V.4. Typical counter-flow flame obtained with this set-up.*

Optical emission spectroscopy is used for diagnostics of this reactive plasma and flame. Spectra of the flame-plasma discharge were obtained by emission spectroscopy in the wavelength range of 153-980 nm.

As verified in chapter IV, heating effects induced by the CDR are rather small and expected to be negligible (i.e. increase by 60 K without NO addition). Within these experimental conditions, a rotational temperature of 325 K is found with an uncertainty of  $\pm 10 \text{ K}$ . Therefore, excited species and radicals produced by the discharge can only be the result of chemical excitation by the discharge.

### V.1.3. Influence of the plasma on flame shape

The following pictures show the effect of oxidizer plasma activation on the macroscopic flame behaviour.

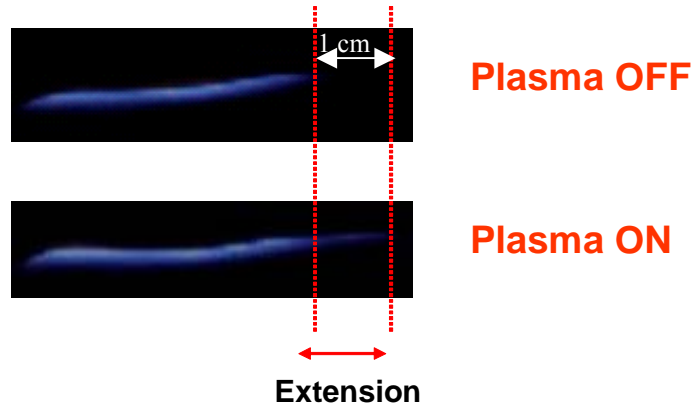


Fig.V.5. Effect of discharge on the shape of the counterflow flame ( $\Phi = 6.8$ ).

It is clearly seen that a more elongated flame is obtained in the presence of the plasma discharge. Indeed, a reproducible supplementary flame front with a weak, blue light emission has been observed (a  $\sim 1$  cm length flame extension is observed in Fig.V.5).

Finally, we also observed that the flame is stable at higher strain rate with the discharge ON. The extinction limit of this flame has therefore been investigated. The equal injection velocities of fuel and oxidizer are increased gradually, while keeping all other parameters fixed. At some point, the flame extinguishes. In the presence of plasma, the injection gas velocities at which the flame extinguishes was increased by 10% which corresponds to an extinction strain rate of  $270 \text{ s}^{-1}$ . This supports qualitatively the numerical results presented in section III.2.4.6.

### V.1.3. Plasma effects on flame emission spectroscopy

For a deeper investigation of the flame front, emission spectroscopy was carried out. The typical radical structures, especially  $\text{CH}^*$ , are expected to be more intense with the discharge. Emission spectra corresponding to the following transitions will be presented (Table V.1).

molecule/atom	transition	vibration	wavelength $\lambda$ (nm)
OH	$A^2\Sigma^+ - X^2\Pi$	$\Delta v=0$	307
CH	$A^2\Delta - X^2\Pi$	$\Delta v=0$	431
$\text{C}_2$	$d^3\Pi_g \rightarrow a^3\Pi_u$	$\Delta v = -1$	560
$\text{C}_2$	$d^3\Pi_g \rightarrow a^3\Pi_u$	$\Delta v = 0$	515
$\text{C}_2$	$d^3\Pi_g \rightarrow a^3\Pi_u$	$\Delta v = +1$	470
O	$^5S - ^5P$		777

Table V.1. Molecules detected by spectral analysis of chemiluminescence of the laminar counterflow methane-oxygen-helium flame (equivalence ratio :  $\Phi = 6.8$ ).

Visible emission spectra of the flame have been obtained at atmospheric pressure. The figures of the present section (Figs.V.6 to V.9) summarize the results obtained in a  $\text{CH}_4 - \text{O}_2/\text{He}$  counter flow flame. CH (430 nm A-X band system),  $\text{C}_2$  (Swan bands), and OH ( $A^2\Sigma^+ \rightarrow X^2\Pi$  system) radicals have been detected in the flame. Oxygen atoms have been also detected and the O atomic lines at 777 nm

can be clearly identified. In complement to results presented in this section, spontaneous emission fingerprints of  $\text{OH}^*$ ,  $\text{C}_2^*$ ,  $\text{O}^*$ ,  $\text{C}_2^*$  and  $\text{OH}^*$  are detailed in appendix 7.

It is particularly evident for  $\text{CH}^*$  (Fig.V.6), which is one of the most important tracers of the reaction zone, that the comparison of the spectra taken without and with the discharge shows that the spectral structure is more intense when activating the discharge. The spontaneous emission of  $\text{CH}^*$  radicals increases by 22 % at its peak when activating CDR. As expected, the effect of the discharge on the production of O atoms is also very high (fig.V.7).

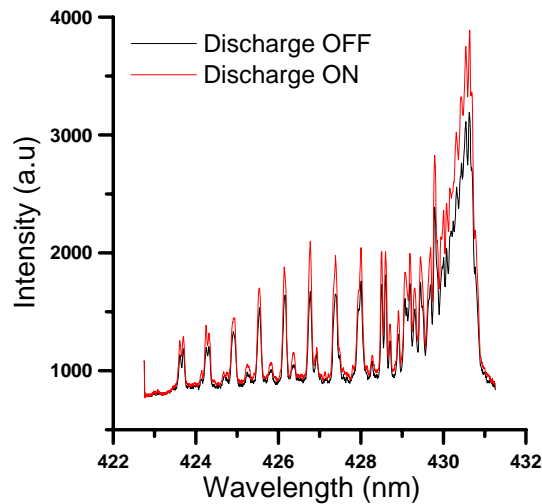


Fig.V.6. Effect of the discharge on spontaneous emission spectra of  $A^2\Delta - X^2\Pi$  transition of R-branch CH radical in counter flow diffusion flame ( $\text{CH}_4$ ) / ( $\text{O}_2 + \text{He}$ ).

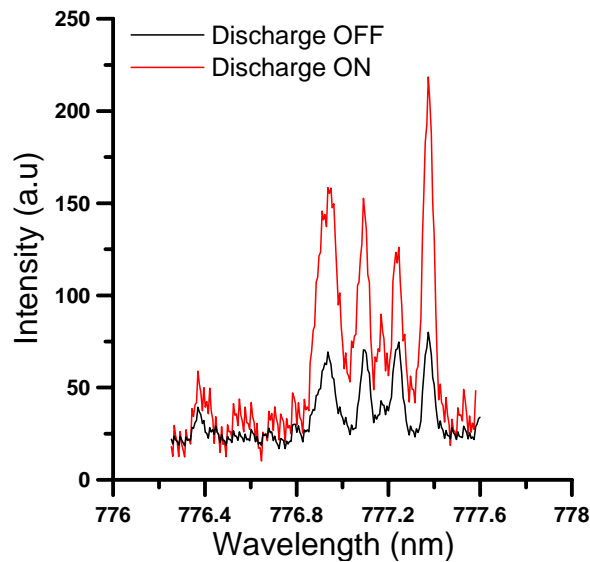


Fig.V.7. Effect of the discharge on spontaneous emission spectra of O atoms ( $^5S - ^5P$  transition) in counter flow diffusion flame ( $\text{CH}_4$ ) / ( $\text{O}_2 + \text{He}$ ).

The following figures (Figs.V.8) focus on the  $\text{C}_2$  Swan bands. These bands, which are due to the ( $d^3\Pi_g \rightarrow a^3\Pi_u$ ) transition, have been registered in the absence and presence of plasma.

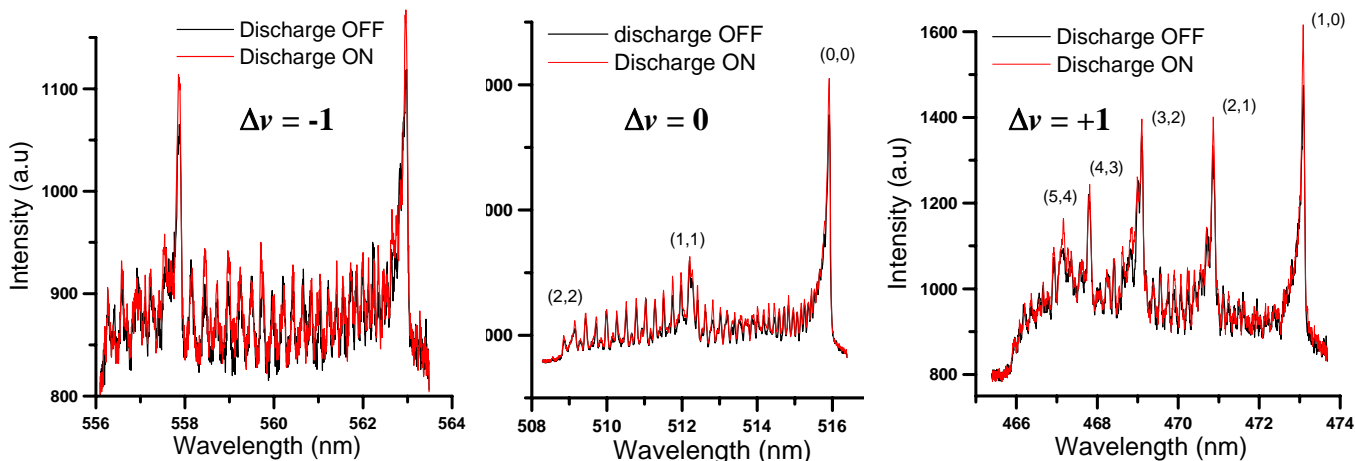


Fig.V.8. Effect of the discharge on spontaneous emission spectra of  $C_2$  (Swan band  $d^3\Pi_g \rightarrow a^3\Pi_u$ ,  $\Delta v = -1$  (left),  $\Delta v = 0$  (middle) and  $\Delta v = +1$  (right) in counter flow diffusion flame ( $CH_4$ ) / ( $O_2+He$ ).

The main peaks (heads) are more intense when activating the discharge. For  $C_2$  ( $\Delta v = -1$ ), the spontaneous emission of this system increases by 5 % at its peaks. This enhancement of  $C_2$  radical emission is also observed for the other  $C_2$  systems. This increase reaches 10 % for the  $\Delta v = +1$  and  $\Delta v = 0$  band systems.

Finally, the effect of oxidizer activation on OH (A-X) emission is presented in Fig.V.9.

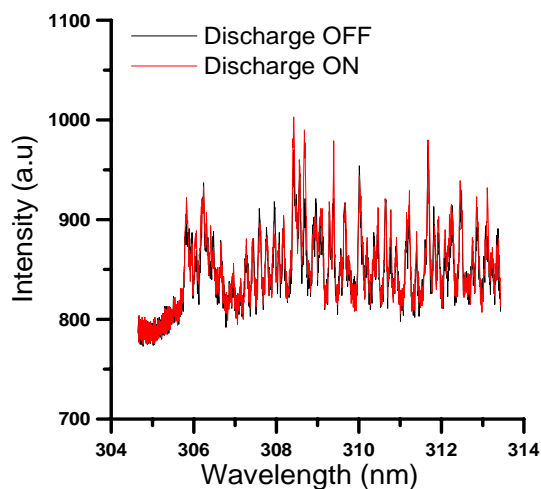


Fig.V.9. Effect of discharge on spontaneous emission spectra of OH ( $A^2\Sigma \rightarrow X^2\Pi$ , (0,0)) in counter flow diffusion flame ( $CH_4$ ) / ( $O_2+He$ ).

The spontaneous emission of OH\* radicals has been recorded to show the modification of combustion with the discharge, but emission intensity remains almost constant (increase of 3%). The generation of additional chemically active radicals by the non thermal plasma discharge demonstrates the interest of CDR on combustion intensification.

## V.1.4. Conclusions on counterflow configuration

The counterflow configuration is usually considered as a reference configuration, since it is very stable, well controllable, and has been extensively investigated and characterized in hundreds of studies. We therefore decided to retain it for the first measurements. The positive conclusions of this study are :

1- It is indeed possible to integrate the plasma discharge (CDR) in the burner.

2- When activating the CDR, the flame structure is clearly modified; the active reaction zone becomes longer.

3- Using spectroscopy, it has been demonstrated that radical species concentrations increase noticeably when starting the CDR. Plasma activation leads to an increase of CH by 22%, of C<sub>2</sub> by 5% to 10%, of OH by 3%.

Nevertheless, a major problem appeared with this configuration: we have been unable to measure any excited oxygen in the flame region! Considering the results of the previous chapters, three main reasons explain this disappointing observation:

- Under atmospheric conditions, the production of excited oxygen is reduced, and the deexcitation is very fast.

- In a counterflow configuration, the distance between the injection slit and the flame is relatively long and cannot really be reduced.

- The O<sub>2</sub> concentration has to be very high when using air (21%) thus leading to very low O<sub>2</sub>(b<sup>1</sup>Σ<sub>g</sub><sup>+</sup>) concentration (see Fig.IV.31a).

This suggests suitable modifications :

1- The next burner should be adapted for low pressure conditions. Even if counterflow burners can in principle be employed at reduced pressure, this is quite complex.

2- Furthermore, it is advantageous to switch from a counter-current injection to a co-current injection. In this manner, the distance between the ejection slot and the flame can be reduced. Thus, the excited oxygen produced in the CDR can influence the reaction process immediately after leaving the discharge cell. Indeed, the influence of the excited oxygen species and radicals on the global combustion process depends on the location at which they are released. It would be useless to add supplementary radicals directly in the reaction zone due to the already existing species excitation, since the temperature is rather high there. The production of radicals from the discharge is negligible compared to those naturally formed due to the chemical reactions. On the other hand, if the radicals are produced too far before the reaction zone, they will recombine and only lead to a negligible temperature increase.

A partially premixed configuration would furthermore allow having a low O<sub>2</sub>-concentration flow through the CDR and adding further O<sub>2</sub> (necessary for combustion) through the primary premixed flow. It is therefore clear that another burner configuration as well as working at reduced pressure is essential to obtain a high impact of the discharge on the flame properties.

As a consequence, we decided to develop a co-current partially-premixed burner, integrating the discharge and suitable for low-pressure measurements. In order to facilitate optical characterization, a two-dimensional slot burner structure is retained.

## V.2. Low pressure co-flow hybrid burner for partially premixed combustion

### V.2.1. Introduction

We have demonstrated that at atmospheric pressure, the excited species produced in the discharge modify the flame structure and the spectral characteristics.

On the other hand, we have demonstrated that the production yield of excited oxygen species (particularly O<sub>2</sub>(b<sup>1</sup>Σ<sub>g</sub><sup>+</sup>) and O<sub>2</sub>(a<sup>1</sup>Δ<sub>g</sub>)) is increased at reduced pressure. Therefore a new burner, allowing to work at low pressure and in a partially premixed configuration has been developed in order to obtain stronger effects of O<sub>2</sub>(b<sup>1</sup>Σ<sub>g</sub><sup>+</sup>) and O<sub>2</sub>(a<sup>1</sup>Δ<sub>g</sub>) on the flame structure. It is worth noting that the amount and type of excited species present in the post-discharge at reduced pressure will certainly differ from that at atmospheric pressure. As a consequence, one could expect different chemical processes involved in the reaction zone.

The transport of these species to the reaction zone should highly influence the stabilization process and enhance combustion rate and this must now be checked experimentally. Therefore, the investigation of the combustion processes in the on/off discharge conditions will be carried out.

Emission spectroscopy measurements in the flame allow obtaining much more details on how combustion processes change for example by investigating spontaneous emission of main flame excited radicals  $\text{CH}^*$  or  $\text{OH}^*$  in presence of oxidizer activation. The modification of the flame structure by the plasma discharge is presented.

## V.2.2. Hybrid low-pressure partially premixed plasma-burner

A specific burner for a partially premixed flame configuration has thus been developed (Fig.V.10 and V.11), into which the generator of excited oxygen is incorporated. The secondary oxidizer injection ( $\text{O}_2/\text{He}$ ) integrates the discharge section (CDR).

The body of the burner is made of Peek plastic. Both electrodes (DC and pulse DBD) are similar to those described previously. The pulse barrier discharge electrodes were connected to the high voltage pulse power supply. Open DC electrodes have been made of stainless steel and their edges were rounded with curvature radius of about 3.2 mm. The open electrodes were connected to the high voltage DC power supply through matched high-voltage chokes and ballast resistance. The distances between DC electrodes and DBD electrodes are 36 mm and 6.5 mm respectively. The DC voltage is adjusted from 0 up to 2 kV, DC current changed from 0 to 1 A.

The electrical external circuit is described in section IV.2.2.3. Adjustable ballast resistors are connected in series with the DC power supply, the resistance has been set to 940 Ohms.

The low pressure tank (Fig.V.10 and V.11) has been developed specifically for combustion at low pressure. The experimental arrangement is shown in Fig.V.10. The vacuum tank volume is approximately 40 litres. Between the runs, the vacuum tank is pumped down to a few Torr using a two stage Edwards's high vacuum pump (80  $\text{m}^3/\text{h}$ ). Furthermore, the test section pressure and the mass flow rate can be varied independently. This makes the experimental facility suitable for combustion studies and a dump tank is placed between the test section and the high vacuum pump in order to attenuate possible pressure fluctuations. A water cooling system is built on top of the low pressure tank and condensed water droplets are collected via a circuit to a collector. Moreover, a safety valve has been integrated for the case of overpressure in the tank.

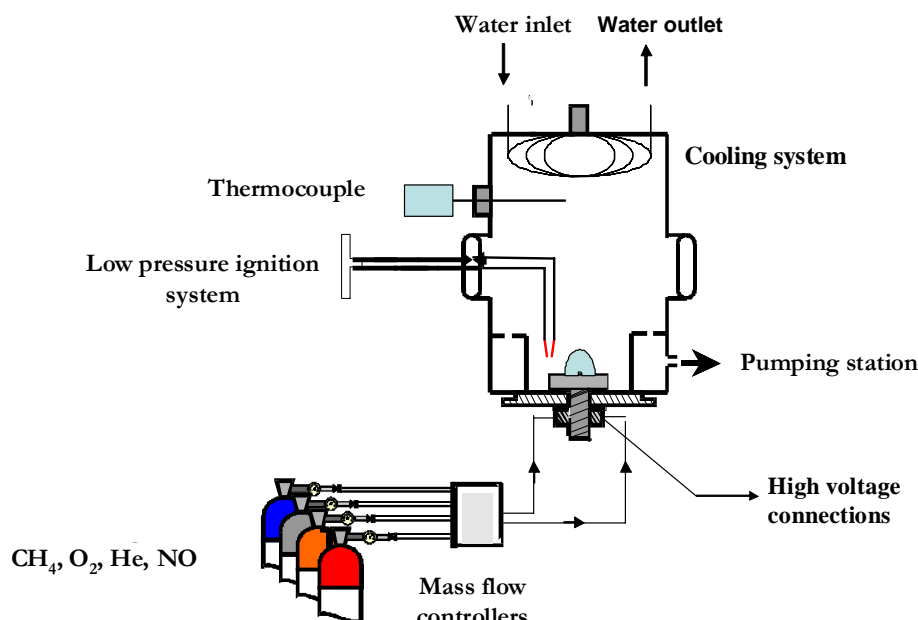
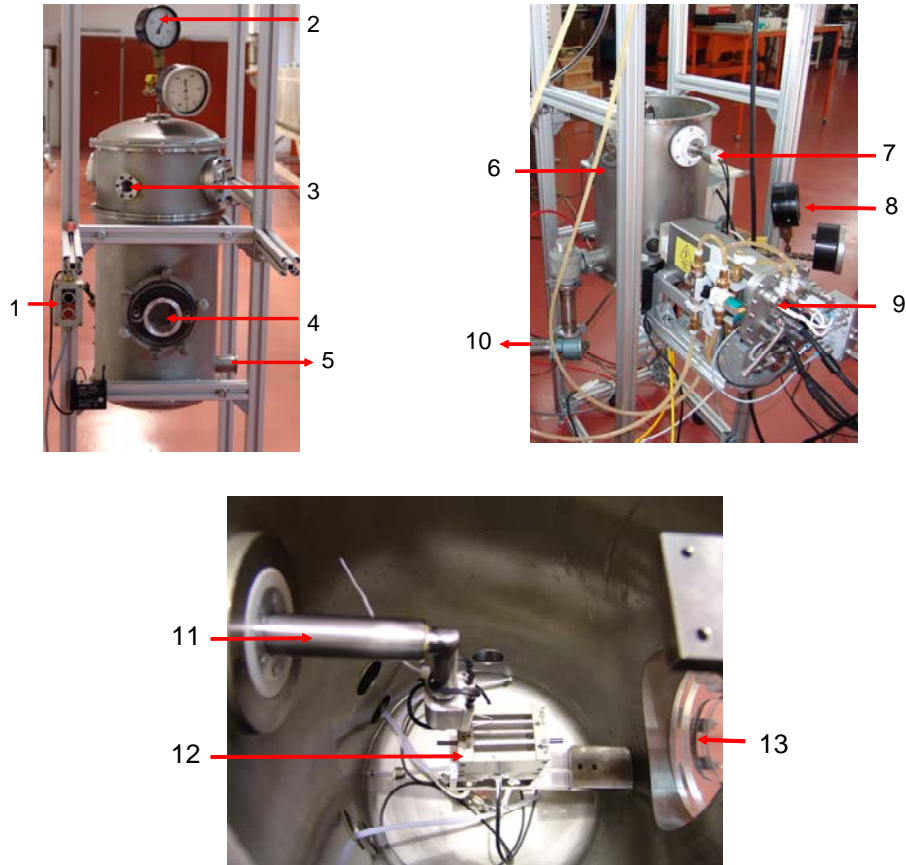


Fig.V.10. Low pressure tank with hybrid burner and connections.



*Fig.V.11. Different views of the low pressure tank housing the hybrid burner.*

1 : voltage source for flame ignition ; (2, 8) : pressure control ; (3, 4, and 13) : CaF<sub>2</sub> visualisation windows ; (5, 10) : pumping line ; 6 : low pressure tank ; (7, 11) : low pressure ignition system ; 9 : pulsed high voltage unit ; (12) : hybrid burner.

Four removable CaF<sub>2</sub> windows allow the use of optical diagnostics. The gaseous mixture was ignited with the use of a continuous spark.

The elaboration of the hybrid plasma-burner prototype for low pressure was made in several stages. Our original objective was the realization of a flame configuration allowing excited oxygen post-discharge flow to reach immediately the flame reaction zone and allowing working at low pressure (thus considerably decreasing the quenching of excited oxygen). In order to increase energy input and to get a nicer discharge, flow uniformity of the gas mixture through the discharge gap has been improved. Several improvements have been implemented :

- First, the gas injection is performed perpendicular to the slot. Also, micro-porous glass (porosity 2) has been inserted downstream of the gas injection.
- Working with the high voltage connections inside the low pressure tank leads to major problems. Therefore, the high voltage connections are done outside of the low pressure tank, avoiding the difficulty of low pressure passage and parasitic discharges.
- All holding parts and screws were made of non conductive material, and high voltage cables were additionally insulated from each other. Hermetically sealed connections were improved in order to avoid leakage problems.

Several construction steps have led to the final version of the burner. In order to avoid any leakage, reduce electromagnetic compatibility problems and speed-up burner integration, four different burner configurations have been developed during the project. Only the fourth (optimized) version of the hybrid burner is shown in Fig.V.12 and described in what follows.

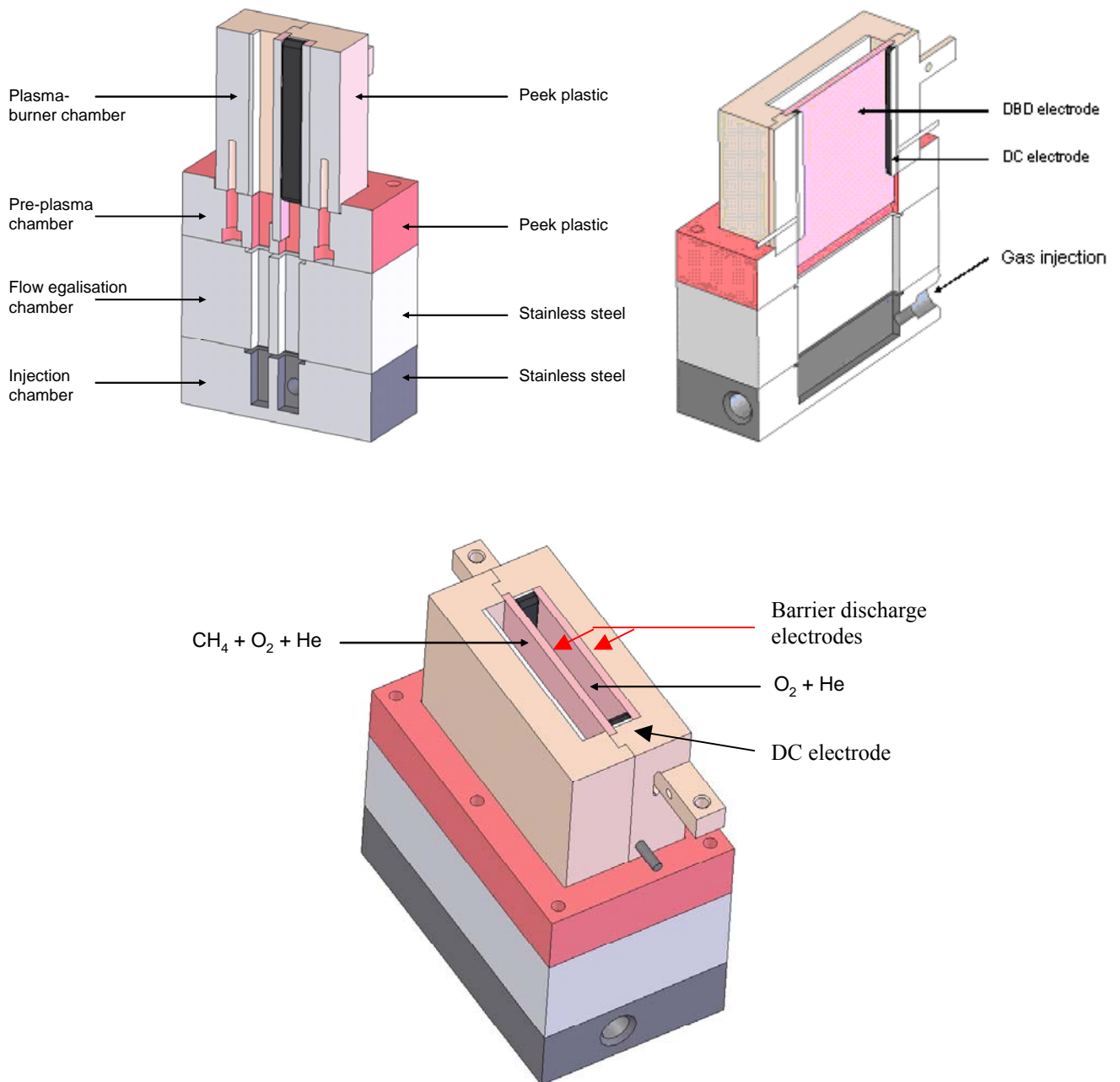


*Fig.V.12. Hybrid slot plasma-burner views.*

The optimized burner consists of two adjacent slots of rectangular cross section sharing an interface that is one of the DBD electrodes. The fuel (methane) and oxidizer (oxygen + helium) flow from the two channels in the base of the burner.

Before the discharge section, three flow equalisation stages are present. The secondary oxidizer and primary mixture slot exit dimensions are  $(6.5 \times 56) \text{ mm}^2$  and  $(5.5 \times 56) \text{ mm}^2$ , respectively. The flow enters the rectangular cross sections and passes successively through a fine grid made of brass, 2 mm diameter glass beads and a glass fiber sheet, which also serves as a flashback stop, and then, for the secondary oxygen, passes between the two electrode blocks.

The two stainless steel DC electrodes are of dimensions  $48 \times 6.5 \times 3 \text{ mm}^3$ . DC electrodes are rounded at the edges to prevent high electric field concentrations and “hot spot” formation in the plasma near the edges. Rounding dimensions are  $R= 0.5$  and  $R= 1.5 \text{ mm}$ . A schematic of the electrodes is presented in Fig.V.13.

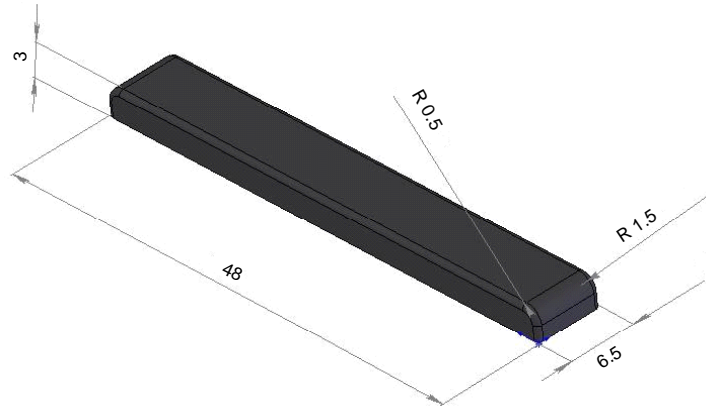


*Fig.V.13. Stainless steel DC electrode.*

The pulsed electrodes, made of stainless steel and insulated from the flow by alumina ceramic plates (1 mm thick each), are powered by a high voltage ( $\sim 20$  kV), short pulse ( $\sim 20$  ns), high repetition rate (up to 25 kHz) plasma generator. The DC electrodes are powered by a Glassman DC power supply 3 kV, 3 A, operated in the voltage-stabilized mode. DC electrodes are placed at both lateral sides of the secondary oxidizer slot.

The external electric circuit and the measurements probes are the same as in previous experiments (Appendix 6). A bridle made of Peek plastic integrating the burner has been developed to fit to the low pressure tank (see Fig.V.10). In such a configuration, the electrical connections are performed out of the low pressure tank, which appears to be a much better solution. Moreover, thanks to the integration of the hybrid burner in a bridle connected to the low pressure tank, pumping system and mass flow meters, the discharge pressure (i.e. stagnation pressure) and the mixture compositions can be varied independently. This makes the experimental facility suitable for combustion studies, both in low-pressure and at intermediate pressure flows.

Gas supply is performed by B50 gas bottles. Gases purity is summarized in table V.2 :

Gas	CH <sub>4</sub> (4.5)	O <sub>2</sub> (3.5)	He (4.6)	NO (N30)
Purity	$\geq 99,995$	$\geq 99,95$	$\geq 99,996$	$\geq 99,9$
Impurities		N <sub>2</sub> + Ar $\leq 500$ ppm H <sub>2</sub> O $\leq 2$ ppm	O <sub>2</sub> $\leq 5$ ppm N <sub>2</sub> $\leq 20$ ppm H <sub>2</sub> O $\leq 5$ ppm	N <sub>2</sub> and other nitrogen oxides: 0.1%

*Table V.2. Gases purity.*

The experimentally used gas feeding supply system is illustrated in Fig.V.14.

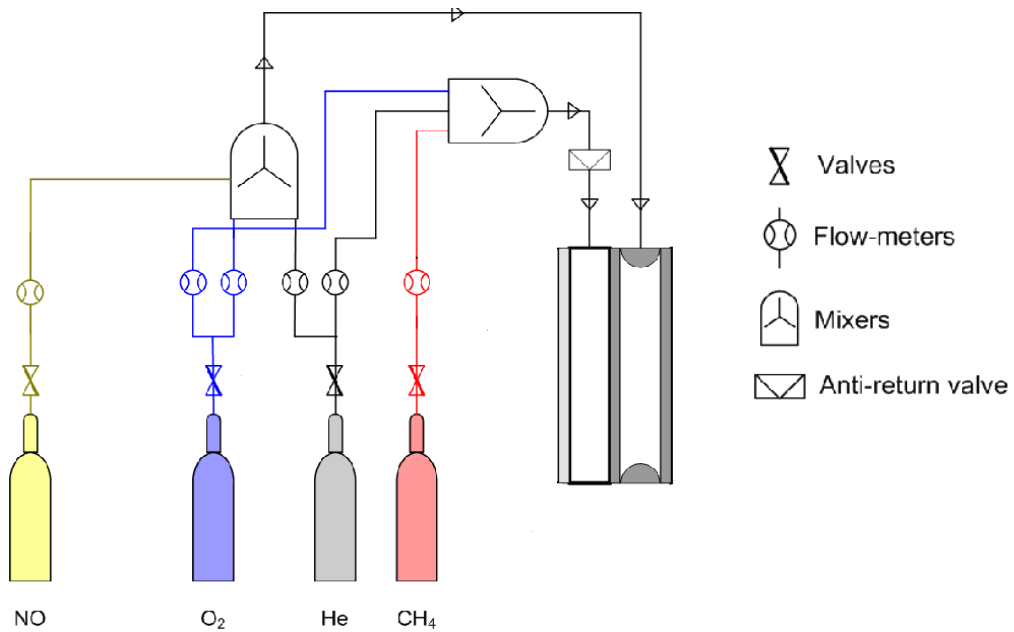


Fig.V.14. Gas feeding for premixed and partially premixed flame.

Helium is connected to a divider allowing the initial helium flow to be divided into two streams: one is sent to a first mixing chamber that will constitute the primary mixture (with  $\text{CH}_4$  and  $\text{O}_2$ ). This mixture is then sent to a burner slot. The second part is sent to a second mixing chamber to form a binary mixture with oxygen. This binary mixture supplies the other crossed discharge plasma slot of the hybrid burner.

The flow control system is composed of six Bronkhorst flowmeters. The whole system is controlled by Bronkhorst HI-TECH series 600 controller, interfaced to a personal computer. Flow meters are calibrated for each gas individually in 7 calibration points within the total range of operation (0 to 2  $\text{m}^3/\text{h}$ ). Thanks to this calibration, the delivered flows can be adjusted with a precision higher than 1%.

Experimentally, the excited oxygen produced in the generator will interact with the premixed flame. Considering the fact that on one hand, higher production of excited oxygen is obtained at lower  $\text{O}_2$  concentration (as demonstrated previously), and on another hand taking into account the stability and homogeneity of the plasma, a maximum content of 6%  $\text{O}_2$  is optimal. But this amount is not sufficient to obtain a stable combustion. Therefore, a primary, premixed flame is used to ensure stable combustion.

The term “partial premixing” is commonly used to refer to the technique of adding oxygen (in quantities less than required for the rich flammability limit) into the fuel. The rich fuel mixture then reacts with oxygen in the combustion chamber. Intentional partial premixing is practiced for reasons of flame stabilization and pollutant emission control. About 30% of natural gas is burnt in the partially premixed mode (Warnatz et al. [225]). This technique is also used in the present burner; the central, premixed feed relies on standard oxygen and ensures a stable flame. A secondary injection involves excited oxygen species at low oxygen volume fraction, in order to ensure a high production rate of excited oxygen.

Output voltage and current of our pulse generator significantly depend on the load. In the case of a real load, as the hybrid plasma-burner, a part of the energy is dissipated into the load and the remaining part is reflected back. We have precisely measured how the output waveforms of the high voltage pulse generator is distorted (current, voltage and calculated power) and we have checked that the crossed discharge electrical characteristics evolve as before. The pulse energy is  $\sim 6.9$  mJ, the maximum voltage is  $\sim 20$  kV, the maximum pulse current is  $\sim 55$  A and the maximum power is  $\sim 570$  kW.

Considering the energy provided to the discharge (7 mJ), this corresponds to an average power of 140 W at 20 kHz frequency.

## V.2.3. Plasma without flame

### V.2.3.1. Direct images

A picture from the image seen through the visualisation window in the absence of discharge is presented in Fig.V.15.

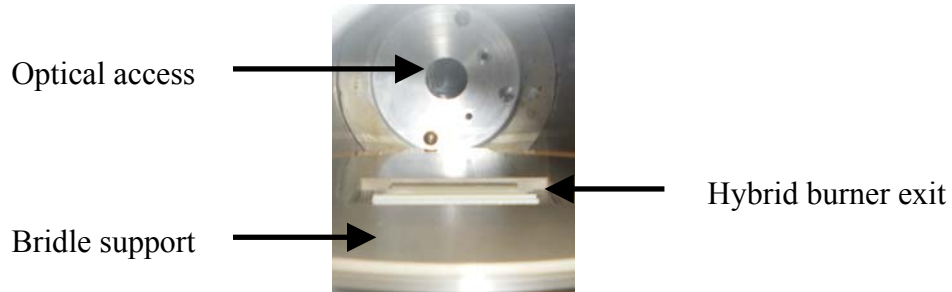


Fig.V.15. Hybrid burner vision picture in the absence of discharge.

A set of discharge pictures in different experimental conditions are shown in Figs.V.16.

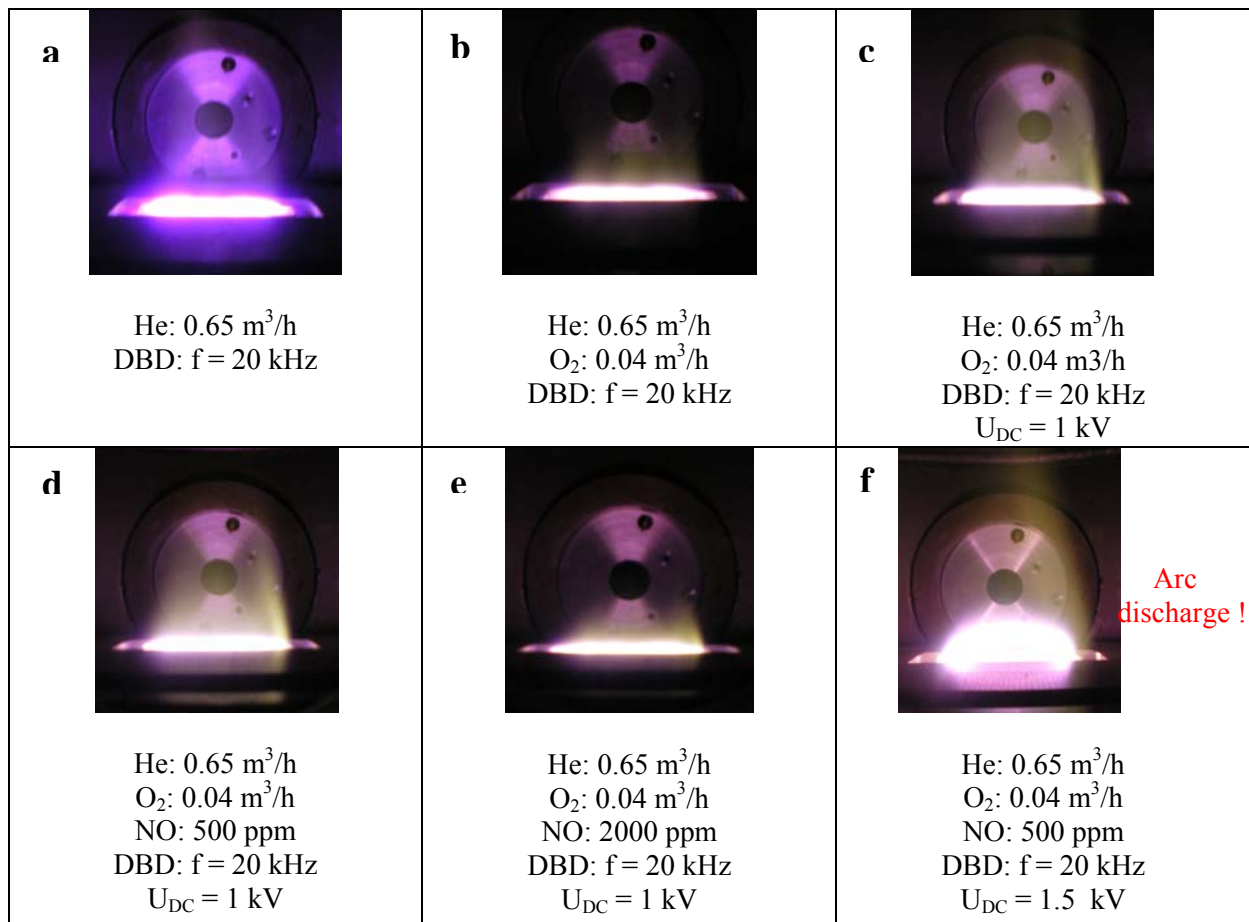


Fig.V.16. Photographs of the pulsed discharge plasma (visualized through the circular CaF<sub>2</sub> window in the low pressure tank) in O<sub>2</sub>/He (NO) flow at P = 120 torr, f = 20 kHz and U<sub>DC</sub> = 0 - 1.5 kV. The flow direction is from bottom to top.

In the entire range of experimental conditions, the pulsed plasma appeared diffuse and stable in the volume. The visible light emission corresponds to the post-discharge region. Indeed, in these

experimental conditions, a post-discharge downstream of the plasma region can be observed. In the case of pure helium gas, the discharge colour is violet (Fig.V.16a). Presence of oxygen leads to a whiter colour (Figs.V.16b to 16f). Increasing the DC sustainer voltage extends this downstream of the discharge section (Figs.V.16c and 16f). Furthermore, at fixed conditions, when adding a low concentration of NO ( $\leq 500$  ppm), the post-discharge length is increased (Fig.V.16d). It is worth noting that increasing further NO concentration leads to a shorter post-discharge length (Fig.V.16e), supporting results of chapter IV. Finally, at higher DC sustainer voltage of 1.5 kV, the discharge current path contracts and the plasma thermalizes into an arc discharge regime (Fig.V.16f). Spectral measurements, as described in section IV.2.3, show the presence of excited oxygen species  $O_2(b^1\Sigma_g^+)$  and excited atomic oxygen  $O^*$ .

### V.2.3.2. Generation of excited oxygen species

Figure V.18 shows the generation of large amounts of active oxygen species when crossing the pulsed discharge with a DC sustainer voltage. In the case with only DBD, no excited oxygen species can be measured in the post-discharge. For better understanding of following figures, in figure V.17, the reactor geometry is summarized in the scheme below :

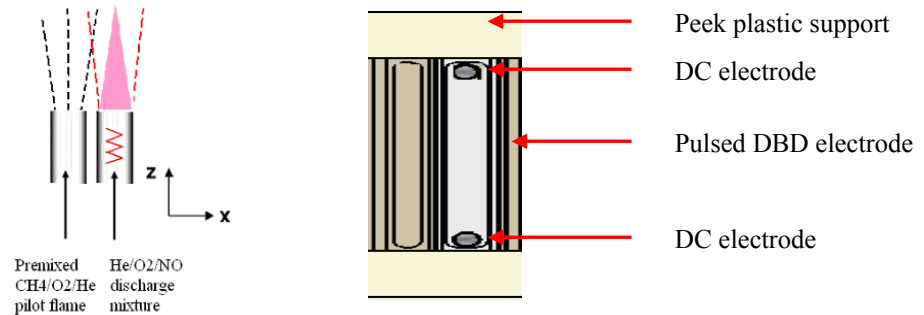


Fig.V.17. Two solts hybrid plasma-burner geometry.

The dotted black and red lines correspond to the premixed flow trajectories and the secondary flow, respectively. The pink colour triangle represents excited species in the post-discharge region.

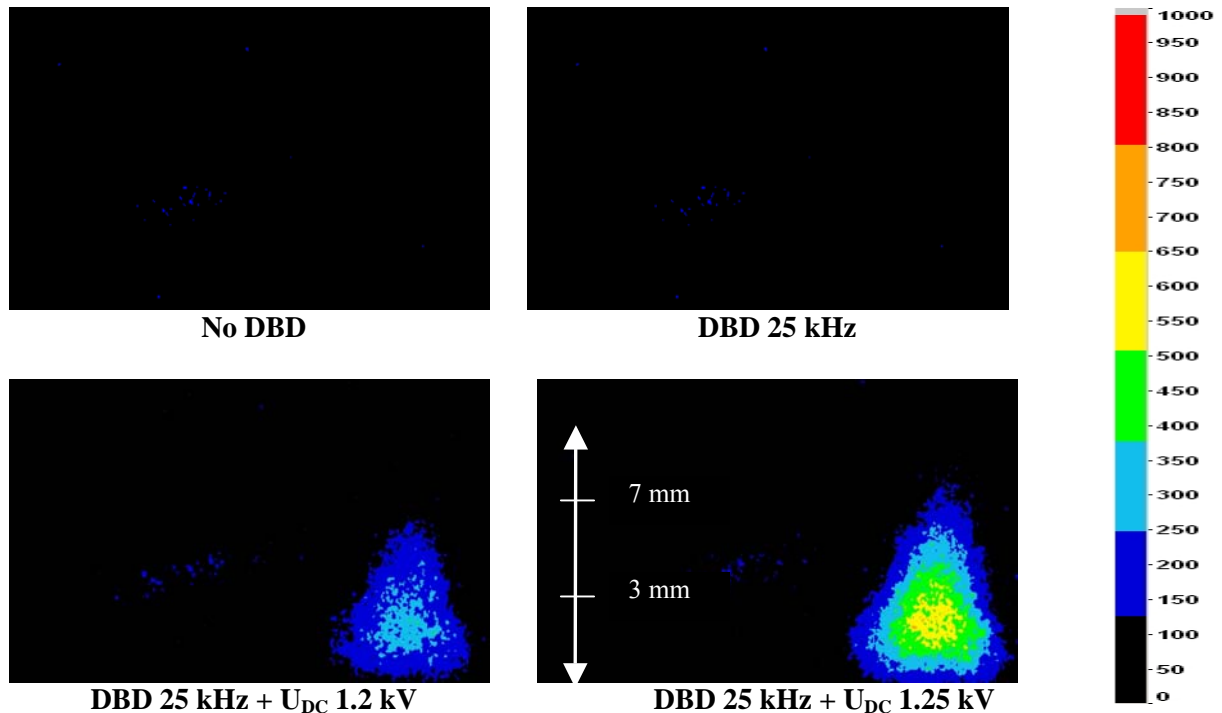


Fig.V.18. Images of  $O_2(b^1\Sigma_g^+)$  species. Experimental conditions : Discharge: He 0.65 +  $O_2$  0.04  $m^3/h$  + 250 ppm NO and frequency  $f= 25$  kHz.

It is worth noting that the limited lifetime for  $O_2(b^1\Sigma_g^+)$  molecules was a great concern at the beginning of this work. Even associated with a long radiative lifetime, collisions with other molecules and diffusion to the electrodes may of course induce a much shorter effective lifetime. Nevertheless, a considerable lifetime has been indeed observed in practical experiments. The above images allow evidencing excited oxygen species population distribution in the post-discharge zone and bring important information on the characteristic relaxation times. In our experimental set-up, excited oxygen is still easily detectable after leaving the generator, at almost 8 mm after the discharge slot exit, which is in good agreement with previous spectroscopic diagnostics presented in Chapter IV. In the case with only DBD, no excited oxygen species can be measured in the post-discharge. When crossing the 25 kHz pulsed DBD with respectively 1.2 kV and 1.25 kV DC sustainer voltage, the excited oxygen species becomes easily detectable after leaving the generator and is increased in terms of emission intensity and of distance reached from the burner exit. Moreover, a conical distribution can be observed. These results are consistent with those presented in the pure plasma studies (see Fig.IV.15) where we have monitored the evolution of the excited oxygen species emission intensity signals as a function of DC sustainer voltage. It was observed that excited oxygen species concentration increases with the increase of the DC sustainer voltage. Also, the “bell” curve shown in section IV.2.4, showing the excited oxygen species emission intensity as a function of the height above the burner slot exit is consistent with the observed excited oxygen spontaneous emission conical profile.

Flame intensification and structure modifications will now be characterized.

## V.2.4. Plasma-assisted combustion

### V.2.4.1. Experimental flow conditions and measurement procedure

Tests have been carried out in order to obtain the best flame conditions and stabilisation, first at atmospheric pressure and then at reduced pressure. Once these preliminary investigations have been accomplished, the plasma/flame ignition procedure was defined to be as follows: the flame is ignited at atmospheric pressure, and then the pressure is gradually decreased while adjusting the gas flows till reaching the desired working pressure and flow values. The crossed discharge can then be ignited. Experimental flow conditions are summarized in the following table V.3 :

	Premixed slot	Discharge slot
CH <sub>4</sub> (m <sup>3</sup> /h)	0.045	–
O <sub>2</sub> (m <sup>3</sup> /h)	0.085	0.02 – 0.04
He (m <sup>3</sup> /h)	0.25	0.25 – 0.65
NO (ppm)	–	250

Table V.3. Experimental flow conditions.

This corresponds to global equivalence ratios varying from 0.9 to 1 and gas exit velocities of 34 cm/s (premixed slot) and 20 to 53 cm/s (secondary oxidizer slot).

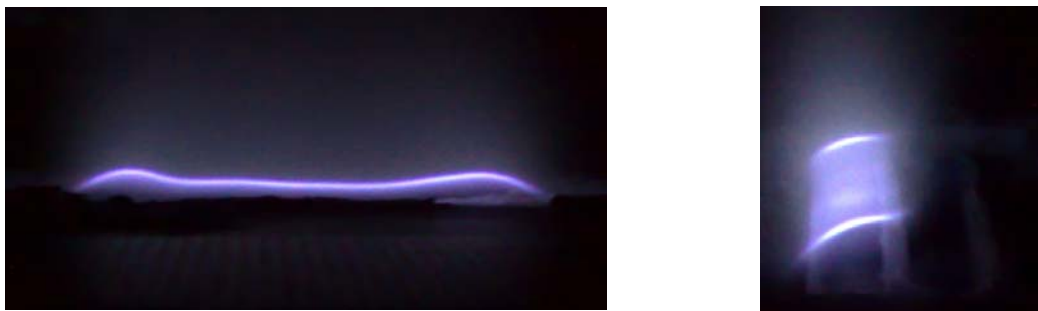


Fig.V.19. Pictures of the flame. (Left) : front view and (right) : side view.

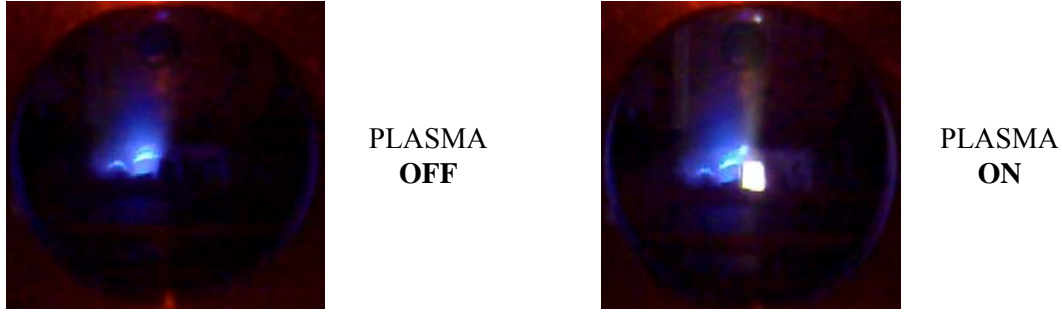


Fig.V.20. Pictures of flame without and with plasma (both side views).

The partially premixed flame is very stable (see Fig.V.19) with a quite flat structure. Photographs of the partially premixed flame, without and with the pulsed plasma discharge are shown in Fig.V.20 for comparison. One can observe the increase of flame extension and flame luminosity. The white rectangular emission comes from the plasma in the discharge volume. The plasma discharge (post-discharge) and flame base are spatially separated, indicating that the discharge is a steady supplier of reactive species but not an instantaneous flame ignition source.

When starting the CDR, the flame is visually extended towards the plasma burner slot. In order to analyse this effect, we have systematically carried out measurements at different experimental conditions, using optical emission spectroscopy for OH\*, CH\*, C<sub>2</sub>\* and O<sub>2</sub>(b<sup>1</sup>Σ<sub>g</sub><sup>+</sup>) to qualitatively understand the flame structure modifications in the presence of the plasma. In this way, the mapping of the main reaction front marker radicals throughout the flame is obtained.

It is important to retain two important experimental observations :

- In the presence of the premixed pilot flame, starting the CDR leads visually to an extension of the flame zone.
- In the absence of the pilot flame, no auto-ignition has been obtained when activating by the CDR.

In the next sections, we seek to evidence and better understand the role played by the discharge in the flame structure. For this purpose, spontaneous emission is recorded with the intensified CCD camera Nanostar LaVision described in chapter II. In all studied cases, the camera exposure time is 50 μs, 13 images are accumulated. A 105 mm objective focuses the image on the ICCD camera.

Observation of the spontaneous emission of OH\*, CH\* and C<sub>2</sub>\* in the flame is then performed using interferential filters described in Table V.4. These species, which give a signature of the reaction zone, will allow checking the flame structure. Also, excited oxygen O<sub>2</sub> (b<sup>1</sup>Σ<sub>g</sub><sup>+</sup>) is observed at 762 nm at the exit of the burner.

Radical	Transition	Central wavelength (nm)	FWHM (nm)
OH*	A <sup>2</sup> Σ <sup>+</sup> → X <sup>2</sup> Π	307	10
CH*	A <sup>2</sup> Δ → X <sup>2</sup> Π	431	10
C <sub>2</sub> *	d <sup>3</sup> Π <sub>g</sub> → a <sup>3</sup> Π <sub>u</sub>	515	10
O <sub>2</sub> *	b <sup>1</sup> Σ <sub>g</sub> <sup>+</sup> → X <sup>3</sup> Σ <sub>g</sub> <sup>-</sup>	762 + 775	20

Table V.4. Interferential filter description.

In order to distinguish electronically excited oxygen O<sub>2</sub>\* emitting at central wavelength 762 nm and excited atomic oxygen O\* emitting at 777 nm, in addition to the interferential filter 762 ± 20 nm, a short pass filter at 775 nm is used, insuring that O\* emission is correctly filtered.

Experiments were conducted as follows. For a given experimental condition, images of :

- 1- Flame without (O<sub>2</sub>/He/NO) secondary flow (not shown here) ;
- 2- Flame with secondary flow (WITHOUT plasma) ;
- 3- Flame with secondary flow (WITH plasma) :
  - 3a- Only DBD ;
  - 3b- Combined discharge (DBD + DC) ;

- 3c- Without NO (not shown here) ;
- 3d- With NO ;

have been systematically acquired. Examples of such images will be presented in the next sections.

### V.2.4.2. Direct flame visualization

In figures V.21 and V.22, two sets of frames collected without and with discharge are shown. No filter is used here; therefore the total emission in the visible range is collected. Results are compared for a DBD frequency of 20 and 25 kHz. The graduation is expressed in counts (saturation is reached at 4095 counts). Side views pictures are shown below :

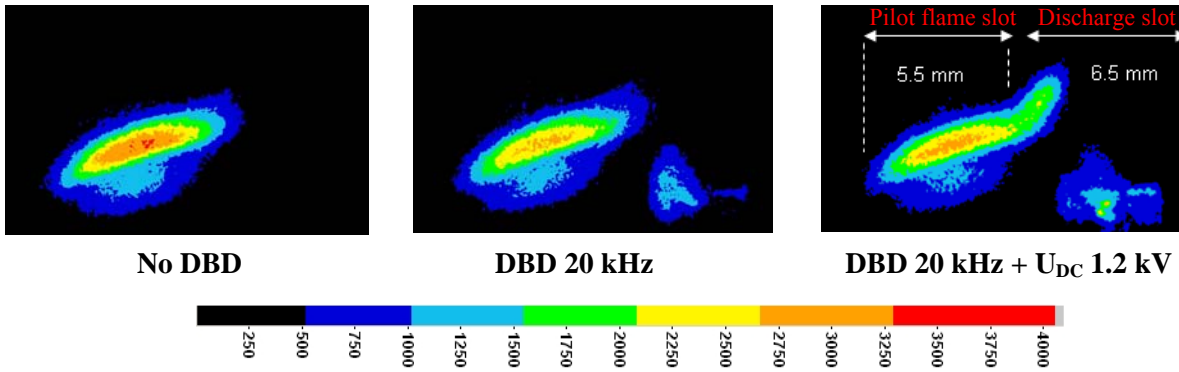


Fig.V.21. Total emission in the visible range. Experimental conditions : Discharge : He 0.65 + O<sub>2</sub> 0.04 m<sup>3</sup>/h + 250 ppm NO and frequency f= 20 kHz.

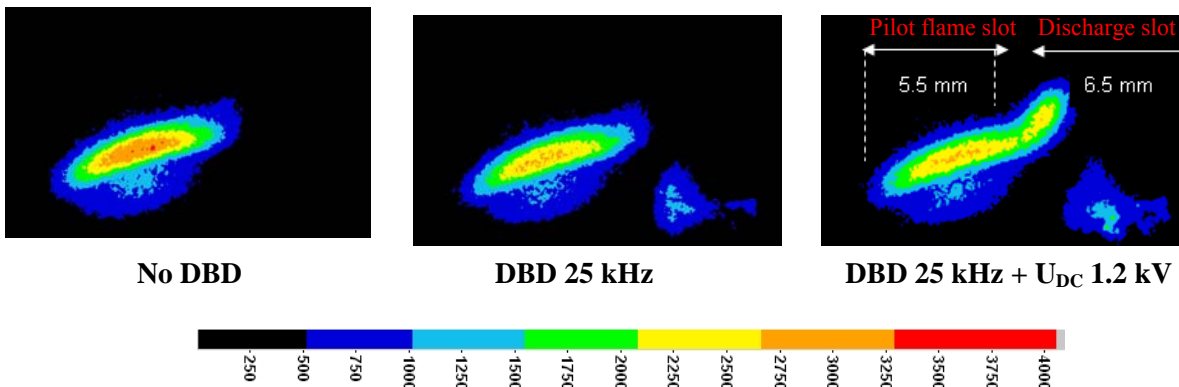


Fig.V.22. Total emission in the visible range. Experimental conditions : Discharge : He 0.65 + O<sub>2</sub> 0.04 m<sup>3</sup>/h + 250 ppm NO and frequency f= 25 kHz.

It is worth noting that in all presented cases, one can observe the light emitted by the post-discharge, corresponding to the very luminous excited species emissions on the right side of the image. Naturally, the visible emission includes singlet oxygen emission at 762 nm. It can be seen on these images that the injection of excited oxygen species in the flame reaction zone is at the origin of flame extension.

In the case with only pulsed DBD, where it has been previously demonstrated that electronically excited oxygen is not produced, no flame extension effect is visible. Running the discharge in a crossed discharge mode, with parameters corresponding to the production of electronically excited oxygen, flame extension is obviously observed. Furthermore, one can observe that working with DC sustainer voltage of 1.2 kV and passing from 20 to 25 kHz pulse repetition rate leads to a higher flame extension associated with a higher luminosity. Also, we can see that for the OFF and ON discharge conditions, no change in the main flame stabilization height above the burner is observable.

Finally, it must be noticed that there exists a non-emitting zone between the post-discharge flow (coming out of the discharge, on the right part of the images) and the main flame reaction zone, due to

the separation wall between both slots. This darker zone is not only observed at the burner basis but also between the post-discharge area and the flame reaction zone (i.e. below the main flame zone). This observation corroborates the fact that excited oxygen concentration is locally reduced.

In figure V.23, the visual findings are summarized in a scheme, where the solid lines represent the schematic flame front. The dotted black and red lines correspond to the premixed flow trajectories and the secondary flow, respectively. The pink colour triangle represents excited species in the post-discharge region.

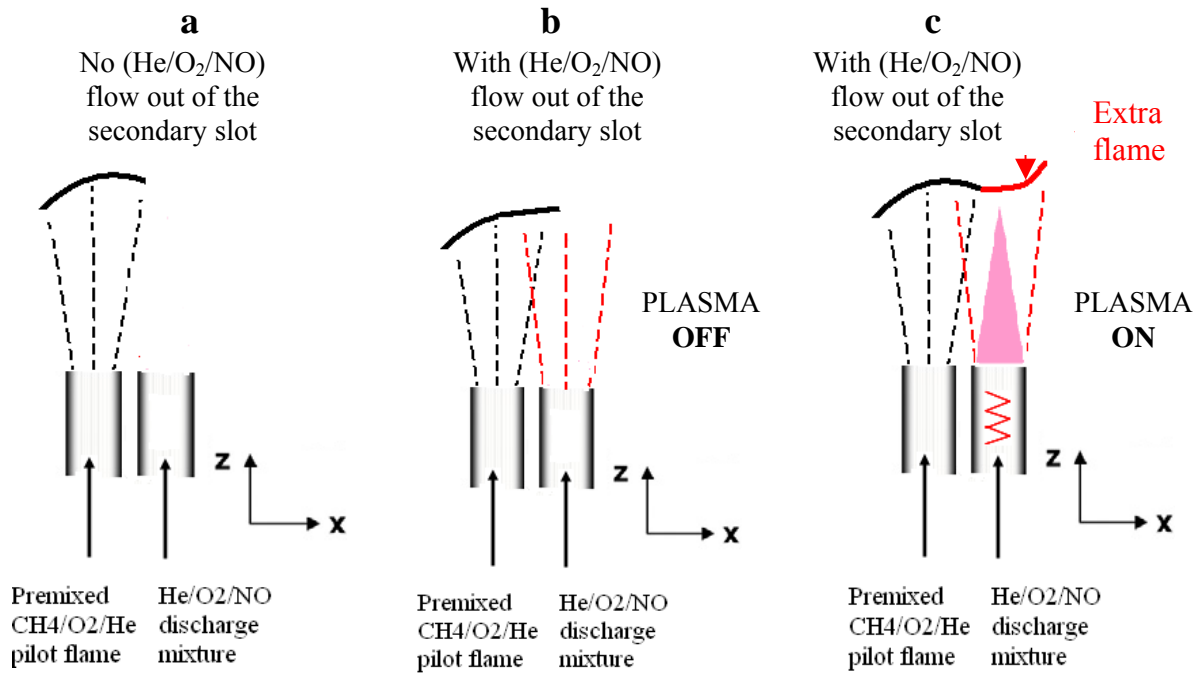


Fig.V.23. Schemes of flame extension (side views). Without secondary flow (only premixed pilot flame) (left) ; with secondary flow without plasma (middle) and with secondary flow with plasma (right).

The different steps are described more precisely in what follows :

- a- The premixed (CH<sub>4</sub>/O<sub>2</sub>/He) flame is alone (i.e. primary flow). There is no (He/O<sub>2</sub>/NO) flow through the discharge slot (i.e. secondary flow).
- b- The premixed (CH<sub>4</sub>/O<sub>2</sub>/He) flame is distorted by the (He/O<sub>2</sub>/NO) flow coming out of the discharge slot. In this case, no activation by the CDR is performed (plasma OFF condition).
- c- Premixed (CH<sub>4</sub>/O<sub>2</sub>/He) flame interacting with the activated (He/O<sub>2</sub><sup>\*</sup>/NO) flow coming out of the ignited discharge (schematized in Fig.V.23c in pink colour). An extra-flame is created and the luminescence of the initial flame is modified (plasma ON condition, i.e. oxidizer activation by the CDR).

### V.2.4.3. Spontaneous emission of flame front markers

Figure V.24 shows that the injection of excited oxygen species in the flame reaction zone leads to a modification of the flame structure (similar observations to previous non spectral images). Exciting the oxidizer stream is at the origin of an increased production of excited radicals. We will consider now the influence of excited O<sub>2</sub><sup>\*</sup> on the presence of OH<sup>\*</sup>, CH<sup>\*</sup> and C<sub>2</sub><sup>\*</sup> in the extra-flame and in the premixed flame itself.

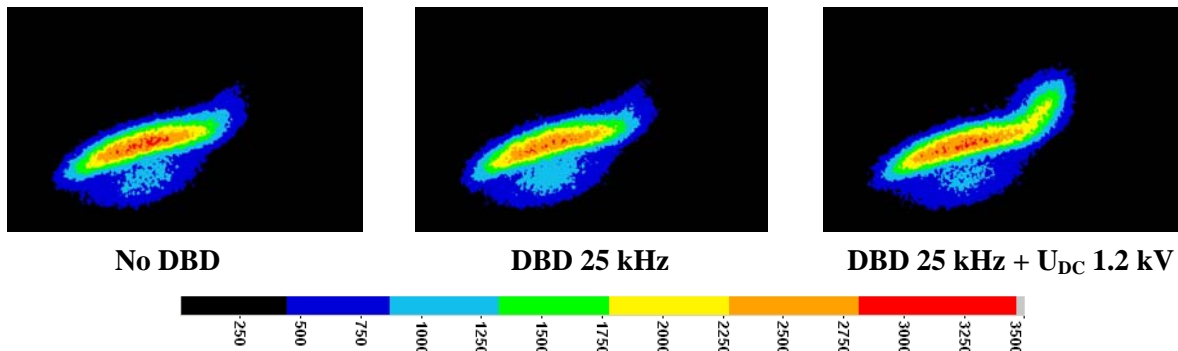


Fig.V.24. Images of OH\*. Experimental conditions : Discharge : He 0.65 + O<sub>2</sub> 0.04 m<sup>3</sup>/h + 250 ppm NO and frequency f= 25 kHz.

In the case of the flame coupled with only a pulsed discharge (i.e. with negligible production of O<sub>2</sub>\*), the OH\* radical emission extension is not observed. But in the case of the flame coupled with a pulsed crossed discharge, with 1.2 kV DC sustainer voltage, this increased production is obvious.

For the CH\* radical spontaneous emission (Fig.V.25) the pulsed crossed discharge (DBD + DC) leads to a slight extension of the CH\* radical.

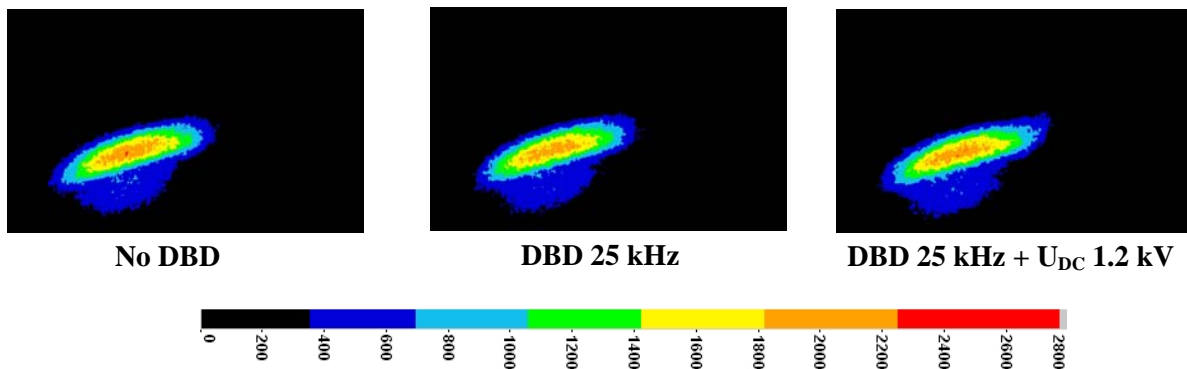


Fig.V.25. Images of CH\*. Experimental conditions : Discharge : He 0.65 + O<sub>2</sub> 0.04 m<sup>3</sup>/h + 250 ppm NO and frequency f= 25 kHz.

The effect of the CDR can still be seen, but at a much lower level than for OH\*.

For C<sub>2</sub>\* radical spontaneous emission (Fig.V.26) the injection of excited oxygen species in the flame reaction zone is again at the origin of a significant extension of the C<sub>2</sub>\* radical production.

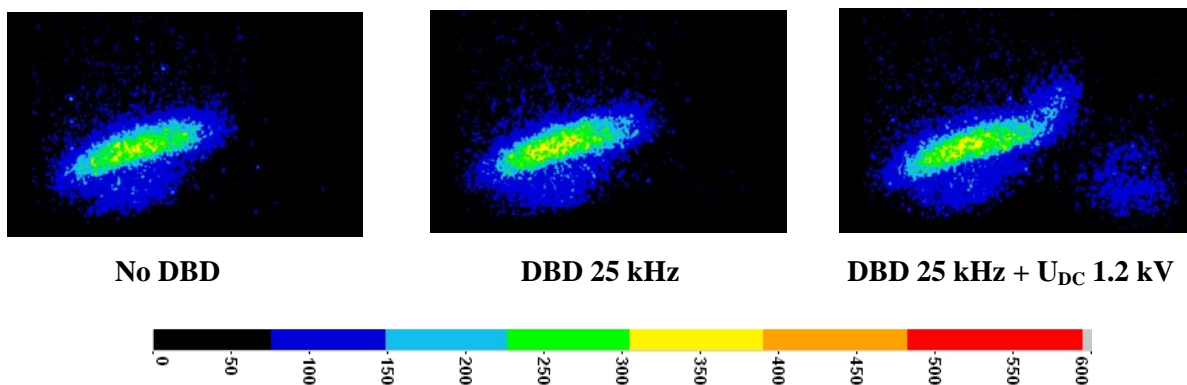


Fig.V.26. Images of C<sub>2</sub>\*. Experimental conditions: Discharge : He 0.65 + O<sub>2</sub> 0.04 m<sup>3</sup>/h + 250 ppm NO and frequency f = 25 kHz.

Concerning  $C_2^*$  distribution images in the flame, the plasma effect is much clearer compared to  $CH^*$ , but less significant differences can be observed compared to the  $OH^*$  radical. Anyway, the changes in the presence of the plasma evidence a flame structure modification.

Three major effects are proposed for the improvement of combustion under plasma assistance: the heating of the gas, the chemical effect of the reactive species created by the plasma, and in the case of the nonpremixed flames, a mixing effect. These mechanisms by which the discharge could affect a gas should be taken into account when using our crossed discharge to intensify combustion. The question raised is if discharge could affect the flame by a thermal effect and therefore, our experimental observation could be due to the local heating of gas and, accordingly, leading to the increase in rate of combustion. In the other hand, the nonequilibrium plasma can lead to a chemical effect on combustion intensification (i.e. the main mechanism of excitation of oxygen molecules by electron-impact). For these discharges, the heating effect will probably superimpose on the chemical effect and amplify it. Chemical and thermal effects of the discharge on the flame stabilization are hard to separate.

As explained previously, the temperature increase induced by the CDR within the oxygen flow is higher in the presence of NO, but still small. In order to further check this issue and to investigate separately the influence of the discharge and that of the excited oxygen in the discharge, all measurements have been also carried out with pure helium and helium/NO flowing in the discharge slot (no oxygen). Although the thermal effect could be lower in pure helium (as it is when no NO is added), no flame modification has been observed in such case when activating the CDR. We can thus infer that the strongest modifications of the flame recorded in this study are only due to the presence of excited oxygen in the discharge and not to a thermal effect.

To conclude, the observed flame intensification and structure modifications show an enhancement of the reactivity (reaction rates), increasing with excited oxygen species production. When considering injection of excited oxygen, new reaction pathways appear, associated with a reduction of energy threshold of chemical reactions, thus favoring additional formation of OH, O, and H species, explaining the observed combustion intensification.

#### **V.2.4.4. Parameter study: influence of time, injection speed and DC sustainer voltage**

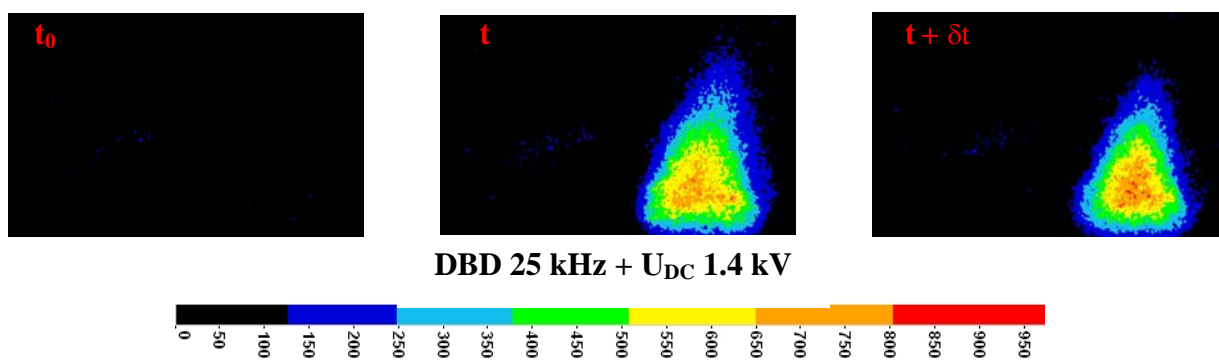
First, a pulse DBD at 25 kHz pulse frequency and DC sustainer voltage of 1.4 kV is considered. These conditions correspond to the upper limit we can apply before instability (glow-to-arc transition) takes place. The spontaneous emission of main radicals as well as excited oxygen has been recorded to show the enhancement of combustion due to the discharge.

The flame originated in the premixed slot, extended downstream through the discharge section, and remained stable as long as the plasma was on. Series of images have been acquired during the discharge duration (2 seconds), allowing us to qualitatively evidence in the following figures a temporal evolution, covering the steps :

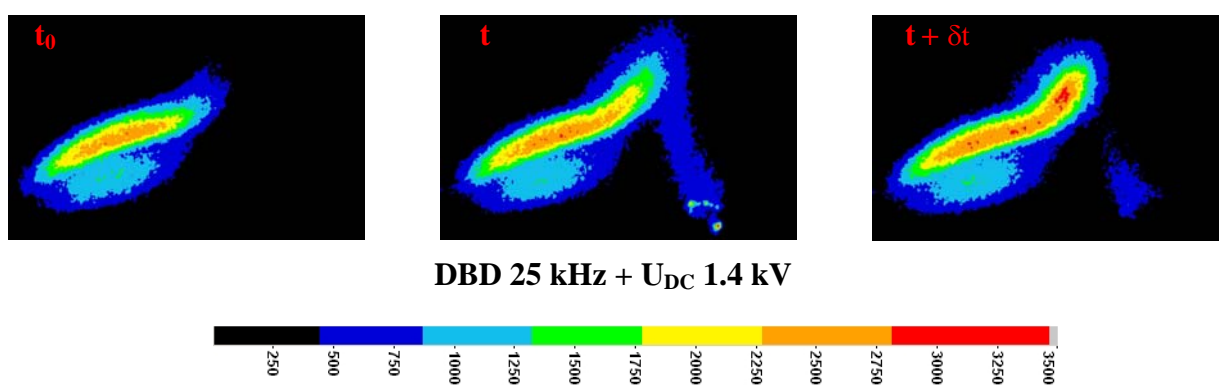
- no plasma (first image = reference image) ;
- with plasma, images are labelled at time  $t$  (middle): maximum flame modification ;
- during the plasma post-discharge decay, at time  $t+\delta t$  (right).

These images show in particular that, while excited oxygen slowly disappears when turning off the CDR, maximum flame modification is observed above the discharge slot. This is particularly visible for  $OH^*$  and might be a result of the non-negligible time needed for travel between discharge cell and reaction zone.

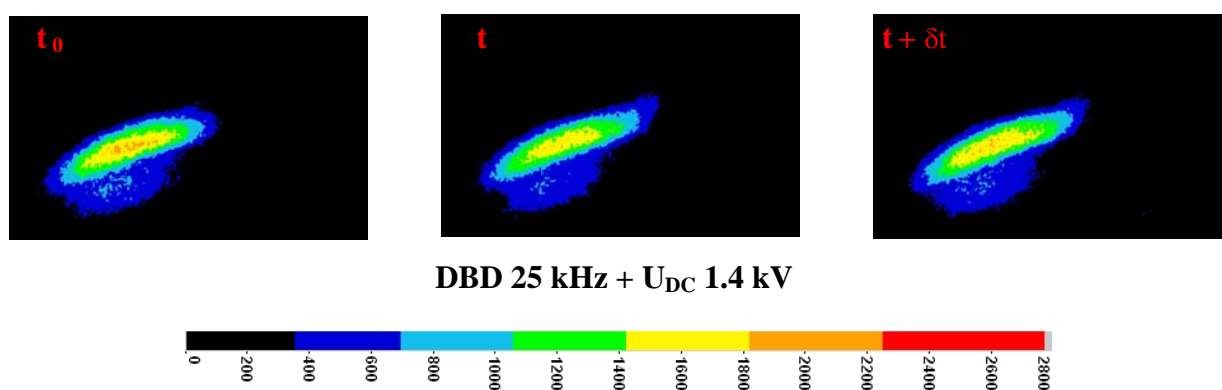
### $O_2^*$ molecule



### OH\* radical



### CH\* radical



### $C_2^*$ radical

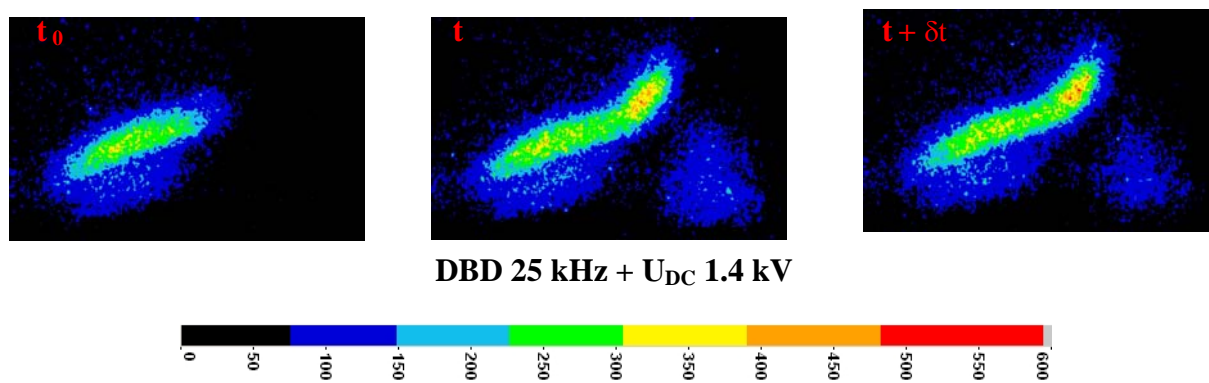
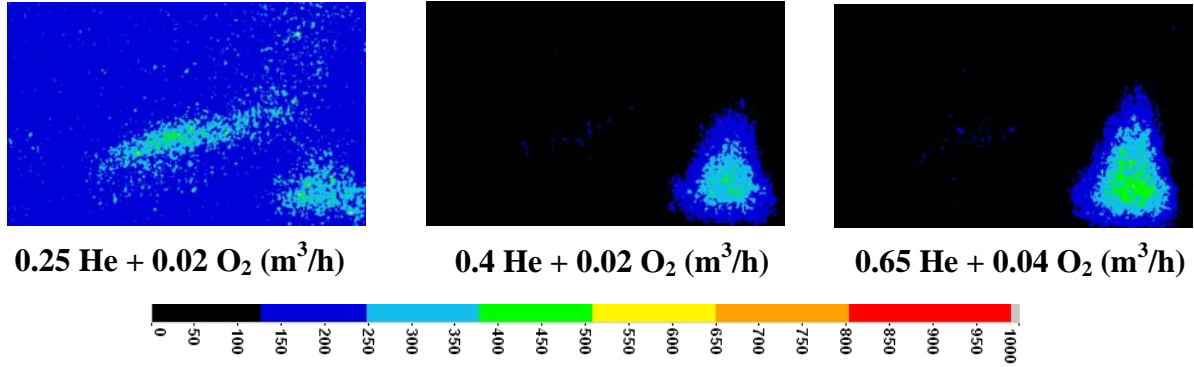


Fig.V.27. Images of  $O_2^*$ , OH\*, CH\* and  $C_2^*$ . Experimental conditions : Discharge: He 0.65 +  $O_2$  0.04  $m^3/h$  + 250 ppm NO and frequency  $f= 25$  kHz.

Further experiments presented in this section are carried out in  $O_2/He$  binary mixture with admixture of 250 ppm of NO. The discharge parameters are DBD = 25 kHz and DC sustainer voltage  $U_{DC} = 1.2$  kV. Other experiments at different oxidizer flow conditions have been performed but are not shown here. Also, only  $O_2^*$  and  $OH^*$  are presented.

### $O_2^*$ molecule



### $OH^*$ radical

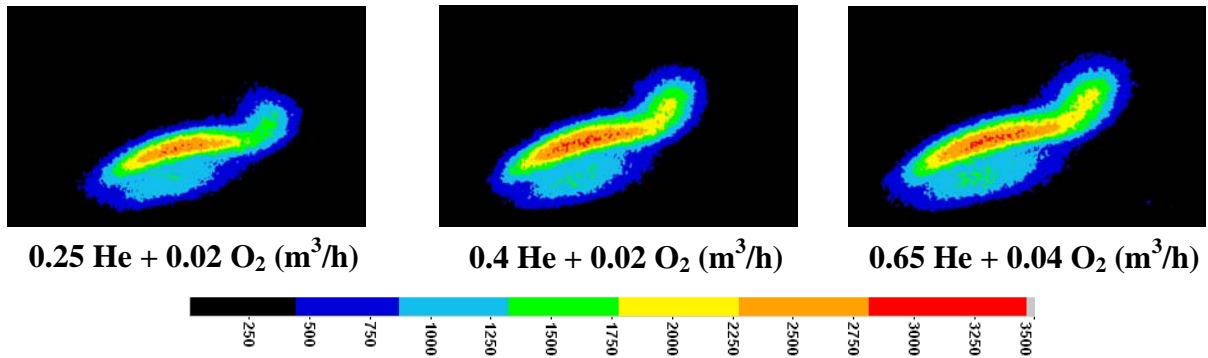


Fig.V.28. Images of  $O_2^*$  and  $OH^*$ . Effect of secondary flow. Experimental conditions :  $He/O_2 + 250$  ppm NO;  $U_{DC} = 1.2$  kV and frequency  $f = 25$  kHz.

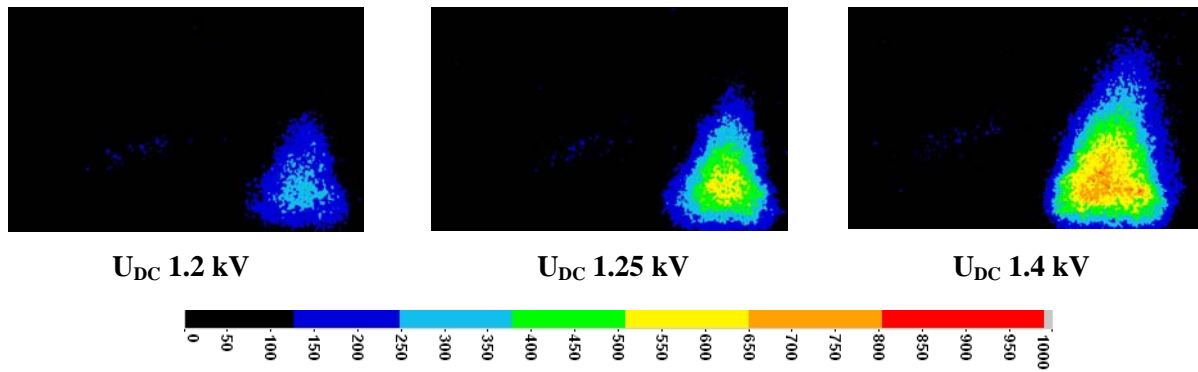
Figure V.28 shows the influence of secondary mixture injection flow rates. Due to the relatively short life of the majority of the excited species, the shorter the delay between the production zone and the flame front, the stronger the effect on the flame should be. In these conditions, the chemical effect should be amplified.

First, one can observe that the quantity of  $O_2^*$  present in the post-discharge increases when increasing the flow-rate through the CDR (secondary mixture). Furthermore, one can assume that excited oxygen species reach more efficiently the reaction zone (faster transport). As a consequence, flame modification and intensification are enhanced.

Without CDR, with increasing flow speeds, the partially premixed flame is lifted off from the burner exit. The lifted flame experiences blowout when the flow speed is too high. In the presence of 18 kV peak voltage, 25 kHz repetition rate pulsed discharge, the total flow speed before flame blow-out is found to increase by 10%. The observation that blow-out is delayed confirms again the significant effect of the discharge on enhancing flame stability.

Figure V.29 shows the role played by the DC sustainer discharge on flame modification. Experiments presented here are again carried out in  $O_2/He : 0.65 He + 0.04 O_2$  ( $m^3/h$ ) binary mixture with admixture of 250 ppm of NO. The discharge parameters are DBD = 25 kHz and DC sustainer voltage  $U_{DC} = 1.2 - 1.4$  kV. The scales are the same as that used previously for the different visualized species.

### O<sub>2</sub>\* molecule



### OH\* radical

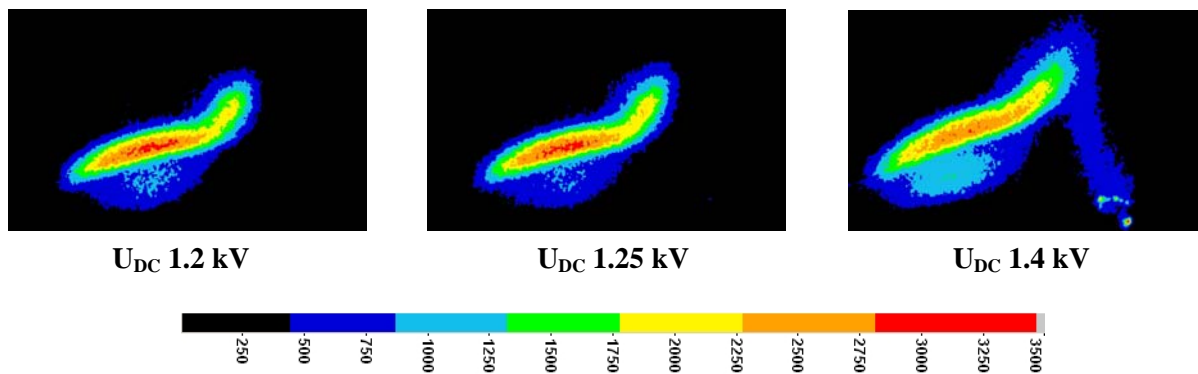


Fig.V.29. Images of O<sub>2</sub>\* and OH\*. Effect of DC sustainer voltage. Experimental conditions : Discharge: 0.65 He + 0.04 O<sub>2</sub> (m<sup>3</sup>/h) + 250 ppm NO and frequency  $f = 25$  kHz.

Fig.V.29 demonstrates again, in agreement with chapter IV, that flame intensification increases when increasing the DC power until arcing is obtained (above 1.4 kV). The quantity of excited oxygen generated by the CDR is considerably increased when going from  $U_{DC} = 1.2$  kV to 1.4 kV.

### V.2.4.5. Quantitative analysis of flame extension

The employed conditions correspond to an O<sub>2</sub>/He (0.65 He + 0.04 O<sub>2</sub> (m<sup>3</sup>/h)) binary mixture with addition of 250 ppm of NO. Pulsed dielectric barrier discharge is set at pulse repetition rate of 25 kHz, and DC sustainer voltage is fixed at 1.4 kV.

	MAXIMUM	AVERAGE
OH*	- 5 %	+ 37 %
CH*	- 16 %	+ 12 %
C <sub>2</sub> *	+ 34 %	+ 19 %

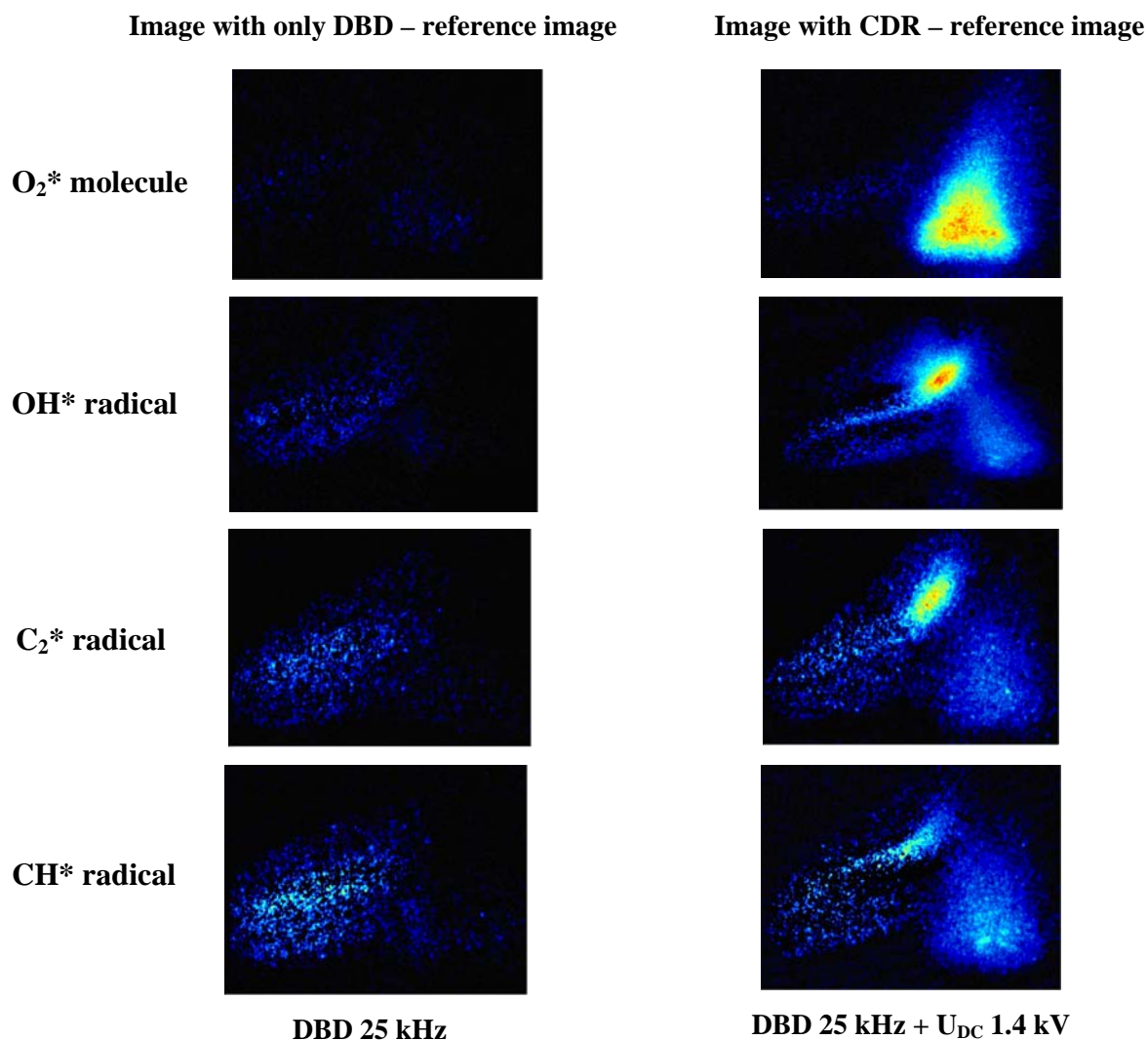
Table V.5. Image statistics.

Table V.5 presents results obtained after batch processing of the acquired images via Davis software. “Maximum” refers to the highest pixel value (thus, maximum emission) and “average” means the average intensity of all image pixels. The obtained values allow us to roughly quantify the increase or decrease of studied radicals.

In table V.5, the values are compared with and without activating the CDR, computed as :

$$(\text{value}_{\text{with CDR}} - \text{value}_{\text{without CDR}}) / \text{value}_{\text{without CDR}}$$

Furthermore, in order to better evidence the discharge effects, for a given experimental series, we subtract the reference image (i.e. without plasma). Corresponding results are presented in Fig.V.30 and allow to better evidence the flame extension.



*Fig.V.30. Experimental conditions : Discharge : 0.65 He + 0.04 O<sub>2</sub> (m<sup>3</sup>/h) + 250 ppm NO, f = 25 kHz. The reference image (without plasma) has been subtracted from the image with only DBD (left) and with CDR (right).*

It can be clearly seen that only negligible effects are observed with only pulse DBD (where no singlet oxygen is produced), while a large flame extension associated with an increase of spontaneous emission is observed when starting the CDR. When comparing the molecules OH\*, CH\* and C<sub>2</sub>\*, it can be observed that the most significant effects of the pulsed crossed discharge is for OH\* and C<sub>2</sub>\* excited radicals. Flame extension is observed associated with a faster flame attachment.

The highest effect of plasma being observed for the OH\* molecule, we have therefore decided to use Laser Induced Fluorescence (LIF) for OH radical (in its fundamental electronic state). The LIF apparatus, described in chapter II, utilizes a 10 Hz repetition rate Nd:YAG laser with 355 nm output. The 355 nm beam pumps a tunable dye laser, which is associated with a doubling crystal placed after the dye laser to generate the required UV wavelength of 282.66 nm to pump the Q1(5) transition of OH.

Preliminary results have been obtained with LIF, but no relevant results of plasma-flame experiments could finally be obtained. A major problem appeared ; due to electromagnetic interference which affected the laser (Q switch and flash lamp triggers), the ICCD camera trigger, and

the PC controlling the dye laser tuning, we have been unable to acquire any image of the flame in presence of CDR.

Fig.V.31 shows an OH LIF image of the flame without plasma oxidizer activation.

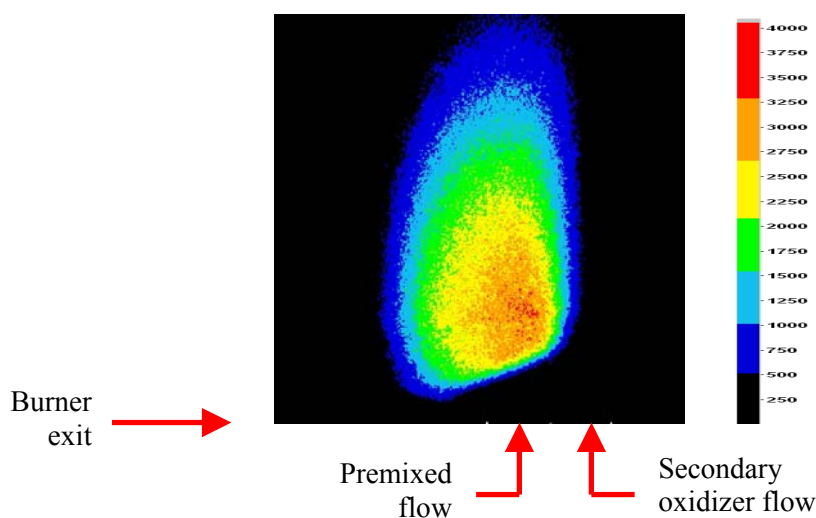


*Fig.V.31. LIF OH image of partially premixed flame at global equivalence ratio of 1. Secondary slot flow is :  $0.65 \text{ He} + 0.04 \text{ O}_2 \text{ (m}^3/\text{h)} + 250 \text{ ppm NO}$ .*

Even by connecting all instruments to power circuits separate from that of the pulser, this couldn't be overcome. Furthermore, the pulser/test cell was placed on a separate table, electrically insulated from the laser table surface. Nevertheless, it was still impossible to carry out LIF measurements. Further progress will therefore attempt to solve these huge electromagnetic compatibility problems.

## V.2.4.6. Discussion and synthesis

When comparing 2D radical emission images in standard flame and in plasma-supported flame, it is visible that plasma leads to an increase and extension of main radicals and particularly of OH\* above the discharge burner slot. An additional flame appears in this region. We have demonstrated that two discharge types ; a pulse DBD at 25 kHz frequency and a pulsed crossed discharge (DBD + DC) give different results :

- With only the DBD, i.e. where no excited oxygen is produced, no flame extension is observed.
- With the CDR, where previous results on production and detection of metastable atomic and molecular oxygen have been successful, the plasma discharge increases the flame extent and the main radical production. It is clearly observable that the excited oxygen states have long enough lifetimes to be able to produce direct chemical effects on the flame.
- Results of chapter IV show that the oxidizer flow temperature increase is not significant, which excludes thermal effects and supports chemical effects induced by the presence of excited oxygen O<sub>2</sub>\*

The combustion enhancement is more intense at higher secondary flow-rate, at higher DC sustainer voltage and in the presence of a small amount of NO. These findings confirm that of chapter IV. Operating at higher flowrate, the penetration of excited species into the flame zone increases, thus increasing the observed flame intensification. The results evidence an average overproduction of OH\* (+37%), C<sub>2</sub>\* (+19%) and CH\* (+12%).

As a consequence electronically excited O<sub>2</sub>\* appears to be a very efficient way to promote methane combustion. The post-discharge is a source of long-lived radicals or indirectly of stable species that influence flame properties. In this case, a flame can be stabilized and extended through accelerated chemical reactions. Indeed, electronic excitation influences the course of a chemical reaction by

increasing the energy content of the system or by affecting access to different potential energy surfaces.

When activating the CDR, a darker zone is observed between the post-discharge area and the flame reaction zone. This observation corroborates the fact that excited oxygen concentration is locally reduced. This suggests that excited oxygen present nearby the flame zone reacts and induces chemical reactions, thereby increasing the flame reactivity.

Furthermore, we wondered if it is possible that the pulsed plasma discharge provides a direct means of flame ignition. Attempts have been carried out, but no ignition has been reached using only the CDR. The reason could be that in our conditions, the active species concentrations produced by the discharge are not sufficiently high to initiate the combustion. Chintala et al. [113] reported that photochemical ignition of  $\text{H}_2/\text{O}_2$ ,  $\text{H}_2/\text{air}$ , and  $\text{CH}_4/\text{O}_2$  mixtures using excimer laser occurs only when high radical concentrations (of the order of  $10^{17} \text{ cm}^{-3}$ ) are produced. No quantitative measurements have been performed but comparable levels of radical concentrations may not be reached here.

Finally, results from numerical simulation of hydrogen flames in presence of excited oxygen species (chapter III) are qualitatively in agreement with those obtained experimentally. The effect of adding excited oxygen in the fresh gases is similar for all radicals, the flame width increases when increasing the amount of excited oxygen.

### V.3. Conclusions

The partially premixed flame configuration has been extensively investigated at low pressure. We finally decided to retain this configuration due to its capacity to reduce the distance between the CDR and the flame and the possibility to separate a secondary oxygen flow in which excited oxygen can be produced under optimal conditions. Furthermore, this burner is well adapted to low pressure conditions ( $\sim 120$  Torr), where excited oxygen is produced in higher quantity. The positive conclusions of this study are :

1- It is indeed possible to integrate the plasma discharge (CDR) in the burner. The hybrid burner is integrated in a bridle, adapted to the low pressure tank. Therefore, electrical connections are made at atmospheric pressure, avoiding parasitic discharge development.

A partially premixed methane flame is obtained and has been spectroscopically investigated through main tracers of the reaction zone:  $\text{OH}^*$ ,  $\text{CH}^*$ ,  $\text{C}_2^*$  band emission with and without the plasma discharge.

2- As for the atmospheric pressure counterflow flame configuration, but much more noticeably, the flame structure is clearly modified when activating the CDR. The active reaction zone becomes larger. When activating the CDR, a stable flame appears in a region where no flame is found in the standard configuration.

3- Using emission spectroscopy, it has been demonstrated that radical species intensity increase noticeably when starting the CDR. Plasma activation leads to an average increase of  $\text{CH}^*$  by 12%, of  $\text{C}_2^*$  by 19% and of  $\text{OH}^*$  by 37%. This quantitative analysis of flame extension is not in accordance with that at atmospheric pressure (counterflow flame), where the increase of  $\text{CH}^*$  is noticeable, while  $\text{OH}^*$  is almost constant. This can be explained by the fact that the composition of the post-discharge is different. In particular, the concentration of  $\text{O}_2^*$  in the flame reaction zone is increased with this partially premixed configuration. The observed discrepancy between both burners might therefore reveal the difference between a direct effect of excited oxygen in the reaction zone (partially premixed burner) compared to an indirect combustion intensification (atmospheric counterflow burner), for which all excited oxygen has been converted long before reaching the flame.

4- The increase of DC sustainer voltage and secondary oxidizer flow speed leads to a higher flame extension.

5- The CDR induced the extension of the flame by producing an active stream of species that assist the oxidation process, rather than providing a direct ignition of the flame (e.g. by local heat release). Indeed, we have been unable to ignite the flame just by using the CDR.

Numerical simulations of hydrogen combustion presented in chapter III have shown that when considering 5% of excited oxygen in the oxidizer mixture, the extinction strain rate of a counterflow flame  $\varepsilon_e$  is increased by 7%. Even if it is impossible to compare quantitatively the simulations of

section III.2 (hydrogen flames) with the experiments of chapter V (methane flames), qualitative evolutions may be compared. The same trend has been experimentally demonstrated with methane combustion, where an increase by 10% is observed for the extinction strain-rate.

Furthermore, premixed hydrogen flame simulations reveal that when increasing the percentage of  $O_2^*$  in the mixture (which corresponds in our experiments to an increase of the DC sustainer voltage), the flame modifications are more pronounced and characterized by (see section III.2): a steeper slope on the fresh gas side, higher peak radical concentrations, a wider flame and a bimodal structure appearing particularly for  $OH^*$ , with a large peak on the fresh gas side and a secondary, lower peak on the burnt gas side. The numerical findings of section III.2 are qualitatively confirmed by the present experimental results, as follows :

- The largest modification is observed for  $OH^*$  (Fig.V.30), sometimes with a structure reminding of a bimodal structure (see e.g. Fig.V.29).
- Flame modifications increase with DC voltage (and hence with the amount of excited oxygen).
- Available radical emissions increase when activating the CDR (see table V.5, right column).
- The CDR leads always to an extension of the flame zone, similar to the flame widening observed in one-dimensional simulations.

These experimental results suggest that chemical reactions involving excited oxygen molecules and radicals produced in the plasma increase flame reactivity. The excited  $O_2^*$  molecules can deexcite with emission of radiation and then react further according to  $CH_4 + O_2 \rightarrow CH_3 + HO_2$  reaction, or else, while still excited, react with  $CH_4$ . Since the energy that is carried by the excited  $O_2(a^1\Delta_g)$  and  $O_2(b^1\Sigma_g^+)$  are 94 kJ/mol and 157 kJ/mol respectively, the energies required for the reactions :

$O_2(a^1\Delta_g) + CH_4 \rightarrow CH_3 + HO_2$  and  $O_2(b^1\Sigma_g^+) + CH_4 \rightarrow CH_3 + HO_2$  are sufficiently small that they may occur. In addition to normal  $O_2$ , these new reaction pathways give additional radicals  $CH_3$  and  $HO_2$  that can begin a new chain.

Electronic energy is much more efficient than rotational and translational ones to activate chemical reactions. Thus, chemical transformations with the participation of electronically excited molecules, even in the lowest electronic levels, is several orders more rapid than with fundamental molecules ( $v=0$ ). Moreover, a reason of the acceleration of combustion with participation of these excited molecules is the intensification of the formation of active atoms H, O and radicals OH as well as the amplification of chain-branching mechanisms.

Atoms or molecules in metastable states are particularly effective as energy carriers in chemical reactions. The energy stored in the excited molecule can be used for a chemical reaction; if this happens, the excited state molecule may :

- 1- lose its excitation energy without producing any chemical reaction ;
- 2- be dissociated by the collision with the other molecule ;
- 3- react with the collision partner ;
- 4- simply transfer its energy to the collision partner, which then carries out the actual reaction.

If a suitable excited state is produced, as, for example, for  $O_2^*$  and  $OH^*$ , they carry with them the energy necessary for a new reaction pathway. Therefore, many reaction channels become energetically possible.

## Chapter VI : Conclusions and perspectives

Despite its apparent simplicity, the O<sub>2</sub> molecule exhibits a number of rather unusual properties with respect to magnetic behaviour, spectroscopy, energy transfer processes, and chemical reactivity. The oxygen molecule has at least four long-living metastable states. Most interesting are its two singlet states. Electronically excited oxygen O<sub>2</sub>(a<sup>1</sup>Δ<sub>g</sub>) and O<sub>2</sub>(b<sup>1</sup>Σ<sub>g</sub><sup>+</sup>) are reservoirs of electronic energy (carrying excitation energy of 0.981 eV or 94 kJ/mole and 1.65 eV or 157 kJ/mol, respectively). In response to the modern challenges in combustion applications, various approaches have been proposed to enhance ignition and combustion by means of an electrical discharge. Since the radiative lifetime of these metastables are long, the use of excited oxygen in combustion seems promising, as excited atoms and molecules react much faster than the non-excited ones. Furthermore, these species can be generated with a high energetic efficiency.

Activation of oxygen leading to production of singlet oxygen and excited atomic oxygen can be realized by electrical discharge, laser radiation, UV radiation, chemiluminescence reactions. One of the most effective methods of excitation of vibrational and electronic states of atoms and molecules is electron impact in an electrical discharge. Nonequilibrium pulse dielectric barrier and crossed discharges have been used in this study. We have demonstrated that high voltage pulses are an efficient way to generate active species in binary mixtures O<sub>2</sub>/helium.

Pulsed non-equilibrium discharges exhibit very interesting characteristics that can be quite different from that of those driven by conventional means such as AC voltage. Nanosecond pulses with low duty cycles can sustain stable plasmas at relatively low power budgets and without contributing to a noticeable temperature increase of the heavy species (nonthermal plasma).

The energy provided to the discharge is ~7 mJ, corresponding to an average power of 140 W at 20 kHz pulse repetition rate, respectively. This power is much less than the typical heating power of flames of practical interest, usually several kilowatts or more.

To maximize the effect of singlet oxygen in combustion, it is essential to understand the mechanisms governing its formation and deactivation. After an exhaustive review of the state of the art, the first part of this document was dedicated to the development of a plasma facility aimed at producing electronically excited oxygen species. We have carried out experimental research concerning O<sub>2</sub>(b<sup>1</sup>Σ<sub>g</sub><sup>+</sup>) production in nanopulsed dielectric barrier discharges in pure O<sub>2</sub> and in its mixtures with argon and helium in particular and studied a wide range of pressures (10-760 Torr) and discharge parameters.

Theoretical studies have indicated that sufficient fractions of O<sub>2</sub>(b<sup>1</sup>Σ<sub>g</sub><sup>+</sup>) and O<sub>2</sub>(a<sup>1</sup>Δ<sub>g</sub>) may be produced in an electrical discharge. Results of those studies along with experimental results show that electric excitation is a very complicated process that must be investigated with advanced diagnostics combined with modeling. A parametric study with the Bolsig software establishes that it may be possible to attain effective singlet oxygen production in subsonic flow. Due to its sub-optimal operation, the pulsed dielectric barrier discharge could not generate excited oxygen. Numerical simulations of electron energy distribution function allowed making important decisions for the development of a new plasma reactor. The idea was to separate the task of ionization from that of energy deposition. Therefore, crossed discharge reactors, where a pulsed dielectric barrier discharge ionization is coupled with a DC discharge, have been developed and optimized.

Specific energy deposition into the discharge and reduced electric field are the main quantitative parameters characterizing the processes leading to production of singlet oxygen. Evidence of effective production of O<sub>2</sub>(b<sup>1</sup>Σ<sub>g</sub><sup>+</sup>) at atmospheric and reduced pressure has been shown by emission spectroscopy using low, medium and high resolution spectrometers.

The high resolution set-up allows to determine rotational and vibrational plasma temperature (from N<sub>2</sub><sup>+</sup> and O<sub>2</sub>\* emission spectra) as well as flame temperature (from CH\* emission spectra). A typical plasma rotational temperature typically of ~ 360 K has been determined. These plasma temperature measurements allow excluding a strong thermal effect during plasma-flame experiments.

The effects of systematic changes in operating parameters on the performance of the generator led to modifications and improvements with the objective of maximizing the O<sub>2</sub>\* yield. We were then able to generate, for the first time, electronically excited singlet oxygen at atmospheric pressure. Concerning

experimental conditions needed to optimize the  $O_2(b^1\Sigma_g^+)$  yield, our wide set of experiments underline several important discharge parameters. The optimal conditions are :

- reduced pressure up to 120 Torr ;
- a relatively high flow velocity through the CDR (50 cm/s) ;
- less than 10%  $O_2$  diluted in helium. This allows to reduce the temperature rise in the discharge. The diluent also reduces the amount of flow expansion caused by  $O_2$  dissociation, which in turn increases the residence time and leads to higher specific energy deposition ;
- a high DC sustainer voltage. It was demonstrated that the  $O_2(b^1\Sigma_g^+)$  population grows approximately linearly as a function of the discharge power (~1.5 kV maximum, before arcing) ;
- a pulse repetition rate between 20-25 kHz ;
- a reduced electric field  $E/n \sim 10$  Td. It is worth noting that the addition of an inert gas such as helium may promote higher  $O_2^*$  yield by allowing the discharge to operate at a more favourable  $E/n$  than does pure  $O_2$  ;
- addition of 250 ppm of nitric oxide (NO) permits to scavenge atomic oxygen, and therefore reduces the  $O_2^*$  quenching.

In a second step, the opportunity that electronically excited singlet oxygen molecules might be involved as a reactive intermediate to promote combustion has been checked. In order to assist a  $CH_4/O_2/He$  flame at atmospheric and reduced pressures, all steps have been successfully optimized : oxygen excitation in a plasma discharge, thereby forming an excited oxygen flux; that of transporting the excited oxygen into the reaction zone; and finally that of obtaining a sufficient  $O_2^*$  lifetime, allowing to reach the targeted reaction zone.

To investigate this issue, a counter-flow diffusion burner has first been designed and constructed. The burner has been adapted to fit the crossed discharge reactor. An increase of the concentrations of excited radicals has been observed in the flame, which means an enhancement of combustion. A comparison of the radical emission spectra taken without and with the discharge shows, that the spectral structures are more intense when activating the discharge. This is particularly evident for  $CH^*$  (+22%). However,  $OH^*$  molecule shows only a slight increase of 3%. Unfortunately, it was not possible to detect any excited oxygen in the vicinity of the flame. In order to solve this issue, a partially-premixed co-flow burner operating at reduced pressures has been developed. In this manner, excited oxygen species are produced in higher quantities and their lifetime is increased. Integration of the previously optimized crossed discharge reactor within the partially-premixed burner allowed us to study and quantify how combustion processes are modified in the presence of electronically-excited oxygen molecules. Using emission spectroscopy in the flame, combustion intensification is clearly observed when excited oxygen species come out of the discharge reactor. Excited oxygen survives during enough time to finally reach the flame reaction zone. Visualisation of main flame radicals allows to observe a net increase in particular of  $OH^*$  and  $C_2^*$  radicals in the case of oxidizer plasma activation. When considering oxygen excitation, new reactive pathways can appear, leading to production of additional excited radicals.

As a complement, a numerical study has been devoted to the ignition and combustion of diluted hydrogen-air mixtures including electronically-excited  $O_2^*$  molecules, as they appear in the experiments. All computations rely on a detailed reaction scheme implemented within the package CHEMKIN. The reaction mechanism involves the excited species  $O_2^*$ ,  $O^*$  and  $OH^*$ . Results show that in the presence of excited oxygen in the initial mixture, a reduction of the ignition delay and of the minimum inflammation temperature is observed, together with an increase of the laminar flame speed, the thermal flame thickness and of the concentration of all main radicals. The extinction strain rate increases with oxygen excitation. These simulations indicate that it may be possible to attain significant flame intensification levels even at low  $O_2^*$  mole fraction in the fresh gas mixture (5% or less). Even if a quantitative comparison is impossible (simulations consider hydrogen combustion while methane is used as fuel in the experiments), qualitative comparisons reveal a good agreement between numerical predictions and experimental observations. This is an encouraging first step.

It is worth noting that temperature is a critical issue. The inferred plasma flow temperatures are much lower than the autoignition temperature of methane at these pressure and temperature

conditions. These results strongly suggest that combustion intensification occurs by a purely non-thermal mechanism.

Experimental work that should now follow is Laser Induced Fluorescence on OH molecule. We have attempted at the end of this study such LIF measurements, but electromagnetic compatibility problems with ICCD camera prevented any plasma-flame analysis. LIF could indeed give very interesting, quantitative results. Also, numerical simulations of methane combustion in presence of excited oxygen species and validations with the present experimental work would be very interesting. Within this study, the numerical part has been carried out only for hydrogen combustion, because unfortunately, kinetic data of methane combustion with excited species are not available yet.

Finally, the present findings implied that the discharge is a source of reactive species that intensify combustion and increase flame stability.

Furthermore, a similar work plan to that undertaken in the present study but concerning this time fuel “activation” seems to be very interesting.

The possibility of using the discharge to improve ignition would also be a very important subject for practical applications. The generation of additional chemically active radical species by the non thermal plasma discharge may well affect the ignition chemistry and, therefore, the ignition delay time. A common problem is that ignition occurs only in a small volume of the flow, which may result in an incomplete combustion due to the slow lateral flame propagation speed compared to the axial flow velocity. Using nonequilibrium plasmas for initial radical production can be attractive for practical applications, especially if plasma sustained in volume and at reasonable power budget.



## References

1. S.M. Starikovskaia, *Plasma assisted ignition and combustion*. J. Phys. D: Appl. Phys., 2006. **39**: p. R265-R299.
2. A. Ricard, *Plasmas réactifs*. Editions SFV. 1995.
3. J. Koulidiati, *Etude spectroscopique des molécules carbonées diatomiques. Application au diagnostic des plasmas d'hydrocarbures*. Ph.D thesis, in Université d'Orléans. 1991: Orléans, France.
4. M. Da Silva, *Simulation des propriétés radiatives du plasma entourant un véhicule traversant une atmosphère planétaire à vitesse hypersonique*. Ph.D thesis, in Université d'Orléans. 2004: Orléans, France.
5. A.P. Napartovich, *Overview of atmospheric pressure discharges producing nonthermal plasma*. Plasmas and Polymers, 2001. **6**(1/2): p. 1-14.
6. H.R. Griem, *Principles of plasma spectroscopy*. Cambridge: Cambridge University Press, 1997.
7. A. Thorne, A. Litzen, S. Johansson, ed. *Spectrophysics: Principles and applications*. 1999, Springer: Berlin.
8. A. Fridman, A. Chirokov, A. Gustol, *Non-thermal atmospheric pressure discharges*. J. Phys. D: Appl. Phys., 2005. **38**: p. R1-R24.
9. B. Eliasson, M. Hirth, U. Kogelschatz, *Ozone synthesis from oxygen in dielectric barrier discharges*. J. Phys. D: Appl. Phys., 1987. **20**: p. 1421-1437.
10. A.M. Falick, B.H. Mahan, R.J. Myers, *Paramagnetic resonance spectrum of the ( $a^1\Delta_g$ ) oxygen molecule*. The Journal of Chemical Physics, 1965. **42**(5): p. 1837-1838.
11. M. Vialle, M. Touzeau, G. Gousset, C.M. Ferreira, *Kinetics of  $O(^1S)$  and  $O(^1D)$  metastable atoms in a DC oxygen glow discharge*. J. Phys. D: Appl. Phys., 1991. **24**: p. 301-308.
12. D. Bersis, D. Katakis, *Surface effects in the production of ozone in the silent discharge*. J. Chem. Phys., 1997. **40**.
13. Xudong Xu, M.J. Kushner, *Multiple microdischarge dynamics in dielectric barrier discharges*. Journal of Applied Physics, 1998. **84**(8).
14. C. Kruger, T. Owano, C. Laux *Experimental investigation of atmospheric pressure nonequilibrium plasma chemistry*. IEEE Transactions on Plasma Science, 1997. **25**(5): p. 1042-1051.
15. L. Yu, C. Laux, C. Kruger, R. Zare, *Direct-current glow discharges in atmospheric pressure air plasmas*. J. Appl. Phys., 2002. **91**: p. 2678.
16. M.M. Kekez, M.R. Barrault, J.D. Craggs, *Spark channel formation*. J. Phys. D: Appl. Phys., 1970. **3**: p. 1886-1896.
17. T. Yokoyama, M. Kogoma, T. Moriwaki, S. Okazaki *The mechanism of the stabilisation of glow plasma at atmospheric pressure*. J. Phys. D: Appl. Phys., 1990. **23**: p. 1125-1133.
18. S. Okazaki, M. Kogoma, M. Uehara, Y. Kimura *Appearance of stable glow discharge in air, argon, oxygen and nitrogen at atmospheric pressure using a 50 Hz generator*. J. Phys. D: Appl. Phys., 1993. **26**: p. 889-892.
19. N. Gherardi, G. Gouda, E. Gat, A. Ricard, F. Massines, *Transition from glow silent discharge to micro-discharges in nitrogen gas*. Plasma Sources Sci. Technol., 2000. **9**: p. 340-346.
20. R. Brandenburg, V.A. Maiorov, Yu.B. Golubovskii, H.E. Wagner, J. Behnke, J.F. Behnke, *Diffuse barrier discharges in nitrogen with small admixtures of oxygen: discharge mechanism and transition to the filamentary regime*. J. Phys. D: Appl. Phys., 2005. **38**: p. 2187-2197.
21. Z. Navratil, R. Brandenburg, D. Trunec, A. Brablec, P. Stahel, H.E. Wagner, Z. Kopecky, *Comparative study of diffuse barrier discharges in neon and helium*. Plasma Sources Sci. Technol., 2006. **15**: p. 8-17.
22. G. Gouda, F. Massines, *Role of excited species in dielectric barrier discharge mechanisms observed in helium at atmospheric pressure*. Electrical Insulation and Dielectric Phenomena, 1999. **2**: p. 496-499.
23. J.J. Thomson, *Recent researches in electricity and magnetism*, in Oxford: Clarendon. 1893: p.115.

24. S.A. Bozhenkov, S.M. Starikovskaia, A.Y. Starikovskii, *Deflagration-to-detonation control by non-equilibrium gas discharges and its applications for pulsed detonation engine*, in *Moscow Institute of Physics and Technology Reports, Dolgoprudny, Russia*, astar@neq.mipt.ru.
25. S.M. Starikovskaia, N.B. Anikin, S.V. Pancheshnyi, A.Y. Starikovskii, *Time resolved emission spectroscopy and its applications to study pulsed nanosecond high-voltage discharges*, in *Moscow institute of Physics and technology: Dolgoprudny, Russia*.
26. N.B. Anikin, E.I. Mintousov, S.V. Pancheshnyi, D.V. Roupasov, V.E. Sych, A.Y. Starikovskii, *Nonequilibrium plasmas and its applications for combustion and hypersonic flow control*, in *41st Aerospace Sciences Meeting and Exhibit, AIAA 2003-1053*. 2003: Reno, Nevada. p. 1-11.
27. A.Y. Starikovskii, *Initiation of ignition by the action of a high-current pulsed discharge on a gas*. *Combustion, Explosion and Shock Waves*, 2003. **39**(6): p. 619-626.
28. S.M. Starikovskaia, E.N. Kukaev, A.Y. Kuksin, M.M. Nudnova, A.Y. Starikovskii, *Analysis of the spatial uniformity of the combustion of a gaseous mixture initiated by a nanosecond discharge*. *Combustion and Flame*, 2004. **139**: p. 177-187.
29. N.B. Anikin, S.M. Starikovskaia, A.Y. Starikovskii, *Oxidation of C1-C10 hydrocarbons in stoichiometric and lean mixtures with air and oxygen under the action of nanosecond discharge*. *American Institute of Aeronautics and Astronautics*, 2004: p. 1-12.
30. C.W. McCluskey, *The search for metastables and molecular ions in discharges*. *Ph.D thesis*, in *University of Texas at Austin*. 2002: Texas.
31. C. Yamabe, A.V. Phelps, *Excitation of the  $O_2(a^1\Delta_g)$  state by low energy electrons in  $O_2-N_2$  mixtures*. *J. Chem. Phys*, 1983. **78**(6): p. 2984-2989.
32. L.R. Martin, R.B. Cohen, J.F. Schatz, *Quenching of laser induced fluorescence of  $O_2(b^1\Sigma_g^+)$  by  $O_2$  and  $N_2$* . *Chemical Physics Letters*, 1976. **41**(2): p. 394-396.
33. L.T. Cupitt, G.A. Takacs, G.P. Glass, *Reaction of hydrogen atoms and  $O_2(a^1\Delta_g)$* . *International Journal of Chemical Kinetics*, 1982. **14**: p. 487-497.
34. A. A. Ionin, Y. M. Klimachev, A. A. Kotkov, I. V. Kochetov, A. P. Napartovich, L. V. Seleznev, D. V. Sinitsyn, and G. D. Hager, *Non-self-sustained electric discharge in oxygen gas mixtures: singlet delta oxygen production*. *J. Phys. D : Appl. Phys.*, 2003. **36**: p. 982-989.
35. A. Bourig, V. Lago, J.P. Martin, K. Pliavaka, F. Pliavaka, S. Gorbатов, *Generation of singlet oxygen in HV pulsed + DC crossed discharge at atmospheric pressure for oxygen-enhanced combustion*. *International Journal of Plasma Environmental Science and Technology*, 2007. **1**(1): p. 57-63.
36. A.M. Starik, N.S. Titova, B.I. Loukhovitski, *Laser-induced excitation of target molecules as an efficient approach to control the combustion and technological chemical processes*. *International Conference on Lasers, Applications and Technologies. Proceedings of SPIE*, 2005. **6053**: p. 1-10.
37. D.L. Carroll, J.T. Verdeyen, D.M. King, J.W. Zimmerman, J.K. Laystrom, B.S. Woodarb, N. Richardson, K. Kittell, J.M. Kushner, W.C. Solomon, *Measurement of positive gain on the 1315 nm transition of atomic iodine pumped by  $O_2(a^1\Delta_g)$  produced in an electric discharge*. *Applied Physics Letters*, 2004. **85**(7): p. 1320-1322.
38. W.T. Rawlins, S. Lee, W.J. Kessler, S.J. Davis, *Observations of gain on the  $I(^2P_{1/2} - ^2P_{3/2})$  transition by energy transfer from  $O_2(a^1\Delta_g)$  generated by a microwave discharge in a subsonic-flow reactor*. *Applied Physics Letters*, 2005. **86**(051105): p. 1-3.
39. S.N. Foner, R.L. Hudson *Metastable oxygen molecules produced by electrical discharges*. *J. Chem. Phys.*, 1956. **25**(3): p. 601-602.
40. A. P. Napartovich, A. Deryugin, and I. Kochetov, *Discharge production of the singlet delta oxygen for an iodine laser*. *J. Phys. D : Appl. Phys.*, 2001. **34**: p. 1827-1833.
41. A. Hicks, S. Norberg, P. Shawcross, W.R. Lempert, J.W. Rich, I.G. Adamovich, *Development of a non-self-sustained electric discharge pumped oxygen-iodine laser*, in *36<sup>th</sup> Plasmadynamics and Laser conference. AIAA-2005-4916*. 2005: Toronto.
42. J.T. Verdeyen, D.M. King, D.L. Carroll, W.C. Solomon, *Diagnostic development for the ElectriCOIL flow system*, in *Proceedings of the Gas and Chemical Lasers and Intense Beam Applications III Conference: SPIE, Bellingham, WA*. 2002: San Jose, CA.

43. A. N. Vasiljeva, K. S. Klopovskiy, A. S. Kovalev, D. V. Lopaev, Y. A. Mankelevich, N. A. Popov, A. T. Rakhimov, T. V. Rakhimova, *On the possibility of  $O_2(a^1\Delta_g)$  production by a non-self-sustained discharge for oxygen-iodine laser pumping*. J. Phys. D : Appl. Phys., 2004. **37**: p. 2455-2468.
44. D.S. Stafford, M.J. Kushner,  *$O_2(a^1\Delta_g)$  production in He/ $O_2$  mixtures in flowing low pressure plasmas*. Journal of Applied Physics, 2004. **96**(5): p. 2451-2465.
45. O.V. Braginskiy, A.N. Vasilieva, K.S. Klopovskiy, A.S. Kovalev, D.V. Lopaev, O.V. Proshina, T.V. Rakhimova, A.T. Rakhimov, *Singlet oxygen generation in  $O_2$  flow excited by RF discharge: I. Homogeneous discharge mode: alpha-mode*. J. Phys.D: Appl. Phys., 2005. **38**: p. 3609-3625.
46. T.V. Rakhimova, A.S. Kovalev, A.T. Rakhimov, K.S. Klopovsky, D.V. Lopaev, Y.A. Mankelevich, O.V. Proshina, O.V. Braginsky, A.N. Vasilieva, *Radio-frequency plasma generation of singlet oxygen in  $O_2$  and  $O_2:Ar$  (He) mixtures*, in 34<sup>th</sup> *Plasmadynamics and Lasers Conference, AIAA 2003-4306*. 2003: Orlando, Florida.
47. E.W. Gray, E.A. Ogryzlo, *The cooperative emission bands of 'singlet' molecular oxygen*. Chemical Physics Letters, 1969. **3**(9): p. 658-660.
48. A. Hicks, S. Norberg, P. Shawcross, W.R. Lempert, J. W. Rich, I.G. Adamovich, *Singlet oxygen generation in a high pressure non-self-sustained electric discharge*. J. Phys.D: Appl. Phys., 2005. **38**: p. 3812-3824.
49. F.D. Findlay, *Visible emission of molecular oxygen*. Canadian Journal of Physics, 1970. **48**: p. 2017-2111.
50. D.L. Carroll, J.T. Verdeyen, D.M. King, J.W. Zimmerman, J.K. Laystrom, B.S. Woodard, G.F. Benavides, K. Kittell, M.J. Kushner, W.C. Solomon, *Continuous-wave laser oscillation on the 1315 nm transition of atomic iodine pumped by  $O_2(a^1\Delta_g)$  produced in a electric discharge*. Applied Physics Letters, 2005. **86**(111104): p. 1-3.
51. R.F. Heidner III, C.E. Gardner, T.M. El-Sayed, G.I. Segal, J.V.V. Kasper, *Temperature dependence of  $O_2(a^1\Delta_g)+O_2(a^1\Delta_g)$  and  $I(^2P_{1/2})+O_2(a^1\Delta_g)$  energy pooling*. J. Phys. Chem., 1981. **74**(10): p. 5618-5626.
52. D.S. Stafford, M.J. Kushner,  *$O_2(a^1\Delta_g)$  production in He/ $O_2$  mixtures in flowing low pressure plasmas*. J. Phys. D: Appl. Phys., 1999. **32**: p. 3004-3012.
53. D.M. King, D.L. Carroll, J.K. Laystrom, J.T. Verdeyen, M.S. Sexauer, W.C. Solomon, *ElectricCOIL: preliminary experiments of excited oxygen generation by RF discharge*, in *Proceedings of the International Conference on Lasers*, Press STS, Editor. 2001: Mc Lean VA. p. 265-272.
54. J. Schmiedberger, H. Fuji, *Radio-frequency plasma jet generator of singlet delta oxygen with high yield*. Appl. Phys. Lett., 2001. **78**: p. 2649.
55. N. P. Vagin, A. A. Ionin, Yu. M. Klimachev, I. V. Kochetov, A. P. Napartovich, D. V. Sinitsyn, N. N. Yuryshv, *Glow discharge in singlet oxygen* Plasma Phys. Rep., 2003. **29**(3): p. 211.
56. A. Hicks, S. Tirupathi, Y. Utkin, N. Jiang, W.R. Lempert, J.W. Rich, I.V. Adamovich, K. Galbally-Kinney, W.J. Kessler, W.T. Rawlins, P.A. Mulhall, S.J. Davis, *Gain measurements in a non-self-sustained electric discharge pumped oxygen-iodine laser cavity*, in 37<sup>th</sup> *AIAA Plasmadynamics and Lasers Conference, AIAA 2006-3754*. 2006: San Francisco, CA.
57. A. Hicks, Y. Utkin, W.R. Lempert, J.W. Rich, I.V. Adamovich, *Progress in development of a non-self-sustained electric discharge pumped oxygen-iodine laser*, in 44<sup>th</sup> *Aerospace Sciences Meeting and Exhibit. AIAA Paper 2006-1359*. 2006: Reno, Nevada.
58. A. Hicks, Yu.G. Utkin, K. Frederickson, W.R. Lempert, J.W. Rich, I.V. Adamovich, *Continuous wave operation of a non-self-sustained electric discharge pumped oxygen-iodine laser*, in 45<sup>th</sup> *Aerospace Sciences Meeting and Exhibit. AIAA Paper 2007-1191*. 2007: Reno, Nevada.
59. R.F. Heidner III, C.E. Gardner, G.I. Segal, T.M. El-Sayed, *Chain-reaction mechanism for  $I_2$  dissociation in the  $O_2(a^1\Delta_g)$  - I atom laser*. J. Phys. Chem., 1983. **87**: p. 2348-2360.
60. C.H. Church, F.G. Frederick, D.N. Assanis, *Use of singlet delta oxygen to enhance the performance of internal combustion engines, diesel engines in particular*. US Patent and Trademark Office 20030094163, 2003.

61. A. Vincent-Randonnier, S. Larigaldie, P. Magre, V. Sabel'nikov, *Experimental study of a methane diffusion flame under dielectric barrier discharge assistance*. IEEE Trans. Plasma Sci., 2007. **35**: p. 223-232.
62. R. Kato, I. Kimura. *Numerical simulation of flame-stabilization and combustion promotion by plasma jets in supersonic air streams*. in *Proc. 26th Int. Symp. on Combustion 1996*. Pittsburg, PA.
63. K.Takita, *Ignition and flame-holding by oxygen, nitrogen and argon plasma torches in supersonic airflow*. Combustion and Flame, 2002. **128**(3): p. 301-313.
64. G. Lou, A. Bao, M. Nishihara, S. Keshav, Y.G. Utkin, J. William, W.R. Lempert, I.V. Adamovich, *Ignition of premixed hydrocarbon-air flows by repetitively pulsed, nanosecond pulse duration plasma*. Proceedings of the Combustion Institute, 2007. **31**: p. 3327-3334.
65. A.M. Starik, N.G. Dautov *On a possibility of promotion of combustion for H<sub>2</sub>-O<sub>2</sub> mixture by excitation of molecular vibrational degrees of freedom*. Dokl. Phys., 1994. **39**: p. 424-433.
66. A.M. Starik, N.S. Titova, *Low-temperature initiation of the detonation combustion of gas mixtures in a supersonic flow under excitation of the O<sub>2</sub>(a<sup>1</sup>Δ<sub>g</sub>) state of molecular oxygen*. Dokl. Phys., 2001. **46**: p. 627-632.
67. A.M. Starik, B.I. Lukhovitskii, V.V. Naumov, N.S. Titova, *On combustion intensification mechanisms in the case of electrical-discharge-excited oxygen molecules*. Tech. Phys., 2007. **52**: p. 1281-1290.
68. W.S. Choi, Y. Neumeier, J. Jagoda, *Stabilization of a combustion process near lean blow off (LBO) by an electric discharge*, in *42<sup>nd</sup> Aerospace Sciences Meeting and Exhibit, AIAA 2004-982*. 2004: Reno, Nevada.
69. D. Han, M.G. Mungal, *Simultaneous measurement of velocity and CH layer distribution in turbulent non-premixed flames*. Proc. Combust. Inst., 2001. **28**: p. 261-267.
70. L. Muñiz, M.G. Mungal, *Effects of heat release and buoyancy on flow structure and entrainment in turbulent nonpremixed flame*. Combustion and Flame, 2001. **126**(1-2): p. 1402-1420.
71. C.D. Carter, J.M. Donbar, J.F. Driscoll, *Simultaneous CH-PIV imaging of turbulent nonpremixed flames*. Appl. Phys. B, 1998. **66**(1): p. 129-132.
72. S. Prakash, S. Nair, T.M. Muruganandam, Y. Neumeier, T. Lieuwen, J. Seitzman, B.T. Zinn, *Acoustic sensing and mitigation of lean blow out in premixed flames*, in *43<sup>rd</sup> AIAA Aerospace Sciences Meeting and Exhibit. AIAA-2005-1420*. 2005: Reno, Nevada.
73. S. Tachibana, S. Zimmer, Y. Kurosawa, K. Suzuki, *The effects of location of secondary fuel injection on the suppression of combustion oscillation*, in *2<sup>nd</sup> Asian Joint Conference on Propulsion and Power*. 2005: Kitakyushu, Japan.
74. R.W. Schefer, M. Namazian, J. Kelly, *Velocity measurements in a turbulent nonpremixed bluff-body stabilized flame*. Combust. Sci. Technol., 1987. **56**(4-6): p. 101-138.
75. D.T. Yegian, R.K. Cheng, *Development of a lean premixed low swirl burner for low NO<sub>x</sub> practical applications*. Combust. Sci. Technol., 1998. **139**(1-6): p. 207-227.
76. S. Archer, A.K. Gupta, *The role of confinement on flow dynamics under fuel lean combustion conditions*, in *2<sup>nd</sup> International Energy Conversion Engineering Conference. AIAA 2004-5617*. 2004: Providence, Rhode Island.
77. W. Kim, H. Do, M.G. Mungal, M.A. Cappelli, *Optimal discharge placement in plasma-assisted combustion of a methane jet in cross flow*. Combustion and Flame, 2008. **153**: p. 603-615.
78. H.F. Calcote, *Electrical properties of flames: burner flames in transverse electric fields* Proc. Combust. Inst., 1949. **3**(1): p. 245-253.
79. H.F. Calcote, C.H. Berman, *Increased methane-air stability limits by a DC electric field*, in *Fossil Fuel Combustion Symposium*. 1989, p.25-31: Houston, Texas.
80. M.L. Polanyi, G.H. Markstein, *Phenomena in electrically and acoustically disturbed flames*, in *Project SQUID Technical Report*, Laboratory Cornell Aeronautical, Editor. 1947.
81. G.P. Tewari, J.R. Wilson, *Experimental study of the effects of high frequency electric fields on laser-induced flame propagation*. Combustion and Flame 1975. **24**(2): p. 159-167.
82. C.S. Maclatchy, R.M. Clements, P.R. Smy, *An experimental investigation of the effect of microwave radiation on a propane-air flame*. Combustion and Flame, 1982. **45**: p. 161-169.

83. S.H. Won, M.S. Cha, C.S. Park, S.H. Chung, *Effect of electric fields on reattachment and propagation speed of tribrachial flames in laminar coflow jets*. Proc. Combust. Inst., 2007. **31**: p. 963-970.
84. F.J. Weinberg, K. Hom, A.K. Oppenheim, K. Teichman, *Ignition by plasma-jet*. Nature, 1978. **272**: p. 341-343.
85. F.B. Carleton, I.M. Vince, F.J. Weinberg, *Structure and extinction of near-limit flames in a stagnation flow*. Proc. Combust. Inst., 1983. **19**: p. 1523-1531.
86. A.J.J. Lee, F.J. Weinberg, *A novel ignition device for the internal combustion engine*. Nature, 1984. **311**: p. 738-740.
87. W.-S. Choi, Y. Neumeier, J. Jagoda, *Stabilization of a combustion process near lean blow off (LBO) by an electric discharge*, in *42nd Aerospace Sciences Meeting and Exhibit, AIAA 2004-982*. 2004: Reno, Nevada.
88. S.A. Bozhenkov, S.M. Starikovskaia, A.Yu. Starikovskii, *Nanosecond gas discharge ignition of H<sub>2</sub> and CH<sub>4</sub> containing mixtures*. Combustion and Flame, 2003. **133**: p. 133-146.
89. E.I. Mintoussov, S.V. Pancheshnyi, A.Y. Starikovskii, *Propane-air flame control by non-equilibrium low temperature pulsed nanosecond barrier discharge*, in *42<sup>nd</sup> AIAA Aerospace Sciences Meeting and Exhibit*. 2004: Reno, Nevada
90. D. Galley, G. Pilla, D. Lacoste, S. Ducruix, F. Lacas, D. Veynante, C.O. Laux, *Plasma-enhanced combustion of a lean premixed air-propane turbulent flame using a nanosecond repetively pulsed plasma*, in *43<sup>rd</sup> AIAA Aerospace Sciences meeting and Exhibit, AIAA 2005-1193*. 2005.
91. S. Pancheshnyi, D. Lacoste, A. Bourdon, C.O. Laux, *Propane-air mixtures ignition by a sequence of nanosecond pulses*, in *European Conference for Aerospace Sciences*. 2005: Moscow, Russia.
92. S.M. Starikovskaia, I.N. Kosarev, A.V. Krasnochub, E.I. Mintoussov, A.Y. Starikovskii, *Control of combustion and ignition of hydrocarbon-containing mixtures by nanosecond pulsed discharges*, in *43<sup>rd</sup> AIAA Aerospace Sciences Meeting and Exhibit*. 2005: Reno, Nevada.
93. A.Yu. Starikovskii, *Plasma supported combustion*. Proc. Combust. Inst., 2005. **30**(2): p. 2405-2417.
94. E.I. Mintoussov, A.A. Nikipelov, S.M. Starikovskaia, A.Yu. Starikovskii, *Mechanisms of nanosecond barrier discharge influence on flame propagation*, in *44<sup>th</sup> AIAA Aerospace Sciences Meeting and Exhibit*. 2006: Reno, NV.
95. G. Lou, A. Bao, M. Nishihara, S. Keshav, Y.G. Utkin, I.V. Adamovich, *Ignition of ethylene-air and methane-air flows by low-temperature repetively pulsed nanosecond discharge plasma*, in *44<sup>th</sup> AIAA Aerospace Sciences Meeting and Exhibit*. 2006: Reno, NV.
96. N. Chintala, A. Bao, G. Lou, I.V. Adamovich, *Measurements of combustion efficiency in nonequilibrium RF plasma-ignited flows*. Combustion and Flame, 2006. **144**(4): p. 744-756.
97. S.M. Starikovskaia, N.B. Anikin, I.N. Kosarev, N.A. Popov, A.Yu. Starikovskii, *Analysis of ignition by nonequilibrium sources. Ignition of homological series of hydrocarbons by volume nanosecond discharge*, in *44th AIAA Aerospace Sciences Meeting and Exhibit. AIAA 2006-616*. 2006: Reno, NV.
98. E.I. Mintoussov, E.Y. Svetlana, A.A. Nikipelov, S.S. Starikovskaia, A.Yu. Starikovskii, *Plasmachemical processes in plasma-assisted combustion*, in *45<sup>th</sup> AIAA Aerospace Sciences Meeting and Exhibit. AIAA 2007-1354*. 2007: Reno, NV.
99. N.A. Popov, I.A. Kossyi, *Effect of nonequilibrium excitation of hydrogen-oxygen mixture on ignition*, in *45th AIAA Aerospace Sciences Meeting and Exhibit. AIAA 2007-1031*. 2007: Reno, NV.
100. W. Kim, H. Do, M.G. Mungal, M.A. Cappelli, *Investigation of NO production and flame structure in plasma enhanced premixed combustion*. Proc. Combust. Inst., 2007. **31**(2): p. 3319-3326.
101. W. Kim, H. Do, M.G. Mungal, M.A. Cappelli, *Plasma-discharge stabilization of jet diffusion flames*. IEEE Trans. Plasma Sci., 2006. **34**(6): p. 2545-2551.
102. A.M. Warris, F. Weinberg, *Ignition and flame stabilization by plasma jets in fast gas streams*. Twentieth Symposium (International) on Combustion, 1984: p. 1825-1831.

103. C. Laux, G. Pilla, S. Pancheshnyi, D. Pai, L. Caillault, D. Lacoste, A. Bourdon, D. Veynante. *Plasma-assisted combustion using nanosecond repetitively pulsed discharges*. in *Proceedings of the XXVIII International Conference on Phenomena in Ionized Gases*. 2007. Czech Republic.
104. G. Pilla, D. Galley, D. Lacoste, F. Lacas, D. Veynante, C. Laux, *Stabilization of a turbulent premixed flame using a nanosecond repetitively pulsed plasma*. IEEE Transactions on Plasma Science, 2006. **34**(1): p. 2471-2477.
105. A.M. Starik, N.S. Titova, *Possibility of initiation of combustion of CH<sub>4</sub>-O<sub>2</sub> (Air) mixtures with laser-induced excitation of O<sub>2</sub> molecules*. Combust. Explos. Shock Waves, 2004. **40**(5): p. 499-510.
106. L.A. Rosocha, Y. Kim, G.K. Anderson, S. Abbate, *Combustion enhancement using silent electrical discharges*. Int. J. Plasma Envir. Sci. Technol., 2007. **1**(1): p. 8-13.
107. V V Smirnov, O.M. Stelmakh, V.I. Fabelinsky, D.N. Kozlov, A.M. Starik, N.S. Titova, *On the influence of electronically excited oxygen molecules on combustion of hydrogen-oxygen mixture*. Phys. D: Appl. Phys., 2008. **41**: p. 192001-192007.
108. D.M. Silver, *Electronically excited oxygen*, in *Report number 2000-1*. 2000, U.S. Army Research Office: Washington Pentagon.
109. H. B. Babcock, L. Herzberg, *Fine structure of the red system of atmospheric oxygen bands*. The Astrophysical Journal, 1948. **108**: p. 167-190.
110. G.C. Light, *The effect of vibrational excitation on the reaction of O(<sup>2</sup>P) with H<sub>2</sub> and the distribution of vibrational energy in the product OH* J. Chem. Phys., 1978. **68**: p. 2831-2843.
111. A. Klimov, V. Brovkin, V. Bityurin, V. Vinogradov, D. VanWie, *Plasma assisted combustion*, in *39th Aerospace Sciences Meeting and Exhibit, AIAA 2001-0491*. 2001: Reno, Nevada.
112. V.P. Zhukov, V.A. Sechenov, A.Y. Starikovskii, *Spontaneous ignition of methane-air mixtures in a wide range of pressures*. Combustion, Explosion, and Shock waves, 2003. **39**(5): p. 487-495.
113. N. Chintala, R. Meyer, A. Hicks, B. Bystricky, J.W. Rich, W.R. Lempert, I.V. Adamovich, *Non-thermal ignition of premixed hydrocarbon-air and CO-air flows by nonequilibrium RF plasma*, in *42<sup>nd</sup> AIAA Aerospace Sciences Meeting and Exhibit, AIAA 2004-0835*. 2004: Reno, Nevada.
114. L.A. Rosocha, D.M. Coates, D. Platts, S. Stange, *Plasma-enhanced combustion of propane using a silent discharge*. Physics of plasmas, 2004. **11**(5).
115. S. Pancheshnyi, D. Lacoste, A. Bourdon, C. Laux, *Ignition of propane-air mixtures by a repetitively pulsed nanosecond discharge*. IEEE Transactions on Plasma Science, 2006. **34**(1): p. 2478-2487.
116. A.V. Krasnochub, E.I. Mintoussov, M.M. Nudnova, A.Y. Starikovskii, *Flame blow-off velocity control: the importance of proper organization of nanosecond barrier discharge*. XXVII<sup>th</sup> ICPIG, Eindhoven, the Netherlands, 2005.
117. A. Facault, *Spectre d'émission de l'atome d'oxygène*. Nouveau traité de chimie minérale, ed. Paul Pascal Masson et company. 1960, Paris.
118. R. Rydberg, *Rydberg-Klein-Rees method for determining potential energy curves of diatomic molecules from band spectra*. Ann. Physik, 1931. **73**: p. 376.
119. A.L.G. Rees. *The calculation of potential-energy curves from band-spectroscopic data*. in *Proc. Phys. Soc.* 1947. London.
120. D. L. Albritton, A.L. Schmeltekopf, R.N. Zare, *Vector correlations in dissociative photoionization of diatomic molecules in the VUV range*. J. Chem. Phys., 1979. **71**: p. 3271.
121. L. Campbell, M.A. Green, M.J. Brunger, P.J.O. Teubner, *Determination of differential cross sections for electron-impact excitation of electronic states of molecular oxygen*. Physical Review A, 2000. **61**(022706): p. 1-7.
122. F.R. Gilmore, *Potential energy curves for N<sub>2</sub>, NO, O<sub>2</sub>, and corresponding ions*. Journal of Quantitative Spectroscopy and Radiative Transfer, 1965. **5**(2): p. 390.
123. G. Herzberg, *Molecular spectra and molecular structure. Spectra of diatomic molecules*. Vol. 1. 1965, New Jersey: D. van Nostrand Company.

124. D.L. Huestis, R.A. Copeland, K. Knutsen, T.G. Slanger, R.T. Jongma, M.G.H. Boogarts, G. Meijer, *Branch Intensities and Oscillator Strengths for the Herzberg Absorption Systems in Oxygen*. Canadian Journal of Physics, 1994. **72**: p. 1109.
125. K. Yoshino, J.R. Esmond, J.E. Murray, W.H. Parkinson, A.P. Thorne, R.C. Learner, G. Cox, *Band oscillator strengths of the Herzberg I bands of O<sub>2</sub>*. J. Chem. Phys., 1995. **103**: p. 1243.
126. G.H. Dieke, H.D. Babcock, *The structure of the atmospheric absorption bands of oxygen*. Journal of Physics, 1927. **13**: p. 670-678.
127. D.L. Albritton, W.J. Harrop, A.L. Schmeltekopf, R.N. Zare, *Resolution of the discrepancies concerning the optical and microwave values for B<sub>0</sub> and D<sub>0</sub> of the (X<sup>3</sup>Σ<sub>g</sub><sup>-</sup>) State of O<sub>2</sub>*. Journal of Molecular Spectroscopy, 1973. **46**: p. 103-118.
128. H. Kanamori, M. Momona, K. Sakurai, *Diode-laser spectroscopy of the atmospheric oxygen band (b<sup>1</sup>Σ<sub>g</sub><sup>+</sup> - X<sup>3</sup>Σ<sub>g</sub><sup>-</sup>)*. Canadian Journal of Physics, 1989. **68**: p. 313-316.
129. H. Naus, S.J. van der Wiel, W. Ubachs, *Cavity-ring-down spectroscopy on the (b<sup>1</sup>Σ<sub>g</sub><sup>+</sup> - X<sup>3</sup>Σ<sub>g</sub><sup>-</sup>) (1,0) band of oxygen isotomers*. Journal of Molecular Spectroscopy, 1998. **192**: p. 162-168.
130. H. Naus, W. Ubachs, *The b<sup>1</sup>Σ<sub>g</sub><sup>+</sup> - X<sup>3</sup>Σ<sub>g</sub><sup>-</sup> (3-0) Band of <sup>16</sup>O<sub>2</sub> and <sup>18</sup>O<sub>2</sub>*. Journal of Molecular Spectroscopy, 1999. **193**: p. 442-445.
131. R. Klotz, C.M. Marian, S.D. Peyerimhoff, B.A. Hess, A.J. Buenker, *Calculation of spin-forbidden radiative transitions using correlated wavefunctions: Lifetimes of b<sup>1</sup>Σ<sub>g</sub><sup>+</sup>, a<sup>1</sup>Δ<sub>g</sub> states in O<sub>2</sub>, S<sub>2</sub> and SO*. J. Chem. Phys., 1984. **89**(2): p. 223.
132. A. Wallace Jones, A.W. Harrison, *Interferometric spectra of the Earth's airglow (1.2 to 1.6 μm)*. J. Atmos. and Terr. Phys., 1958. **13**: p. 45-48.
133. J.F. Noxon, A. Vallance Jones, *Observation of the (0,0) band of the (a<sup>1</sup>Δ<sub>g</sub> - X<sup>3</sup>Σ<sub>g</sub><sup>-</sup>) system of oxygen in the day and twilight airglow*. Nature, 1962. **196**(4850): p. 157-158.
134. L. Biennier, D. Romanini, A. Kachanov, A. Campargue, B. Bussey-Honvault, R. Bacis, *Structure and Rovibrational analysis of the [O<sub>2</sub>(a<sup>1</sup>Δ<sub>g</sub>)v=0 - [O<sub>2</sub>(X<sup>3</sup>Σ<sub>g</sub><sup>-</sup>)v=0]<sub>2</sub> transition of the O<sub>2</sub> dimer*. Journal of Chemical Physics, 2000. **112**(14): p. 6309-6321.
135. R.L. Miller, A.G. Suits, P.L. Houston, R. Toumi, J.A. Mack, A.M. Wodtke, *The "ozone deficit" problem: O<sub>2</sub>(X) + O(<sup>3</sup>P) from 226 nm ozone photodissociation*. Science, 1994. **265**(5180): p. 1831-1836.
136. S. Yoshida, K. Shimizu, T. Sawano, T. Tokuda, T. Fujioka, *Observation of chemical laser oscillation in the visible range*. Applied Physics Letters, 1989. **54**(24): p. 2400-2401.
137. G. Fournier, *Réactivité dans les plasmas*. Editions Physique. 1983.
138. V. Naumov, F. Pliavaka, S. Gorbатов, J.P. Martin, V. Lago, *Generation of excited oxygen in combined discharge*, in *INTAS meeting*. 2005: Varena, Italy.
139. A.J. Phillips, F. Peters, P.A. Hamilton, *Precision emission and absorption spectroscopy of the oxygen atmospheric bands (b<sup>1</sup>Σ<sub>g</sub><sup>+</sup> - X<sup>3</sup>Σ<sub>g</sub><sup>-</sup>) from Fourier Transform Spectroscopy*. Journal of Molecular Spectroscopy, 1997. **184**: p. 162-166.
140. S.M. Newman, I.C. Lane, A.J. Orr-Ewing, *Integrated absorption intensity and Einstein coefficients for the O<sub>2</sub> a<sup>1</sup>Δ<sub>g</sub> - X<sup>3</sup>Σ<sub>g</sub><sup>-</sup> (0,0) transition: A comparison of cavity ringdown and high resolution Fourier transform spectroscopy with a long-path absorption cell*. Journal of Chemical Physics, 1999. **110**(22): p. 10749-10757.
141. L.R. Brown, C. Plymate, *Experimental line parameters of the oxygen A band at 760 nm*. Journal of Molecular Spectroscopy, 2000. **199**: p. 166-179.
142. L.C. O'Brien, H. Cao, J.J. O'Brien, *Molecular constants for the v = 0, b<sup>1</sup>Σ<sub>g</sub><sup>+</sup> excited state of O<sub>2</sub>: improved values derived from measurements of the oxygen A-band using intracavity laser spectroscopy*. Journal of Molecular Spectroscopy, 2001. **207**: p. 99-103.
143. R.M. Badger, A.C. Wright, R.F. Whitlock, *Absolute intensities of the discrete and continuous absorption bands of oxygen gas at 1.26 and 1.065 μm and the radiative lifetime of the (a<sup>1</sup>Δ<sub>g</sub>) state of oxygen*. The Journal of Chemical Physics, 1965. **43**(12): p. 4345-4350.
144. J.F. Noxon, *Oxygen spectra in dayglow, twilight and during an eclipse*. Nature, 1967. **213**: p. 350-352.
145. J.H. Miller, R.W. Boese, L.P. Giver, *Intensity measurements and rotational intensity distribution for the oxygen A-band*. Journal of Quantitative Spectroscopy & Radiative Transfer, 1969. **9**: p. 1507-1517.

146. J.K.G. Watson, *Rotational line intensities in the  $^3S - ^1S$  electronic transitions*. Canadian Journal of Physics, 1968. **46**: p. 1637-1643.
147. I. Kovács, *Rotational structure in the spectra of diatomic molecules*. Elsevier. 1969, New York.
148. K.P. Huber, G. Herzberg, *Molecular spectra and molecular structure, constants of diatomic molecules*. Molecular spectra and molecular structure. 1979, New York: Van Nostrand-Reinhold.
149. Western, C. M., *PGOPHER, a Program for Simulating Rotational Structure*, University of Bristol.
150. J.W. Brault, *Detection of electric quadrupole transitions in the oxygen A band at 7600 Å*. Journal of Molecular Spectroscopy, 1980. **80**(2): p. 384-387.
151. S.L. Cheah, Y.P. Lee, J.F. Ogilvie, *Wavenumbers, strengths, widths and shifts with pressure of lines in four bands of gaseous  $^{16}O_2$  in the systems  $a^1\Delta_g - X^3\Sigma_g^-$  and  $b^1\Sigma_g^+ - X^3\Sigma_g^-$* . Journal of Quantitative Spectroscopy & Radiative Transfer 2000. **64**: p. 467-482.
152. W.L. Wiere, M.W. Smith, B.M. Miles, *Atomic transition probabilities*. National Stand. Ref. Data. Serv., 1969. **2**(22): p. 186-200.
153. C. Laux, R. Gessman, C. Kruger, F. Roux, F. Michaud, S. Davis, *Rotational temperature measurements in air and nitrogen plasmas using the first negative system of  $N_2^+$* . Journal of Quantitative Spectroscopy and Radiative Transfer, 2001. **68**(4): p. 473-482.
154. F. Roux, F. Michaud, M. Vervloet, *High resolution Fourier spectrometry of  $^{14}N_2$  violet emission spectrum: extensive analysis of the  $C^3\Pi_u - B^3\Pi_g$  system*. Journal of Molecular Spectroscopy, 1993. **158**: p. 270-277.
155. H. Kakinuma, M. Sakamoto, Y. Kasuya, H. Sawai, *Characteristics of Cr Schottky amorphous silicon photodiodes and their application to linear image sensors*. IEEE Trans. Electron. Devices, 1990. **37**: p. 128-133.
156. M. Niedre, M.S. Patterson, B.C. Wilson, *Direct near-infrared luminescence detection of singlet oxygen generated by photodynamic therapy in cells in vitro and tissues in vivo*. Photochemistry and Photobiology, 2005. **75**(4): p. 382-391.
157. J. Luo, S.L. Suib, M. Marquez, Y. Hayashi, H. Matsumoto, *Decomposition of  $NO_x$  with low-temperature plasmas at atmospheric pressure: Neat and in the presence of oxidants, reductants, water, and carbon dioxide*. J. Phys. Chem. A, 1998. **102**: p. 7954-7963.
158. S.M. Starikovskaia, A.Y. Starikovskii, D.V. Zatsepin, *Hydrogen oxidation in a stoichiometric hydrogen-air mixture in the fast ionization wave*. Combustion Theory and Modelling, 2001. **5**: p. 97-129.
159. S.A. Bozhenkov, *Chemical reactions and ignition control by nanosecond high-voltage discharge*, in *11<sup>th</sup> AIAA/AAAF International Conference Space Planes and Hypersonic Systems and Technologies*. 2002.
160. G. Hancock, L. Lanyi, J.P. Sucksmith, B.K. Woodcock, *Atoms, radicals and ions observed in plasmas-their gas phase and surface chemistry*. Pure and Applied Chemistry, 1994. **66**(6): p. 1207-1214.
161. S.A. Lawton, S.E. Novick, H.P. Broida, A.V. Phelps, *Quenching of optically pumped  $O_2(b^1\Sigma_g^+)$  by ground state  $O_2$  molecules*. The Journal of Chemical Physics, 1977. **66**(3).
162. M. Touzeau, M. Vialle, A. Zelligui, G. Gousset, M. Lefebvre, M. Pealat, *Spectroscopic temperature measurements in oxygen discharges*. J. Phys. D : Appl. Phys, 1991. **24**: p. 41-47.
163. S. Cheskis, A. Kovalenko, *Detection of atomic oxygen in flames by absorption spectroscopy*. Appl. Phys. B, 1994. **59**: p. 543-546.
164. J.B. Paul, L. Lapson, J.G. Anderson, *Ultrasensitive absorption spectroscopy with a high-finesse optical cavity and off-axis alignment*. Applied Optics, 2001. **40**(27): p. 4904-4910.
165. D. Baer, M. Gupta, A. O'Keefe, J.B. Paul, *Recent advances in off-axis integrated cavity output spectroscopy*. Diode Lasers and Applications, Proceedings of SPIE, A. Fried editions, 2002. **4817**.
166. S. Williams, M. Gupta, T. Owano, D. Baer, A. O'Keefe, D.R. Yarkony, S. Matsika, *Quantitative detection of singlet oxygen  $O_2$  by cavity-enhanced absorption*. Optical Letters, 2004. **29**: p. 1066-1072.

167. S. Popovic, M. Raskovic, S.P. Kuo, L. Vuskovic, *Reactive oxygen emission from microwave discharge plasmas* Journal of Physics : Conference Series, 2007. **86**(012013): p. 1-15.
168. D.S. Sayres, E.J. Moyer, T.F. Hanisco, J.M. StClair, F.N. Keutsch, A. O'Brien, N.T. Allen, L. Lapson, J.N. Demusz, M. Rivero, T. Martin, M. Greenberg, C. Tuozzolo, G.S. Engel, J.H. Kroll, J.B. Paul, J.G. Anderson, *A new cavity based absorption instrument for detection of water isotopologues in the upper troposphere and lower stratosphere*. Review of Scientific Instruments, 2009. **80**(044102): p. 1-14.
169. T.G. Slanger, G. Black, *Interaction of  $O_2(b^1\Sigma_g^+)$  with  $O(^3P)$  and  $O_3$* . J. Chem. Phys., 1979. **70**(7): p. 3434-3438.
170. R.L. Gättinger, *Observation and interpretation of the  $O_2(a^1\Delta_g - X^3\Sigma_g^-)$  airglow emissions*. Canadian Journal of physics, 1968. **46**: p. 1613-1626.
171. K. Tachibana, A.V. Phelps, *Excitation of the  $O_2(a^1\Delta_g)$  state by low energy electrons*. J. Chem. Phys., 1981. **75**(7): p. 3315-3320.
172. S.A. Lawton, A.V. Phelps, *Excitation of the  $b^1\Sigma_g^+$  state of  $O_2$  by low energy electrons*. J. Chem. Phys., 1978. **69**(3): p. 1055-1068.
173. A. Granier, S. Mottin, *Plasmas froids: Cinétiques, transports et transferts*. Collections Integrations. 2005, Université de St-Etienne.
174. R. Castel, E.J. Iglesias, J. Ruiz-Camacho, *Glow discharge plasma properties of gases of environmental interest*. Braz. J. Phys., 2004. **34**(4b).
175. W. Lochte-Holtgreven, *Plasma diagnostics*. Amsterdam: North-Holland. 1968.
176. A.C. Eckbreth, *Laser diagnostics for combustion temperature and species*. Combustion Science and Technology Book, ed. Ltd Taylor and Francis. 1996.
177. J.W. Daily, *Laser induced fluorescence spectroscopy in flames*. Progress in Energy and Combustion Science, 1997. **23**(2): p. 133-199.
178. G. Dixon-Lewis, M.D. Smooke, J. Warnatz, G.H. Evans, R.S. Larson, R.E. Mitchell, L.R. Petzold, W.S. Reynolds, M. Caracotsios, W.E. Stewart, P. Glarborg, C. Wang, O. Adigun, W.G. Houf, C.P. Chou, S.F. Miller, P. Ho, D.J. Young, *CHEMKIN release 4.0., Reaction Design, Inc*. 2004: San Diego, California.
179. J.P. Boeuf, L.C. Pitchford, W.L. Morgan *Bolsig Software*, in *LAPLACE (CNRS) and Kinema Research*, [www.siglo-kinema.com/bolsig.htm](http://www.siglo-kinema.com/bolsig.htm), Editor. 2000.
180. G.J.M. Hagelaar, L.C. Pitchford, *Solving the Boltzmann equation to obtain electron transport coefficients and rate coefficients for fluid models*. Plasma Sources Science and Technology, 2005. **14**: p. 722-733.
181. A. Bourig, J.P. Martin, V. Lago, D. Thévenin, K. Zähringer, *Hydrogen combustion in presence of excited oxygen produced by non thermal plasma: experimental and numerical study*, in *Nonequilibrium processes in combustion and plasma based technologies*. 2006: Minsk, Belarus. p. 121-125.
182. Z.Z. Li, A. Kazakov, F.L. Dryer, *An updated comprehensive kinetic model of hydrogen combustion*. International Journal of Chemical Kinetics, 2004. **36**: p. 1-10.
183. M. O'Conaire, H.J. Curran, J.M. Simmie, W.J. Pitz, C.K. Westbrook, *A comprehensive study of hydrogen oxidation*. Int. J. Chem. Kinetic, 2004. **36**: p. 603-622.
184. A.A. Konnov, *Detailed reaction mechanism for small hydrocarbons combustion*. 2005, release 0.5 <http://homepages.vub.ac.be/~akonnov/>.
185. O.B. Skrebkov, S.P. Karkach, V.M. Vasilev, A.L. Smirnov, *Hydrogen-oxygen reactions behind shock waves assisted by  $OH(^2\Sigma^+)$  formation*. Chem. Phys. Letters, 2003. **375**(3-4): p. 413-418.
186. I. Orlandini, U. Riedel, *Modelling of NO and HC removal by non-thermal plasmas*. Combust. Theory Modelling, 2001. **5**: p. 447-462.
187. I. Orlandini, U. Riedel, *Chemical kinetics of NO removal by pulsed corona discharges* J. Phys. D: Appl. Phys, 2000. **33**: p. 2467-2474.
188. I. Orlandini, U. Riedel, *Numerical simulation of NOx-Removal by Pulsed Corona Discharges - The Effect of Ethene*. 38th Aerospace Sciences Meeting & Exhibit, AIAA 2000-0720, 2000.
189. L.B. Ibragimova, G.D. Smekhov, O.P. Shatalov, *Recommended rate constants of chemical reactions in  $H_2-O_2$  gas mixture with electronically excited species  $O_2(a^1\Delta_g)$ ,  $O(^1D)$ ,  $OH(^2\Sigma^+)$*

- involved, in *Institute of Mechanics of Lomonosov, Moscow State University, Moscow*. 2003, <http://www.chemphys.edu.ru/pdf/2003-01-20-001.pdf/>.
190. Gaussian 03, Gaussian, Inc. 2004, <http://www.gaussian.com/home.htm>.
191. J.O. Hirschfelder, C.F. Curtiss, R.B. Bird, *Molecular theory of gases and liquids* 1964, Chapman and Hall, John Wiley & Sons.
192. D. L. Baulch, C. T. Bowman, C. J. Cobos, R. A. Cox, Th. Just, J. A. Kerr, M. J. Pilling, D. Stocker, J. Troe, W. Tsang, R. W. Walker, J. Warnatz, *Evaluated Kinetic Data for Combustion Modeling*. Journal of Physical Chemistry and Reference Data, 2005. **34**(3): p. 757-1397.
193. R. Atkinson, D.L. Baulch, R.A. Cox, J.N. Crowley, R.F. Hampson, R.G. Hynes, M.E. Jenkin, M.J. Rossi, J. Troe, *Evaluated kinetic and photochemical data for atmospheric chemistry. IUPAC subcommittee for gas kinetic evaluation*. 2005, <http://www.iupackinetic.ch.cam.ac.uk/>.
194. S.P. Sander, M.J. Kurylo, V.L. Orkin, D.M. Golden, R.E. Huie, B.J. Finlayson-Pitts, C.E. Kolb, M.J. Molina, R.R. Friedl, A.R. Ravishankara, G.K. Moortgat, *Chemical kinetics and photochemical data for use in atmospheric studies*. 2003, <http://jpldataeval.jpl.nasa.gov/>.
195. W.G. Mallard, F. Westley, J.T. Herron, R.F. Hampson, D.H. Frizzell, M. Frenklach, T. Bowman, G. Smith, B. Gardiner, in *NIST Standard Reference Database 17, NIST Chemical Kinetics Database*. 1998, <http://www.me.berkeley.edu/gri-mech/>.
196. G.P. Smith, D.M. Golden, M. Frenklach, N.W. Moriarty, B. Eiteneer, M. Goldenberg, C.T. Bowman, R.K. Hanson, S. Song, W.C. Gardiner, *GRI-Mech 3.0 Combustion Model*. 2003, [http://www.me.berkeley.edu/gri\\_mech](http://www.me.berkeley.edu/gri_mech).
197. *Leeds Master Chemical Mechanism*. <http://mcm.leeds.ac.uk/MCM/>, 2001.
198. C.K. Westbrook, W.J. Pitz, *Combustion chemical kinetic mechanisms. Lawrence Livermore National Laboratory*. 2004, <http://www-cms.llnl.gov/combustion/combustion/home.html>.
199. N.M. Marinov, C.K. Westbrook, W.J. Pitz, *Detailed and global chemical kinetic model for hydrogen*. Transport Phenomena in Combustion. Taylor and Francis. Vol. 1. 1996, Washington DC.
200. A.M. Starik, N.S. Titova, *Kinetics of detonation initiation in the supersonic flow of the H<sub>2</sub> + O<sub>2</sub> (Air) mixture in O<sub>2</sub> molecule excitation by resonance laser radiation*. Kinetics and Catalysis, 2003. **44**(1): p. 28-39.
201. D.L. Carroll, J.T. Verdeyen, D.M. King, B.S. Woodard, L.W. Skorski, J.W. Zimmerman, W.C. Solomon, *Modeling of the ElectriCOIL system*. IEEE Journal of Quantum Electronics, 2003. **39**(9): p. 1150-1159.
202. G.D. Smekhov, O.P. Shatalov. *Modeling of hydrogen-oxygen mixture combustion and calculation of the ignition time*. in *Proc. of the Europ. Conf. for Aerospace Sciences*. 2005. Moscow, Russia.
203. J. Warnatz, *Calculation of the structure of laminar flat flames: flame velocity of freely propagating hydrogen-air and hydrogen-oxygen flames*. Ber. Bunsenges. Phys. Chem., 1978. **82**: p. 643-649.
204. N. Lamoureux, N. Djebali-Chaumeix, C.E. Paillard, *Laminar flame velocity determination for H<sub>2</sub>-air-He-CO<sub>2</sub> mixtures using the spherical bomb method*. Experimental Thermal Fluid Science, 2003. **27**(4): p. 385-393.
205. O.C. Kwon, G.M. Faeth, *Flame/stretch interactions of premixed hydrogen-fueled flames: measurements and predictions*. Combustion and Flame, 2001. **124**(4): p. 590-610.
206. K. Kohse-Höinghaus, J.B. Jeffries, *Applied combustion diagnostics*. 2002: Taylor and Francis Editions.
207. Y. Hidaka, K. Sato, Y. Henmi, H. Tanaka, K. Inami, *Shock-tube and modeling study of methane pyrolysis and oxidation*. Combustion and Flame, 1999. **118**(3): p. 340-358.
208. K. Seshadri, F.A. Williams, *Laminar flow between parallel plates with injection of a reactant at high reynolds number* International Journal of Heat and Mass Transfer, 1978. **21**(2): p. 251-253.
209. J. Luque, D.R. Crosley, *LIFBASE: database and spectral simulation program*, in *SRI International*. 1999.

210. F. Massines, A. Rabehi, P. Decomps, R.B. Gadri, P. Segur, C. Mayoux, *Experimental and theoretical study of a glow discharge at atmospheric pressure controlled by dielectric barrier*. Journal of Applied Physics, 1998. **83**(6): p. 2950-2957.
211. M. Laroussi, X. Lu, V. Kolobov, R. Arslanbekov, *Power consideration in the pulsed dielectric barrier discharge at atmospheric pressure*. Journal of Applied Physics, 2004. **96**(5): p. 3027-3029.
212. J. Scharer, W. Rich, I. Adamovich, W. Lempert, K. Akhtar, C. Laux, S. Kuo, C. Kruger, R. Vidmar, R. Barker. *High frequency air plasmas, in non-equilibrium air plasma at atmospheric pressure*. in R.J. Barker (eds.), *Institute of Physics Publishing*. 2005. Bristol.
213. Paschen, F., *Ueber die zum Funkenübergang in Luft, Wasserstoff und Kohlensäure bei verschiedenen Drucken erforderliche Potentialdifferenz*. Annalen der Physik, 1889. **273**(5): p. 69-75.
214. Y.P. Raizer, *Gas discharge physics*. Springer-Verlag; 1 edition. 2001, Berlin.
215. A.E. Hill, *Continuous uniform excitation of medium-pressure CO<sub>2</sub> laser plasmas by means of controlled avalanche ionization*. Appl. Phys. Lett., 1973. **22**: p. 670.
216. N. A. Generalov, V. P. Zimakov, V. D. Kosynkin, Yu. P. Raizer, D. I. Roitenburg, *Preionization of a gas by electrodeless capacitive pulses in lasers operating in the pulse-periodic regime* Soviet Journal of Quantum Electronics, 1978. **8**(5): p. 663-665.
217. A. Hicks, Y. Utkin, W.R. Lempert, J.W. Rich, I.V. Adamovich, *Continuous wave operation of a non-self-sustained electric discharge pumped oxygen-iodine laser*. Applied Physics Letters, 2006. **89**(241131): p. 1-3.
218. A. Hill, *The next generation of controlled avalanche discharge gas lasers*. International Conference on Lasers, NM: STS Press. 2000, Albuquerque.
219. F. Massines, G. Gouda, *A comparison of polypropylene-surface treatment by filamentary, homogeneous and glow discharges in helium at atmospheric pressure*. J. Phys. D: Appl. Phys., 1998. **31**(24): p. 3411-3420.
220. E. Croquesel, N. Gherardi, S. Martin, F. Massines. *High pressure low temperature plasma chemistry*. in *Proc. HAKONE VII 7th Int. Symp. on High Pressure Low Temperature Plasma Chem.* 2000.
221. F. Massines, P. Segur, N. Gherardi, C. Khamphan, A. Ricard, *Physics and chemistry in a glow dielectric barrier discharge at atmospheric pressure: diagnostics and modeling*. Surface and Coatings Technology, 2003. **174-175**: p. 8-14.
222. D.S. Stafford, *Modeling of singlet-delta oxygen yields in flowing electric discharges*, in *Louisiana State University*. 1999: Ph.D thesis. Illinois at Urbana-Champaign.
223. Y.V. Savin, L.V. Goryachev, A.A. Adamenkov, Y.A. Adamenkov, S.P. Ilyin, Y.V. Kolobyanin, E.A. Kudryashov, B.A. Vyskubenko, T.V. Rakhimova, Y.A. Mankelevich, N.A. Popov, *Traveling microwave discharge as a singlet ( $a^1\Delta_g$ ) oxygen source*. AIAA Paper 2003-4305, 2003.
224. A. Tachibana, K. Nakamura, T. Yano, Y. Sugiyama, S. Tanimura, *Quantum chemical study of ion-molecule reactions in N<sub>2</sub>+O<sub>2</sub> system*. J. Phys. Chem. A, 1999. **103**(29): p. 5749-5757.
225. J. Warnatz, U. Maas, R.W. Dibble, *Combustion*. Springer-Verlag. 1996, New-York.
226. J. W. Butterbaugh, L. D. Baston, H. H. Sawin, *Measurements and analysis of radio frequency glow discharge electrical impedance and network power loss*. J. Vac. Sci. Technol. A, 1990. **8**(2): p. 916.
227. R.J. Litchford, T.J. Madden. *An examination of unsteady flow predictions for the chemical oxygen-iodine laser*. in *34<sup>th</sup> AIAA Plasmadynamics and Lasers Conference*. 2003. Orlando, Florida.
228. P.A. Davidovich, S.V. Harbatau, I.V. Kurnosau, F.V. Pliavaka, Y.M. Prykhodzka, S.A. Zhdanok. *High frequency solid state generators of nanosecond high voltage pulses to excite gas discharges*. in *VI International School-seminar, "Nonequilibrium processes and their applications*. 2002. Minsk.
229. S.V. Harbatau, P.A. Davidovich, I.V. Kurnosau, F.V. Pliavaka, Y.M. Prykhodzka, *1 kW 100 kHz high voltage pulse generator to excite nonequilibrium gaseous plasma*, in *Heat and Mass Transfer Institute. Internal report*. 2003: Minsk, Belarus.



# Appendices

## Appendix 1. Hund vectorial coupling

### Description

The movement of electrons, of molecule nuclei, the resultant spin and eventually the individual electron spins are not totally independent one from another. There are interactions between these movements. This is evident because the movement of nuclei and electrons produce a magnetic field. The intrinsic property of spin is its magnetic moment.

In one hand, there is interaction between the magnetic field created by electron movements and nuclei, and in the other hand, the proper individual electrons spin resultant.

In 1926, Hund was the first to examine these phenomena, classify and model the typical interactions names case (a), (b), (c), (d) and (e). It is worth noting that case (a) and case (b) are the most important and will be presented.

The following nomenclature will be used :

$\vec{L}$  : Electronic angular momentum and  $\vec{\Lambda}$  its projection on the internuclear axis

$\vec{S}$  : The electrons spin resultant and  $\vec{\Sigma}^*$  its projection on the internuclear axis

$\vec{\Omega}$  : Total electronic angular momentum along the internuclear axis

$\vec{N}$  : The nuclei rotational angular momentum, perpendicularly to internuclear axis

$\vec{K}$  : The resultant vector of  $\vec{N}$  and  $\vec{\Lambda}$

$\vec{J}$  : The resultant angular momentum of molecule ;  $\vec{J} = \vec{\Omega} + \vec{N}$  or  $\vec{J} = \vec{\Lambda} + \vec{S}$  if  $\vec{\Omega}$  is not defined

### Hund coupling case (a)

The interaction between the nuclei rotation and the movement of electrons  $\vec{L}$  and  $\vec{S}$  is very weak.  $\vec{L}$  and  $\vec{S}$  are in rapid precession around the internuclear axis and  $\vec{S}$  for axial component  $\vec{\Sigma}^*$  which takes  $2S+1$  values between  $-S$  and  $+S$ .

The coupling  $\vec{\Omega} = \vec{\Lambda} + \vec{\Sigma}$  is produced and  $\Omega = |\Lambda - S|, \dots, \Lambda + S$ . The resultant angular momentum of

the molecule  $\vec{J} = \vec{\Omega} + \vec{N}$  and the corresponding quantum number  $J$  takes the values  $J = \Omega, \Omega+1, \Omega+2,$  etc., (the energy levels for  $J < \Omega$  do not exist).

The Hund cases (a) are applied for  $\Lambda > 0$ . The associated schematic vectorial diagram is presented in Fig.A1.1.

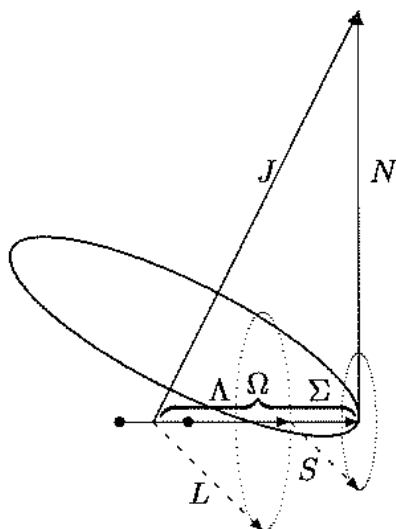


Fig.A1.1. Vectorial diagram of Hund coupling case (a).

### **Hund coupling case (b)**

The case (b) is applied for  $\Lambda = 0$  (which corresponds to  $\Sigma$  states), but also for  $\Lambda > 0$ , only if the spin-orbit coupling between  $\vec{\Lambda}$  and  $\vec{\Sigma}$  is weak due to the weakness of the magnetic field associated with  $\vec{L}$ .  $\vec{S}$  is not determined anymore according to the molecule axis and  $\vec{\Sigma}$  do not exist (then  $\vec{\Omega}$  is not defined as well as the quantum number  $\Omega$ ). Values of  $\vec{\Lambda}$  and  $\vec{N}$  form a resultant  $\vec{K} = \vec{\Lambda} + \vec{N}$ , around it,  $\vec{\Lambda}$  and  $\vec{N}$  are present. The corresponding quantum number  $K$  takes the values  $K = \Lambda + 1, \Lambda + 2 \dots$ . Vectors  $\vec{K}$  and  $\vec{S}$  form a total angular momentum  $\vec{J} = \vec{K} + \vec{S}$  of the molecule, having a fixed direction, around it, are  $\vec{K}$  and  $\vec{S}$ . For a given value of  $K$ , the corresponding quantum number  $J$  takes the values  $K + S, K + S - 1, \dots, (K - S)$  and then, each energy level described by  $K$  is composed of  $2S + 1$  sub-levels.

The associated schematic vectorial diagram is presented in Fig.A1.2.

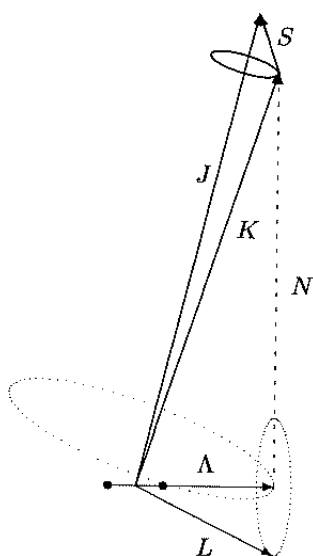


Fig.A1.2. Vectorial diagram of Hund coupling case (b).

### Other Hund coupling cases

For the so-called Hund coupling case (c), the resultant  $\vec{J}$  coming from the strong interaction between vectors  $\vec{L}$  and  $\vec{S}$  is determined according to the internuclear axis. The Hund coupling case (c) is generally realized by the very heavy molecules.

For case (d), the coupling of  $\vec{L}$  with the internuclear axis is very weak; the coupling of  $\vec{S}$  with the internuclear axis and with  $\vec{L}$  is even weaker.  $\vec{L}$ , in these conditions, couples directly with  $\vec{N}$  to form  $\vec{K}$ , whose associate quantum number takes the values  $N+L, \dots, |N-L|$ . The spin  $\vec{S}$  finally couples with  $\vec{K}$  to form the total angular momentum of the molecule  $\vec{J} = \vec{K} + \vec{S} = \vec{N} + \vec{L} + \vec{S}$ . The energy associated to this coupling is very weak.

## Appendix 2. Comparisons between Hitran, Pgopher and our simulation program

Figures A2.1 show high resolution rotationally resolved emission spectra of A-band and infrared band comparison using two different programs : Hitran and Pgopher.

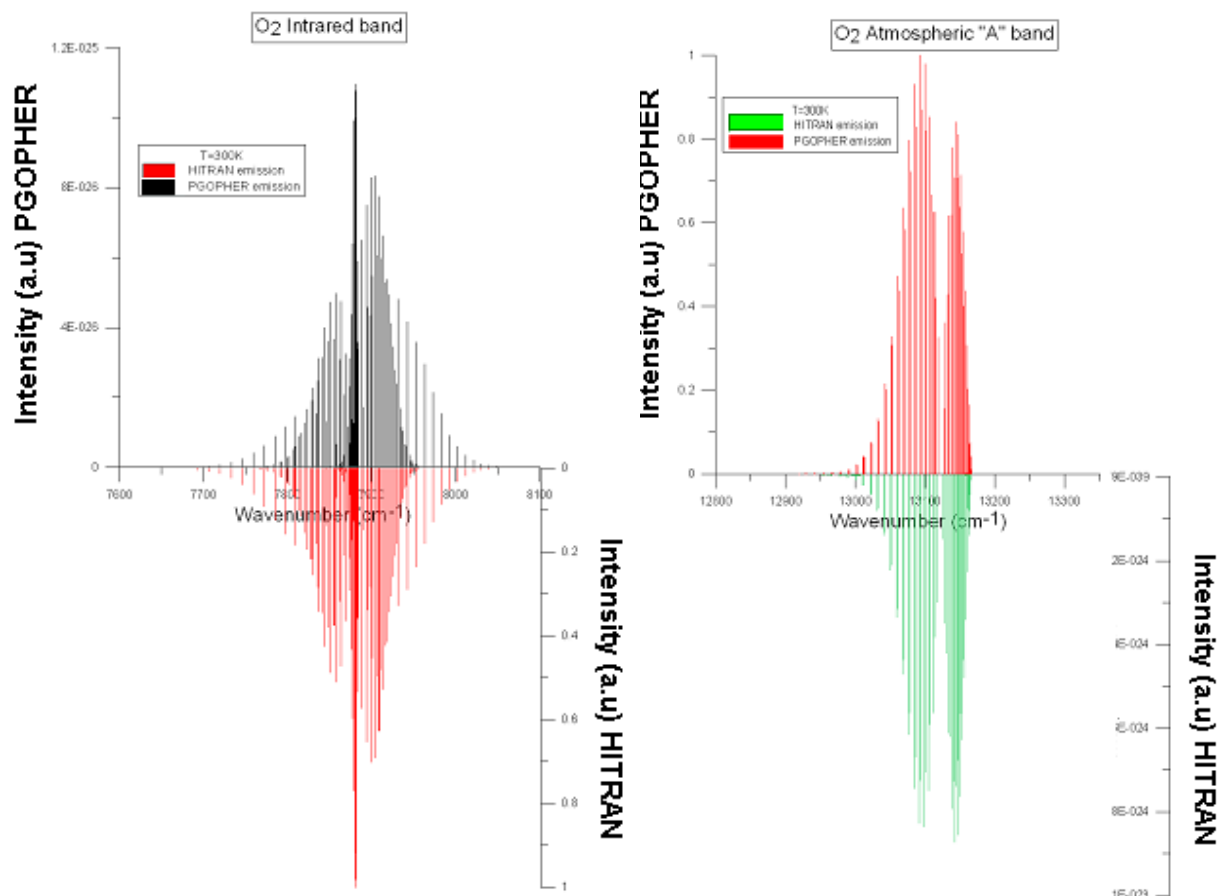


Fig.A2.1. Simulated high resolution rotational emission spectra of gaseous  $^{16}\text{O}_2$  in the band (right) :  $b^1\Sigma_g^+(v=0) \rightarrow X^3\Sigma_g^-(v=0)$  and (left) :  $b^1\Sigma_g^+(v=0) \rightarrow X^3\Sigma_g^-(v=0)$ . Comparison between two simulation programs.

The position of lines taking Pgopher<sup>®</sup> or Hitran<sup>®</sup> programs are determined and corresponds with a very good accuracy. For each line, we comfort the fact that a perfect fit is observed using one program or the other.

Figures A2.2 show a comparison of intermediate resolution emission spectra of A-band and infrared band using our simulation program. It can be observed that the agreement between the two computed spectra is very satisfactory. The very slight systematic deviation between the two calculated values is probably due to the fact that the values of certain molecular constants which have to be used in the determination of the lines positions are not exactly the same.

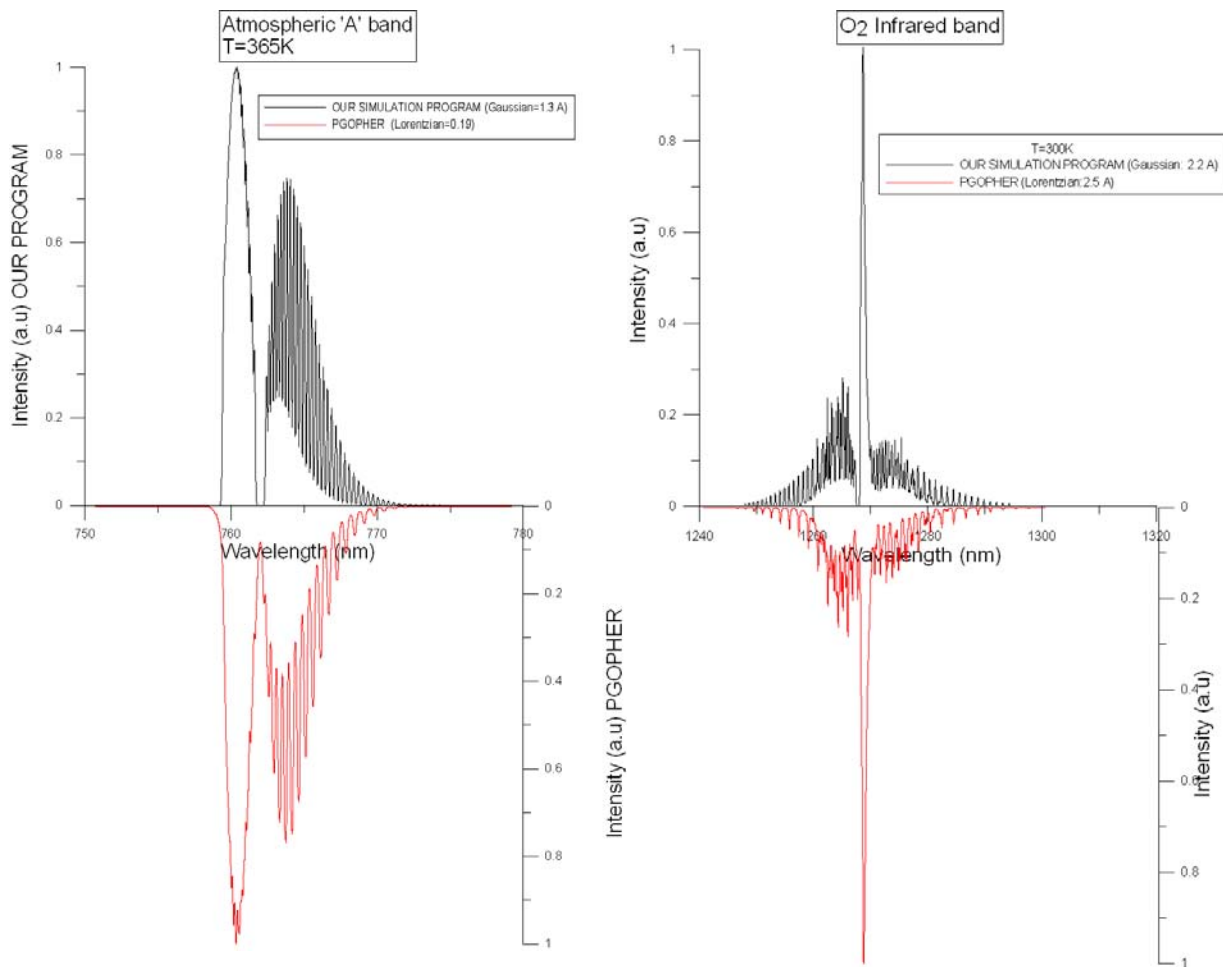


Fig.A2.2. Simulated intermediate resolution rotational emission spectra of gaseous  $^{16}\text{O}_2$  in the band (right):  $b^1\Sigma_g^+(v=0) \rightarrow X^3\Sigma_g^-(v=0)$  and (left):  $b^1\Sigma_g^+(v=0) \rightarrow X^3\Sigma_g^-(v=0)$ . Comparison between two simulation programs.

From these sets of spectra, it is now possible to predict accurately the transitions between these states. We are then able to compare calculated and experimental emission spectra and to measure the associated rotational temperature.

### Appendix 3. Emission line identification

Identification of different vibrational systems ( $v_1v_2$ ) of  $O_2(b^1\Sigma_g^+)$  atmospheric A-band,  $O_2^+(b^4\Sigma_g^-)$  first negative system,  $N_2^+(B^2\Sigma_u^+)$  first negative system and  $N_2(C^3\Pi_u)$  second positive system is presented in the following tables. The emission line strength is represented by a gradation of blue. The darkest blue means a high strength emission band.

$O_2(b^1\Sigma_g^+)$		0	0	1	1
Atmospheric A band	$v_1v_2$	R	P	R	P
	0	761,90	763,70		
	1			768,43	774,00

Table A3.1.  $O_2(b^1\Sigma_g^+)$  atmospheric A-band line identification.

$O_2^+(b^4\Sigma_g^-)$	$v_1v_2$	0	1	2	3	4	5
1 <sup>-</sup> system	0	602,64	641,87	685,63	733,47		
	1	563,19	597,34	635,10			
	2	529,57	559,75	592,56			
	3	500,56	527,47	556,66	588,34		
	4		499,80	525,90	554,07	584,73	
	5			499,20	525,10	552,10	581,40
	6					524,10	
	7						523,40

Table A3.2.  $O_2^+(b^4\Sigma_g^-)$  first negative system line identification.

$N_2^+(B^2\Sigma_u^+)$	$v_1v_2$	0	1	2	3	4	5	6
1 <sup>-</sup> system	0	391,44	427,81	470,92	522,83			
	1	358,21	388,43	423,65	465,18	514,88		
	2	330,80	356,39	385,79	419,91	459,97	507,66	
	3		329,87	354,89	383,54	416,68	455,41	501,27
	4			329,34	353,83	381,81	413,50	451,59

Table A3.3.  $N_2^+(B^2\Sigma_u^+)$  first negative system line identification.

$N_2(C^3\Pi_u)$	$v_1v_2$	0	1	2	3	4	5	6	7	8
2 <sup>+</sup> system	0	337,13	357,69	380,49	405,94	434,36	466,73			
	1	315,93	333,9	353,67	375,54	399,84	426,97	457,43		
	2	297,68	313,60	330,90	350,05	371,05	394,30	420,05	449,02	
	3	281,98	296,20	311,67	328,53	346,90	367,19	389,46	414,18	441,68
	4		281,43	295,32	310,40	326,81	344,60	364,17		

Table A3.4.  $N_2(C^3\Pi_u)$  second positive system line identification.



## Appendix 5. Reaction scheme for hydrogen oxidation involving electronically-excited oxygen molecules.

This MSU kinetic model has been obtained by Ibraguimova et al. [189].  
Units are in mole-cm-sec-cal.

### 1. Reaction mechanism

No.	Reactions	Domain of validity $\Delta T, 10^3 \text{ K}$	A	n	E, K	$\Delta \log k$
1	$\text{H}_2 + \text{O}_2 \rightarrow \text{H} + \text{HO}_2$	1.0-2.5	1.94E+14	0	29770	0.2
	$\text{H} + \text{HO}_2 \rightarrow \text{H}_2 + \text{O}_2$	0.25 – 2.0	2.39E+13	0.1	711	0.2
2	$\text{H}_2 + \text{O}_2 \rightarrow \text{O} + \text{H}_2\text{O}$	1.0 – 2.5	3.0E+13	0	35000	-
3	$\text{H}_2 + \text{O}_2 \rightarrow \text{OH} + \text{OH}$	0.76 – 2.5	4.47E+11	0	17338	0.5
	$\text{OH} + \text{OH} \rightarrow \text{H}_2 + \text{O}_2$	0.25 – 3.0	1.7E+13	0	24100	0.8
4	$\text{H}_2 + \text{M} \rightarrow \text{H} + \text{H} + \text{M}$					
	M=Ar	1.0-8.0	2.23E+14	0	48350	0.2
	M=H <sub>2</sub>	1.0-8.0	3.46E+14	0	48350	0.24
	M=O <sub>2</sub>	1.0-8.0	3.46E+14	0	48350	0.5
	M=H <sub>2</sub> O	0.6-2.0	8.48E+19	-1.1	52530	0.7
	$\text{H} + \text{H} + \text{M} \rightarrow \text{H}_2 + \text{M}$					
	M=Ar	0.5-2.5	6.48E+17	-1	0	0.5
	M=H <sub>2</sub>	0.3-5.0	9.72E+16	-0.6	0	0.5
	M=H <sub>2</sub> O	0.3-2.0	1.0E+19	-1	0	0.7
	M=H	0.3-5.0	3.2E+15	0	0	0.5
5	$\text{O}_2 + \text{M} \rightarrow \text{O} + \text{O} + \text{M}$					
	M=Ar	2.0-4.1	1.5E+18	-1	59380	0.17
	M=O <sub>2</sub>	2.0-5.0	9.8E+24	-2.5	59380	0.3
	M=O	2.0-5.0	3.5E+25	-2.5	59380	0.4
	M=O <sub>3</sub> , H <sub>2</sub> O	2.0-5.0	1.2E+19	-1	59380	1
	$\text{O} + \text{O} + \text{M} \rightarrow \text{O}_2 + \text{M}$					
	M=Ar	0.3-4.0	1.89E+13	0	-900	0.11
	M=O <sub>2</sub>	0.3-4.0	1.5E+16	-0.41	0	0.23
	M=O	0.3-4.0	5.34E+16	-0.41	0	0.2
	M=O <sub>3</sub>	0.3-4.0	1.3E+14	0	-900	0.8
6	$\text{H}_2 + \text{O}_2 + \text{O}_2 \rightarrow \text{HO}_2 + \text{HO}_2$	0.5 – 3.0	2.0E+17	0	13000	-
7	$\text{H}_2 + \text{OH} \rightarrow \text{H} + \text{H}_2\text{O}$	0.2-4.1	2.53E+8	1.48	1700	0.5
	$\text{H}_2\text{O} + \text{H} \rightarrow \text{H}_2 + \text{OH}$	0.5-2.5	1.87E+14	0	10433	0.3
8	$\text{OH} + \text{OH} \rightarrow \text{H}_2\text{O} + \text{O}$	0.25-4.1	1.5E+9	1.14	50	0.2
	$\text{H}_2\text{O} + \text{O} \rightarrow \text{OH} + \text{OH}$	0.25-3.0	5.75E+13	0	9052	0.2
9	$\text{O}_2 + \text{H} \rightarrow \text{OH} + \text{O}$	0.3-5.3	8.65E+14	-0.24	8200	0.1
	$\text{OH} + \text{O} \rightarrow \text{H} + \text{O}_2$	0.16-2.5	8.91E+12	0	-251	0.3
10	$\text{H}_2 + \text{O} \rightarrow \text{OH} + \text{H}$	0.3-4.1	5.1E+4	2.67	3160	0.5
	$\text{OH} + \text{H} \rightarrow \text{O} + \text{H}_2$	0.3-2.5	4.88E+3	2.8	1950	0.3
11	$\text{O}_2 + \text{O} + \text{M} \rightarrow \text{O}_3 + \text{M}$					
	M=Ar	0.2-2.5	4.3E+12	0	-1050	0.6
	M=O <sub>2</sub>	0.2-3.0	3.26E+19	-2.06	0	0.6
	M=O	0.22-3.0	2.28E+15	-0.5	-700	0.3
	M=O <sub>3</sub>	0.22-3.0	1.67E+15	-0.51	-700	0.36

	$O_3+M \rightarrow O_2+O+M$					
	M=Ar	0.2-3.0	2.48E+14	0	11430	0.1
	M=O <sub>2</sub>	0.3-3.0	1.54E+14	0	11600	-
	M=O	0.2-3.0	2.48E+15	0	11430	
	M=O <sub>3</sub>	0.3-3.0	4.4E+14	0	11600	0.2
12	$O_2+H+M \rightarrow HO_2+M$					
	M=Ar	0.3-4.1	6.1E+17	-0.8	0	0.5
	M=O <sub>2</sub>	0.5-3.0	2.7E+18	-1	0	0.7
	M=H <sub>2</sub>	0.3-2.0	2.09E+18	-0.8	0	0.5
	M=H <sub>2</sub> O	0.3-2.0	1.56E+18	-0.8	0	0.5
	$HO_2+M=O_2+H+M$					
	M=Ar	20.5-3.0	2.1E+15	0	23000	0.2
	M=O <sub>2</sub>	0.5-3.0	2.8E+15	0	23000	0.3
13	$H_2O_2+M \rightarrow OH+OH+M$					
	M=Ar	0.95-1.5	6.0E+16	0	22900	0.3
	M=H <sub>2</sub>	0.50-2.5	3.2E+17	0	23820	-
	M=H <sub>2</sub> O <sub>2</sub>	0.5-0.95	2.51E+18	0	24154	-
	$OH+OH+M=H_2O_2+M$					
	M=Ar	0.3-3.0	6.33E+23	-2.53	42	
	M=H <sub>2</sub> O	0.3-0.4	1.44E+18	0	0	0.4
14	$H+OH+M \rightarrow H_2O+M$					
	M=Ar	0.3-3.0	8.3E+21	-2	0	0.3
	M=H <sub>2</sub>	0.5-3.0	2.0E+20	-1	0	-
	M=OH	1.74-1.86	8.34E+15	0	0	-
	M=H <sub>2</sub> O	0.3-3.0	1.4E+23	-2	0	0.5
	$H_2O+M=H+OH+M$					
	M=Ar	0.3-2.5	4.0E+23	-2.2	59000	0.6
	M=O <sub>2</sub>	2.0-6.0	3.5E+15	0	52920	0.5
	M+H <sub>2</sub> O	2.0-5.0	1.6E+17	0	57491	0.3
15	$H+O+M \rightarrow OH+M$	0.3-2.5	4.71E+18	-1	0	0.7
	$OH+M=O+H+M$					
	M=Ar,O <sub>2</sub>	0.3-2.5	2.41E+15	0	50000	0.7
16	$OH+O+M \rightarrow HO_2+M$					
	M=Ar	0.3-2.5	8.0E+16	0	0	2.0
17	$OH+H_2O \rightarrow H_2+HO_2$	0.25-3.0	7.9E+9	0.43	36100	1.4
18	$O_2+OH \rightarrow O+HO_2$	0.3-2.5	2.23E+13	0	26500	0.5
	$HO_2+O \rightarrow OH+O_2$	0.22-2.5	1.75E+13	0	-200	0.3
19	$HO_2+H \rightarrow OH+OH$	0.3-4.1	1.69E+14	0	440	0.4
	$OH+OH \rightarrow H+HO_2$	0.25-2.5	1.2E+13	0	20200	1.0
20	$OH+HO_2 \rightarrow H_2O+O_2$	0.25-4.1	2.85E+13	0	-250	0.13
	$H_2O+O_2 \rightarrow OH+HO_2$	0.5-3.0	5.6E+13	0.17	36600	1.5
21	$OH+O_3 \rightarrow O_2+HO_2$	0.22-2.5	9.6E+11	0	1000	0.6
22	$O_2+O_2 \rightarrow O_3+O$	0.25-3.0	1.2E+13	0	50500	0.6
	$O_3+O \rightarrow O_2+O_2$	0.2-1.0	4.82E+12	0	2060	0.3
23	$O_2+OH \rightarrow H+O_3$	0.25-3.0	4.4E+7	1.44	38600	2.0
	$O_3+H \rightarrow OH+O_2$	0.2-2.0	6.87E+13	0	437	0.7
24	$HO_2+O_3 \rightarrow OH+O_2+O_2$	0.2-1.0	1.66E+11	-0.284	1000	0.45
25	$H_2+HO_2 \rightarrow H_2O_2+H$	0.3-2.5	3.01E+13	0	13100	0.5
	$H+H_2O_2 \rightarrow HO_2+H_2$	0.3-1.0	1.69E+12	0	1890	0.3
26	$H_2+H_2O_2 \rightarrow H_2O+OH+H$	0.5-3.0	8.69E+12	0.5	18347	-
27	$H_2O_2+O_2 \rightarrow HO_2+HO_2$	0.3-2.5	5.42E+13	0	20000	0.7
	$HO_2+HO_2 \rightarrow H_2O_2+O_2$	0.3-2.5	1.8E+12	0	0	0.5
28	$H+H_2O_2 \rightarrow H_2O+OH$	0.3-1.0	1.02E+13	0	1800	0.3

	$\text{OH} + \text{H}_2\text{O} \rightarrow \text{H} + \text{H}_2\text{O}_2$	0.4-1.0	2.4E+14	0	40500	1.0
29	$\text{H}_2\text{O} + \text{HO}_2 \rightarrow \text{OH} + \text{H}_2\text{O}_2$	0.3-2.5	2.8E+13	0	16500	0.3
	$\text{OH} + \text{H}_2\text{O}_2 \rightarrow \text{H}_2\text{O} + \text{HO}_2$	0.3-1.45	4.46E+12	0	477	0.5
30	$\text{H}_2\text{O} + \text{O}_2 \rightarrow \text{O} + \text{H}_2\text{O}_2$	0.5-2.5	3.4E+10	0.52	44800	1.4
	$\text{O} + \text{H}_2\text{O}_2 \rightarrow \text{H}_2\text{O} + \text{O}_2$	0.3-2.5	8.4E+11	0	2130	1
31	$\text{H}_2\text{O}_2 + \text{O} \rightarrow \text{OH} + \text{HO}_2$	0.28-1.0	1.08E+12	0	2000	0.35

*Table A5.1. Rate constants of reactions in an H/O system with particles in ground state. Dimensions are in  $(\text{cm}^3/\text{mol})^{m-1}/\text{s}$ ,  $m$  is the order of reaction.*

No.	Reactions	$\Delta T, 10^3 \text{ K}$	A	n	E, K	$\Delta \log k$
32	$\text{OH}^* + \text{H}_2 \rightarrow \text{H}_2\text{O} + \text{H}$	1.0-2.5	1.0E+14	0	276	-
33	$\text{OH}^* + \text{M} \rightarrow \text{OH} + \text{M}$					
	M=Ar	1.0-2.5	2.9E+9	0.5	0	-
	M=O <sub>2</sub> ,H <sub>2</sub>	1.0-2.5	2.9E+11	0.5	0	-
	M=H <sub>2</sub> O	1.0-2.5	2.9E+13	0.5	0	-
34	$\text{OH}^* \rightarrow \text{OH} + \text{h}\nu$		1.4E+6	0	0	-
35	$\text{H}_2 + \text{HO}_2 \rightarrow \text{H}_2\text{O} + \text{OH}^*$	1.0-2.2	4.8E+19	-1.7	19000	-
36	$\text{O} + \text{H} + \text{M} \rightarrow \text{OH}^* + \text{M}$					
	M=Ar	1.0-2.5	3.0E+18	-1	0	-
	M=O <sub>2</sub> ,H <sub>2</sub>	1.0-2.5	3.0E+18	-1	0	-
	M=OH	1.0-2.5	1.5E+19	-1	0	-
37	$\text{O}^* + \text{H} + \text{M} \rightarrow \text{OH}^* + \text{M}$					
	M=Ar	1.0-2.5	1.5E+18	-1	0	-
	M=H <sub>2</sub> ,O <sub>2</sub>	1.0-2.5	4,77E+18	-1	0	-
38	$\text{OH}^* + \text{O}_2 \rightarrow \text{O}_3 + \text{H}$	1.0-2.5	2.3E+12	0.5	0	-
39	$\text{OH}^* + \text{O}_2 \rightarrow \text{HO}_2 + \text{O}$	0.5-3.0	1.2E+12	0.5	0	-
40	$\text{OH}^* + \text{H}_2\text{O} \rightarrow \text{H}_2\text{O}_2 + \text{H}$	0.5-3.0	7.5E+12	0	276	-
41	$\text{O}_2^* + \text{M} \rightarrow \text{O} + \text{O} + \text{M}$	1.0-3.0	2.6E+18	0	48188	-
42	$\text{O}_3 + \text{M} \rightarrow \text{O}_2^* + \text{O} + \text{M}$	0.3-3.0	1.3E+14	0	11400	-
	$\text{O}_2^* + \text{O} + \text{M} \rightarrow \text{O}_3 + \text{M}$	0.3-3.0	6.9E+12	0	-1050	-
43	$\text{HO}_2 + \text{M} \rightarrow \text{O}_2^* + \text{H} + \text{M}$	0.2-2.2	6.9E+14	0	23000	-
	$\text{O}_2^* + \text{H} + \text{M} \rightarrow \text{HO}_2 + \text{M}$	0.2-2.2	1.5E+15	0	-500	-
44	$\text{O}_2^* + \text{M} \rightarrow \text{O}_2 + \text{M}$					
	M=Ar	0.3	5.0E+3	0	0	-
	M=H <sub>2</sub>	0.3	2.7E+6	0	0	-
	M=O <sub>2</sub>	0.5-2.0	1.0E+6	0	0	-
	M=O,H	0.5-2.0	4.2E+8	0	0	-
	M=OH,H <sub>2</sub> O,HO <sub>2</sub> ,H <sub>2</sub> O <sub>2</sub>	0.5-2.0	3.4E+6	0	0	-
45	$\text{H} + \text{HO}_2 \rightarrow \text{O}_2^* + \text{H}_2$	0.3-2.5	4.8E+7	1.67	3162	-
46	$\text{O}^* + \text{O}_2 \rightarrow \text{O} + \text{O}_2$	0.3	6.03E+12	0	0	0.4
47	$\text{O}_2^* + \text{O}_3 \rightarrow \text{O}_2 + \text{O}_2 + \text{O}$	0.28-2.0	3.13E+13	0	2840	-
48	$\text{O}_2^* + \text{H}_2 \rightarrow \text{H}_2\text{O} + \text{O}^*$	0.5-2.5	3.5E+13	0	20000	-
49	$\text{O}_2^* + \text{O}_2 \rightarrow \text{O}_3 + \text{O}$	0.3-2.5	1.2E+13	0	39604	-
50	$\text{O}_2^* + \text{H} \rightarrow \text{OH} + \text{O}$	0.25-2.5	1.1E+14	0	3188	-
	$\text{OH} + \text{O} \rightarrow \text{O}_2^* + \text{H}$	0.3-2.5	5.8E+12	0	6224	-
51	$\text{O}_2^* + \text{H}_2 \rightarrow \text{OH} + \text{OH}$	0.25-2.5	1.7E+15	0	17000	-
52	$\text{O}_2^* + \text{OH} \rightarrow \text{H} + \text{O}_3$	0.25-2.5	4.4E+7	1.44	27225	-
53	$\text{O}_2^* + \text{OH} \rightarrow \text{O} + \text{HO}_2$	0.25-2.5	1.3E+13	0	17000	-
54	$\text{O}_3 + \text{OH} \rightarrow \text{HO}_2 + \text{O}_2^*$	0.25-2.5	4.8E+11	0	1000	-
55	$\text{O}_3 + \text{HO}_2 \rightarrow \text{OH} + \text{O}_2 + \text{O}_2^*$	0.25-2.5	1.0E+10	0	1000	-
56	$\text{HO}_2 + \text{HO}_2 \rightarrow \text{H}_2\text{O}_2 + \text{O}_2^*$	0.25-2.5	9.0E+12	0	500	-
57	$\text{O}_2 + \text{O}^* \rightarrow \text{O}_2^* + \text{O}$	0.3	1.2E+13	0	0	-
58	$\text{O}^* + \text{H}_2 \rightarrow \text{OH} + \text{H}$	0.1-2.1	8.7E+13	0	-14	-
59	$\text{HO}_2 + \text{H} \rightarrow \text{H}_2\text{O} + \text{O}^*$	1.0-2.5	1.7E+12	0.46	678	-
60	$\text{O}^* + \text{M} \rightarrow \text{O} + \text{M}$					
	M=Ar	0.11-0.33	3.0E+11	0	0	-
	M=O <sub>2</sub>	0.2-0.35	1.93E+13	0	67	-
	M=O	0.298	3.0E+12	0	0	0.3
61	$\text{O}^* + \text{H}_2\text{O} \rightarrow \text{OH} + \text{OH}$	0.2-0.35	1.3E+14	0	0	-
62	$\text{O}^* + \text{O}_3 \rightarrow \text{O} + \text{O} + \text{O}_2$	0.2-1.0	7.9E+13	0	0	-

Table A5.2. Rate constants of supplementary reactions in an H/O system with particles in electronically excited state. Dimensions are in  $(\text{cm}^3/\text{mol})^{m-1}/\text{s}$ ,  $m$  is the order of reaction.

## 2. Thermochemistry data for excited species

The CHEMKIN 4 software is designed by default to work with thermodynamic data in the form used by NASA. In this case, seven coefficients are needed for each of two temperature ranges. Thermodynamic data coefficients for excited species  $\text{O}^*$ ,  $\text{O}_2^*$  and  $\text{OH}^*$  are presented below, as obtained from the software GAUSSIAN<sup>®</sup> [190] :

```

O*          O 1          G 300.000 4000.000 1000.000

0.25473243E+01 -0.30650157E-04 -0.36488581E-08 0.50632783E-11 -0.50388354E-15
0.52603966E+05 0.49057715E+01 0.29447184E+01 -0.16245506E-02 0.23936879E-05
-0.15974853E-08 0.40121429E-12 0.52524704E+05 0.29896558E+01

O2*        O 2          G 300.000 4000.000 1000.000

0.33675704E+01 0.12173838E-02 -0.51541280E-06 0.95880813E-10 -0.64228138E-14
0.12559464E+05 0.39428670E+01 0.38815479E+01 -0.35698672E-02 0.10762475E-04
-0.10154052E-07 0.32388956E-11 0.12593236E+05 0.21460579E+01

OH*        O 1H 1       G 300.000 4000.000 1000.000

0.29509641E+01 0.90260926E-03 -0.16713934E-06 0.85924661E-11 0.44182766E-15
0.50648280E+05 0.52307803E+01 0.35142308E+01 0.11573344E-02 -0.43109152E-05
0.52789017E-08 -0.19440835E-11 0.50410237E+05 0.18863960E+01

```

## Appendix 6. Pulse power supply parameters

### Abstract

---

Nonequilibrium plasmas driven by nanosecond high voltage pulses have been proven to produce high-energy electrons, which in turn lead to enhanced ionization and excitation [211]. Literature results showed that a relatively large volume diffuse DBD can be generated at atmospheric pressure with repetitive narrow voltage pulses.

Amongst their attractive features is the ability to achieve enhanced gas phase chemistry without the need for elevated gas temperatures. To further enhance the plasma chemistry, pulsed operation with pulse widths in the nanosecond range has been suggested.

Without any adjustment in the matching network, the electrical power of the power source cannot be transferred to the discharge in an efficient way. Matching networks used in real processing systems are not ideal and can absorb a considerable fraction (up to 90% [226]) of the total incident power. Therefore, the power supply used to ignite the discharge is presented in this section. It is studied to get a much improved power transfer to the plasma.

---

### 1. Discharge study, optimisation and adaptation

Recent plasma technologies imply to use high frequency generators of very short pulses. This is necessary for such processes as singlet molecular oxygen production [13, 36], magnetohydrodynamics systems, hypersonic flow combustion [26, 227]. High frequencies (i.e. tens of kilohertz) are also necessary to treat fast (Mach numbers  $> 3$ ) gas flow without breakthrough.

Present high voltage pulse generator (HVPG) is a laboratory device designed by Chemical Physics Technology, Inc (Minsk). It is designed for various applications, in general to excite gaseous plasma for different conditions. It is a high frequency solid-state generator of nanosecond high voltage pulses formed by magnetic compression. Using of HVPG needs connecting to mains (AC 180-260V, 3kW max) and to cooling (city water,  $\sim 4$  l/min). High voltage pulse generator consists of two basic parts: Main Unit and High Voltage Unit. They are shown in Fig.A6.1.



*Fig.A6.1. High voltage pulse generator.*

The following tables show the characteristics of high frequency generator of nanosecond high voltage pulses and that of high voltage DC power supply used in experimental work. The DC sustainer voltage is provided by a Glassman high current, low voltage (3.4 A, 3 kV, 10 kW max) DC power supply, operated in voltage stabilization mode.

Output pulse amplitude <sup>1</sup>	≥ 25 kV	
Pulse width, FWHM	~ 15 ns	
Pulse polarity	positive or negative	
Pulse repetition rate, adjustable	1 – 100000 Hz	
Pulse energy	up to 10 mJ	
Output power	up to 1 MW	
Operation modes	1. Single pulse 2. Burst of pulses 3. Continuous (up to 50 kHz)	
Mains	180 – 260 VAC, 50-60 Hz, 3 kW max, 1 Phase	
Power factor	≥ 0.98	
Dimensions and weights	Main unit	470x516x162 mm <sup>3</sup> ; 23 kg
	HV unit	160x390x120 mm <sup>3</sup> ; 11 kg

<b>High voltage DC power supply Glassman LQ3P3.4 series</b>	
Output voltage	0 – 3 kV
Output current	0 – 3.4 A
Polarity	positive

<sup>1</sup> Strongly depends on load

Table A6.1. HV-PPS: High voltage pulse power supply and DC-HVPS: Direct current high voltage power supply characteristics.

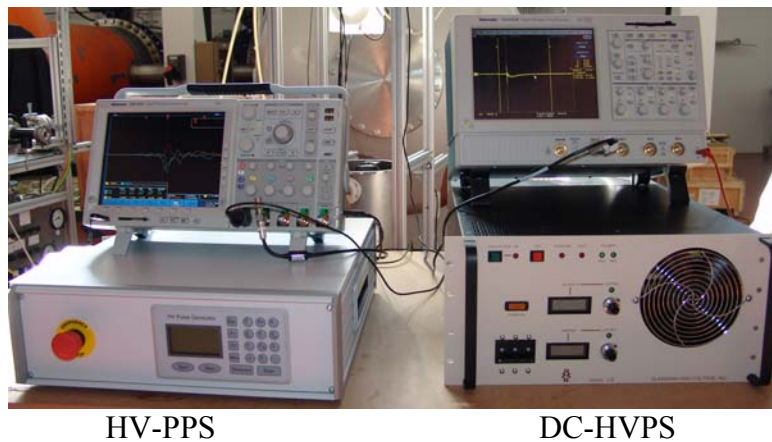


Fig.A6.2. HV-PPS : High voltage pulse power supply ; DC-HVPS : Direct current high voltage power supply.

The pulser has a low-voltage TTL pulse output synchronized with the main high voltage pulses, which can be used to trigger the DC power supply.

### 1.1. Main Unit of HVPG

Mains feed the Power Factor Corrector (PFC) unit and auxiliary power supplies. PFC Unit provides stabilized voltage 500 V to feed High Voltage Modulator Unit at load up to 2.5 kW. An efficiency about 0.95 and power factor about 0.98 are ensured. Microprocessor-based controller monitors basic parameters of the PFC Unit (output voltage and current, temperature in critical points) and controls it. High Voltage Modulator Unit converts DC voltage into pulses with length about 1 μs

and peak current up to 100 A. High-power Insulated Gate Bipolar Transistors (IGBT) are used as power switches.

## 1.2. High Voltage Unit

The high voltage unit is a separate device placed near the load. Power pulses are delivered to high-voltage transformer and resonantly charge capacitor of secondary winding circuit. Then magnetic compression line shortens pulses. The transformer and saturable chokes of the magnetic compression line are returned to initial magnetic state during the pause between pulses using magnetic bias circuit. The transformer and chokes of the first section of the magnetic compression line are wound on cobalt-based amorphous alloy tape toroidal cores. Chokes of next sections are wound on 10 and 5  $\mu\text{m}$  thick permalloy tape cores. To reach desired electric strength and ensure heat elimination, HV Unit is constructed as stainless steel hermetic bath filled with low boiling ‘electronic liquid’ FC-3284 for  $\frac{3}{4}$  of volume. Other  $\frac{1}{4}$  is filled with “electronic gas” PFG-3218 at slight overpressure. It is done to avoid ingress of air into the unit and to increase breakdown voltage of a gas phase during an evaporating cooling. The hydraulic system consists of magnetic drive gear pump, filter, flow sensor and pressure sensor. These elements serve to make liquid flow through magnetic cores cases, because the transformer and saturable chokes need extremely force cooling. To condensate vapors of electronic liquid, heat exchanger connected to water-cooling system is used. HV Unit has filling valve and safety valve. Under emergency conditions, if the pressure in the unit exceeds  $\sim 8$  bar, safety valve membrane breaks to prevent HV unit destruction.

Acquisition node is placed near flange of HV unit and connected to main unit via fiber optic CAN bus. This node serves to collect data from different sensors mounted into bath and hydraulics.

## 1.3. Matching discharge to power source [214, 228]

Loads for this sort of power supplies, i.e. discharge reactors, are not active and linear as a rule, thus energy transfer from generator is an additional problem. Specific load adaptation is required in each case taken separately.

The capacitors  $C_1$  and  $C_2$  are charged in resonant mode up to voltage  $\sim 32$  kV through high voltage transformer. Short output pulses production is possible as a result of using magnetic compression circuits. Three compression stages provide rise time shortening of pulse by a factor of  $\sim 100$ .

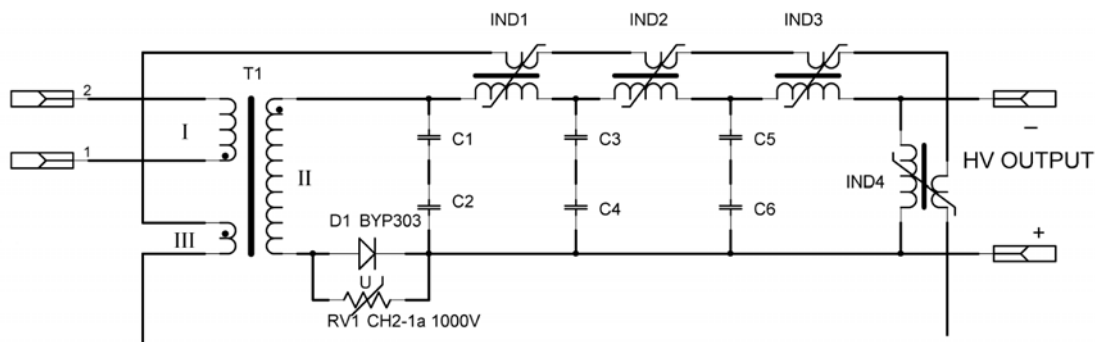
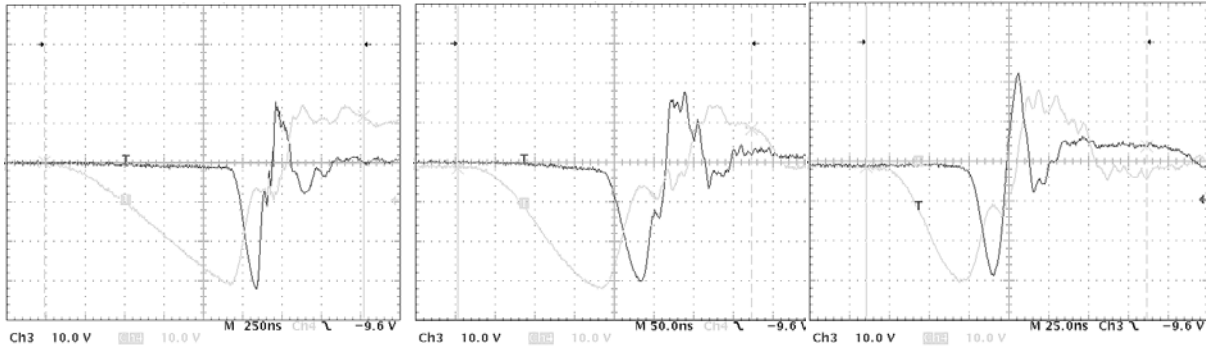


*Fig.A6.3. Compression electrical circuit.*



Ch3,Ch4 – 10kV/div;  
Ch4 – C1,C2 voltage; Ch3 –  
C3,C4 voltage

Fig.A6.4. Stage 1.

Ch3,Ch4 – 10kV/div;  
Ch4 – C3,C4 voltage; Ch3 –  
C5,C6 voltage

Fig.A6.5. Stage 2.

Ch3,Ch4 – 10kV/div; Ch4  
– C5,C6 voltage; Ch3 – output  
voltage

Fig.A6.6. Stage 3.

Figs.A6.4-A6.6 [229] show voltage shape at each stage of compression. High voltage transformer and chokes Ind1 and Ind2 are made on toroidal cores of cobalt-based amorphous alloy to reach acceptable level of eddy current losses. Cores of chokes Ind3 and Ind4 are produced of Permalloy. For this sort of power supplies, discharge reactors are not active and linear (in radioelectronic sense). Thus energy transfer from generator to load is an additional problem. In Figs.A6.7 we can see oscillogramms, which illustrate energy dissipation on resistive adapted load and real (barrier discharge reactor) load.

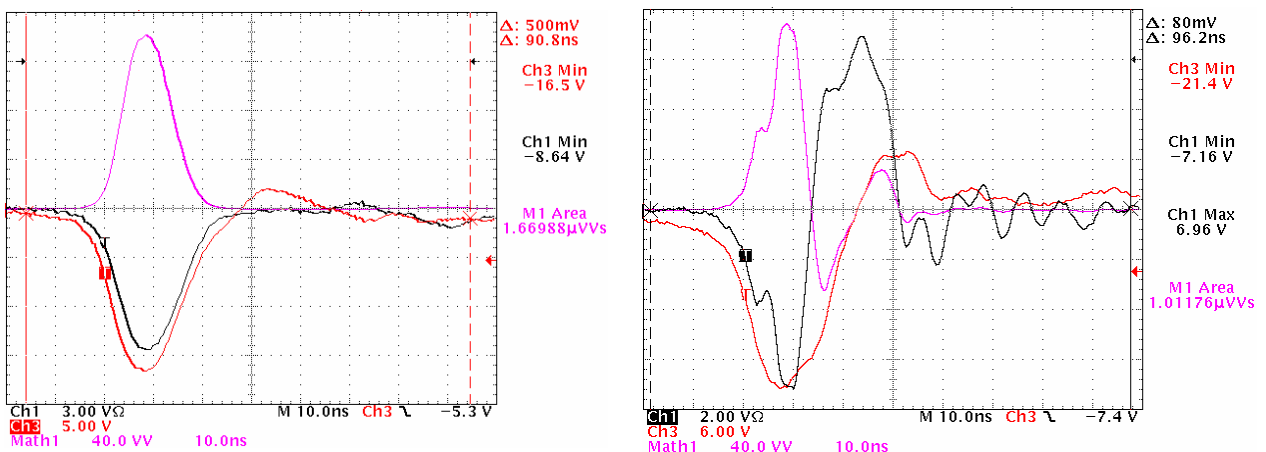


Fig.A6.7. (Left) : Active load typical single-pulse oscillograms : voltage, current and calculated power (Right) : Distorted crossed discharges load output waveforms.  $F=25$  kHz. Both : 5%  $O_2$  in helium, atmospheric pressure.

Output voltage and current depend significantly on load. Active load is pure resistive matched load, for our generator it is  $\sim 200$  Ohms. "No load" means generator has only external capacitor as load, and in this almost all energy is reflected back to generator. In case of real load, as crossed barrier discharge reactor, a part of energy is dissipated into load and remaining part is reflected back. The figure A6.7 presents two examples and show precisely how output waveforms of the high voltage pulse generator will be distorted. On all oscillograms, red curve is voltage (divider 1:1000), black one is current (1 V = 10 A), magenta one is calculated power = voltage\*current.

Typical forward and reflected pulse energies produced by the pulse generator are 6-8 mJ/pulse. Basically, at the present conditions nearly 40% of power generated by the pulser is reflected back to the load and generator recuperation system allows returning this part of energy to PFC output capacitor. This power passes through power corrector, chokes, ballast resistor, then through the last capacity of power factor corrector (PFC). This energy is kept till the next pulse (kind of recuperation).

In this reflected energy, half is dissipated in the ballast and half is effectively recovered in capacity of PFC for next high voltage pulse.

Therefore, optimized load impedance matching is an important point (Figs.A6.8). The aim is to extract a maximum power from the power supply. The following scheme shows results of a schematic simulation using Micro-Cap<sup>®</sup> of energy transfer processes at different loads.

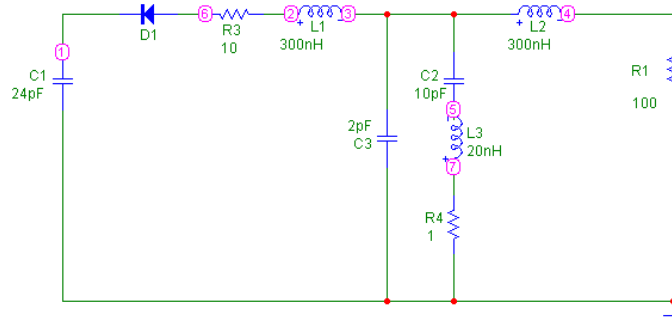


Fig.A6.8. Schematic simulation using Micro-Cap<sup>®</sup>.

This schematic is a simplified model of pulse generator output stage with connected “active” (resistive) load. The circuit is elementary but it shows general behaviour of generator-load system fine enough. The parts C3, L2 and R1 model load. The resistance R1 represents the active load resistance. Also the output stage of generator is modelled; particularly C1 which is the last capacitor of third magnetic compression stage, L1 is the inductance of saturated magnetic choke. The diode D1 represents the 'virtual' part to imitate valve properties of magnetic choke. Other components are set as 'parasitic' elements.

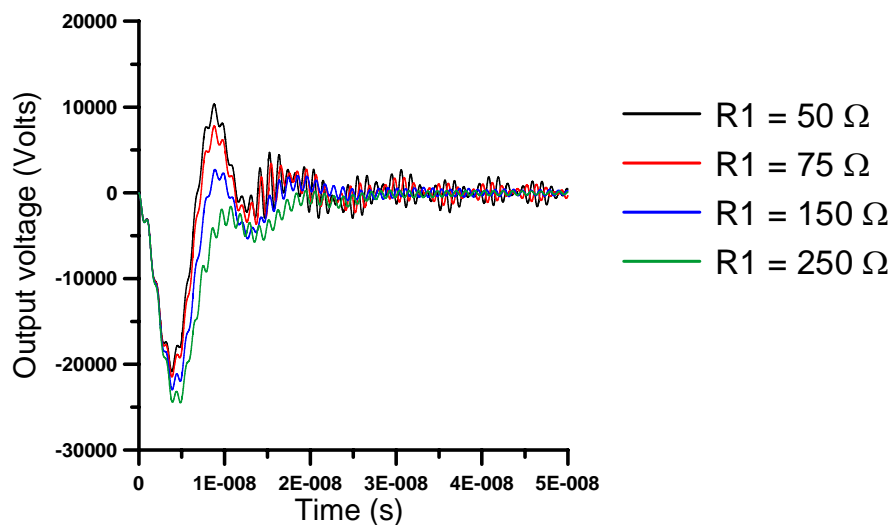


Fig.A6.9. Simulated output voltage for different active load resistance.

The active load resistance R1 is varying and the output pulse is modelled.

For this model we consider only output stage of magnetic compression line - parts C5,C6 on Fig.A6.8 (C1 on model), IND3 in the saturated state (L1 on the model) and suppose we have active load (R1) connected to HV output. Other elements on model are parasitic values such as series inductances of load and wires, additional capacitance between output leads etc...The values of these components are partially measured and others are estimated analytically.

In the initial state C1 is charged up to ~30 kV and then it discharges to the load. Only this process is modelled.

## 1.4. Calibration

For an active load case, almost all energy is dissipated in the active load. In our case, four resistances, having a resistivity of 200 ohms, which correspond to the impedance of the generator, are used as active load. This active load is a special volume resistance. They are made of ceramic, with carbon based active mass into. They have low inductance, can carry high current (up to 100 A) and it is possible to apply high voltage (15 kV and more). We made calibration with such active load. Current and voltage are measured by probes, and rise time, fall time and shift are compared. It should be equal.

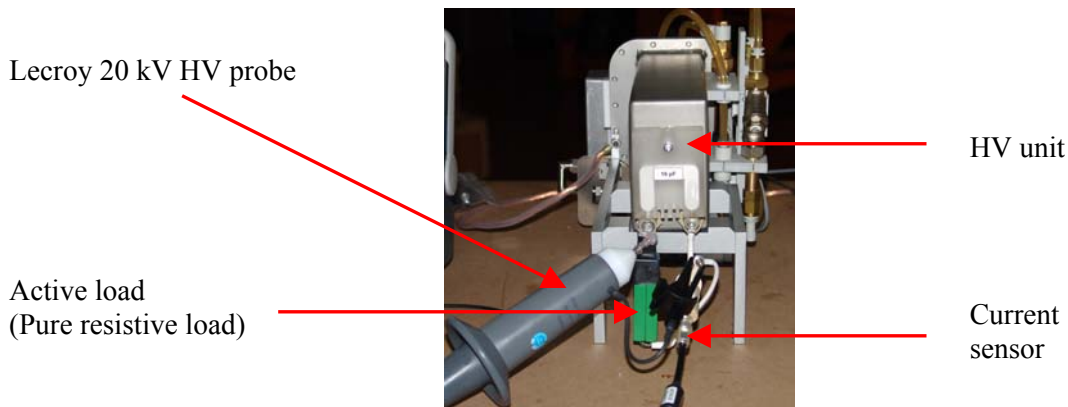


Fig.A6.10. Photos of experimental set-up.

The pulse voltage and current and the DC sustainer current are measured using appropriate materials.

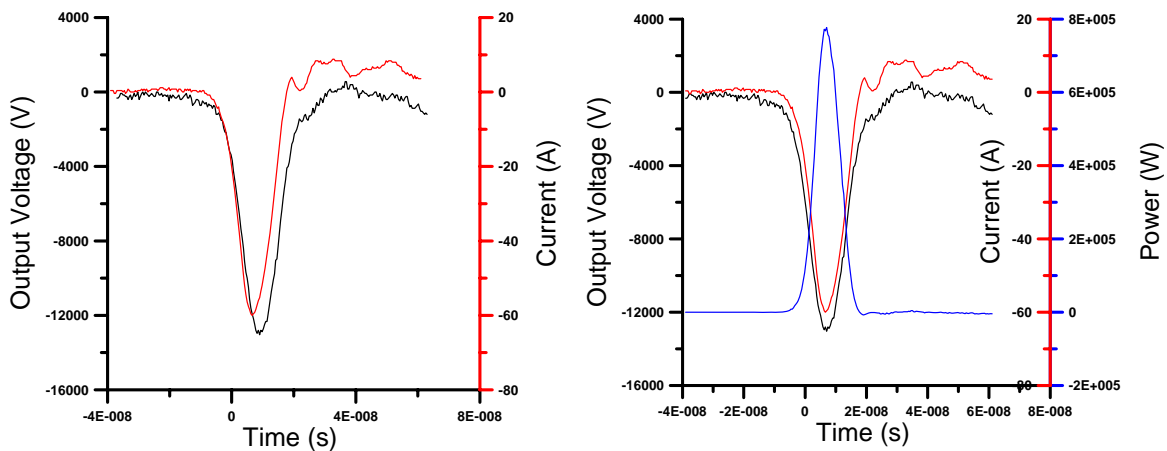


Fig.A6.11. Left) : with phase shift and right) : with deskew.

Channel 1 (oscilloscope)	Voltage probe set-up
Deskew on channel 1 (ns)	2
Pulse energy (mJ)	7.4

Table A6.2. Oscilloscope calibration.

It is worth to note that the pulse energy is calculated as temporal integration of momentary power. High voltage cables used to link current and high voltage probes are low loss cables adapted by length to high voltage probe to reach the same phase shift to the signal.

We observe some phase shift between current and voltage signals. This phase shift comes from cables and probes. A deskew (shift correction) of 2 ns is implemented for voltage signal. This deskew corresponds to shift necessary to reach the maximum pulse energy.

## Appendix 7. Spontaneous emission of CH\*, O\*, C<sub>2</sub>\* and OH\*

### CH\* molecule

The rotationally resolved A<sup>2</sup>Δ - X<sup>2</sup>Π and B<sup>2</sup>Σ<sup>-</sup> - X<sup>2</sup>Π transitions of CH\* emission spectra is presented in Fig.A7.1. they are characterized by a high resolution and an opened spectra structure.

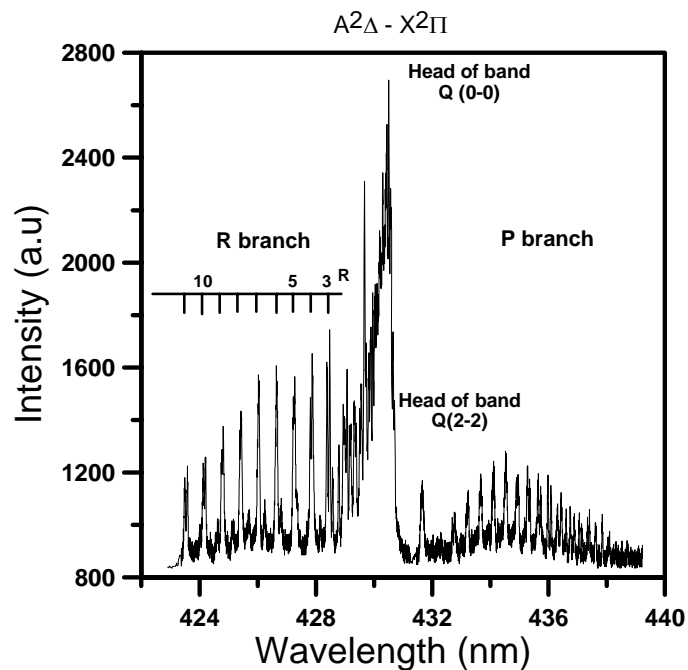


Fig.A7.1. Experimental spontaneous emission spectra of A<sup>2</sup>Δ - X<sup>2</sup>Π transition of CH\* radical in a counter flow diffusion flame (CH<sub>4</sub>+He) / (O<sub>2</sub>+He) ( $\Phi=6,8$  ;  $\varepsilon=180$  s<sup>-1</sup>).

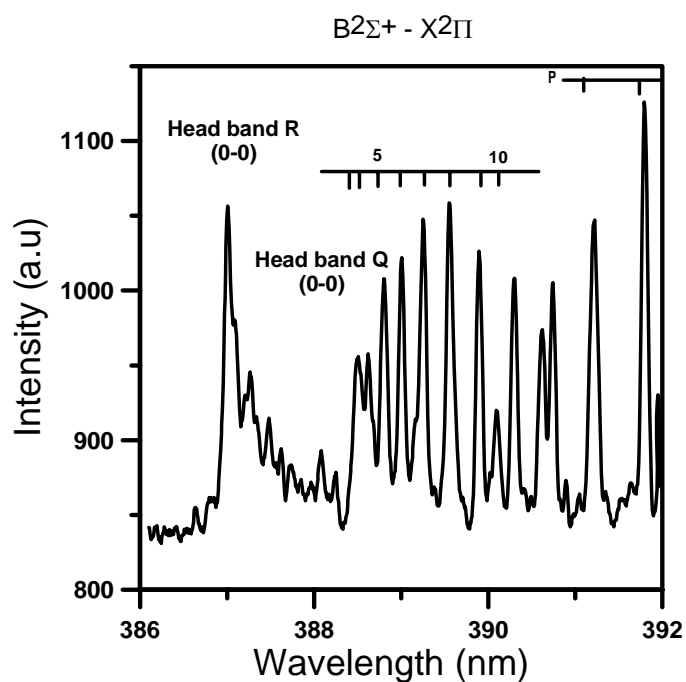
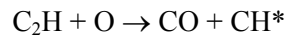
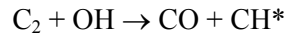


Fig.A7.2. Experimental spontaneous emission spectra of B<sup>2</sup>Σ<sup>-</sup> - X<sup>2</sup>Π transition of CH\* radical in a counter flow diffusion flame (CH<sub>4</sub>+He) / (O<sub>2</sub>+He) ( $\Phi=6,8$  ;  $\varepsilon=180$  s<sup>-1</sup>).

The observation of CH\* ( $A^2\Delta$  or  $B^2\Sigma^-$ ) usually occurs higher in the reaction zone than  $C_2$  suggests that it might be formed from  $C_2$  by the reactions :



Which are very exothermic and sufficient to bring CH up to its excited states  $A^2\Delta$  or  $B^2\Sigma^-$ .

The  $B^2\Sigma^- - X^2\Pi$  system is in the near ultraviolet with strong R and Q band with heads at 387.2 nm and 388.9 nm respectively. It is characterised by a head of the Q lines of the (0-0) band that emerges at 314.4 nm among the OH ultraviolet lines. Another line may be observed at 315.7 nm is the head of the (1-1) band.

### OH\* molecule

The existence of the OH\* molecule in flames is proven through the ultraviolet bands with a widely open structure ; the strongest of which lies at  $\lambda$  306.4 nm. Due to the importance of OH\* in the kinetics of flames, the ultraviolet bands have extensively and thoroughly been studied.

The following figure A7.3 show the emission spectra of the ( $v' = 0 ; v'' = 0$ ) of the electronic transition  $A^2\Sigma^+ - X^2\Pi$  of OH\*.

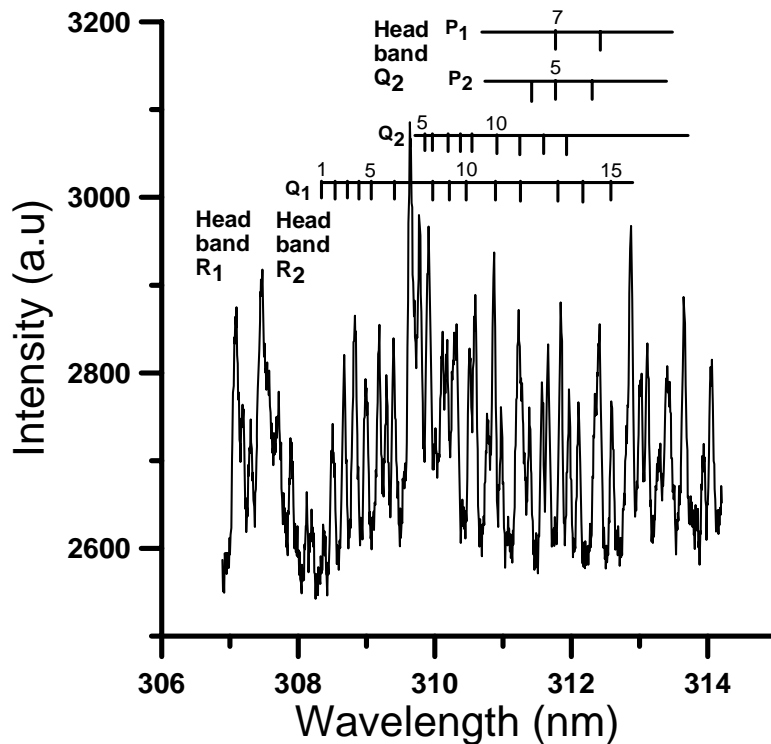


Fig.A7.3. Experimental spontaneous emission spectra of ( $A^2\Sigma \rightarrow X^2\Pi$ , (0,0)) transition of OH\* radical in a counter flow diffusion flame ( $CH_4+He$ ) / ( $O_2+He$ ) ( $\Phi=6,8 ; \varepsilon=180 s^{-1}$ ).

The good spectral resolution permits identification of head bands and of different rotational transitions. It is worth noting that transitions of (0-0) band are also stronger than that of (1-1) band and these bands overlaps from  $\lambda = 312$  nm.

### Comparison plasma ON and plasma OFF

The spontaneous emission of OH\*, O\*, C<sub>2</sub>\* and CH\* radicals has been recorded to show the modification of combustion with the discharge. The generation of additional chemically active radicals by the non thermal plasma discharge demonstrates the interest of CDR on combustion intensification.

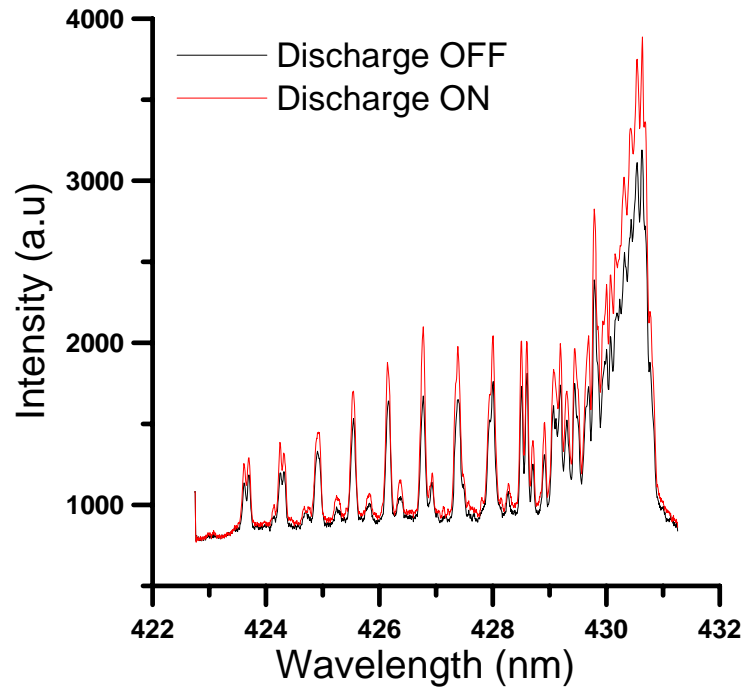


Fig.A7.4. Effect of the discharge on spontaneous emission spectra of  $A^2\Delta - X^2\Pi$  transition of R-branch CH radical in counter flow diffusion flame ( $CH_4$ )/ ( $O_2+He$ ).

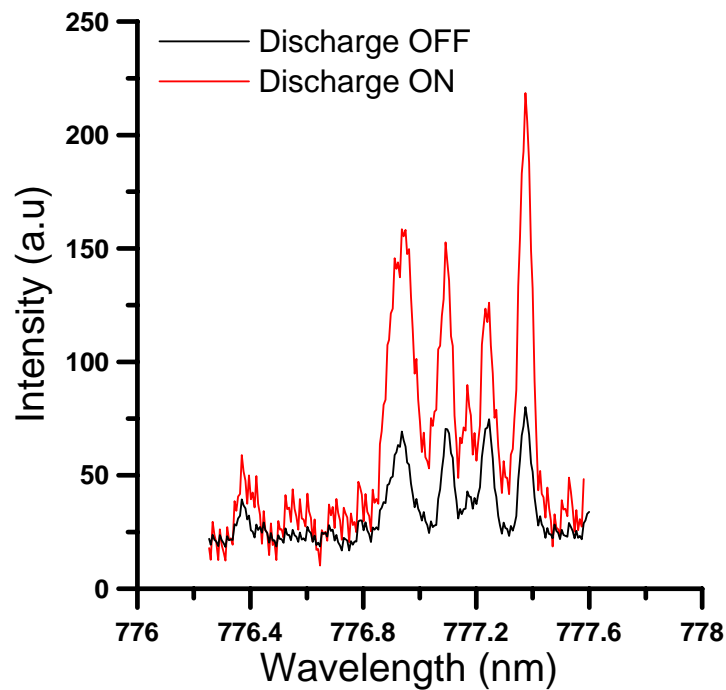
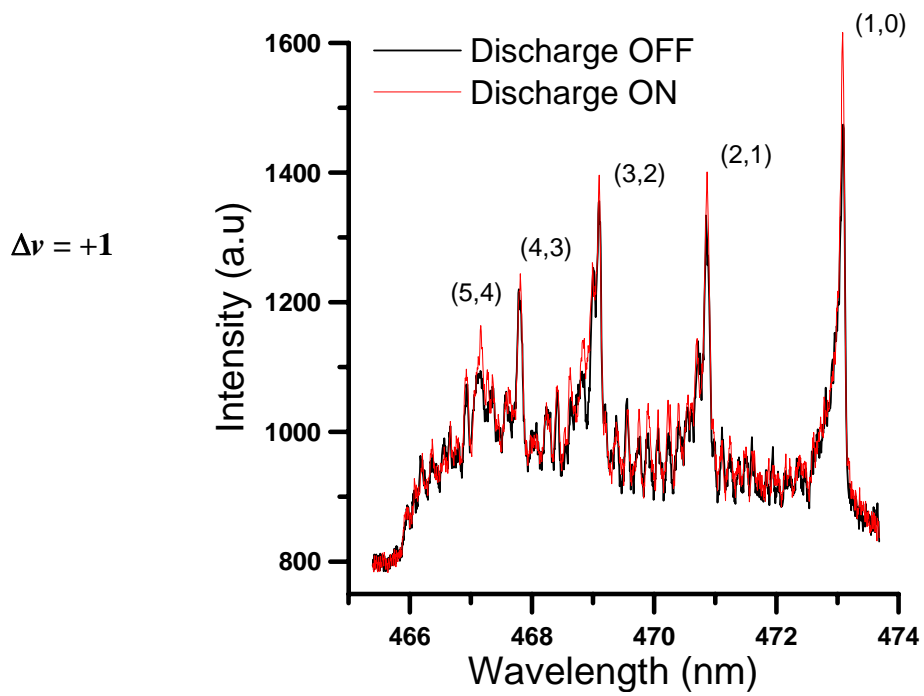
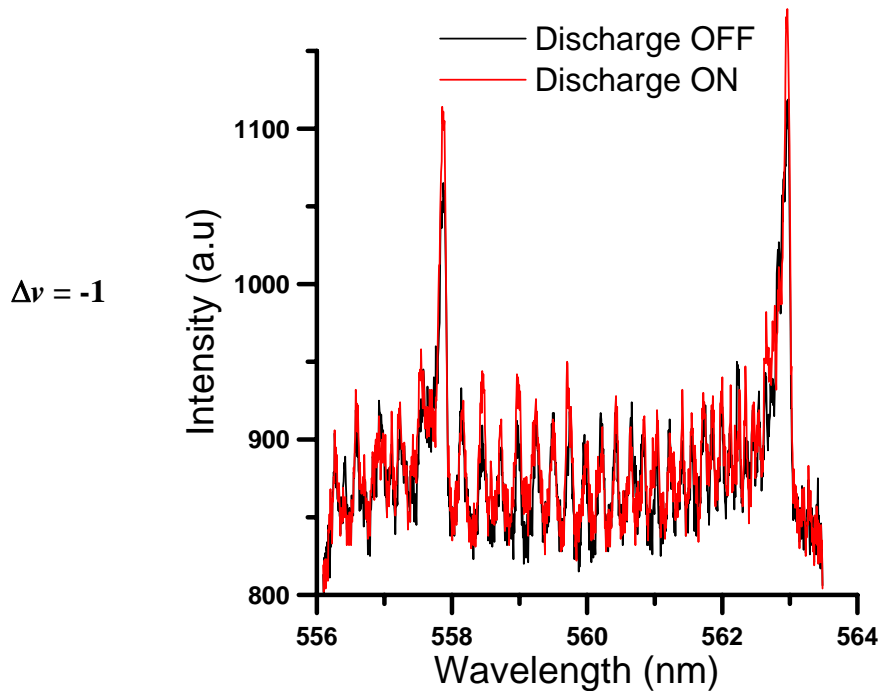


Fig.A7.5. Effect of the discharge on spontaneous emission spectra of O atoms ( $\dot{S}S^5P$  transition) in counter flow diffusion flame ( $CH_4$ ) / ( $O_2+He$ ).

The following figures focus on the C<sub>2</sub> Swan bands.



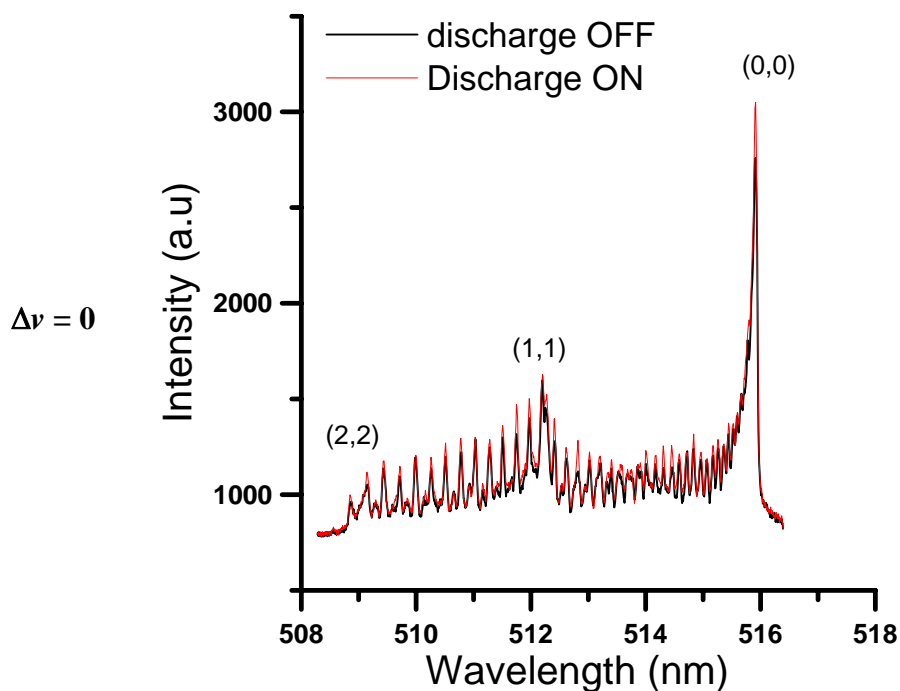


Fig.A7.6. Effect of the discharge on spontaneous emission spectra of  $C_2$  (Swan band  $d^3\Pi_g \rightarrow a^3\Pi_u$ ,  $\Delta v = -1$  (left),  $\Delta v = 0$  (middle) and  $\Delta v = +1$  (right) in counter flow diffusion flame ( $CH_4$ ) / ( $O_2+He$ ).

Finally, the effect of oxidizer activation on OH (A-X) emission is presented in Fig.A7.7.

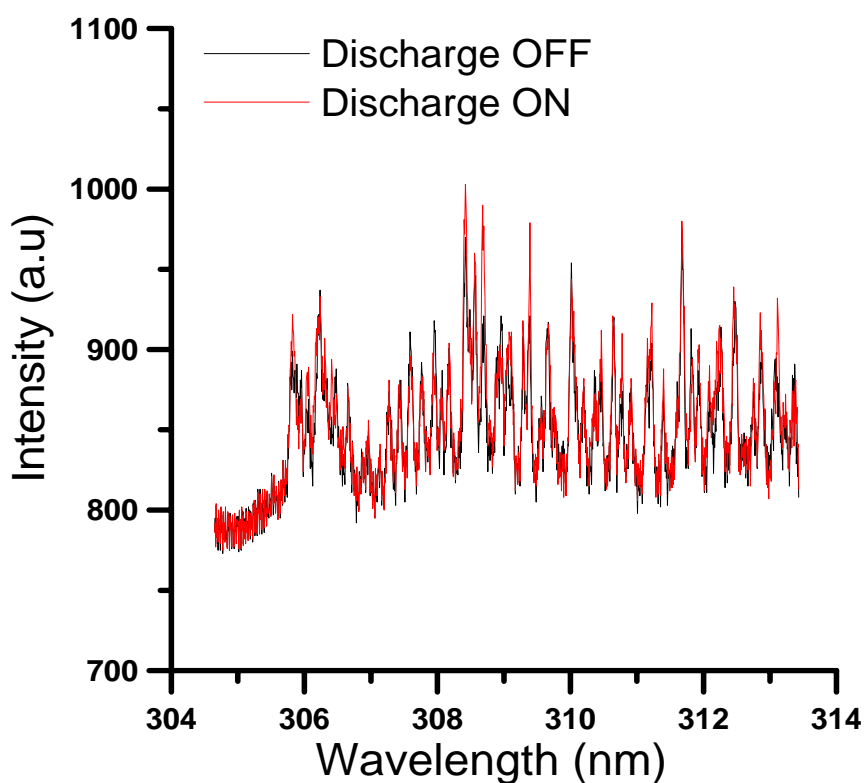


Fig.A7.7. Effect of discharge on spontaneous emission spectra of OH ( $A^2\Sigma \rightarrow X^2\Pi$ , (0,0)) in counter flow diffusion flame ( $CH_4$ ) / ( $O_2+He$ ).

# Curriculum Vitae

## PERSONAL DATA

Date of Birth: 18 April 1982  
Place of Birth: Iknioun, Morocco  
Citizenship: French  
Marital Status: Married



## EDUCATION AND TRAINING

- 2005 - 2008** Doctor-Engineer in Chemical Engineering and Processes (French-German Ph.D)  
• Institute for Combustion, Aerothermics, Reactivity and Environment (ICARE)  
National Center of Scientific Research (CNRS) – Orléans, France  
• Laboratory of Fluid Dynamics and Technical Flows (LSS)  
Magdeburg University – Germany
- 2004 - 2005** Master's Degree in Applied Chemistry, Energy and Environment, with honors  
• University of Orléans, France
- 2001 - 2004** Bachelor's Degree in Chemical Engineering, with honors  
• Institute for Applied Chemistry – Chemical Engineer diploma with honors  
Orléans, France
- 2000** Scientific Baccalaureate in Physics and Chemistry, with honors  
• Jehan de Beauce School, Chartres, France

## WORK EXPERIENCE

### Up to now

EDF Research and Development – France  
Energy efficiency in industrial processes

### 2005-2008

Ph.D Plasma-Assisted Combustion  
Combustion improvement and reduction of pollutant emissions in combustion processes using non-thermal plasma

### Nov. 2004 – Aug. 2005

CNRS: Laboratory of Combustion and Reactive Systems (LCSR)  
PSA Peugeot-Citroën - France  
Master's thesis: Processes of formation and oxidation of soot particles in diesel-like engine conditions.  
Experimental study by shock tube and numerical simulation

### Jul-Aug. 2004

SUEZ-ENVIRONNEMENT  
International Centre for Water and Environment Research (CIRSEE) – France  
Assistant Engineer: Analytical Expertise Department  
Validation of methods for analyzing Volatile Organic Compounds (VOCs) resulting from domestic waste and products masking and neutralizing odors in air by adsorption-thermodesorption-GC-MS.

### Aug. 2003 - Feb. 2004

KIWA WATER RESEARCH Nieuwegein, the Netherlands  
UV/H<sub>2</sub>O<sub>2</sub> Advanced Oxidation Process for water treatment and Catalytic decomposition of H<sub>2</sub>O<sub>2</sub>

**July – Aug. 2001**

PPP - Maintenon, France

Technician

Production of ceramic from alumina (Al<sub>2</sub>O<sub>3</sub>) powder using the double compression technique

Physical measurements of ceramic product

**July – Aug. 2000**

NEW-YORK APPLICATIONS - ORANGE subcontractor, Dourdan, France

Production of advertising hoardings in the framework of name change from «Itineris» to «Orange»

Telecom Company

**2002-2003** (During school holidays)

Post Office, Auneau, France

Postal sorting and distribution.

# Own scientific production

## Journal articles

A. Bourig, D. Thévenin, G. Janiga, K. Zähringer, “Numerical Modeling of H<sub>2</sub>-O<sub>2</sub> Flames Involving Electronically-Excited Species O<sub>2</sub>(a<sup>1</sup>Δ<sub>g</sub>), O(<sup>1</sup>D) and OH(<sup>2</sup>Σ<sup>+</sup>)”, *Proceedings of the Combustion Institute*, Vol.34, in press (2009).

A. Bourig, V. Lago, J.-P. Martin, K. Pliavaka, F. Pliavaka, S. Gorbatov, “Generation of singlet oxygen in HV pulsed + DC crossed discharge at atmospheric pressure for oxygen-enhanced combustion”, *International Journal of Plasma Environmental Science and Technology*, Vol.1, No.1, p.57 (2007).

## Conference communications with article in proceedings

K. Zähringer, A. Bourig, J.-P. Martin, D. Thévenin, “Combustion enhancement through electronically excited oxygen”, Deutscher Flammentag, Bochum, September (2009) (submitted).

K. Pliavaka, A. Bourig, K. Zähringer, D. Thévenin, J.-P. Martin, V. Lago, E. Barbosa, F. Pliavaka, S. Gorbatov, S. Shushkou, E. Prihodzja, “effects of singlet oxygen produced by crossed discharge on methane combustion”, *Nonequilibrium processes in combustion and plasma based technologies*, Belarus, Minsk (2008).

A. Bourig, J.-P. Martin, V. Lago, D. Thévenin, K. Zähringer, F. Pliavaka, S. Gorbatov, “Plasma generation of excited oxygen and combustion enhancement”, *Proceedings of the 18<sup>th</sup> International Symposium on Plasma Chemistry*, Kyoto, Japan (2007).

A. Bourig, J.-P. Martin, V. Lago, D. Thévenin, K. Zähringer, “Modelling of the production of excited oxygen molecules in a crossed discharge (barrier discharge and CW discharge)”, *Proceedings of the 18<sup>th</sup> International Symposium on Plasma Chemistry*, Kyoto, Japan (2007).

A. Bourig, J.-P. Martin, D. Thévenin, V. Lago, K. Zähringer, “Combustion promoted by excited oxygen: Generation of singlet oxygen at atmospheric pressure and application to a counter-flow nonpremixed flame”, *3<sup>rd</sup> European combustion meeting*, Chania, Crète (2007).

A. Bourig, V. Lago, J.-P. Martin, K. Pliavaka, F. Pliavaka, S. Gorbatov, “Generation of singlet oxygen in HV pulsed + DC crossed discharge at atmospheric pressure for oxygen-enhanced combustion”, *5<sup>th</sup> International Symposium on Non Thermal Plasma and Technology*, île d’Oléron (2006).

A. Bourig, J.-P. Martin, V. Lago, D. Thevenin, K. Zähringer, “Hydrogen combustion in presence of excited oxygen produced by non thermal plasma: experimental and numerical study”, *Nonequilibrium processes in combustion and plasma based technologies*, Belarus, Minsk (2006).

K.F. Pliavaka, S.V. Gorbatov, S.V. Shushkou, F.V. Pliavaka, A.P. Chernukho, S.A. Zhdanok, V.V. Naumov, A.M. Starik, A. Bourig, J.-P. Martin, “Singlet oxygen production in electrical non-self-sustained HV pulsed + DC cross-discharge at atmospheric pressure with application to plasma assisted combustion technologies”, *Nonequilibrium processes in combustion and plasma based technologies*, Belarus, Minsk (2006).

## Poster communications

A. Bourig, V. Lago, J.-P. Martin, K. Pliavaka, F. Pliavaka, S. Gorbatov, A. Chernukho, V. Naumov, "Generation of singlet oxygen in crossed discharge and pulsed dielectric barrier discharge at atmospheric pressure for oxygen-enhanced combustion", *31<sup>st</sup> International symposium on Combustion*, Heidelberg, Germany (2006).

A. Bourig, J.-P. Martin, V. Lago, D. Thévenin, K. Zähringer, K.V. Pliavaka, F.V. Pliavaka, S.V. Gorbatov, "Application of a non self sustained nanosecond pulsed discharge to a diffusion flame", *Aerospace Thematic Workshop on Fundamentals of Aerodynamic-Flow and Combustion Control by Plasmas*, Varena, Italy (2007).

K. Pliavaka, A. Bourig, V. Lago, J.-P. Martin, F. Pliavaka, S. Gorbatov, A. Chernukho, "Development of a HV pulsed power supply and of a crossed discharge reactor for excited O<sub>2</sub> generation", *Aerospace Thematic Workshop on Fundamentals of Aerodynamic-Flow and Combustion Control by Plasmas*, Varena, Italy (2007).





**Ali BOURIG**

## **MODIFICATION DE LA COMBUSTION EN PRESENCE D'ESPÈCES EXCITÉES**

Aujourd'hui, il semble que la méthode la plus prometteuse pour intensifier la combustion repose sur l'excitation hors-équilibre du mélange gazeux, qui permet ainsi de modifier la cinétique chimique. Pour obtenir une excitation efficace des degrés de liberté électronique et vibrationnel des molécules, l'utilisation d'une alimentation pulsée associée à une énergie des électrons adéquate est proposée. Ce travail de thèse porte sur l'application de générateur d'impulsion électrique haute fréquence capable de délivrer des pulses de 20 kilovolts pendant 20 nanosecondes ayant des temps de montée de l'ordre de 5 nanosecondes en combustion. Cette étude s'articule autour de deux grands axes de recherche. Le premier est la génération, à pression atmosphérique et à pression réduite, d'espèces excitées (oxygène électroniquement excité  $O_2(a^1\Delta_g)$ ,  $O_2(b^1\Sigma_g^+)$  et oxygène atomique excité) ainsi que leur caractérisation par spectroscopie d'émission. Le second axe de recherche concerne leur utilisation pour l'intensification de la combustion. La première partie expérimentale s'est focalisée sur la génération d'oxygène électroniquement excité par plasma décharge à barrière diélectrique et décharge croisée dans des mélanges  $O_2/He$  et  $O_2/Ar$ . La décharge croisée est une cellule à barrière diélectrique pulsée qui est croisée avec une composante continue (DC). Dans ce cas, l'étape d'ionisation est réalisée par la DBD pulsée alors que la composante continue supporte le courant électrique entre chaque pulse. Le gaz produit par cette installation est étudié de manière exhaustive par spectroscopie d'émission. Ce travail, indispensable pour caractériser l'installation et obtenir les conditions initiales nécessaires pour les calculs de flamme, repose sur différents spectromètres et caméras. La première des applications potentielles dans le domaine de la combustion concerne l'intensification de la combustion par activation de l'oxygène. La conception de prototypes de brûleurs hybrides, intégrant un réacteur plasma nous a permis de valider cette technique d'intensification de la combustion et de la comparer à une flamme classique sans plasma.

Finalement, la modélisation des paramètres fondamentaux d'une flamme de prémélange et de diffusion est entreprise par le logiciel CHEMKIN. L'effet promoteur de l'oxygène excité sur une flamme d'hydrogène a pu être modélisé.

**Mots clés** : Plasma hors équilibre, décharge croisée,  $O_2(a^1\Delta_g)$ ,  $O_2(b^1\Sigma_g^+)$ , combustion assistée par plasma.

## **COMBUSTION MODIFICATION USING EXCITED SPECIES**

Nowadays it seems that the most promising method for accelerating combustion is the non-equilibrium excitation of the gas mixture components, which allows one to affect the chemical reaction kinetics. To enable more efficient excitation of the electronic and vibrational degrees of freedom, one should use short-duration (nanosecond) pulses with a high reduced electric field.

The present work focuses on the application of high frequency high voltage pulse discharges capable of delivering an electric pulse of 20 kV during 20 ns with controlled voltage rise time of 5 ns and at a frequency up to 25 kHz in combustion. This study articulates around two major research axis; that of the generation of excited species and particularly the feasibility to produce excited oxygen species in its singlet electronic states  $O_2(a^1\Delta_g)$  and  $O_2(b^1\Sigma_g^+)$  by a non-thermal electric discharge, at reduced pressure until atmospheric pressure and its characterization by emission spectroscopy. The second research axis concerns their use for the intensification of combustion. The experimental part of the study concerns investigation of singlet oxygen production in the application of a dielectric barrier discharge in  $O_2/He$  and  $O_2/Ar$  binary mixtures. The second discharge is a special crossed discharge plasma-chemical reactor that has been developed. This crossed discharge consists of a hybrid discharge in which short high voltage pulses produce ionization while a comparatively low electric field supports the electric current between ionizing pulses. The gas produced by this installation is intensively studied by emission spectroscopy. This work, indispensable to characterize the installation and to obtain initial conditions necessary for flame calculations, relies on different spectrometers and intensified camera. The first potential in the combustion field is to significantly improve combustion efficiency and reduce pollutant emissions using oxidizer "activation". Conception and development of hybrid plasma burner prototypes, integrating crossed discharge plasma reactor allows us to validate this application by comparing with a classical flame without plasma activation.

Finally, modelling of premixed flame fundamental parameters is undergone with CHEMKIN software. The promoting effect of excited oxygen on hydrogen flame has been characterized.

**Keywords** : nonequilibrium plasma, combined crossed discharge,  $O_2(a^1\Delta_g)$ ,  $O_2(b^1\Sigma_g^+)$ , plasma assisted combustion.

**Institut de Combustion Aérothermique Réactivité et Environnement (ICARE),  
1C Avenue de la recherche scientifique, Orléans, France.**

**Lehrstuhl Strömung smechnik & Strömung stechnik (LSS)**

**Otto-von-Guericke Universität**

**Universitätsplatz 2, D-39106 Magdeburg, Germany.**

